

**Optimal manoeuvres and
aeroservoelastic co-design of very
flexible wings**

Salvatore Maraniello

Imperial College London
Department of Aeronautics

This thesis is submitted for the degree of Doctor of Philosophy
and the Diploma of Imperial College London

December 2016

Declaration

I hereby declare that this thesis is the product of my own research only and no parts of it has been submitted for another degree. References or quotations from other works are fully acknowledged.

The copyright of this thesis rests with the author and is made available under a Creative Commons Attribution Non-Commercial No Derivatives licence. Researchers are free to copy, distribute or transmit the thesis on the condition that they attribute it, that they do not use it for commercial purposes and that they do not alter, transform or build upon it. For any reuse or redistribution, researchers must make clear to others the licence terms of this work.

Salvatore Maraniello

Hey, do you never say goodbye?
And now I'm so sorry
For everything I've done.

Acknowledgements

I long wondered how it would feel to write the acknowledgements of my thesis. After many year, today I finally got the answer and I can guarantee you: it is actually very fun! Without any doubt the very first person I wish to thank is my supervisor, Rafael Palacios, for being relatively patient and not complaining too much when I misbehaved. It is largely his merit — or responsibility, depending from the point of view — if I managed to endure up to this point. There is no way I can express my gratitude to him, because some parts of this journey have been very twisted yet he has always been there, and I am not even sure he fully realises how important his mentorship and advises have been in certain moments. So thanks, Rafa!

After Rafa, I wish to mention the mentors of my past: Marcus Louroza and Thomas Wilson from Airbus, and Sergio De Rosa from Federico II; and my high school Maths teacher, Vincenzo Auricchio, because ultimately it is his fault if I started to like this stuff. I am also grateful to the UK Engineering and Physical Science Research Council for giving me this opportunity and I hope I have made it count.

A proper acknowledgement would not be such without thanking a few of the people I have met in this city during these years. Without their friendship, the laughs and the crazy times together I would have never made it through these years with a sane mind. Therefore, a big thank you goes to — in order of appearance: the old office people, of whom I am the last, for welcoming me and for the laps around Hyde park! Mitch, Elvira and Anna, for summer 2013 (why did you leave me alone?) and to Max, for being my *old friend* here in London. Miguel, Cecilia, Anouk and Irene for the endless nights in Chilton. Marilia, for all the troubles and the morning coffees. My office neighbours, the MULTISOLVE people, with whom I shared some of the most painful and happiest moments of this journey (I know one day the nostalgic part of me will miss the h-bar dinners and the weekends in college!). And many of the other PhD students here at Imperial, who have been great companions and most of which I can proudly/unfortunately call friends.

Finally, a big thanks goes to my family, who has always been there for me, and to myself. Though the happy memories of these years have made them some of the best in my entire life, in recent times life has been tough. But I pulled myself together and of that I am very proud.

Abstract

The single shooting method is applied to the optimal control of very flexible aeroelastic wings and the combined structural and control design (co-design) of geometrically nonlinear beam models in vacuum. As large deflections occur, the dynamical properties of these systems can undergo substantial changes. Efficient actuation strategies require characterising, and possibly exploiting, these phenomena. With this purpose, geometrically-nonlinear models are built using composite beams and an unsteady vortex-lattice aerodynamics description. Optimal control is employed to identify actuations time-histories. Numerical solutions are obtained via single-shooting and sequential quadratic programming upon parametrisation of the control input. The approach is also extended to assess the feasibility of an integrated design strategy for active geometrically-nonlinear structures.

Numerical studies are first presented for a very flexible actuated pendulum with large rigid-body motion. The impact of local (B-splines) and global (discrete sines) basis functions is investigated for increasing levels of actuation authority, underlining the importance of the time-frequency resolution of the parametrisation on the convergence properties and outcome quality of the process. Locking between control and structural vibrations around specific design points is found, thus highlighting the limitations of a sequential design approach. Simultaneous designing of control law and structure is seen, instead, to explore more efficiently larger portions of the design space.

The lateral manoeuvring of very flexible partially-supported wings is then considered. A flight-dynamics model based on elastified stability derivatives is shown to capture the relevant dynamics either under slow actuation or for stiff wings, and it is hence used as a reference. Embedding the full aeroelastic description into the optimisation framework expands the space of achievable manoeuvres, allowing for quick wing response with low structural vibrations or large lateral forces with minimal lift losses.

Contents

Acknowledgments	7
Abstract	9
List of figures	13
List of tables	17
1 Introduction	19
1.1 Literature review and theoretical concepts	22
1.1.1 Aeroelastic modelling methods	23
1.1.2 Flight-dynamics of very flexible aircraft	26
1.1.3 Architectures for optimal control	31
1.1.4 Co-design of very flexible actuated structures	34
1.1.5 Relevant optimisation algorithms	36
1.2 Open problems and research questions	37
1.3 Present approach	39
1.4 Dissertation outline	41
1.5 Publications based on this work	42
2 Aeroelastic modelling of geometrically nonlinear wings	45
2.1 Rigid-flexible body dynamics of a geometrically-exact beam	46
2.1.1 Notation and frames of reference	46
2.1.2 Finite rotations	47
2.1.3 Kinematic relations	49
2.1.4 Dynamics of the unrestrained beam	51
2.1.5 Enforcing kinematic constraints	55
2.1.6 Discretised form of the equations of motion	57
2.1.7 Time marching scheme	58
2.2 Unsteady vortex-lattice method	60
2.2.1 Solution of potential flow using singularity elements	60
2.2.2 Numerical solution via vortex-elements	62

2.2.3	Aerodynamic loads	66
2.3	Multidisciplinary integration and fluid-structure interaction	67
2.3.1	Mapping between structural and aerodynamics discretisations . . .	67
2.3.2	Time integration	69
3	Numerical solution of the optimal control problem	71
3.1	Problem statement	71
3.2	Numerical solution	73
3.3	Control parametrisations	77
3.4	Problem formulation vs. optimal control nature	79
3.5	The SLSQP algorithm	84
3.5.1	Optimality conditions	85
3.5.2	Wilson-Han-Powell method	86
3.5.3	Algorithm efficiency	88
4	Optimal control of very flexible structures	91
4.1	Structural model verification	92
4.2	Compound pendulum: problem description	95
4.3	Optimal actuation of a compound pendulum	97
4.3.1	<i>Stiff</i> pendulum	98
4.3.2	<i>Flexible</i> pendulum	101
4.3.3	Path dependency vs. problem formulation	102
4.4	Parametrisation vs. system nonlinearity	105
4.5	A multi-resolution strategy	107
5	Co-design of flexible active structures	111
5.1	Problem description	111
5.2	Initial condition: sequential vs. co-design	113
5.3	Robustness of the design	116
5.4	Impact of frequency resolution	117
6	Optimal manoeuvres with very flexible wings	121
6.1	Rolling dynamics of very flexible wings	122
6.1.1	Equilibrium of the hinged wing	122
6.1.2	Model verification and stability study	123
6.1.3	Roll dynamics under fixed control	124
6.2	Roll Dynamics using elastified stability derivatives	129
6.2.1	Elastified flight-dynamics model	129
6.2.2	Elastified stability derivatives	131
6.3	Optimal control of flexible wings	135
6.3.1	Assessment of the optimal control approach	136

6.3.2	Trade-off between fast and smooth wing response	140
6.3.3	Unconventional manoeuvres - combining lateral and vertical dynamics	142
7	Conclusions	147
7.1	Summary	147
7.2	Key contributions	149
7.3	Recommendations for future work	153
	Bibliography	155
A	Numerical methods for quadratic programming	163
A.1	Primal active set strategy	163
A.2	Least-squares method of Lawson and Henson	165
B	Details of the SLSQP algorithm	169
B.1	ℓ_1 test function	169
B.2	Approximation of Hessian matrix	170
C	Gradient convergence test	173

List of Figures

1.1	Some representative HALEs.	20
1.2	Impact of structural reinforcement on the flying shape of very high aspect-ratio wings.	21
2.1	Definition of frames of reference over the very flexible structure	47
2.2	Cut-out of the potential flow solution domain of the potential flow problem.	61
2.3	Schematics of wing and wake vortex lattices.	63
2.4	Comparison of different models of wake for a high-aspect-ratio wing during a rolling manoeuvre.	66
2.5	Loosely coupled scheme for aeroelastic solution.	70
3.1	Comparison between third-order B-splines obtained when doubling the non-dimensional frequency $2T f_{max}$	79
3.2	Optimal ailerons deflections and wing response for problems (3.24), (3.29) and (3.33).	81
4.1	Geometry of rigid compound pendulum.	92
4.2	Time histories of the tip position of a free falling rigid pendulum in horizontal position at time $t = 0$ s.	93
4.3	Time histories of the attitude of the local frame A , described in terms of pitch (Θ), roll (Φ) and yaw angles.	94
4.4	Error between the numerically predicted period of oscillation and the one provided by the analytical solution in eq. (4.3) for different time steps and initial pitch attitudes, Θ_0 , of the body frame A	94
4.5	Free falling hinged flexible beam (the beam is horizontal at time $t = 0$ s).	95
4.6	Flexible pendulum geometry	95
4.7	Snapshots (25 frames per second) of the <i>stiff</i> pendulum response for the optimal actuation with a control maximum frequency $f_{max} = 2$ Hz using a DSS parametrisation. (Initial shape in red)	98
4.8	Time histories under optimal control of the <i>stiff</i> pendulum using different parametrisations of the torque signal.	99

4.9	Snapshots (25 fps) of the <i>stiff</i> pendulum response for the optimal actuation obtained using a B-spline parametrisation with $N_c = 43$ control points ($f_{max} = 10$ Hz). Initial shape in red.	100
4.10	Cost function, I , associated to a <i>rigid</i> pendulum when varying the amplitude of the sine waves parametrising the actuating torque, M_Y	100
4.11	Snapshots (25 fps) of the <i>flexible</i> pendulum response for $t \in [1.60, 2.00]$ s with optimal control parametrisation having a maximum frequency $f_{max} = 1.5$ Hz. (Initial shape in red)	102
4.12	Time histories under optimal control of the <i>flexible</i> pendulum using different parametrisations of the torque signal.	103
4.13	Snapshots (25 fps) of the <i>flexible</i> pendulum response for the optimal actuation obtained using a B-spline parametrisation with $N_c = 19$ control points ($f_{max} = 4$ Hz). Initial shape in red.	104
4.14	Comparison between spline and DSS optimal actuation for <i>flexible</i> pendulum case and no penalty factor.	104
4.15	Design of experiment for different parametrisations and level of actuation P_{max}	106
4.16	Optimal actuation frequency content ($ x_{ci} $) using a DSS parametrisation ($f_{max} = 6$ Hz) and a constrained problem formulation (4.8). Different levels of actuation, P_{max} , are allowed.	106
4.17	Optimal actuation in the transition region ($l_3 = 0.0750$ m and $P_{max} = 4$) using different parametrisations.	107
5.1	Optimal actuation provided by the co-design using different starting conditions and parametrisations.	114
5.2	Visualisation of velocity profile for a high bandwidth actuation, modelled with a reduced number of sine waves, for structural designs in the neighbourhood of $l_3 = 0.1$ m. Points A , B and C correspond to the coordinates of the local maxima found for $l_3 = 0.1$ m	115
5.3	Tip horizontal position and torque moment M_Y time histories for $t \geq 1.8$ s. Results are for the <i>stiff</i> pendulum under the reduced DSS parametrised actuations corresponding to points A, B and C in Fig. 5.2a.	116
5.4	Optimal control torque (parametrised with B-splines) for structural designs in the proximity of $l_{ref} = 0.0715$ m for small ($P_{max} = 2$) and large ($P_{max} = 6$) amplitude oscillations.	118
6.1	Steady-level flight trimmed conditions for different values of the stiffness parameter σ	123
6.2	Visualisation of first two natural modes — vertical bending and in-plane bending/torsion — of a $\sigma = 1.1$ wing clamped at its root.	125

6.3	Ailerons deflection used for the study of the nominal rolling manoeuvre performance of flexible wings and snapshots of wing response for $\sigma = 1$ and $\sigma = 50$	126
6.4	Roll attitude and lateral force time history for an ailerons antisymmetric deflection with different values of the stiffness parameter σ	126
6.5	Comparison of loads distribution at different times of the nominal rolling manoeuvre for wings having a stiffness of $\sigma = 1$ and $\sigma = 10$	127
6.6	Tip bending deflection (normalised by the semi-wing span) and torsion during the nominal rolling manoeuvre for a wing of stiffness parameter $\sigma = 1.1$	128
6.7	Definition of frames of references used for the flight-dynamics model . . .	130
6.8	Rigid and elastified stability derivatives for wings of different flexibility, σ , around a level flight equilibrium point.	132
6.9	Total lateral force, expressed as a function of roll attitude through the analytical relation (6.8) and through a full aeroelastic analysis, for a very flexible ($\sigma = 1$) and a stiff ($\sigma = 50$) wing.	133
6.10	Wing response to an antisymmetric aileron deflection from elastified flight-dynamics model and full aeroelastic analysis.	134
6.11	Decomposition into the terms appearing in eq. (6.6) of the total rolling moment for $\sigma = 1$ under the aileron deflection defined in Fig. 6.3a. . . .	134
6.12	Reference anti-symmetric actuations and aeroelastic response for wings different stiffness. The control inputs have been derived for different maximum excitation frequency, f_{max} , based on the EFDM description. . . .	138
6.13	Details of the $\sigma = 1.1$ wing full aeroelastic response to the ailerons input in Fig. 6.14.	139
6.14	Optimal anti-symmetric actuations $\beta_L = -\beta_R$ for wings of different stiffness obtained via single-shooting (using a full aeroelastic model) against the reference cases (based on the EFDM description).	140
6.15	Wings response, computed through a full aeroelastic analysis, to the ailerons input in Fig. 6.14.	140
6.16	Impact of segmentation in defining the optimal actuation on a very flexible wing ($\sigma = 1.1$).	141
6.17	Integral kernel of eq. (6.12) for optimal manoeuvres computed with and without segmentation of the cost function. The kernel is evaluated for different values of the weight w_S , associated to the lateral force error during the second stage of the manoeuvre.	142
6.18	Optimal aileron inputs, and wing response, associated to the lift-constrained rolling manoeuvre of a $\sigma = 1.5$ wing for anti-symmetric and independent actuation.	143

6.19	Front view of the aerodynamic loads acting on a wings of different stiffness parameter, σ , at the end of a rolling manoeuvre performed using both anti-symmetric and independent aileron commands.	145
6.20	Visualisation of the roll attitude and isolines of the lateral and vertical forces produced at the steady state by a $\sigma = 1.1$ and a $\sigma = 1.5$ wing for different aileron deflections (β_L, β_R) . Points A, B, C and D correspond to representative configurations.	146
6.21	Comparison of the aerodynamic loads and wing deformed configuration of representative points of the space (β_L, β_R) shown in Fig. 6.20a.	146
C.1	Second-order Taylor reminder, \mathcal{T} , as a function of the perturbation size, h . The FD gradient is computed for different steps, Δx	174

List of Tables

1.1	Possible modelling scenarios for vehicles dynamics and stability analysis according to Baldelli et al. [1].	27
4.1	Pendula structural properties for the optimal control problem.	97
4.2	Optimal control results of the <i>stiff</i> pendulum using different parametrisations.	98
4.3	Optimal control results of the <i>flexible</i> pendulum using different parametrisations.	102
4.4	Optimal control results for the <i>stiff</i> and <i>flexible</i> pendulum using the constrained formulation (4.8) and setting $P_{max} = 6$	103
4.5	Optimal control results at different stages of a multi-resolution based process using a DSS parametrised actuation ($f_{max} = 12$ Hz).	108
5.1	Results of the combined optimisation problem using DSS control parametrisations of different basis size. Percentage values are with respect to the optimal control only case (DOE).	112
5.2	Results of the combined optimisation problem using spline control parametrisations of different basis size. Percentage values are with respect to the optimal control only case (DOE).	113
5.3	Performance gains obtained using a two-stage co-design strategy.	117
5.4	Results of the combined optimisation using a multi-resolution strategy and a DSS parametrisation. Two different actuation bandwidth of 4 Hz and 6 Hz has been chosen to start the process.	120
6.1	Hinged wing properties.	122
6.2	Flutter speeds for wings of different stiffness, σ , at flying attitude as per Fig. 6.1a.	124
6.3	Steady state performance of wings of different stiffness σ when allowing, or not, the control surfaces to move independently. Note that $F_T = 0.4L$	144

Chapter 1

Introduction

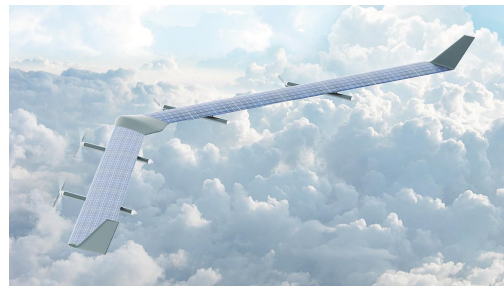
Since the early 1930s, when the transition from wood and fabric to metal aeroplanes occurred, aircraft design has been predominantly characterised by relatively heavy materials and stiff structures [2, 3]. While the quest for high efficiency and low structural weight have always represented the leitmotiv of aeronautical engineering, slightly oversized airframes often offered the only practical solution for increasing the robustness of aircraft design. By introducing a level of conservatism, these allowed to overcome some of the modelling uncertainties associated to the design process and guarantee, this way, safe flight. The need to boost airliners revenue, fuel prices uncertainties and, more recently, growing concerns about climate change, are, however, only a few of the factors which kept encouraging the chase for higher fuel efficiency. In civil aviation, this trend translated in the launch of the Airbus A350 XWB and the Boeing 787 Dreamliner aircraft families. Aside for improved engine economy and low drag wings, the large cut-down in operational cost and CO₂ emissions claimed by their manufactures is also merit of a considerable weight reduction, achieved through a large use of composite materials (arriving to around 50 % of the total structural weight) in the wing and the fuselage primary structures.

The level of weight reductions in civil or, more generally, manned aircraft is, however, bounded by the presence of humans and by the safety requirements associated to it [4]. Uninhabited aerial vehicles (UAVs) offer, instead, an expanded design range in which aircraft concepts capable, or aiming to, satisfy extreme operational requirements can fit. Recent developments in communications systems and airborne sensors, in particular, have lead to a large interest for high-altitude long-endurance (HALE) unmanned aircraft, that could be used for surveillance, reconnaissance or also as pseudo-satellites [5–7]. These novel aircraft concepts are required extremely long missions if not even *perpetual* flight. Some HALE prototypes, like the solar powered Airbus Zephyr 7 — which set a world record 336 h flight at altitudes above 70 000 ft, have already took flight (Fig. 1.1a). Others, like the over 40 m wing-span facebook Aquila (Fig. 1.1b), are still in early development, but their target missions would last months and would require flying

at altitudes between 60 000 ft and 90 000 ft.



(a) Airbus Zephyr 7
Image credit: Airbus Defence & Space



(b) facebook Aquila
Image credit: facebook

Figure 1.1: Some representative HALEs.

Aircraft range mainly depends on weight, engine efficiency and lift to drag ratio [8]. As lift is constrained by the aircraft weight, reducing drag is possibly the primal goal of aircraft design when endurance requirements are extreme. To better understand what are the main parameters affecting the vehicle drag, one can refer to the drag polar equation [4]

$$C_D = C_{D0} + \frac{C_L^2}{\pi e AR} \quad (1.1)$$

which provides a quick estimate of the dependency of the drag coefficient, C_D , upon the lift coefficient, C_L . In eq. (1.1) C_{D0} is the zero lift drag, which depends upon the wing profile drag and the friction and pressure drag produced by all the aircraft components — fuselage, engines, control surfaces, etc. The second term in eq. (1.1) is, instead, referred to as induced drag and is inherently associated to the lift. This is, in fact, due to the downwash produced by the wing tip vortices structures, and depends on the wing aspect ratio, AR . The Oswald factor e is a correction term of order one which, at subsonic speeds, will depend on the wing planform only.

The drag polar equation shows that large AR s, hence large wing spans, are essential for reducing drag and increasing flying autonomy. Furthermore, large wing areas are needed for producing enough lift when flying at relatively low speeds and altitudes above 60 000 ft, where the air density is below 10 % the sea level values. From a structural perspective, however, large wing spans also imply potentially high bending moments at the wing root. To withstand these, the wing can be reinforced, as shown by the truss-braced wing concept of the SUGAR Volt hybrid aircraft, Fig. 1.2a [9]. As underlined by the survey from Cavallaro and Demasi [10], however, the assessment of which class of aircraft may benefit more from *joined wings* concepts is still an open research questions, especially due to the highly multidisciplinary nature of these systems. In particular, a very careful design would be required to ensure robustness against buckling and flutter instabilities while maintaining light airframes. These concepts remain very promising for large transportation aircraft, whose layout provides greater margin than in HALE

aircraft. In the latter case, instead, most design solutions still consider slender and very flexible wings, possibly exhibiting large deflections in flight, as the best compromise for achieving large wing spans while minimising structural weight. This was the case of the Helios aircraft shown in Fig. 1.2b.



(a) Sugar Volt hybrid aircraft
Image credit: Boeing



(b) NASA Helios HALE
Image credit: NASA

Figure 1.2: Impact of structural reinforcement on the flying shape of very high aspect-ratio wings.

Designing this kind of vehicles is, however, a challenging task, especially because modelling techniques have long been tailored for stiffer wings, which exhibit small structural deformations and frequency separation between flight-dynamics and structural modes [3]. Exploiting these features, structural models are often based on linear descriptions, while flutter and flight-dynamics analysis are separated [1]. The first ones, in particular, commonly adopt a frequency description, while the latter rely either upon flex-to-rigid corrections of the aircraft stability derivatives [3, 11] or the mean-axis approximation [12, 13]. The inadequateness of these techniques for the modelling of very flexible wings vehicles was proved by the mishap of the NASA Helios prototype in 2004 which, according to the subsequent technical investigation, was due to an unexpected change of the wing configuration following a gust. The related report highlighted the need to develop *more advanced multidisciplinary (structures, aeroelastic, aerodynamics, atmospheric, materials, propulsion, controls, etc.) "time-domain" analysis methods appropriate to highly flexible, morphing, vehicles and procedure to control wing dihedral in flight* [14].

An excellent re-examination of design procedures for very flexible vehicles is provided by Cesnik et al. [3]. In this work, four major areas of improvements with respect to standard procedures are identified:

1. *the deformed aircraft geometry [...] should now be the baseline in weight, structural and stability analyses;*
2. *transient dynamic simulations should include large nonlinear displacements;*
3. *aeroelastic models should incorporate rigid-body motion;*

4. flight-dynamics models should incorporate nonlinear aeroelastic effects.

In order to address these points, a number of fully coupled simulation strategies, based on a geometrically nonlinear description of the wing structural model [15, 16], have been developed in the last two decades [17–19]. As a consequence of point 4, however, the complexity of the aircraft flight-dynamics description is largely increased and becomes harder to define and assess manoeuvres on the vehicle, particularly regarding their optimality with respect to any energy efficiency or handling quality based performance requirement. On the other hand, unconventional manoeuvres which exploit aeroelastic effects may also be employed to enhance performance. Control surfaces, for instance, could morph the very flexible wing and correct its aerodynamics, so as to improve handling qualities or reduce structural loads. Also the vibrational dynamics, likely to arise during manoeuvring when airframes have low stiffness, may be exploited for extra performance; if not possible, the impact of vibrations suppression on the vehicle manoeuvrability features should still be minimised. These considerations lead directly to the main scope of this research, which will consider optimal control for defining manoeuvres with very flexible wings.

As numerical methods for optimal control are closely linked to the theory of optimisation, a framework for optimal control of very flexible vehicles would, ideally, also allow for a relatively straightforward extension to an integrated structural/control design. In fact, dynamic effects are likely to be relevant when actuating very flexible structures and it is important to assess how vibrations and actuation mutually influence each other from an early stage development phase [20]. For this reason, this research may have a relevant impact not only in the design of very flexible wings HALE aircraft but also on other novel structures characterised by geometrically nonlinear dynamic response, such as novel horizontal axis wind turbines (HAWT).

1.1 Literature review and theoretical concepts

As briefly introduced in the preface of this chapter, a methodology for defining manoeuvres for vehicles with very flexible wings requires firstly establishing a computationally efficient description of their flight-dynamics. The state of the art for the aeroelastic modelling of geometrically nonlinear wings is, therefore, presented in Sec. 1.1.1. Sec. 1.1.2 will, instead, show how these methodologies are exploited to characterise the flight-dynamics of very flexible aircraft and how the model fidelity changes when the control of these systems is considered.

Next in order, a methodology to define manoeuvres needs to be chosen. For this reason Sec. 1.1.3 will review relevant numerical methods for optimal control. As this work will also include studies on the co-design of active structures, an overview of the topic, which shows connections of this research with non-aeronautical fields like robotics, is presented in Sec. 1.1.4. A final discussion on state of the art of gradient-based

optimisation algorithms will conclude this review (Sec. 1.1.5).

1.1.1 Aeroelastic modelling methods

Models for flight-dynamics and, more generally, FSI differ greatly in terms of scope, hence accuracy and computational cost. The literature is vast. Here, the focus will be on modelling techniques for the flight-dynamics of very flexible vehicles. A high fidelity modelling of these systems based on CFD and nonlinear FEM would require structural and aerodynamic models with an extremely large number of degrees of freedom and characterised by complex dynamic interactions. While this kind of analysis is possible [21–23], its computational cost is still prohibitive for applications in pre-design or time-domain optimisation. A compromise between accuracy and computational cost is, therefore, necessary. Through reduction techniques, geometrically-exact beam models (GEBM) are therefore widely used to model slender wings, while the modelling of low speed aerodynamics typically exploits boundary elements methods or strip-line theory. Developments and features of these solution techniques are presented in the remaining part of this section.

Coupled rigid/flexible body dynamics of slender bodies

Structural models for aeroelastic analysis of flexible aircraft should address three main requisites. From a physical perspective, they should capture accurately the large wing deflections, which change the aerodynamic features of the vehicle. As the stiffness of the primary structures is reduced, however, the natural frequency of the vibrational modes is also decreased and coupling effects between flexible and rigid dynamics are strengthened. By modifying the airframe inertial properties, deflections impact the rigid-body dynamics, while gyroscopic loading have a non-negligible contribution to the deformed wing shape. These effects are crucial, as they make the very flexible vehicles particularly vulnerable to atmospheric gust and affect its manoeuvrability features. Numerical models should, therefore, describe them adequately. For an efficient integration in a multidisciplinary FSI framework, however, a structural model should also limit the computational cost associated to time-domain analysis. This is especially true in pre-design phase, when a large number of analysis may be required in order to gain an insight into the complex dynamics of these vehicles.

In order to obtain computationally treatable models, the wing and fuselage of the very flexible vehicle are generally modelled through beam finite elements (FE). Due to their slenderness, in fact, large scale deflections are typically dominant along the span-wise direction, while only small scale displacements occur along the other dimensions. Furthermore, a number of cross-sectional reduction techniques have been developed to account for the latter [24, 25]: these allow considering warping effects and to condensate in one-dimensional elements the cross-sectional properties of more complex composite

structures. More recently, Wang et al. [26] have also proposed a reduction technique for condensing a full three-dimensional FE models into a one-dimensional description based on nonlinear beam elements. The use of unidimensional elements does not only provide a computational saving but is also less likely to incur into numerical instabilities [27]. For this reason, their use has spread widely not only for HALE aircraft modelling, but also in other applications involving very slender components, such as HAWT [28–30].

Conventional linear beam elements are, however, not adequate for capturing the large deflections that may occur with very flexible wings. Geometrically-exact beam models (GEBM) are, instead, required [31]. However, while displacements and rotations can be arbitrarily large, GEBM typically assume linear material constitutive equations, i.e. small deformations. Earlier GEBM formulations, in particular, dealt directly with displacements and rotations as primary variables [32, 33]. These descriptions assumed isotropic materials, but formulations based on anisotropic ones are also found [19]. Several parametrisations can be used to describe rotations: Simo and Vu-Quoc [34], for instance, adopted quaternions, while Gerardin and Cardona [35] exploited Cartesian rotation vectors to reduce the problem size. In FE implementations, however, the rotations within each element are obtained by interpolations and objectivity issues can arise, i.e. the strain field may not be invariant under rigid-body rotations [36, 37]. Fine meshing and high order elements are necessary to address this point [38].

On the contrary, strain based descriptions [39, 40] use force and moment strains as independent variables and do not integrate rotations during the solution process. As a result, simple shape functions can be used without incurring into objectivity issues and also the shear locking is avoided [40]. However, as the displacement field need to be obtained as a post-processing step, the advantages of this description are reduced when integrated into a FSI analysis framework.

Hodges [15], instead, introduced a mixed three-field variational formulation, in which constitutive and kinematic relations are enforced simultaneously to Hamilton’s principle. This simplifies the solution process, but increases the number of independent variables — displacements and rotations plus the associated strains and velocities. A two field description, solving the equations with respect to velocity and strains only, can thus be introduced [41]. Also this formulation guarantees objectivity and, if external forces do not depend on the body orientation, the nonlinearity of the system is also reduced. A procedure to build an intrinsic beam description from a full three dimensional finite-element model has been proposed by Wang et al. [26].

In all these theories the dynamics of the beam reference line is always derived with respect to an inertial frame of reference. These formulations, therefore, inherently include coupling inertial effects between rigid-flexible body dynamics, making them especially suitable for flight-dynamics applications. An assessment of these models was done by Palacios et al. [19]. Numerical studies showed quadratic convergence when employing an intrinsic description, which is reduced to linear for the displacement based solution.

Overall, strain-based and intrinsic models provide better convergence rates, as rotations are not integrated. Displacements based formulations, instead, suffer from objectivity issues and require careful meshing. However, FSI coupling and the implementation of kinematic constraints are facilitated.

Low-speed aerodynamics

Low to medium fidelity tools are the predominant choice for FSI problems dealing with dynamics of very flexible structures and attached, high-Reynolds, flows — for typical HALE aircraft this is of the order 10^5 , but can be as large as 10^7 for large HAWTs. While high fidelity CFD based solutions, typically employing RANS or LES [21, 22], are becoming more common, they are still computationally demanding and not yet adequate when a large number of time-domain analysis is required, as in preliminary design or time-domain optimisation. Therefore, their applicability remains confined to single analysis [23] or static aeroelastic optimisation [42, 43].

As large portions of the flight envelope of a typical HALE aircraft are characterised by low-speed and fully-attached aerodynamics, potential theory can be used. The flow is thus assumed to be inviscid, incompressible and irrotational [8, 44]: while only the induced drag can be modelled, under these flow conditions the lift prediction is accurate enough to characterise the aeroelastic behaviour of HALE lifting surfaces. Boundary elements methods, in particular, allow for an efficient numerical treatment of these flows: the problem of determining the three dimensional velocity field around the wing is, in fact, reduced to a two-dimensional one, where the unknowns are the intensities of a number of elementary solutions, also known as singularities, distributed over the aerodynamic surfaces. For this reason, this class of solutions is also referred to as panel methods. In order to satisfy the conservation of the angular momentum, however, a modelling of the wake is also required. Through an appropriate choice of singularities and wake evolution assumptions, different methods are obtained [44]: an excellent classification of these, based on the kind of flow solutions (unsteady vs. steady, frequency vs. time domain) and reduced aeroelastic frequencies validity range is provided by Murua et al. [45].

In particular, the doublet-lattice method (DLM) has long been the standard industrial tool for the low speed unsteady aerodynamics of fixed wing aircraft [46, 47]. As the formulation is in the frequency domain, the DLM is particularly suitable for flutter and aeroelastic analysis: the impact of structural vibrations can, in fact, be computed at different frequencies by assuming small out-of-plane perturbations of the doublet panning [48, 49]. While the method can be extended to the time-domain through rational-function approximations [50], corrections are required for computing steady loads [1, 45] for flight-dynamics and the wing kinematics is limited: displacements need to be small and normal to the lifting surface, while the wake is commonly assumed to be flat.

In the unsteady vortex-lattice method (UVLM), instead, lifting surfaces can undergo

arbitrarily-large geometrical changes. While based on a linear theory, nonlinearities are introduced in the solution by boundary conditions enforcement at the lifting surfaces. Furthermore, the free-force wake is derived as part of the solution enforcing conservation of the angular momentum in the flow field [44]. In particular, as large deflections occur, this *follows* the wing, which allows capturing the lag of the unsteady aerodynamic forces over a wide range of reduced aeroelastic frequencies [51, 52]. For these features, the method has been employed in a number of aeroelastic simulations of very flexible aircraft dynamics [31, 45, 53]. Note that, while the solution process is in the time-domain, a linearisation of the model under the assumption of frozen geometry allows to express the aerodynamics in state-space form, which makes it suitable for stability analysis [45]. Importantly, the explicit modelling of the wake allows to simulate the interference between different aerodynamic surfaces [54], which is critical for the analysis of T-tail flutter or unconventional aircraft configurations [55].

Finally, the very high aspect-ratio characteristic of HALE aircraft wings has often justified the use of strip-line based aerodynamics [8]. Several aeroelastic frameworks [39, 56] have, for instance, used the finite states model of Peters et al. [57], which exploits the aerodynamic data of the wing cross-sections and includes stall and tip losses corrections. The flat wake assumption and the absence of span-wise coupling associated to this approach, however, makes them to lose accuracy as large out-of-plane, but possibly also in-plane, bending deflections occur. Especially at low frequencies, the three-dimensional effects associated to these configurations, which are captured by the UVLM, are important [19]. At higher frequencies, instead, the span-wise correlation is reduced and the accuracy of finite states models improves. Despite their lower fidelity, however, strip methods allow for an easier integration of semi-empirical corrections based on aerofoil data. These have also been recently proposed for UVLM, although they require substantial calibration [51, 53].

1.1.2 Flight-dynamics of very flexible aircraft

Modelling the fluid-structure interaction of a flying vehicle requires a multidisciplinary effort which easily translates in very expensive computational models. However, aircraft design has long been characterised by relatively stiff wings, exhibiting small structural deformations and with high-frequency structural dynamics. Therefore, flight-dynamics and aeroelastic analysis, whose responses would typically be separated by an order of magnitude, could traditionally be disjointed without loss of accuracy [3]. This distinction is captured in Tab. 1.1, where computational models for FSI analysis are classified based on the fidelity of their structural and aerodynamics descriptions [1].

Flight-dynamics has traditionally been concerned with the manoeuvring of a rigid aircraft. Low frequency responses, in particular, allowed using quasi-steady aerodynamics [58]. Aeroelastic analysis would, instead, refer to the stability of a flexible vehicle [59] and higher frequency dynamics and an unsteady aerodynamics description, typi-

Aerodynamic forces	Structural dynamics	
	Omitted	Included
Quasi-steady	Flight-dynamics	Quasi-steady aeroelastic
Unsteady	Full-frequency flight-dynamics	Full aeroelastic

Table 1.1: Possible modelling scenarios for vehicles dynamics and stability analysis according to Baldelli et al. [1].

cally based on a DLM, would thus be required. Furthermore, the aircraft attitude could be frozen, hence allowing to linearise the rigid-body dynamics or to exploit clamped structural models. This customisation is, however, not possible when dealing with very flexible aircraft flight dynamics, as deflections may be nonlinear and inertial coupling between rigid and flexible body dynamics arise [3]. The remaining part of this section will, therefore, discuss how modelling techniques evolved to deal with this extra degree of complexity and to merge flight-dynamics and aeroelasticity.

From stiff to very flexible wings

Tools for flexible vehicle flight simulation often rely on *elastified* stability derivatives, obtained upon correction of the rigid-aircraft stability derivatives with flex-to-rigid ratios provided by a linear quasi-static aeroelastic analysis [3, 11, 60]. This approach leads to the easiest simplification: structural deflections are assumed to be very small and their inertial effects, as well as the rigid/flexible body coupling, are neglected; vibrations are high frequency and do not impact the wing aerodynamics; this is quasi-steady and described through stability and control derivatives only. As shown in this work, elastification of the stability derivatives is possible also as a first approximation of the response of very flexible vehicle, as long as the wing deformed configuration at trim is used as a reference.

For loads prediction and flight control development, however, inertial effects may become relevant even when structural vibrations are within the linear regime. To account for these, flight-dynamics equations can be augmented with a finite-element model of the aircraft primary components. Widely spread is the mean-axes approach [61], which relies on the identification of a floating frame in which the angular and linear momenta of the vibrational motion are null [62]. An advantage of this formulation is that the inertia coupling terms responsible for gyroscopic effects and the Coriolis force can be easily identified and, under the hypothesis of low-energy/small-amplitude vibrations, neglected [12, 13, 63]. This leads to a set of structurally and inertially decoupled equations of motion: mean and principal axes can be assumed to coincide [62] and a modal representation of the vehicle structure dynamics based on its free-free modes can be

superimposed to the rigid dynamics equations [63, 64].

Coupling effects can, however, be relevant also when the structural dynamics is linear [12, 65]. In this case, the mean axes formulation becomes more involved [12, 13, 65]. A unified formulation accounting for these effects has been derived by Meirovitch and Tuzcu [58] employing a linear structural model and quasi-steady aerodynamics. Similarly, Baldelli et al. [1] extended a DLM based aeroelastic framework to incorporate their flight-dynamics; rational functions are employed to approximate the aerodynamic forces in the time-domain and a full aeroelastic model is obtained.

As wings with higher aspect ratio and flexibility are considered, however, large deflections can occur not only within different points of the flight envelope but also within a single manoeuvre. As shown by the Helios mishap [14], these can strongly affect the aerodynamic features of the vehicle and need, therefore, to be captured. In order to address this, a number of fully coupled simulation strategies, based on a geometrically exact description of the wing structural model, have been developed in the last two decades [18, 19, 31, 53, 66, 67]. Importantly, GEBM are inertial-frame methods and automatically account for the coupling between rigid and flexible body dynamics.

A first work from Drela [66] led to the develop of ASWING, a framework for very flexible aircraft flight-dynamics. Beam elements linked via nonlinear joints were used to model the large deflections of an isotropic wing, while a lifting line model with compressibility corrections described the aerodynamics. These simplifications allowed to obtain a computationally tractable model, adequate for preliminary design and for both time-domain and stability analysis. Numerical studies for the SensorCraft program verified the importance of inertial coupling effects on the dynamics of very flexible vehicles [68].

An extension to composite beams arrived with Patil et al. [56, 67], which coupled an intrinsic GEBM description of the wing with a finite-state aerodynamic model [57], including stall and corrections for unsteady effects. This solver formed the core of the NATASHA (Nonlinear Aeroelastic Trim And Stability of HALE Aircraft) framework [69], which has later been used to investigate a number of nonlinear effects associated to the large wing flexibility. Limit cycle oscillations were, for instance, found to occur above flutter speed due to nonlinear stiffness effects [56, 70]. As a result of the large dihedral, instead, phugoid instabilities [69] and a reduction of the flutter speed [70, 71] have been observed. By modelling the vehicle as a multi-beam body, furthermore, the flight-dynamics and the stability of the trimmed aircraft could also be investigated for a range of different manoeuvres [17, 72].

In parallel to those developments, Cesnik and Brown [39] adopted a strain-based structural dynamics formulation and finite-state aerodynamics. This facilitated the modelling of piezocomposite actuators embedded in the wing, whose feasibility was studied focusing on rolling manoeuvres. The investigation also highlighted coupling effects between actuation input and the first anti-symmetric roll mode of the wing. This solution provided the foundation for UM/NAST, the University of Michigan Nonlinear Aeroelas-

tic Simulation Toolbox [18, 73]. Investigations from the same research group focused on full-vehicle flight-dynamics studies. By comparing different flight-dynamics formulations — i.e. a rigid, a linearised and a nonlinear structural model — Shearer and Cesnik [18] assessed the importance of nonlinear effects due to large deflections during asymmetric manoeuvres. Su and Cesnik [73], instead, provided a detailed analysis on body-freedom flutter. Numerical investigations were assessed against experimental results, proving that the rigid/flexible body coupling can alter the flutter modes of the vehicle.

ASWING [66], NATASHA [69] and UM/NAST [18, 73] all rely on a finite-state aerodynamic description, predominantly justified by the large aspect-ratio of HALE aircraft. For capturing more accurately three-dimensional effects, Wang et al. [53] coupled the UVLM with an intrinsic GEBM structural model in the NANSI (Nonlinear Aerodynamics/Nonlinear Structure Interaction) framework. Their investigations focused on gust response and outlined the importance of this higher fidelity description in identifying the instabilities associated to large wing dihedral angles. Murua et al. [54] also employed a UVLM description coupled with a displacements based geometrically-exact description of the structure. The resulting framework (SHARP, Simulation of High Aspect-Ratio Planes) has been extensively verified in following investigations [16, 29, 45, 74, 75], which included assessments of the wake-tail interference effects [74], the development of linearisation techniques aiming to reduce the computational cost associated to flight dynamic analysis [75] and applications to loads control in large HAWT blades [29].

With the aim of improving the accuracy of the aerodynamics description, Hallissy and Cesnik have also developed a coupled aeroelastic solution based on an Euler flow and an intrinsic GEBM [76]. Comparisons against UM/NAST [18, 73] shows good agreements but highlights that the lower fidelity description can be conservative. However, the analysis presented in this work are limited to stability and flutter, hence the wing does not experience large deflections from its trim configuration. The higher computational cost of this solution and the meshing problems that may result when large geometrical changes during a single analysis make, overall, CFD based approaches still prohibitive.

From a completely different perspective, instead, Klöckner et al. [77] focused on creating a multi-disciplinary description of the solar-powered vehicle. This resulted into a framework integrating the aircraft fundamental systems, i.e. modelling its aerodynamics, propulsion and energy systems, actuators and aeroelastic behaviour. Even an environmental module describing the atmosphere properties and predicting the solar irradiation patterns was included. A relatively low-fidelity description of each of these models was, however, required: the quasi-steady aerodynamics, for instance, is based upon tabulated values derived from VLM analysis and corrected through Xfoil data, while the aeroelastic analysis are based on a DLM description. Nonetheless, this created an environment which, through appropriate adjustment of the modelling fidelity of each sub-system, could potentially be employed at any stage of the vehicle design cycle, from pre-design analysis to the integration in a feedback control system.

Overall, in the last two decades a large number of studies have investigated the features of very flexible wings. This required a paradigm shift in the analysis, with the integration of flight-dynamics and aeroelasticity and the development of new tools based on a nonlinear description of the vehicle flight-dynamics. These investigations underlined the higher complexity of these systems and large differences with respect to the dynamics of conventional aircraft. Next section will, therefore, present how previous studies have addressed the flight control of these vehicles.

Control of very flexible aircraft

As suggested by the Helios mishap report [14], the assumption of linear time invariant systems may not be enough to describe the behaviour of very flexible aircraft. While control synthesis could benefit from a nonlinear aeroelastic description, up to date the proposed control strategies are still largely based on linear methods [16, 78, 79].

A typical solution for stability and flutter analysis consists on linearising the aeroelastic system around a forward flight trimmed condition. Exploiting the unified flight-dynamics formulation of Meirovitch and Tuzcu [58], Tuzcu et al. [79] have built a feedback LQR control for flutter suppression. In order to capture the effects of the large wing deflections at trim, Patil and Hodges [78] worked on a linearisation of a geometrically-exact description of the wing. State output feedback (SOF) control for flutter suppression and gust loads alleviation (GLA) proved high sensitivity to the sensor placement, with measurements at wing root, where twist and bending are typically higher, providing best performance. Importantly, larger perturbations required a nonlinear SOF control, obtained by gain scheduling over various wing configurations.

Following works on GLA also adopted linearisation around trim of the vehicle longitudinal dynamics and investigated the performance of different controllers. Dillsaver et al. [80], for instance, exploited the strain based formulation of UM/NAST to implement an LQG controller monitoring changes of the wing curvature. In order to investigate the maximum achievable performance through a linearised aeroelastic formulation, instead, Cook et al. [81] assumed a full-state feedback control. This work confirmed the difficulties of controlling these systems with a linear model as deflections become very large. To overcome these limitation, Haghighat et al. [82] exploited a modal representation of the system and used modal predictive control (MPC), which was found to be superior to an LQR architecture. Also this work highlighted the importance of accounting for the inertial coupling in control synthesis. These finding were confirmed by Simpson et al. [83] which used a reduced order representation of the flexible aircraft dynamics based on a geometrically-exact structural description and preserving inertial coupling effects [16]. As MPC allows for constraints, this formulation also introduced saturation of the actuators. Wang et al. [84], instead, used Hodges intrinsic beam theory [41] to provide a reduced order model with only quadratic nonlinearities. Control synthesis was, however, still based on a linearised model.

Feedback control has also been exercised for trajectory tracking. Raghavan and Patil [63] used the mean axes approximation and, assuming small deflections, decoupled the rigid-body and the flexible structural dynamics. As shown by Hesse et al. [75], however, neglecting gyroscopic couplings has a relevant impact on the vehicle dynamics even when deflections are small, meaning that the applicability of the mean axes approximation should be limited to dynamics with small angular accelerations. Furthermore, when manoeuvring very flexible vehicles, large geometric changes may alter significantly the dynamical features of the wing during the manoeuvre itself. Estimation of the trajectory should, therefore, be based upon a nonlinear aeroelastic description of the aircraft.

To address this point, Shearer and Cesnik [85] developed a heuristic method for trajectory control based on a geometrically-exact description of the wing dynamics. The architecture is composed by an outer loop, which mimics the behaviour of a human pilot, and an inner one, which stabilises the fast dynamics. However, a number of assumption on the vehicle dynamics are made, while longitudinal and lateral dynamics are handled separately. As shown by Dillsaver et al. [86], therefore, this method lacks of robustness and required corrections to avoid instabilities, including gains scheduling at different stages during manoeuvring. Aside from this limitation, the use of an heuristic approach makes it clear that the achieved control is likely not to be optimal.

Overall, previous works aiming at regulation of the very flexible aircraft dynamics showed that consistent linearisation techniques (i.e. preserving inertial coupling effects) around trim conditions capture the relevant aeroelastic features of these vehicles, hence allowing control synthesis at a reasonable computational costs. As shown by Patil and Hodges [78], such control architectures can be improved by repeating the linearisation around each point of the flight envelope and employing gain schedule procedures. However, under sufficiently large perturbations, linear descriptions will eventually fail to predict the system dynamics [84]. Studies on trajectory tracking [85, 86] and flight-dynamics [75] have shown that a nonlinear description is also required when the aim is to manoeuvre the aircraft, as relevant geometrical changes are likely to occur. In this case, however, control architectures for manoeuvring can become very involved — therefore the use of heuristic approaches — and may lack of robustness due to the high complexity of the system dynamics [85, 86].

1.1.3 Architectures for optimal control

The review in Sec. 1.1.2 showed the potential advantage of considering nonlinear models in the control synthesis of very flexible aircraft. This applies not only for the feedback control of the vehicle dynamics under disturbances, but also when the objective is to determine efficient strategies for manoeuvring, i.e. for open-loop analysis. Especially in the latter case, a methodology should be able to deal with the nonlinear behaviour of a flexible wing as an opportunity for extra performance, rather than a constraint. From this perspective, therefore, the task of identifying very flexible aircraft manoeuvres

for optimal performance can be recast as an open-loop optimal control problem with respect to the time histories of the aerodynamic control surfaces. The contemporary optimisation of other vehicle design features may also be integrated in this formulation. As it will be discussed in Sec. 1.1.4, and given the high importance of dynamic effects in determining critical operative conditions for very flexible vehicles, this would provide the great advantage of allowing to consider the interaction between control and structural dynamics from a very early stage of the design process.

Hence, a brief review of available methodologies for the numerical solution of optimal control problem is included in this section. For more detailed revisions, the reader is remanded to Betts [87, 88], Sargent [89] and Conway [90], which focus on numerical solutions techniques, and Bryson [91], which gives an interesting historical perspective on the topic and links to a number of engineering applications. Due to the strong connection between the theories of optimal control and optimisation, a parallelism between architectures for multidisciplinary design optimisation (MDO) and numerical strategies for optimal control exists. This aspect has recently been reviewed by Allison and Herber [20] and Martins and Lambe [92], among others.

Optimal control problems can be solved through an *optimise-discretise* approach, leading to indirect methods [89, 93]. These techniques require the analytical derivation of the Euler-Lagrange optimality conditions associated the problem — optimisation step [20, 88]. These relations form a system of ordinary differential equations, with initial and terminal conditions on the Lagrange multipliers and the state functions [90]. Optimal control results from the solution of this multiple-points boundary value problem, which can be obtained numerically through a shooting method — discretisation step [89]. Indirect methods have been exploited in the earliest applications to aerospace engineering, which dealt with trajectory optimisation of rockets. Breakwell [94], for instance, solved this problem through forward and a backward shooting, while later solutions improved the stability of the approach by means of multiple shooting [91]. Of relevance for HALE aircraft are the works from Klesh and Kabamba [95], which used a simplified flight-dynamics description of a solar-powered UAV to obtain optimal trajectories for perpetual flight, and Ma et al. [96], which derived closed form solutions for optimal turning trajectories.

Indirect methods require an explicit derivation the optimality conditions associated to the problem, which may be a very complex task — for instance, in problems involving disequality constraints, an a prior estimate of the constrained subarcs sequence is required. Furthermore, the resulting two-boundary problem is likely to be ill-conditioned [88]. The applicability of these approaches is, therefore, bounded to systems governed by relatively simple dynamics. To achieve optimal control with more complex dynamics, a *discretise-optimize* approach is then introduced (direct methods). In direct transcription (DT), both state and control trajectories are discretised in time and numerical integration is used to convert the differential equations holding the system dynamics into a

set of algebraic equations [91, 97, 98]. These are enforced as constraints of a nonlinear optimisation problem, which is solved with respect to the parametrisation of state and control input. In MDO this architecture is referred to as an all-at-once or simultaneous analysis and design [92]. The optimiser will solve concurrently physics and optimal control problems, which typically provides good convergence rates; the sparsity of the algebraic constraints can also be exploited to speed up the sensitivity analysis whenever analytical derivatives expressions are not available [20].

DT methods, however, typically lead to very large optimisation problems [99]. The numerical method used to integrate the system dynamics equations becomes, therefore, crucial [90]. Earlier works using direct collocation would employed piecewise polynomial and fixed-order integration formula [97]. To reduce the mesh size, higher-order methods based on Lagrange polynomials and Gaussian quadrature have been more recently implemented [98–100]. These approaches also aim to preserve the sparsity of the constraints Jacobian, which is necessary to ensure computational efficiency [100]. Nonetheless, DT still requires a compromise between the number of states and the time horizon length, which determines the total size of the optimisation problem to be solved. In particular, flight-dynamics applications are restricted to point-mass models with a few states [101–104]. Betts and Cramer [101], for instance, optimised the flight path of a commercial aircraft considering only a longitudinal flight-dynamics; Drury and Whidborne [102], instead, defined a point-mass method based on a more accurate quaternion description of the aircraft attitude; including a model of its photovoltaic system, both Hosseini and Mesbahi [104] and Spangelo and Gilbert [103] finally applied DT to the path planning of a solar powered UAV.

In order to minimise the size of the resulting optimisation problem, only the control input can be parametrised [90]. In this case the state needs determining at each iteration of the optimisation process through an integration of the system dynamics equations. A multidisciplinary feasible architecture (MDF) is obtained [20, 92]. This approach is referred to as control vector parametrisation (CVP) or also single-shooting method and reduces the size of the associated nonlinear programming problem to its minimum [90, 105]. While not exploiting the sequential dynamics, CVP allows exploiting well tested optimisation algorithms to reliably handle path constraints [91]. Importantly, state and control can be defined on different meshes, meaning that fine resolutions can be used to integrate stiff dynamic equations.

One of the first application of the CVP is from Kelley [106], which defined state and control input on coinciding fixed grid. An adjoint formulation provided the gradient and a steepest descent method drove the optimisation problem to a solution. While earlier works required penalty functions [89], later implementations took advantage of more and more efficient optimisation algorithms to handle constraints [91]. When a direct approach is used for the sensitivity analysis, path constraints can be enforced on the time grid nodes [107–109] without excessively increase the computational cost

of the optimisation. This strategy is implemented by Kraft in the TOMP (Trajectory Optimisation by Mathematical Programming) Fortran package [110], which employs a SQP algorithm for the nonlinear programming solution [111]. Through appropriate integration, however, path constraints can also be scalarised [105, 112–114], which suits better adjoint based algorithms. While convergence properties are typically reduced with respect to grid enforcement [115, 116], in fact, the total amount of constraints handled by the optimiser is reduced. Overall, shooting methods are commonly used in conjunction with gradient based optimisers [108–110, 116], so as to contain the cost associated to the optimisation problem.

In the majority of cases, piecewise constant or linear control parametrisations are employed [105, 110, 117]. Higher-order parametrisations can, however, be beneficial; Fabien [109], for instance, proved that piecewise cubic polynomials need fewer nodes than piecewise linear schemes to accurately represent the control input, hence leading to more efficient solutions. Other techniques to reduce the amount of control points consider the switching times, i.e. the nodes of the time mesh, as design variables [112–114, 118] or employ adaptive parametrisations techniques [116, 117, 119], which sequentially solve the optimal control problem on refined grids.

As a downside, the single-shooting can in some cases lack robustness: especially for complex dynamics and long time horizons, instabilities may arise when integrating the system dynamics [99]. Also, terminal constraints may not be handled very efficiently [89]. When required, these issues can be tackled switching to an Individual Discipline Feasible (IDF) architecture, thus leading to the multiple-shooting method [120]. The time horizon is partitioned into intervals in which the system dynamics is integrated independently, while additional shooting constraints guarantee the continuity of state and control [91]. Overall, the integration of the system dynamics becomes more robust due to the shorter length of the integration interval. Higher computational efficiency can, furthermore, be obtained by tailoring the optimisation algorithm to exploit the sparsity of the constraints Jacobian [107]. However, the larger the number of states and intervals in which the time horizon is divided, the larger is the increase of the associated NLP problem size.

1.1.4 Co-design of very flexible actuated structures

As discussed by Cesnik et al. [3], due to their large flexibility, critical operation conditions of HALE aircraft may be subject to significant structural vibrations. Furthermore, as outlined by the Helios mishap report [14], these are also likely to be associated with complex rigid-flexible flight-dynamics. These considerations extends to a wider class of advanced engineering systems characterised by light and very flexible primary components, including soft robotic manipulators [121] and large HAWT blades. Overall, due to the importance of dynamic effects, accounting for the interaction between control and aircraft aeroelastic/structural response becomes highly relevant for design.

Actively controlled mechanical systems often provide better dynamical characteristics than non-controlled, or passive, ones. However, the integration of the controller usually comes late in the design process [20]. This typically relies on a sequential approach: the aircraft primary structures, for instance, are initially sized for passive response and an active control is introduced only in a later stage, after the main features of the system have been established [122]. This process can be iterated but, looking at it from the perspective of a MDO problem, there is substantial evidence that optimality is not guaranteed at the coupled system level [92, 123]. As shown by Fathy et al. [123], a first approach for reaching a true option is a nested or bi-level strategy, in which, for each iteration of the plant optimisation process, the control is also optimised [124, 125]. An alternative approach, which is likely to end up in a faster convergence, may be to optimise plant and control simultaneously. This leads to the concept of combined design or co-design [20].

The advantages of an integrated design approach have long been proved in space structures design [124, 125], robotics [126] and noise and vibration control [127, 128]. These studies were based on a linear representation of the closed-loop system dynamics, which facilitated the approach to design. Asada et al. [126], for instance, directly manipulated the position of the closed-loop system eigenvalues, while Rao [125] expressed the control gains in terms of the system energy properties. In this sense, the work from Onoda and Haftka [124] best fits the modern idea of combined design, as, aside from exploring a nested approach similar to that presented by Rao [125], they also optimised the system simultaneously with respect to optimiser gains and structural design parameters.

When dealing with the dynamics of structures outside the linear regime, however, integrating the design approaches becomes a much more challenging task. Common MDO architectures, in fact, rarely allow to take advantage of the fact that the control is inherently dependent on the evolution of a system in time [20]. The larger computational cost associated to a time-dependent nonlinear analysis, is, therefore, not balanced by the optimisation approach, resulting in relatively inefficient architectures. Co-design studies dealing with complex structural dynamic models have required, therefore, to reduce the analysis cost, either using metamodels [129] or limiting the size of the systems [130, 131].

For this reason, nonlinear systems for aeroservoelasticity studies have also required reduced-size models and linearised formulations [132–135]. Early works from Suzuki and Yonezawa [132, 133] employed quasi-steady aerodynamics with linear FEM to co-design aeroelastic wings with linear feedback control for gust loads alleviation. More recently, instead, Haghighat et al. [134] used a flight-dynamics model with linear FEs and quasi-steady lifting-line aerodynamics for modelling longitudinal manoeuvres and gust response of a HALE aircraft; Jackson and Livne [135], instead, employed linear aerodynamics and a modal representation of a strain actuated UAV longitudinal dynamics. In both cases the vehicle structural properties were optimised together with the gains of a LQR feedback control.

Overall, only a combined design strategy can guarantee optimality at the coupled system level and, with respect to a nested approach, may lead to a computationally more efficient architecture. As underlined by Allison and Herber [20], however, efficient optimisation architectures, exploiting the sequential dynamics of these systems, still require development. As a result, only low-medium fidelity models have been so far employed for aeroservoelastic optimisation purposes.

1.1.5 Relevant optimisation algorithms

The numerical solution of optimal control and co-design relies on nonlinear programming techniques and, therefore, the whole process depends on the efficiency and robustness of these algorithms. Not surprisingly, the spread of direct methods for optimal control is clearly correlated to the increase in performance of optimisation methods [89]. While recent advantages in computing technologies are leading many authors to consider zero-order global algorithms [90], strong computational restrictions still apply even when medium fidelity dynamical models are considered. Instead, gradient-based approaches are often the only solution that guarantees convergence in a feasible number of iterations [136]. A comprehensive review of these methods is outside the scope of this work. However, a brief discussion on the main families of gradient-based optimisation algorithms is presented here so as to outline their applicability bounds. For a more extensive discussion, the reader is referred to one of the excellent textbooks and reviews available on the topic [93, 137–141].

Sequential quadratic programming (SQP) algorithms were developed in the 60s-70s starting from the works of Wilson, Han and Powell [139, 142, 143]. These are amongst the most effective methods for nonlinear constrained optimisation. The design space is reconstructed through successive quadratic approximations and, at each iteration of the optimisation process, the solution of this sub-problem allows finding the next design point to be explored. Well tested techniques for quadratic programming (QP) are used at this stage. These rely on active set strategies and solve the QP sub-problem enforcing the Karush-Kuhn-Tucker (KKT) first-order necessary conditions for optimality [144, 145].

The definition of the QP sub-problem is key for the efficiency of SQP algorithms. Typically, these adopt a quasi-Newton approximation of the Hessian [137] and limited-memory implementations are available for large scale problems [138, 140]. Upon solution of the QP sub-problem, line-search strategies are often used to rescale the step-size: this compromises a sufficient cost decrease with a not-excessive violation of the nonlinear constraints [142, 143, 146]. Alternatively, trust region algorithms will establish a region of confidence in which the quadratic approximation is acceptable [138].

A common SQP algorithm is the Sequential Least Squares Quadratic Programming (SLSQP) from Kraft [111]. This is based on a Broyden, Fletcher, Goldfarb and Shanno (BFGS) update of the Hessian and a ℓ_1 step-acceptance test function [142, 143], while the solution of the QP sub-problems relies on Lawson and Hansons solver [147]. The

algorithm is included in the SciPy Python package [148] and has been used extensively in optimal control [108–110, 116]. The implementation is, however, not adequate for large scale problems, as the sparsity of the Hessian matrices is not exploited. For these situations, a more suitable SQP algorithm is the Sparse Nonlinear Optimiser (SNOPT) from Gill et al. [149]. This employs a limited memory approximation of the Hessian [140] and second order corrections in the line search method. Detailed reviews of SQP methods are provided in Ref. [139, 140].

SQP approaches are typically best suited for nonlinear problems in which the number of active constraints is comparable to that of design variables [138]. For very large problems, however, interior points methods often, but not always, outperform SQP algorithms [138]. This is linked to the combinatorial difficulty of active-set strategies in dealing with inequality constraints [138]. To overcome this, interior point methods introduce barrier terms, which are relaxed as the process approaches a solution. Therefore, all the system constraints are accounted for during the solution of each QP sub-problem. The KKT system size is increased but always shows the same block structure, meaning that specific algorithms can be developed. Nonetheless, these methods are less mature as compared to SQP based approaches, and may lack robustness in some cases [138]. A widely spread interior point algorithm is IPOPT (Interior Point Optimisation) [150], which is based on a line search algorithm. For a more extensive review on interior points methods, the reader is referred to Forsgren et al. [141].

A few studies have compared the performance of the optimisation algorithms discussed above. Perez et al. [151] compared a wide range of SQP methods and zero-gradient optimisers for small size, canonical problems. As expected, the former provided the best performance for smooth design spaces. Furthermore, all SQP algorithm tested in their work showed comparable performance, though the SLSQP algorithm typically required less iterations for convergence. Larger scale problems have instead been considered by Lyu et al. [43], who showed that SNOPT outperforms the SLSQP algorithm as the size of the problem increases. Importantly, however, the number of iterations remains comparable, showing that computational saving is achieved during the QP sub-problem solution. For the test cases proposed by Lyu et al. [43], the interior point required a number of iterations to convergence comparable to the other SQP methods tested.

1.2 Open problems and research questions

As shown in the previous section, in the last two decades several methodologies for predicting the flight dynamics of vehicles with very flexible wings have been developed. They characterise their geometrically nonlinear behaviour and the inertial coupling between rigid and flexible body dynamics. Overall these models are highly nonlinear and can now predict adequately the wing response to prescribed actuation input and external disturbances in the time-domain. While a few works, mainly based on linearisations

around the wing deformed configuration, have focused on the development of feedback control laws for vibration suppression and trajectory tracking [78, 79, 85], to the author's knowledge the problem of formalising the definition of actuation strategies for manoeuvring vehicles with very flexible wings has never been addressed. This leads to the main research question of this work, namely:

1. is optimal control a suitable tool for defining aircraft manoeuvres when wing flexibility may result in large geometrical changes?

As previous studies on trajectory tracking showed that during manoeuvre the aircraft is characterised by nonlinear dynamics [85, 86], it derives that this methodology should interface with the full complexity of a geometrically nonlinear description. In this sense, therefore, the choice of an optimal control approach also derives from the need of providing a realistic understanding of the best performance that these systems can achieve. For this reason, and contrarily to conventional flight dynamic models, this methodology should also include the vehicle structural dynamics, as very light high aspect-ratio wings are more than likely to experience relevant vibrations during manoeuvres. While this work does not deal directly with feedback methods for vibrations control, therefore, it is important to assess whether these can be exploited for enhancing the system performance or, if not, how to suppress them without negatively impacting the aircraft handling qualities. In this sense, the open-loop optimal control can also be used as a reference for the development of feedback control strategies for vibrations suppression/enhancement in wings exhibiting geometrically nonlinear deflections [20].

A generalisation of these considerations paves the way for a further query. While it is important to verify that the optimal control methodology can deal with the complexity of a geometrically nonlinear formulation, it is also relevant to assess whether this can exploit the richness of this description and enhance, this way, the performance of the flexible aircraft during manoeuvring. Unnecessary conservatism, for instance, may be avoided by allowing the process to explore unconventional and/or unintuitive control input. In summary:

2. can optimisation identify actuation strategies that use nonlinear geometrical changes to improve performance?

Overall, as the aeroelastic analysis of very flexible vehicle is associated to high computational costs, the applicability of optimal control translated directly into establishing whether gradient methods for optimisation can be employed. Therefore, addressing these points will also imply determining how the problem definition and the choices made to parametrise the actuation affect the smoothness of the control space explored by the optimiser.

As most of the critical operating conditions of very flexible vehicles — both in terms of loading and stability — are associated with unsteady phenomena, an accurate representation of the coupling between aeroelastic response and control system is a necessary,

but not sufficient, condition to achieve optimal designs. In this respect, previous works have already highlighted the importance of considering as early as possible in the design process the interaction between control and structural dynamics [3, 20]. Though outside of the main scope of this dissertation, therefore, further studies have been included to assess the feasibility of an integrated design approach for controlling very slender beams under strong vibrations. As the effectiveness of gradient-based optimisation approaches depends on the design space smoothness, an estimation of how this is affected when structural design variables are added to the problem is required. This leads to the final query of this research:

3. what are the potential gains of an integrated structural/control design approach?

The following section will highlight the computational approach proposed to address these questions. Further details on the structuring of this thesis will be provided in Sec. 1.4.

1.3 Present approach

The starting point for addressing the research questions presented in Sec. 1.2 is a flight-dynamics model — including nonlinear aeroelastic effects — capable to accurately predict the behaviour of HALE aircraft with very flexible wings. Importantly, such a model could also serve for simulating the aeroelastic behaviour of other novel aeroelastic structures, such as the large blades of novel offshore HAWT.

From a structural perspective, the key physical phenomena to be captured are the rigid/flexible body dynamics coupling and the large geometrical changes of the primary structures. To this purpose, a number of cross-sectional reduction techniques [24, 25] and geometrically-exact beam descriptions [15, 19, 35, 40] have been developed in the last decades (Sec. 1.1.1). In particular, a formulation in displacement and rotations [152], which allows an easy implementation of kinematic constraints, has been chosen for this work. While deflections can be arbitrarily large, local displacements are small and can be characterised by a linear material model. In this respect it is worth to remark that, while the studies presented in this work will focus on simplified geometries and isotropic materials, this structural description allows considering composite materials, which are essential in the design of novel HALE aircraft and HAWT blades. The resulting equations of motion are discretised using finite elements and solved with respect to a moving reference frame [15, 152].

Despite their large aspect-ratio, three-dimensional aerodynamic effects have been shown to be relevant in HALE wings under large bending deflections, especially at low frequencies [19]. For this reason, an unsteady vortex-lattice model [16, 45, 153] is preferred over a strip based description for characterising their low-speed aerodynamics.

Constraints on the control surfaces rate and amplitude will, in fact, aim to ensure fully-attached flows during manoeuvring, hence allowing for a potential flow assumption. The UVLM is essentially linear, and complex flow fields can be defined through a combination of elementary vortex solutions distributed over the lifting surface. As these can undergo arbitrary kinematics, therefore, nonlinearities are introduced at the lifting-surfaces boundaries through the coupling with the nonlinear structural solution.

In order to reduce the computational cost of the coupled fluid-structure interaction analysis, a partitioned solution is used to numerically integrate the aeroelastic equations [154, 155]. Kinematic constraints, which in the studies presented will allow to simplify the wing dynamics, are included through an augmented Lagrangian method [35]. These solutions are implemented in SHARPy, a framework for the Simulation of High Aspect Ratio Planes in Python. This software is the result of the aeroelasticity research group effort and derives from SHARP, a previous Matlab based implementation [16, 54, 75]. The Author, in particular, contributed to the development of the structural solver and the Python version of this code — refer to Sec. 7.2 for details.

The studies presented in this work will focus on open-loop control. As the dynamic behaviour of geometrically nonlinear wings may differ considerably from that of stiffer ones, in particular, an optimal control approach is proposed for defining their actuation input. This choice will, in fact, allow to deal with the extra-degree of complexity due to the large deflections and inertial coupling effects. Furthermore, unconventional actuation strategies can be explored. Aeroelastic systems as those considered in this work are, however, characterised by a large number of states and relatively large time horizons. For limiting the size of the resulting optimisation problem, therefore, a direct shooting method, in which only the control input is parametrised, has been implemented [105]. Despite not exploiting the sequential dynamics, the CVP allows using well tested algorithms for optimisation, which reliably handle constraints [91]. While this method can lack of robustness for long time horizons and complex dynamics [20], the optimisation studies considered in this work did not incur into numerical instabilities and, therefore, a multiple-shooting implementation was not required. On the other hand, single shooting allowed to minimise the problem size and simplified the extension to co-design.

A choice about the optimisation algorithm driving this solution is finally required. As this work deals with dynamics, a global reconstruction of the design space via a zero-order optimisation method is not computationally feasible. A gradient-based implementation [108–110, 116] has been, instead, required for reducing the number of aeroelastic analysis. The sequential least squares quadratic programming (SLSQP) algorithm [111] has been chosen to this purpose. This is a SQP method which performs very well for medium size problems as those considered in this work [43, 151] and has already been integrated in previous single shooting frameworks successfully [109, 110, 116]. Importantly, a robust implementation is available in the open-source SciPy Python package [148]. The extensions of this framework to larger problem may, however, require an

algorithm tailored for large scale optimisation, such as SNOPT [149] or IPOPT [150].

As nonlinearities are introduced in the flight-dynamics of very flexible vehicles through the geometrically-exact structural description (the UVLM is, otherwise, linear), the single-shooting approach is first assessed for the optimal acceleration of a very flexible pendulum in vacuum. Despite of its relative simplicity, in fact, this system shows a number of complex dynamical features — large deflections and inertial coupling — common to HALE aircraft, large HAWT blades and flexible robotic arms. The investigation will explore whether optimal control correctly exploits this complex dynamics, thus linking directly to research questions 1 and 2. As a gradient-based optimiser is used, an assessment of whether — and if so, how — problem definition and discretisation affect the smoothness of the design space is also included. This will be extended to characterise the structural/control co-design space, thus linking to the third research query. These investigations will provide the relevant background knowledge for applying the optimal control approach to the manoeuvring with very flexible wings. More studies will support how the optimal control approach can facilitate the identification of actuation input for rolling under structural dynamics and nonlinear aeroelastic effects.

1.4 Dissertation outline

The remaining part of this thesis is arranged as follows:

Chapter 2 introduces the nonlinear aeroelastic solution implemented in SHARPy. The main feature of the geometrically-exact beam formulation is the modelling of rotations, which describe the orientation of the beams elements and allows, therefore, for large geometrical changes to occur [15, 35]. The derivation includes considerations of the kinematic constraints enforcement and the time marching scheme used to integrate the final equations of motion. Potential flow theory is, instead, the starting point for introducing the UVLM based low-speed aerodynamic description. The chapter will conclude discussing the numerical solution and the structure/aerodynamics coupling scheme.

Chapter 3 presents the general formulation of the optimal control problem defining the actuation of a very flexible structure. The spline and discrete sines parametrisations used to recast this into an finite-dimension optimisation problem are also introduced. A substantial part of the chapter will deal with theory of constraint optimisation: a thorough presentation of sequential quadratic programming is, in fact, important to understand applicability and limitations of the SLSQP algorithm [111] for this class of problems.

Chapter 4 will address the optimal control of very flexible structures in vacuum. Applying the CVP technique, the actuation on the structure has been written as an optimal control problem using both a local (B-spline) and a global (discrete sine series,

DSS) parametrisation. This is used to manipulate the dynamics of a very flexible pendulum, modelled as a beam in hinged configuration and exhibiting large deformations. As the pendulum flexibility increases, not only larger deformations arise, but the level of coupling between rigid and flexible modes also increases. Conceptually, therefore, this problem has many analogies to that of the control of a very flexible aircraft in calm air. In particular, the impact of several factors — namely the level of nonlinearities, the problem formulation and the parametrisation used — on the optimal control results will be assessed.

Chapter 5 will focus on co-design of the active system introduced in Chap. 4. The pendulum structural properties are, therefore, allowed to vary as the actuation input is defined. As a gradient-based optimiser is used, from a different perspective this implies an assessment on how *large* can changes in the structural design space be. Due to the high level of coupling between control and structure, a multidisciplinary feasible (MDF) architecture is used [92]. The implication of different modelling choices for the actuation is shown and guidelines for the co-design process of structures exhibiting strong nonlinear dynamics are finally provided.

Chapter 6 will finally focus on rolling manoeuvres with very flexible wings. A hinged model of a characteristic HALE wing will be used. This constraint, in particular, allows to isolate the dynamics associated to the wing flexibility from that of the rest of the aircraft. In order to emphasize the nonlinear effects captured by the full aeroelastic solution, a lower fidelity flight-dynamics description, based on elastified stability derivatives, has also been derived. Both models are used to define optimal rolling manoeuvres. While in the latter case these can be identified manually, the single shooting optimisation technique has been used to deal with the higher complexity of the full aeroelastic model. This implementation is assessed against the result obtained through the flight-dynamics description and used to investigate the trade-off between different performance indices associated rolling manoeuvres.

Chapter 7 A summary of this work and an outline of the main contributions of this work will be presented.

1.5 Publications based on this work

1. S. Maraniello and R. Palacios. Co-design of very flexible actuated structures. *International Forum on Aeroelasticity and Structural Dynamics*, Saint Petersburg, Russia, July 2015.
2. S. Maraniello, R.J.S. Simpson and R. Palacios. Optimal manoeuvres with very flexible wings. *57th AIAA/ASCE/AHS/ASC Structures, Structural Dynamics, and Materials Conference*, San Diego, California, January 2016.

3. S. Maraniello and R. Palacios. Optimal vibration control and co-design of very flexible actuated structures. *Journal of Sound and Vibration*, 377:1–21, 2016.
4. S. Maraniello and R. Palacios. Geometrically-nonlinear effects in lateral manoeuvres with coupled flight dynamics and aeroelasticity. *58th AIAA/ASCE/AHS/ASC Structures, Structural Dynamics, and Materials Conference*, Grapevine, Texas, January 2017.
5. S. Maraniello and R. Palacios. Optimal rolling manoeuvres with very flexible wings. *AIAA Journal*. [In Print]

Chapter 2

Aeroelastic modelling of geometrically nonlinear wings

This chapter introduces the nonlinear aeroelastic description used in this work for the coupled rigid-flexible body dynamics of very flexible wings. During manoeuvring, these wings are expected to undergo large deflections, which can significantly alter their shape and aerodynamic features. To capture these effects, the wing is modelled as a geometrically exact beam using a displacement-based formulation [15, 19]. Typically, linear beam models are derived using a *small* displacement field defined along the beam span. In a GEBM, instead, the dynamics of the beam reference line is expressed in terms of a position and a rotation vector field which define, respectively, the location and orientation of each infinitesimal element of beam. As a result, and while the material model can still be assumed to be linear (small deformations hypothesis), arbitrarily large geometrical changes are allowed. Importantly, rigid and flexible-body dynamics are derived simultaneously, meaning that the coupling effects associated to the changes of the wing inertial properties are automatically accounted for. Kinematic constraints, which in a preliminary design phase allow to considerably simplify the wing dynamics, can, instead, be conveniently included through the augmented Lagrangian method [35].

For modelling the low speed aerodynamics of HALE aircraft, on the other hand, a methodology based on potential flow theory has been chosen. While this theory is restricted to incompressible and fully-attached flows, in fact, these characterise a wide portion of the flight envelope of HALE aircraft. The unsteady vortex lattice method, in particular, allows to determine unsteady flow solutions even when the aerodynamic surfaces are subjected to large changes of shape. While the UVLM solves linear aerodynamic relations (which derive from Laplace's equation), nonlinearities are introduced in the aeroelastic solution through the enforcement of the boundary conditions at the lifting surface. The modelling of the wake, furthermore, allows to capture the aerodynamics lag over a wide range of reduced aeroelastic frequencies [52].

In this chapter, the building blocks of the nonlinear aeroelastic framework used in this

work, namely the GEBM and the UVLM, are introduced in Sec. 2.1 and 2.2, respectively. The theoretical description of these methodologies follows closely the implementation of Hesse [156] for the GEBM and Murua [52] for the UVLM formulation. In this work, the two solutions have been coupled in a Python-based framework, SHARPy, which allows to simulate the flight-dynamics of very flexible vehicles, possibly under kinematic constraints. Considerations about the numerical integration of the two schemes are presented in Sec. 2.3.

2.1 Rigid-flexible body dynamics of a geometrically-exact beam

The modelling of the coupled rigid-flexible body dynamics of very flexible wings is based on a geometrically-exact displacement based description [15, 19, 35]. Strains are expressed in a local frame defined along the beam reference line. This allows to assume a linear material model (i.e. small local deformation) and use cross-sectional reduction techniques to conveniently define the local properties of the composite beam. Along the beam reference line, elastic deflections are characterised through the position and orientation — expressed through a Cartesian rotation vector — of the local frame with respect to a moving body-attached frame. This allows for large geometrical changes and rigid body dynamics to be included. The orientation of the wing, required to derive the aerodynamic forces, is instead tracked using a quaternion operator.

The description of the GEBM follows closely the notation proposed by Hesse et al. [75] and is organised as follows. In Sec. 2.1.1, the frame of references used to describe the beam rigid and flexible kinematics are introduced. In particular, the Cartesian rotation vector and quaternion operators, which define, respectively, the orientation of the wing and of its cross-sections, are used to address the kinematics of finite rotations. Sec. 2.1.3 will provide the relevant relations describing the beam kinematics, which are required to enforce Hamilton's principle. Determining the position of each cross-section with respect to the inertial frame will allow to describe the virtual work produced by external forces; strains and velocities, both projected in the local frame, will lead to an expression of the internal and kinetic energy density. The equations of motion of the unrestrained beam are obtained in Sec. 2.1.4, while the enforcement of kinematic constraints is discussed in Sec. 2.1.5. Finally, the finite elements discretisation and the time integration scheme will be addressed in Sec. 2.1.6 to 2.1.7.

2.1.1 Notation and frames of reference

For modelling slender, flexible structures, a geometrically-exact multibeam model with coupled rigid-flexible body dynamics is used [15, 35]. The frames of references (FoRs) and the relevant vector quantities defining the beam dynamics are shown in Fig. 2.1

— which also assumes a finite elements discretisation. Note that vectors are indicated in bold and, when required, subscripts will be used to refer to their components. Matrices, instead, are written in capital letters.

At each section of the beam, force and moment strains are expressed into a local frame, B , defined along the beam mean axis, s [15]. The position of a point belonging to the local cross-section is measured relatively to the local frame, B , by the vector ζ . Its position with respect to the inertial frame, G , is defined as

$$\mathbf{X}(s, t, \zeta) = \mathbf{r}(t) + \mathbf{R}(s, t) + \zeta(t) \quad (2.1)$$

where \mathbf{r} and \mathbf{R} are, respectively, the position of the body frame A with respect to G and the relative position of B with respect to A , as shown in Fig. 2.1. The rigid

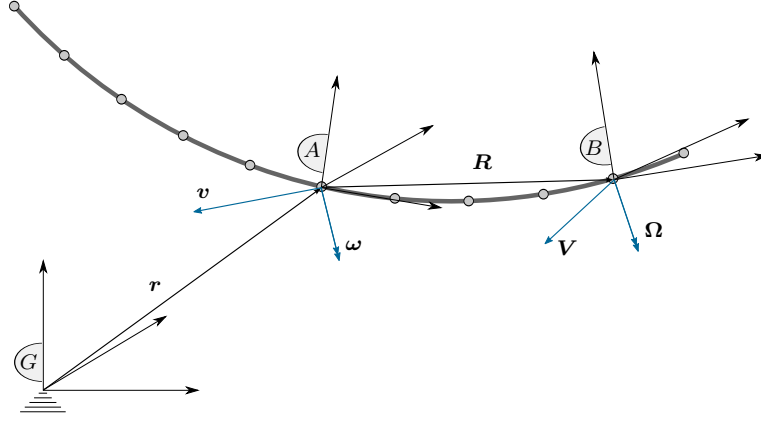


Figure 2.1: Definition of frames of reference over the very flexible structure

body dynamics of the beam is solved in terms of the translational (\mathbf{v}) and rotational ($\boldsymbol{\omega}$) velocity of the body attached frame, A . Similarly, the translational and rotational velocities of the local frame B are defined as \mathbf{V} and $\boldsymbol{\Omega}$. In all cases, these are measured with respect to the inertial frame, G .

It is worth noticing that, so far, the quantities introduced are not projected into any specific frame of reference. When deriving the beam kinematic relations and dynamics equations of motion, however, these will be expressed into one or another frame according to convenience. Subscripts will be used to specify the coordinates system used.

2.1.2 Finite rotations

The description of the A and B frames orientation is a crucial part of the model. According to Euler's rotation theorem, every sequence of rotations around a fixed point can be expressed in terms of a single rotation of amplitude, Ψ , around a fixed axis, $\hat{\mathbf{n}}$. At each time, t , the orientation of the local frame B at the s curvilinear coordinate along the beam reference line can be defined with respect to the body attached frame, A , in

terms of the Cartesian rotation vector (CRV):

$$\mathbf{\Psi}(s, t) = \Psi(s, t) \hat{\mathbf{n}}(s, t) \quad (2.2)$$

Note that in eq. (2.2) the sign of Ψ and the orientation of $\hat{\mathbf{n}}$ define the rotation required to move the frame A over B — and not vice-versa. While other parametrisations of the rotations are possible, the CRV introduces the minimum number of states (three per point) without producing singularities, hence limiting the size of the finite elements discretisation and the computational cost associated to the numerical solution. Furthermore, as rotations become small, $\Psi \rightarrow 0$, the CRV approaches to the linear rotation vector.

The rotation matrix associated to this transformation can be expressed as [35]

$$C^{AB} = C(\mathbf{\Psi}) = I + \frac{\sin \Psi}{\Psi} \tilde{\mathbf{\Psi}} + \frac{1 - \cos \Psi}{\Psi^2} \tilde{\mathbf{\Psi}}^2 = \sum_{k=0}^{\infty} \frac{1}{k!} \tilde{\mathbf{\Psi}}^k \quad (2.3)$$

where I is the unit matrix and $\tilde{(\cdot)}$ is the cross-product operator. This is defined as

$$\tilde{\mathbf{\Psi}} = \begin{pmatrix} 0 & -\Psi_3 & \Psi_2 \\ \Psi_3 & 0 & -\Psi_1 \\ -\Psi_2 & \Psi_1 & 0 \end{pmatrix} \quad (2.4)$$

where Ψ_i is the i -th component of $\mathbf{\Psi}$. Note that in the definition of the rotation matrix C^{AB} , eq. (2.3), a series expansion can be used to avoid the singularity occurring for $\Psi = 0$. Importantly, C^{AB} also defines the coordinate transformation matrix projecting vectors from B to A , i.e.

$$\mathbf{q}_A = C^{AB} \mathbf{q}_B \quad (2.5)$$

where the subscripts indicate the frame in which vector \mathbf{q} is expressed. Finally, from eq. (2.2) it can be also observed that the CRV is non-additive, hence

$$C(\mathbf{\Psi}_a + \mathbf{\Psi}_b) \neq C(\mathbf{\Psi}_a) + C(\mathbf{\Psi}_b) \quad (2.6)$$

This can lead to objectivity issues when the model is discretised via finite elements: in this case, in fact, the rotations inside each element are obtained via interpolation, hence high-order elements and/or fine parametrisations are required to reduce the error associated to the inequality (2.6).

The orientation of the body attached frame A with respect to the inertial frame, G , is instead described by the quaternions. These are very suitable for describing large rotations, which is the case of the floating frame A . This representation, in fact, always allows to define a biunivocal relation between rotation matrix and quaternion vector

[157]. Quaternions are four elements vectors of the form

$$\boldsymbol{\chi} = \begin{Bmatrix} \chi_0 \\ \boldsymbol{\chi}_v \end{Bmatrix} \quad (2.7)$$

whose scalar (χ_0) and vector ($\boldsymbol{\chi}_v$) parts are defined respectively as

$$\chi_0 = \cos \frac{\chi}{2} \quad (2.8a)$$

$$\boldsymbol{\chi}_v = \sin \frac{\chi}{2} \hat{\mathbf{n}} \quad (2.8b)$$

and where the angle χ and the axis $\hat{\mathbf{n}}$ define the rotation from the frame G to A . The associated transformation matrix has no singularities, and can be expressed as

$$C^{GA} = C(\boldsymbol{\chi}) = H(\boldsymbol{\chi})L^T(\boldsymbol{\chi}) \quad \text{with} \quad \begin{aligned} H(\boldsymbol{\chi}) &= \begin{pmatrix} -\boldsymbol{\chi} & \chi_0 I + \tilde{\boldsymbol{\chi}} \end{pmatrix} \\ L(\boldsymbol{\chi}) &= \begin{pmatrix} -\boldsymbol{\chi} & \chi_0 I - \tilde{\boldsymbol{\chi}} \end{pmatrix} \end{aligned} \quad (2.9)$$

From a rotation matrix, C , the corresponding quaternion representation can instead be obtained as described by Steven and Lewis [157, Chap. 1]. An important feature of eq. (2.9) is that no trigonometric relation is involved, which makes this expression less vulnerable to round off errors. Furthermore, a sequence of rotations can be combined using the quaternion multiplication rule [35]. However, this representation is less suitable than CRVs for FE models, as the number of states is increased and the $|\boldsymbol{\chi}| = 1$ property needs to be enforced when interpolating inside finite-elements.

The use of quaternion algebra allows to conveniently express the attitude propagation equation in terms of FoR A angular velocity, $\boldsymbol{\omega}$, as [158]

$$\dot{\boldsymbol{\chi}} = -\frac{1}{2} \begin{pmatrix} 0 & \boldsymbol{\omega}_A^T \\ \boldsymbol{\omega}_A & \tilde{\boldsymbol{\omega}}_A \end{pmatrix} \boldsymbol{\chi} \quad (2.10)$$

It is worth anticipating that, during a full aeroelastic solution, eq. (2.10) is solved together with the wing rigid-flexible body dynamics equations, as external forces may depend on the orientation of the body frame A . For instance, the incidence of the aerodynamic surfaces with respect to the air-stream (and, hence, the aerodynamic loads) depends on the A frame attitude. For very flexible structures, furthermore, structural deflections produced by gravity loads may vary considerably according to the FoR A orientation, with obvious consequence on the wing aerodynamic features.

2.1.3 Kinematic relations

To derive the equations of motion defining the dynamics of geometrically-exact beams, Hamilton's principle is enforced (Sec. 2.1.4). This, however, requires an expression of the internal and the kinetic energy density along the beam, as well as of the the virtual work

done by the external forces. In this section, therefore, the kinematic relation necessary to obtain these quantities — namely position and velocity of each infinitesimal segment of beam and the associated strains — are presented.

The beam kinematics is derived under the assumption that warping effects are negligible, i.e. that the beam cross-sections rotate rigidly. As in very slender structures large scale, span-wise, displacements typically dominate over small scale cross-sectional deformations, this assumption is realistic. Nonetheless, if relevant, warping effects may still be included in this formulation through appropriate cross-sectional reduction techniques [24, 25]. Under this hypothesis, the position of a generic point at the s cross-section with respect to the inertial frame origin is given by

$$\mathbf{X}_G(s, t, \boldsymbol{\zeta}_B) = \mathbf{r}_G(t) + C^{GA}(\boldsymbol{\chi}(t))\mathbf{R}_A(s, t) + C^{GA}(\boldsymbol{\chi}(t))C^{AB}(\boldsymbol{\Psi}(s, t))\boldsymbol{\zeta}_B \quad (2.11)$$

where \mathbf{X} is projected in G coordinates and the B coordinates of the local position vector, $\boldsymbol{\zeta}_B$, is assumed to remain constant as the beam deforms. Note that this relation is required to express the work done by the external forces.

As the beam each cross-sections move rigidly, their kinetic energy is uniquely defined by the translational (\mathbf{V}) and rotational ($\boldsymbol{\Omega}$) velocities of corresponding local frame, B . These quantities are expressed as

$$\mathbf{V}_B(s, t) = C^{BA} \left(\dot{\mathbf{R}}_A(s, t) + \mathbf{v}_A(t) + \boldsymbol{\omega}_A(t)\mathbf{R}_A(s, t) \right) \quad (2.12a)$$

$$\boldsymbol{\Omega}_B(s, t) = T(\boldsymbol{\Psi}(s, t))\dot{\boldsymbol{\Psi}}(s, t) + C^{BA}(\boldsymbol{\Psi}(s, t))\boldsymbol{\omega}_A(t) \quad (2.12b)$$

where $(\dot{\bullet})$ indicates a time derivative; note that in eq. (2.12) the projection into local coordinates has been chosen as the inertial properties of the cross-section are more conveniently described in this frame; this will allow simplifying the expression of the kinetic energy density at each beam segment (Sec. 2.1.4). In eq. (2.12b) the tangential rotation operator [35]

$$T(\boldsymbol{\Psi}) = I + \frac{\cos \Psi - 1}{\Psi^2} \tilde{\boldsymbol{\Psi}} + \left(1 - \frac{\sin \Psi}{\Psi} \right) \frac{\tilde{\boldsymbol{\Psi}}^2}{\Psi^2} = \sum_{k=0}^{\infty} \frac{(-1)^k}{(k+1)!} \tilde{\boldsymbol{\Psi}}^k \quad (2.13)$$

has been introduced. This links the infinitesimal rotation of the local frame, $\delta\boldsymbol{\phi}_B$, to an infinitesimal change in CRV representation, $\delta\boldsymbol{\Psi}$, according to

$$\delta\tilde{\boldsymbol{\phi}}_B = C^{BA}\delta C^{AB} = \widetilde{T\delta\boldsymbol{\Psi}} \quad (2.14)$$

In order to compute the beam internal energy, an expression of the strains is also required. At each time, t , force strains are obtained by comparing the rate of change along the arc-length of the reference line, $\mathbf{R}' = d\mathbf{R}/ds$, against the one associated to the

undeformed beam ($t = 0$). This leads to the following expression

$$\boldsymbol{\gamma}(s, t) = C^{BA}(\boldsymbol{\Psi}(s, t)) \mathbf{R}'_A(s, t) - C^{BA}(\boldsymbol{\Psi}(s, 0)) \mathbf{R}'_A(s, 0) \quad (2.15)$$

where the first component of $\boldsymbol{\gamma}$ is associated to deformations along the tangent of the beam reference line; the others refer, instead, to normal deflections and account for shear effects. Similarly, a compact expression for the moment strains is given by

$$\boldsymbol{\kappa}(s, t) = \mathbf{K}_B(s, t) - \mathbf{K}_B(s, 0) \quad (2.16)$$

where

$$\mathbf{K}_B(s, t) = T(\boldsymbol{\Psi}(s, t)) \boldsymbol{\Psi}'(s, t) \quad (2.17)$$

is the local beam curvature [35]. The first component of \mathbf{K} refers to torsional deformations about the beam reference line, while the other two describe bending strains along the remaining two axis of the B frame. Finally, it is worth noticing that an alternative expression for $\mathbf{K}_B(s, t)$ is obtained from from eq. (2.14) as:

$$\tilde{\mathbf{K}}_B = C^{BA} \frac{d}{ds} C^{AB} \quad (2.18)$$

2.1.4 Dynamics of the unrestrained beam

The equation of motion describing the dynamics of a multi-beam system over a time horizon $[t_1, t_2]$ can be derived enforcing Hamilton's principle of stationary action [159]:

$$\int_{t_1}^{t_2} \int_{\Upsilon} (\delta \mathcal{T} - \delta \mathcal{U} + \delta \mathcal{W}) \, ds \, dt = 0 \quad (2.19)$$

In eq. (2.19), the spatial integration is performed over the one-dimensional domain Υ defined by the union of several interconnected slender bodies. Variations are taken over the kinetic and internal energy density per unit of beam length, \mathcal{T} and \mathcal{U} , and the virtual work per unit of length of the applied, non-conservative, loads, \mathcal{W} . Using the kinematic relations provided in Sec. 2.1.3, the kernel of the integral in eq. (2.19) can be expanded in terms of positions, \mathbf{R} , and rotations, $\boldsymbol{\Psi}$, along the beam reference line and of translational, \mathbf{v} , and rotational, $\boldsymbol{\omega}$, velocities of the body frame, A . As discussed next, this will lead to the weak form of the GEBM equations of motion.

Kinetic energy density

At each segment of the beam, the kinetic energy per unit of length is

$$\mathcal{T} = \frac{1}{2} (\mathbf{V}_B^T \, \boldsymbol{\Omega}_B^T) \mathcal{M} (\mathbf{V}_B^T \, \boldsymbol{\Omega}_B^T)^T = \mathbf{V}_B^T \mathbf{P}_B + \boldsymbol{\Omega}_B^T \mathbf{H}_B \quad (2.20)$$

where \mathbf{P}_B and \mathbf{H}_B are the translational and rotational momenta. In eq. (2.20), projecting the velocities in the local frame, B , allows to express the inertial properties of the beam arc through the cross-sectional mass matrix

$$\mathcal{M} = \begin{pmatrix} mI & -m\tilde{\boldsymbol{\zeta}}_B^{cg} \\ m\tilde{\boldsymbol{\zeta}}_B^{cg} & J \end{pmatrix} \quad (2.21)$$

where m is the mass per unit of length, J the cross-sectional inertia tensor and $\tilde{\boldsymbol{\zeta}}_B^{cg}$ the distance between the beam reference line and the center of mass of the cross-section itself. Note that, while not explicitly stated in eq. (2.21), these quantities will in general depend on the curvilinear coordinate s . The variational form of the kinetic energy becomes

$$\delta\mathcal{T} = [\delta\mathbf{V}_B^T \ \delta\boldsymbol{\Omega}_B^T] \mathcal{M} [\mathbf{V}_B^T \ \boldsymbol{\Omega}_B^T]^T = \delta\mathbf{V}_B^T \mathbf{P}_B + \delta\boldsymbol{\Omega}_B^T \mathbf{H}_B \quad (2.22)$$

Using eq. (2.14) to introduce the virtual rotation of the B frame, $\delta\phi_B$, the variations of translational and rotational velocity can be derived from eq. (2.12) as:

$$\delta\mathbf{V}_B = C^{BA} \left(\delta\dot{\mathbf{R}}_A + \delta\mathbf{v}_A + \tilde{\boldsymbol{\omega}}_A \delta\mathbf{R}_A - \tilde{\mathbf{R}}_A \delta\boldsymbol{\omega}_A \right) + \tilde{\mathbf{V}}_B \delta\phi_B \quad (2.23a)$$

$$\delta\boldsymbol{\Omega}_B = \delta\dot{\phi}_B + C^{BA} \delta\boldsymbol{\omega}_A + \tilde{\boldsymbol{\Omega}}_B \delta\phi_B \quad (2.23b)$$

Variations of the rigid-body velocities $\delta\mathbf{v}_A$ and $\delta\boldsymbol{\omega}_A$ are instead obtained in terms of virtual position, $\delta\mathbf{r}_A$, and rotation, $\delta\boldsymbol{\varphi}_A$, of the frame A as [35]

$$\delta\mathbf{v}_A = \delta\dot{\mathbf{r}}_A + \tilde{\boldsymbol{\omega}}_A \delta\mathbf{r}_A \quad (2.24a)$$

$$\delta\boldsymbol{\omega}_A = \delta\dot{\boldsymbol{\varphi}}_A + \tilde{\boldsymbol{\omega}}_A \delta\boldsymbol{\varphi}_A \quad (2.24b)$$

in which, as done for $\delta\phi_B$ in eq. (2.14), $\delta\boldsymbol{\varphi}_A$ is defined such that $\delta\tilde{\boldsymbol{\varphi}}_A = C^{GA} \delta C^{GA}$.

Internal energy density

Under the assumption of a linear material model, the density of internal energy per unit length, \mathcal{U} , takes the form:

$$\mathcal{U} = \frac{1}{2} [\boldsymbol{\gamma}^T \boldsymbol{\kappa}^T] \mathcal{S} [\boldsymbol{\gamma}^T \ \boldsymbol{\kappa}^T]^T = \frac{1}{2} (\boldsymbol{\gamma}^T \mathbf{F}_B + \boldsymbol{\kappa}^T \mathbf{M}_B) \quad (2.25)$$

where the internal forces and moments, \mathbf{F}_B and \mathbf{M}_B , are expressed in local components. At each curvilinear coordinate s , instead, the 6×6 matrix of elastic coefficients, \mathcal{S} , can be determined through an appropriate cross-sectional analysis [24]. The variation of the internal energy density becomes

$$\delta\mathcal{U} = [\delta\boldsymbol{\gamma}^T \ \delta\boldsymbol{\kappa}^T] \mathcal{S} [\boldsymbol{\gamma}^T \ \boldsymbol{\kappa}^T]^T = \delta\boldsymbol{\gamma}^T \mathbf{F}_B + \delta\boldsymbol{\kappa}^T \mathbf{M}_B \quad (2.26)$$

where force and moment strains variations are derived from eq. (2.15) and (2.16) as:

$$\delta\boldsymbol{\gamma} = C^{BA}\delta\mathbf{R}'_A + \tilde{\mathbf{R}}'_A\delta\phi_B \quad (2.27a)$$

$$\delta\boldsymbol{\kappa} = \delta\phi'_B + \tilde{\mathbf{K}}_B\delta\phi_B \quad (2.27b)$$

Work of external forces

Finally, at each curvilinear coordinate, s , an expression for the virtual work per unit length of the external forces, $\delta\mathcal{W}$, is required. This can be obtained through

$$\delta\mathcal{W} = \int_{\mathcal{A}} \delta\mathbf{X}_G \boldsymbol{\mu}_G d\mathcal{A} \quad (2.28)$$

where $\delta\mathbf{X}_G$ is the virtual position of each point of the cross-section, $\boldsymbol{\mu}_G$ are the applied force and the integration is extended to the whole cross-sectional area, \mathcal{A} . The expression of $\delta\mathbf{X}_G$ is obtained from eq. (2.11), thus leading to

$$\delta\mathcal{W} = \left[\delta\mathbf{r}_G^T C^{GA} + \delta\mathbf{R}_A^T + \delta\boldsymbol{\varphi}_A^T \left(\tilde{\mathbf{R}}_A + C^{AB}\tilde{\boldsymbol{\zeta}}_B C^{BA} \right) \right] C^{AB} \mathbf{f}_B + \delta\phi_B^T \mathbf{m}_B \quad (2.29)$$

where the applied forces, \mathbf{f} , and moments, \mathbf{m} , per unit length

$$\mathbf{f}_B = \int_{\mathcal{A}} \boldsymbol{\mu}_B d\mathcal{A} \quad (2.30a)$$

$$\mathbf{m}_B = \int_{\mathcal{A}} \tilde{\boldsymbol{\zeta}}_B \boldsymbol{\mu}_B d\mathcal{A} \quad (2.30b)$$

have been isolated and expressed in local components.

Equations of motion

The variations of kinetic and internal energy described by eq. (2.22) and (2.26), together with the expression of virtual work in eq. (2.29), can be substituted into Hamilton's principle, eq. (2.19). The weak form of the unconstrained beam equations of motion is thus retrieved:

$$\begin{aligned} & \int_{t_1}^{t_2} \left\{ \int_{\Upsilon} \left[\delta\mathbf{R}_A^T C^{AB} \left(\dot{\mathbf{P}}_B + \tilde{\boldsymbol{\Omega}}_B \mathbf{P}_B - \mathbf{f}_B \right) + \delta\mathbf{R}'_A^T C^{AB} \mathbf{F}_B \right. \right. \\ & \quad + \delta\phi_B^T \left(\dot{\mathbf{H}}_B + \tilde{\boldsymbol{\Omega}}_B \mathbf{H}_B + \tilde{\mathbf{V}}_B \mathbf{P}_B - \tilde{\mathbf{K}}_B \mathbf{M}_B - \tilde{\mathbf{R}}'_A \mathbf{F}_B - \mathbf{m}_B \right) + \delta\phi'_B{}^T \mathbf{M}_B \Big] ds \\ & \quad \left. + \delta\mathbf{r}_G^T C^{GA} \left(\dot{\mathbf{P}}_A + \tilde{\boldsymbol{\omega}}_A \mathbf{P}_A - \mathcal{F}_A \right) + \delta\boldsymbol{\varphi}_A^T \left(\dot{\mathcal{H}}_A + \tilde{\boldsymbol{\omega}}_A \mathcal{H}_A - \mathcal{M}_A \right) \right\} dt = \\ & = \int_{\Upsilon} \left[\delta\mathbf{R}_A^T C^{AB} \mathbf{P}_B + \delta\phi_B^T \mathbf{H}_B \right]_{t_1}^{t_2} ds + \left[\delta\mathbf{r}_G^T C^{GA} \mathbf{P}_A + \delta\boldsymbol{\varphi}_A^T \mathcal{H}_A \right]_{t_1}^{t_2} \quad (2.31) \end{aligned}$$

In eq. (2.31) the total momenta, \mathbf{P} and \mathcal{H} , and external forces, \mathcal{F} and \mathcal{M} , acting on the beam have been collected and expressed in FoR A coordinates. These are defined

as:

$$\begin{aligned}\mathcal{P}_A &= \int_{\Upsilon} C^{AB} \mathbf{P}_B \, ds \quad , \quad \mathcal{H}_A = \int_{\Upsilon} \left(\tilde{\mathbf{R}}_A C^{AB} \mathbf{P}_B + C^{AB} \mathbf{H}_B \right) ds \\ \mathcal{F}_A &= \int_{\Upsilon} C^{AB} \mathbf{f}_B \, ds \quad , \quad \mathcal{M}_A = \int_{\Upsilon} \left(\tilde{\mathbf{R}}_A C^{AB} \mathbf{f}_B + C^{AB} \mathbf{m}_B \right) ds\end{aligned}\tag{2.32}$$

An integration by parts in time has been required to obtain eq. (2.31). This introduces the time derivatives of local and total momenta $\dot{\mathbf{P}}$, $\dot{\mathbf{H}}$, $\dot{\mathcal{P}}$ and $\dot{\mathcal{H}}$, which are associated to the translational and rotational accelerations of each segment of the beam and of the FoR A through eq. (2.12) and (2.20).

The strong form of the equations of motion can finally be derived by enforcing that eq. (2.31) is verified for each variation of positions, \mathbf{R}_A and \mathbf{r}_G , and rotations ϕ_B and φ_A . To this aim, the spatial derivatives $\delta \mathbf{R}'_A$ and $\delta \phi'_B$ are rewritten as

$$\int_{\Upsilon} \delta \mathbf{R}'_A C^{AB} \mathbf{F}_B \, ds = [\delta \mathbf{R}_A C^{AB} \mathbf{F}_B]_{\partial \Upsilon} - \int_{\Upsilon} \delta \mathbf{R}_A C^{AB} \left(\tilde{\mathbf{K}}_B \mathbf{F}_B + \mathbf{F}'_B \right) ds \tag{2.33a}$$

$$\int_{\Upsilon} \delta \phi'^T_B \mathbf{M}_B \, ds = [\delta \phi_B^T \mathbf{M}_B]_{\partial \Upsilon} - \int_{\Upsilon} \delta \phi_B^T \mathbf{M}'_B \, ds \tag{2.33b}$$

where $\partial \Upsilon$ indicates the boundaries of the Υ one-dimensional domain, i.e. the connection point of the beams defining the structural model, and eq. (2.18) has been exploited in order to develop the spatial derivative of the C^{AB} rotation matrix. Substituting eq. (2.33) into the weak form of eq. (2.31) leads to:

$$\begin{aligned}& \int_{t_1}^{t_2} \left\{ \int_{\Upsilon} \left[\delta \mathbf{R}_A^T C^{AB} \left(\dot{\mathbf{P}}_B + \tilde{\mathbf{\Omega}}_B \mathbf{P}_B - \mathbf{f}_B - \tilde{\mathbf{K}}_B \mathbf{F}_B - \mathbf{F}'_B \right) + \right. \right. \\ & \quad + \delta \phi_B^T \left(\dot{\mathbf{H}}_B + \tilde{\mathbf{\Omega}}_B \mathbf{H}_B + \tilde{\mathbf{V}}_B \mathbf{P}_B - \tilde{\mathbf{K}}_B \mathbf{M}_B - \mathbf{M}'_B - \tilde{\mathbf{R}}'_A \mathbf{F}_B - \mathbf{m}_B \right) \Big] ds \\ & \quad + \delta \mathbf{r}_G^T C^{GA} \left(\dot{\mathcal{P}}_A + \tilde{\omega}_A \mathcal{P}_A - \mathcal{F}_A \right) + \delta \varphi_A^T \left(\dot{\mathcal{H}}_A + \tilde{\omega}_A \mathcal{H}_A - \mathcal{M}_A \right) \Big\} dt = \\ & = \int_{\Upsilon} \left[\delta \mathbf{R}_A^T C^{AB} \mathbf{P}_B + \delta \phi_B^T \mathbf{H}_B \right]_{t_1}^{t_2} ds + \left[\delta \mathbf{r}_G^T C^{GA} \mathcal{P}_A + \delta \varphi_A^T \mathcal{H}_A \right]_{t_1}^{t_2} + \\ & \quad - \int_{t_1}^{t_2} \left[\delta \mathbf{R}_A C^{AB} \mathbf{F}_B + \delta \phi_B^T \mathbf{M}_B \right]_{\partial \Upsilon} dt \tag{2.34}\end{aligned}$$

Enforcing that the integral in eq. (2.34) vanishes for each variation of $\delta \mathbf{R}_A$, $\delta \phi_B$, $\delta \mathbf{r}_G$ and $\delta \varphi_A$, leads to the strong form of the unrestrained beam dynamics equations [19]

$$\dot{\mathbf{P}}_B + \tilde{\mathbf{\Omega}}_B \mathbf{P}_B = \tilde{\mathbf{K}}_B \mathbf{F}_B + \mathbf{F}'_B + \mathbf{f}_B \tag{2.35a}$$

$$\dot{\mathbf{H}}_B + \tilde{\mathbf{\Omega}}_B \mathbf{H}_B + \tilde{\mathbf{V}}_B \mathbf{P}_B = \tilde{\mathbf{K}}_B \mathbf{M}_B + \mathbf{M}'_B + \tilde{\mathbf{R}}'_A \mathbf{F}_B + \mathbf{m}_B \tag{2.35b}$$

$$\dot{\mathcal{P}}_A + \tilde{\omega}_A \mathcal{P}_A = \mathcal{F}_A \tag{2.35c}$$

$$\dot{\mathcal{H}}_A + \tilde{\omega}_A \mathcal{H}_A = \mathcal{M}_A \tag{2.35d}$$

whose boundary and initial conditions can be derived from the right-hand side of eq. (2.34) itself. Finally, it is worth remarking that, as in flight dynamics the external loads, \mathbf{f}_B and \mathbf{m}_B , generally depend on the beam orientation with respect to the inertia frame, G , these relation need to be coupled with the attitude propagation equation (2.10).

2.1.5 Enforcing kinematic constraints

Several approaches are available to constrain the kinematics of a dynamical system. A brief overview of the topic, leading to the augmented Lagrangian method used in this work for implementing hinge kinematic constraints, is here presented: for a more detailed discussion, the reader is remanded to the work of Gerardin and Cardona [35].

Defining as

$$\mathbf{c}(\mathbf{v}_A, \boldsymbol{\omega}_A, \mathbf{R}_A, \boldsymbol{\Psi}, \boldsymbol{\chi}) = 0 \quad (2.36)$$

the column vector containing the kinematic constraints enforced to the system dynamics, a first solution consists in applying the implicit function theorem to eq. (2.36). This allows expressing the variation of some of the parameters describing the system dynamics ($\mathbf{v}_A, \boldsymbol{\omega}_A, \mathbf{R}$ or $\boldsymbol{\Psi}$) with respect to the others, thus reducing the number of unknowns. This approach is commonly referred to as constraint elimination method. With reference to the unrestrained beam dynamics described in eq. (2.31) in this work this strategy is used for implementing clamp constraints, which are obtained by enforcing that the body attached frame velocity is null, i.e. $\mathbf{v}_A = \mathbf{0}$. Most commonly, however, strong enforcement of the constraints equations is not preferable, as extensive modifications to the original solution, and its numerical implementation, may be required.

Penalty functions and Lagrange multipliers methods allow to overcome these restrictions, as the equations of motion of the unrestrained beam dynamics only need to be augmented. In the penalty function method, the system size is not increased, as an augmenting term, vanishing only when the constraints are verified, is added to the original equations of motion [35]. The method, however, does not allow for an efficient scaling of the constraints and its performance depend strongly on the choice of the penalty factor. If this is too large, an ill-conditioned systems may be obtained but, if this is not sufficiently large, constraints may be verified with bad approximation. In the Lagrange multiplier method, instead, the constraints equations are added to the original system, and coupling is provided through the Lagrange multiplier. These are determined during the solution process, and offer the main advantage of automatically scaling the constraints equations.

For improving the convergence properties of the Lagrange multipliers method, a small penalty term can be included. This leads to the augmented Lagrangian method, which has been used in this work for developing hinge kinematic constraints. The method is here described in a general form, starting from the analytical formulation behind the equation of motions of the unrestrained beam. For a different derivation, based

on the discretised equations of motion of a dynamical system, the reader can refer to Gerardin and Cardona [35]. The equations of motion of the constrained beam are derived augmenting the Lagrangian describing Hamilton's principle, eq. (2.19), as follows:

$$\int_{t_1}^{t_2} \left[\int_{\Gamma} (\delta\mathcal{T} - \delta\mathcal{U} + \delta\mathcal{W}) ds + \delta \left(k\boldsymbol{\nu}^T \mathbf{c} + \frac{1}{2} p \mathbf{c}^T \mathbf{c} \right) \right] dt = 0 \quad (2.37)$$

In eq. (2.37) $\boldsymbol{\nu}$ is the vector of Lagrange multipliers, k is the scaling factor of the Lagrange multipliers terms and p the penalty factor. As the penalty term $\frac{1}{2} p \mathbf{c}^T \mathbf{c}$ is only used as a regularisation term, p is typically chosen to be considerable smaller than k [35]. Developing the variational form of the second term in eq. (2.37) leads to:

$$\int_{t_1}^{t_2} \left[\int_{\Gamma} (\delta\mathcal{T} - \delta\mathcal{U} + \delta\mathcal{W}) ds + \delta\boldsymbol{\nu}^T (k\mathbf{c}) + \delta\mathbf{c} (k\boldsymbol{\nu} + p\mathbf{c}) \right] dt = 0 \quad (2.38)$$

The term associated to the variation of the Lagrange multipliers implies adding to the equations of motion of the unrestrained beam the scaled set of constraints $k\mathbf{c} = \mathbf{0}$. The one associated to variation of the constraints, $\delta\mathbf{c}$, instead, provides the coupling terms.

Hinge constraints

For modelling a hinge, both the translation and the rotation of the body frame A have to be constrained. In this work, the hinge position and its axis of rotation, $\hat{\mathbf{r}}$, are fixed with respect to the inertial frame, G . The origin of frame A can thus be located the hinge point, and the constraints elimination method can be used to avoid translations.

Restraining the frame A rotations requires, instead, that its angular velocity, $\boldsymbol{\omega}$, is at all times parallel to the hinge axis of rotation, $\hat{\mathbf{r}}$, i.e. $\mathbf{r} \times \boldsymbol{\omega} = \mathbf{0}$. Taken two unit vectors, $\hat{\mathbf{p}}_1^T$ and $\hat{\mathbf{p}}_2^T$, perpendicular to $\hat{\mathbf{r}}$, this condition can be equivalently expressed as¹

$$\mathbf{c} = \begin{pmatrix} \hat{\mathbf{p}}_{1A}^T \\ \hat{\mathbf{p}}_{2A}^T \end{pmatrix} \boldsymbol{\omega}_A = B \boldsymbol{\omega}_A = \mathbf{0} \quad (2.39)$$

Note that, as the angular velocity is expressed in A components in the beam equations of motion, eq. (2.31), the $\hat{\mathbf{p}}_i$ vectors are also projected into the A frame. If these are chosen to be fixed in the inertia frame, G , the transformation $\hat{\mathbf{p}}_{iA} = C^{AG}(\boldsymbol{\chi}) \hat{\mathbf{p}}_{iG}^T$ is required, and the B matrix will depend on the quaternion, $\boldsymbol{\chi}$, associated to the A frame attitude. Alternatively, these can also be chosen to be attached to the A frame, as the projection of the hinge axis of rotation in this frame, $\hat{\mathbf{r}}_A$, is time invariant. In this case B becomes a constant coefficients matrix and the constraints variation is simply:

$$\delta\mathbf{c} = B \delta\boldsymbol{\omega}_A \quad (2.40)$$

¹A similar result is obtained by enforcing $\mathbf{r} \times \boldsymbol{\omega} = \tilde{\mathbf{r}}\boldsymbol{\omega} = \mathbf{0}$, thus replacing the B matrix in eq. (2.39) with the cross-product matrix $\tilde{\mathbf{r}}$. The approach in eq. (2.39) is, however, preferred as it can be extended to constraint the A frame translational degrees of freedom. Furthermore, the $\tilde{\mathbf{r}}$ matrix can have an identically zero row, thus leading to an undetermined system of equations.

Substituting eq. (2.39) and (2.40) into eq. (2.37) allows to retrieve the weak form of the equations of motion of the hinged beam.

2.1.6 Discretised form of the equations of motion

Starting from the weak form of beam rigid-flexible dynamics in eq. (2.31) and (2.37), a finite-element discrete formulation is obtained by expressing positions and rotations as

$$\mathbf{R}_A(s) = \sum_{i=1}^3 N_i(s) \mathbf{R}_A(s_i) \quad (2.41a)$$

$$\mathbf{\Psi}(s) = \sum_{i=1}^3 N_i(s) \mathbf{\Psi}(s_i) \quad (2.41b)$$

where $\mathbf{R}_A(s_i)$ and $\mathbf{\Psi}(s_i)$ are their nodal values within an element. Quadratic shape functions, corresponding to 3-noded elements, are used for this work. Superlinear elements, in particular, allow reducing the objectivity issues associated to the interpolation of the Cartesian rotation vector [38], which arise when the strain field is not invariant under rigid-body rotations [36, 37].

Defining $\boldsymbol{\eta}$ as the column vector containing the nodal values of positions and CRV, the coupled nonlinear flexible/rigid body dynamics equations are finally expressed as:

$$M(\boldsymbol{\eta}) \begin{Bmatrix} \ddot{\boldsymbol{\eta}} \\ \dot{\boldsymbol{\nu}} \end{Bmatrix} + \begin{Bmatrix} \mathbf{Q}_{gyr}^s(\boldsymbol{\eta}, \dot{\boldsymbol{\eta}}, \boldsymbol{\nu}) \\ \mathbf{Q}_{gyr}^r(\boldsymbol{\eta}, \dot{\boldsymbol{\eta}}, \boldsymbol{\nu}) \end{Bmatrix} + \begin{Bmatrix} \mathbf{Q}_{stif}^s(\boldsymbol{\eta}) \\ \mathbf{0} \end{Bmatrix} = \begin{Bmatrix} \mathbf{Q}_{ext}^s(\boldsymbol{\eta}, \boldsymbol{\chi}, \boldsymbol{\nu}, t) \\ \mathbf{Q}_{ext}^r(\boldsymbol{\eta}, \boldsymbol{\chi}, \boldsymbol{\nu}, t) \end{Bmatrix}, \quad (2.42)$$

where $\boldsymbol{\nu}^T = \{\mathbf{v}_A^T, \boldsymbol{\omega}_A^T\}$, $M(\boldsymbol{\eta})$ is the global mass matrix, and \mathbf{Q}_{gyr} , \mathbf{Q}_{stif} , \mathbf{Q}_{ext} are, respectively, gyroscopic, stiffness and external forcing terms. A detailed definition on how the gyroscopic and stiffness terms are built is provided by Hesse and Palacios [152]: their origin can be, however, retrieved by comparing eq. (2.42) with the strong continuous form of the GEBM dynamics in eq. (2.35). From eq. (2.35a) and (2.35b), for instance, it can be understood that the gyroscopic term \mathbf{Q}_{gyr} accounts for the fact that the forces and moments acting at each beam cross-section also depend on the global (frame A) and local (frame B) accelerations. Importantly, this term provides coupling between flexible and rigid-body dynamics. The external forces, \mathbf{Q}_{ext} , instead, includes prescribed loads, aerodynamic and gravitational forces. This term, in particular, defines the coupling the the aerodynamics solution, which is discussed in Sec. 2.3. In general, \mathbf{Q}_{ext} depends on the orientation of the body frame A , and hence on the quaternion $\boldsymbol{\chi}$, meaning that eq. (2.42) needs to be coupled with the attitude propagation equation (2.10).

A linearised form of eq. (2.42) is required for the solution of eq. (2.43) via a Newton-Raphson scheme (Sec. 2.1.7). For a given set of nodal displacements and rotations $\boldsymbol{\eta}^*$

and velocities, $\boldsymbol{\nu}^*$, of the body frame A , this takes the form [35, 152]

$$\begin{aligned} M(\boldsymbol{\eta}^*) \begin{Bmatrix} \Delta \ddot{\boldsymbol{\eta}} \\ \Delta \dot{\boldsymbol{\nu}} \end{Bmatrix} + C_t(\boldsymbol{\eta}^*, \boldsymbol{\nu}^*) \begin{Bmatrix} \Delta \dot{\boldsymbol{\eta}} \\ \Delta \boldsymbol{\nu} \end{Bmatrix} + K_t(\boldsymbol{\eta}^*, \boldsymbol{\nu}^*) \begin{Bmatrix} \Delta \boldsymbol{\eta} \\ \mathbf{0} \end{Bmatrix} = \\ = \Delta \mathbf{Q}_{ext}(\boldsymbol{\eta}^*, \Delta \boldsymbol{\eta}, \boldsymbol{\chi}^*, \Delta \boldsymbol{\chi}, \boldsymbol{\nu}^*, \Delta \boldsymbol{\nu}, t, \Delta t) \end{aligned} \quad (2.43)$$

where C_t and K_t are the damping and stiffness tangent matrices. While the stiffness force in eq. (2.42) only depends on the beam displacements and rotations, the tangent stiffness matrix also includes a contribution from the gyroscopic forces, hence explaining the dependency of K_t on the body frame translational and rotational velocities, $\boldsymbol{\nu}$. The columns of the tangent stiffness matrix associated to $\boldsymbol{\nu}$ are, however, null. Finally, it is worth remarking that the tangent damping matrix C_t does not result from modelling the structural damping — which is, in fact, neglected — but rather derives from the perturbation of the gyroscopic forcing term, \mathbf{Q}_{gyr} [152].

2.1.7 Time marching scheme

The mass matrix in eq. (2.42) contains information on both the rigid and flexible body dynamics of the beam and, as a result of the large spread in eigenvalues, it is generally quite stiff. A number of numerical techniques are available for integrating stiff second order ODEs [160, 161]: these tackle stability issues by introducing a controllable level of artificial damping for damping spurious high-frequency oscillations. In this work, in particular, a Newmark- β method [35] has been developed. For linear problems, this approach can be proven to be unconditionally stable. For nonlinear solutions, higher levels of numerical damping may be required and the method may become too dissipative, especially in the low-frequency range [160]. For the studies presented in this work, however, the level of artificial viscosity required to guarantee stability has been found not to compromise accuracy.

For implementing the Newmark- β integration method, the unknowns appearing in eq. (2.42) and eq. (2.10) are organised in an array $\boldsymbol{\tau} = \{\boldsymbol{\eta}, \int \boldsymbol{\nu}, \int \boldsymbol{\chi}\}^T$ such that $\dot{\boldsymbol{\tau}} = \{\dot{\boldsymbol{\eta}}, \boldsymbol{\nu}, \boldsymbol{\chi}\}^T$ and $\ddot{\boldsymbol{\tau}} = \{\ddot{\boldsymbol{\eta}}, \dot{\boldsymbol{\nu}}, \dot{\boldsymbol{\chi}}\}^T$. Note that the integrals appearing in the definition of $\boldsymbol{\tau}$ have no physical meaning and do not contribute to the system dynamics; however, these have been used here for consistency of notation. Starting from positions ($\boldsymbol{\tau}$), velocities ($\dot{\boldsymbol{\tau}}$) and accelerations ($\ddot{\boldsymbol{\tau}}$) at the time-step n , the structural dynamics solution at the next time-step is expressed by the sum of a predictor and a corrector part as

$$\boldsymbol{\tau}_{n+1} = \boldsymbol{\tau}_p(\boldsymbol{\tau}_n, \dot{\boldsymbol{\tau}}_n, \ddot{\boldsymbol{\tau}}_n) + \boldsymbol{\tau}_c(\ddot{\boldsymbol{\tau}}_{n+1}) \quad (2.44a)$$

$$\dot{\boldsymbol{\tau}}_{n+1} = \dot{\boldsymbol{\tau}}_p(\dot{\boldsymbol{\tau}}_n, \ddot{\boldsymbol{\tau}}_n) + \dot{\boldsymbol{\tau}}_c(\ddot{\boldsymbol{\tau}}_{n+1}) \quad (2.44b)$$

where:

$$\tau_p(\tau_n, \dot{\tau}_n, \ddot{\tau}_n) = \tau_n + \Delta t \dot{\tau}_n + \left(\frac{1}{2} - \theta_2\right) \Delta t^2 \ddot{\tau}_n \quad (2.45a)$$

$$\dot{\tau}_p(\dot{\tau}_n, \ddot{\tau}_n) = \dot{\tau}_n + (1 - \theta_1) \Delta t \ddot{\tau}_n \quad (2.45b)$$

$$\tau_c(\ddot{\tau}_{n+1}) = \theta_2 \Delta t^2 \ddot{\tau}_{n+1} \quad (2.45c)$$

$$\dot{\tau}_c(\ddot{\tau}_{n+1}) = \theta_1 \Delta t \ddot{\tau}_{n+1} \quad (2.45d)$$

The scheme has been shown to be unconditionally stable if the weights θ_1 and θ_2 satisfy

$$\theta_1 = \frac{1}{2} + \nu \quad (2.46a)$$

$$\theta_2 = \frac{1}{4} \left(\theta_1 + \frac{1}{2} \right)^2 \quad (2.46b)$$

where $\nu > 0$ regulates the level of artificial viscosity added to stabilise the scheme [35].

As the integration is initialised ($t = 0$ and $n = 0$) positions and velocities τ_0 and $\dot{\tau}_0$ are given as initial conditions² and the accelerations are found by solving eq. (2.42) for $\ddot{\tau}_0$. However, as the mass matrix is characterised by a very large condition number, its inversion can be inaccurate and give rise to high frequency spurious oscillations. These are especially large when seeking a coupled flexible-rigid body dynamic solution and modelling very slender wings, as the spread in eigenvalues is particularly large. However, if the system is initialised from a steady state, i.e. if no structural vibrations are occurring at $t = 0$, the initial acceleration $\ddot{\tau}_0$ can be obtained via a lagged solution, where the rigid-body dynamics sub-problem is solved first.

During the time-stepping, the correction terms in eq. (2.44), and hence the accelerations $\ddot{\tau}_{n+1}$ at the time-step $n + 1$, need to be determined. These are required to satisfy the residual form of eq. (2.42)

$$\mathcal{R}(\ddot{\tau}_{n+1}) = M(\tau_c(\ddot{\tau}_{n+1})) \ddot{\tau}_{n+1} + \mathcal{Q}(\ddot{\tau}_{n+1}) = 0 \quad (2.47)$$

where $\mathcal{Q} = \mathcal{Q}_{gyr}(\tau, \dot{\tau}) + \mathcal{Q}_{stif}(\tau) - \mathcal{Q}_{ext}(\tau, \dot{\tau})$ includes gyroscopic, elastic and external forces. Eq.(2.47) is solved for $\ddot{\tau}_{n+1}$ using a Newton-Raphson iteration, in which the accelerations at the iteration $k + 1$ are obtained as:

$$\left. \frac{\partial \mathcal{R}}{\partial \ddot{\tau}} \right|_{n+1}^k \left(\ddot{\tau}_{n+1}^{k+1} - \ddot{\tau}_{n+1}^k \right) = -\mathcal{R}_{n+1}^k \quad (2.48)$$

At the first iteration ($k = 0$) the acceleration at time-step $n + 1$ can be conveniently taken to be: $\ddot{\tau}_{n+1}^0 = \ddot{\tau}_n$. Under this assumption, in fact, the positions and velocities at

²In a flight-dynamics solution, this would typically correspond to a steady flight configuration, with the structural nodal velocities being zero and the wing geometry determined by the steady-level flight aerodynamics loads.

time $n + 1$ computed via eq. (2.44) and (2.45) are equivalent, respectively, to a second and first order Taylor expansion. The Jacobian of the residual is obtained linearising eq. (2.47), leading to:

$$\left. \frac{\partial \mathcal{R}}{\partial \ddot{\tau}} \right|_{n+1}^k = \left(M^k + \theta_1 \Delta t C_t^k + \theta_2 \Delta t^2 K_t^k \right) \quad (2.49)$$

For systems involving coupled rigid-flexible body dynamics, the condition number of this matrix is typically lower than the one of the initial mass matrix, thus increasing the stability margin of the numerical solution.

2.2 Unsteady vortex-lattice method

This section introduces the analysis model used in this work to describe the low speed aerodynamics of high aspect ratio wing. In Sec. 2.2.1 basic aspects of potential flow theory and their numerical solution via boundary elements methods will be discussed. The vortex based discretisation and the UVLM will be described in more detail in Sec. 2.2.2. Finally, Sec. 2.2.3 will focus on the computation of the aerodynamic loads.

2.2.1 Solution of potential flow using singularity elements

Unsteady aerodynamics is computed via the UVLM under the assumptions of incompressible, inviscid and irrotational flow. These hypothesis, in particular, prevent the applicability of the method for flight conditions when flow separation is expected, e.g. high angles of attack or large flap deflections, but are realistic when dealing with low-Mach-number aerodynamics on thin wings at low angles of attack. If changes of the wing geometry occur slowly with respect to the flow characteristic time scales, in fact, this is fully attached and vorticity is confined to a thin region around the lifting surface. Due to the inviscid flow assumption, the method can only predict lift and induced drag, while drag effects linked to skin friction and flow separations are not captured. These, however, can be neglected when characterising the aeroelastic behaviour of high-altitude long-endurance aircraft flying at low speed and in attached flow conditions.

The flow velocity field \mathbf{U} is sought inside a volume V enclosing a body of surface S_b . A cut-out of the solution domain is sketched in Fig. 2.2. Using the zero vorticity assumption, $\nabla \times \mathbf{U} = 0$, the velocity field can be expressed in terms of a potential function, Φ , such that $\mathbf{U} = \nabla \Phi$. At very low Mach number, however, the flow can also be assumed to be incompressible, $\nabla \cdot \mathbf{U} = 0$: it derives that the potential function Φ is a solution of the Laplace's equation:

$$\nabla^2 \Phi = 0 \quad (2.50)$$

Laplace's equation is a linear, elliptic partial differential equation and is completed by

two kind of boundary conditions. The first ensures that the flow is tangent to the body (non-penetration) and takes the form:

$$(\nabla\Phi + \mathbf{v}_b) \cdot \hat{\mathbf{n}} = 0 \quad (2.51)$$

where \mathbf{v}_b and $\hat{\mathbf{n}}$ are the velocity of the aerodynamic surface and its unit normal vector. A farfield constraint, instead, ensures that flow disturbances decay at infinity. This is written as

$$\lim_{r \rightarrow \infty} \nabla\Phi = 0 \quad (2.52)$$

whit r measuring the distance from the body.

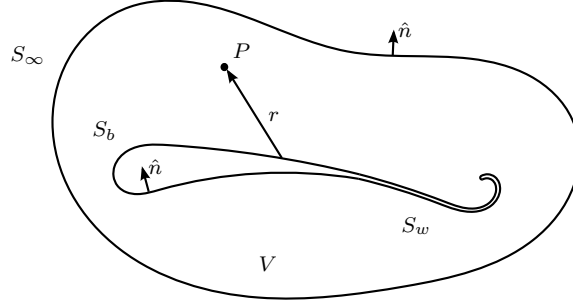


Figure 2.2: Cut-out of the potential flow solution domain of the potential flow problem.

Laplace's equation is verified by a number of basic solutions which can be superimposed to represent complex flow configurations. As shown by Katz and Plotkin [44], a general solution to eq. (2.50) can be obtained by applying Green's function theory. At each point P of the flow field this takes the form

$$\Phi(P) = \frac{1}{4\pi} \int_{S_w+S_b} \mu \frac{\partial}{\partial \hat{n}} \left(\frac{1}{r} \right) dS - \frac{1}{4\pi} \int_{S_b} \sigma \frac{1}{r} dS + \Phi_\infty \quad (2.53)$$

Eq. (2.53) shows that a solution to Laplace's equation is provided by a combination of doublet and sources of intensity μ and σ distributed over the body and wake boundaries, S_b and S_w . These are also referred to as singularity functions as they are not defined on S_b and S_w , hence when $r \rightarrow 0$. It is important to notice that a wake boundary, S_w , has been introduced in eq. (2.53). From a mathematical point of view, this is required so as to account for possible discontinuities of the velocity and/or velocity potential across the wake. From a physical perspective, instead, this allows to verify the conservation of angular momentum (Kelvin's theorem); this aspect will be, in particular, discussed further in Sec. 2.2.2. Finally, in eq. (2.53) Φ_∞ is the contribution arising from the external boundary of the domain, S_∞ , and produced by the free stream, undisturbed, flow (see also Fig. 2.2). Being $\{X, Y, Z\}$ the Cartesian coordinates of the inertial frame,

G , this is written through the scalar product

$$\Phi_\infty = \{X, Y, Z\} \cdot \mathbf{U}_\infty \quad (2.54)$$

where \mathbf{U}_∞ is the free-stream velocity.

The solution obtained in eq. (2.53) transforms a three-dimensional problem into a two-dimensional one, where the aim is to obtain a distribution of basic solutions over the domain boundaries which verify the non-penetration and farfield constraints in eq. (2.51) and (2.52). It is thus particularly suitable to numerical implementations (panel methods). Furthermore, while eq. (2.53) is expressed in terms of doublet and sources, other singularity functions, such as vortex elements, can be used [44]. As lift is associated to nonzero velocity circulation (Joukowski's theorem), these last are especially suited for lift prediction over thin body, i.e. when drag effects are secondary.

The unsteady vortex-lattice method belongs to this class of solutions and approximates the lifting body and its wake as infinitesimally-thin surfaces. As shown in Fig. 2.3, these are discretised as a lattice of quadrangular vortex rings. These singularity elements are equivalent to doublet quadrangular elements [44], hence showing that the method is, in fact, based on the discretisation of the analytical solution in eq. (2.53). Each vortex ring is associated to a circulation strength Γ_k and the velocity induced is provided by the Biot-Savart law. To each element discretising the lifting surface (bound vortices) is associated a collocation point where the non-penetration boundary condition (2.51) is enforced. At each time-step, a row of vortices — whose intensity is determined by enforcing Kelvin's theorem — is shed tangentially at the wing trailing edge, thus building up the wake. This can be either prescribed (hence assuming that shed vortices move according to the undisturbed flow velocity) or computed as part of the flow solution, thus allowing the vortex rings to align with the local flow velocity.

2.2.2 Numerical solution via vortex-elements

In the most general case, i.e. when the wake shape is not prescribed, a flow solution requires computing the circulation strength of the bound and wake vortices, as well as the position of the wake grid coordinates. In this section, the most relevant aspects of this process, namely the enforcement of the non-penetration boundary condition in eq. (2.51) and the modelling of the wake, are outlined: for a more detailed description of the numerical implementation, the reader is referred to Murua [52].

As introduced in Sec. 2.2.1, a distribution of vortex rings singularity elements automatically verifies not only the Laplace's equation (2.50) but also the farfield boundary condition, eq. (2.52). Therefore, the first step of the solution process requires the enforcement of the non-penetration boundary condition in eq. (2.51) at the collocation points associated to the bound singularity elements. As shown in Fig. 2.3, these are placed at the middle of each element. Each each vortex ring is, instead, positioned a

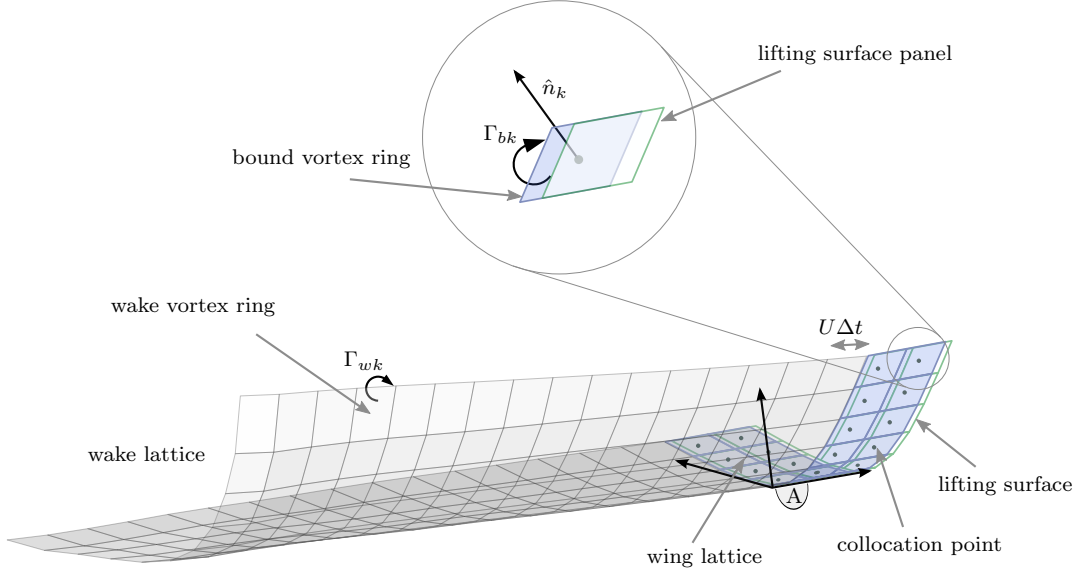


Figure 2.3: Schematics of wing and wake vortex lattices.

quarter of a panel dimension rearwards from the respective lifting surface panel. For two-dimensional cases, in fact, these choices allow for an exact agreement with classical thin-aerofoil theory, even when the wing is discretised with one element in the chord-wise direction [8, 162].

Using the Biot-Savart law, the velocity per unit circulation strength induced by the vortex ring j at the collocation point of the ring element i is:

$$\mathbf{q}_{ij} = -\frac{1}{4\pi} \oint_{C_j} \frac{\mathbf{r}_{ij} \times d\mathbf{s}_j}{|\mathbf{r}_{ij}|^3} \quad (2.55)$$

where the integration is extended over the entire j -th ring, C_j , and \mathbf{r}_{ij} measures the relative position of point i with respect to the infinitesimal segment of vortex, $d\mathbf{s}_j$. At time-step n , therefore, the impermeability condition (2.51) can be expressed as:

$$A_b(\boldsymbol{\zeta}_b) \boldsymbol{\Gamma}_b^n + A_w(\boldsymbol{\zeta}_b, \boldsymbol{\zeta}_w) \boldsymbol{\Gamma}_w^n + \mathbf{w}^n(\boldsymbol{\zeta}_b, \dot{\boldsymbol{\zeta}}_b, \boldsymbol{\nu}, \boldsymbol{\chi}) = 0 \quad (2.56)$$

where $\boldsymbol{\Gamma}_b$ and $\boldsymbol{\Gamma}_w$ are column vectors of length N_b and N_w containing the circulation strength of bound and wave vortices. The wing-wing and wing-wake aerodynamics influence coefficients matrices, A_b and A_w , are defined based on eq. (2.55) as

$$(A_b)_{i,j} = \mathbf{q}_{ij} \cdot \hat{\mathbf{n}}_i \quad , \quad i, j = 1 \dots N_b \quad (2.57a)$$

$$(A_w)_{i,j} = \mathbf{q}_{ij} \cdot \hat{\mathbf{n}}_i \quad , \quad i = 1 \dots N_b \quad , \quad j = 1 \dots N_w \quad (2.57b)$$

where $\hat{\mathbf{n}}_i$ is the normal unit vector of the i -th panel. As underlined in eq. (2.56), these

depend on the bound and wake vortex rings coordinates, ζ_b and ζ_w , thus providing a first coupling term with the structural and control disciplines. The first two terms in eq. (2.56) return the velocity induced by the vortex rings system on the collocation points, while the vector \mathbf{w} contains all the non-circulatory normal velocity. This accounts for the movement of aerodynamic control surfaces and for gust induced velocity, as well as for the lifting surface rigid-body motion (through its velocities, $\boldsymbol{\nu} = (\mathbf{v}^T, \boldsymbol{\omega}^T)^T$, and orientation, $\boldsymbol{\chi}$), deflections,³ ζ_b , and rate of deflections, $\dot{\zeta}_b$.

The enforcement of the non-penetration condition in eq. (2.56) provides a set of N_b independent algebraic equations. These are not enough to determine the state of all the variables describing the flow field, namely the vortex elements intensity $\boldsymbol{\Gamma}_b$, $\boldsymbol{\Gamma}_w$ and the wake grid coordinates ζ_w . For achieving the system closure, further physical conditions on the wake dynamics (addressing the wake circulation, $\boldsymbol{\Gamma}_w$) are required, including a model for the wake propagation — i.e. a criterion on how to set ζ_w .

As introduced in Sec. 2.2.1, modelling the wake surface is required to satisfy Kelvin's theorem. In a potential flow, in fact, the total circulation, Γ_{tot} , around a curve consisting of the same fluid particles flow has to remain constant, i.e.:

$$\frac{d\Gamma_{tot}}{dt} = 0 \quad (2.58)$$

As lift is associated to a production of circulation (Joukovsky's theorem, [8, 44]), therefore, vorticity has to be shed behind the lifting surface so as to verify eq. (2.58) and, thus, building up the wake. In the UVLM method, in particular, the cross-sections of the lifting surface are assumed to be streamlines, hence the shedding occurs at the trailing edge. Furthermore, as no external forces are acting on the wake, the circulation of the vortex rings remains constant as they move downstream (third Helmholtz's theorem [44]). In reality, large dissipation typically occurs beyond the near field, and this approximation becomes inaccurate. Nonetheless, the influence of the vortex rings on the velocity field nearby the wing also decreases as these move downstream, hence bounding the error associated to this assumption.

Following these consideration, it derives that the circulation strength of the wake vortices, $\boldsymbol{\Gamma}_w$, in eq. (2.56) is a known quantity, exception made for those terms associated to the line of vortices shed at the trailing edge. Their value can, however, be determine enforcing Kelvin's condition: using a first order integration scheme, eq. (2.58) leads to

$$\boldsymbol{\Gamma}_{w_0}^n = \boldsymbol{\Gamma}_{b_{TE}}^{n-1} \quad (2.59)$$

where the column vector associated to the circulations strength of the wake vortices shed at time-step n , $\boldsymbol{\Gamma}_{w_0}^n$, is enforced to be equal to the trailing edge bound vortices at the previous time-step, $\boldsymbol{\Gamma}_{b_{TE}}^{n-1}$. An important, yet not obvious, consequence of this

³These determine the orientation of the vortex rings, which is required to extract the normal component of the velocities at the collocation points.

condition is that the time-step size is now constrained. As the bound and wake trailing edge vortices have the same circulation strength, they should also approximatively have the same area. Hence, the time-step will depend on both the chord-wise size of the last row of panels and the flow speed, U_∞ . In particular, assuming M equally spaced rows of panels in the chord-wise direction, this leads to:

$$\Delta t = \frac{c}{M|U_\infty|} \quad (2.60)$$

Further details of the time-stepping procedure are provided by Mauermann [51] and Murua [52]. Here it is worth underlining that, when a steady solution is sought, eq. (2.59) allows to retrieve the Kutta condition at the lifting surface trailing edge line [163]. This states that the flow leaves the body smoothly, i.e. such that there is no pressure jump between lower and upper streamline occurs. This is ensured by enforcing that the circulation around the trailing edge line at each span-wise location, γ_{TE} , is null, hence leading to:

$$\gamma_{TE} = \Gamma_{w_0} - \Gamma_{b_{TE}} = 0 \quad (2.61)$$

Finally, the wake propagation needs to be addressed. This step is required so as to retrieve the wake grid coordinate, ζ_w , and, therefore, evaluate the wing-wake aerodynamics influence coefficient matrix in eq. (2.56). For the wake to be a free force surface, vortex rings need to align with the local flow speed, so as to satisfy Helmholtz's theorem. This can be achieved updating the wake grid corner points position at each time step. The process is, however, computationally expensive, as it requires to evaluate the induced velocity produced by all of the other vortex rings in the field. For this reason, the wake grid coordinates ζ_w can be updated once per time-step using a first order explicit Euler integration scheme. This method has proven good accuracy for the low-frequency flight-dynamics of very flexible vehicles as changes in wake geometry occur smoothly and can be captured adequately using sufficiently refined time-steps [74].

The force free wake obtained through this approach for a large dihedral wing during a rolling manoeuvre is shown in Fig. 2.4a. In the figure, the tip vortices structures and the wake roll up produced by the ailerons deflections can be observed. As vortices are carried downstream, their induced velocity at the wing decreases rapidly: in the numerical implementation, therefore, the wake is cut a number of chords downstream the wing and its length is determined via a convergence study.

A computationally cheaper — yet very accurate for the low frequency dominated studies presented in this work — approach for defining the wake is to neglect the vortex induced velocity and update the wake grid based on the free stream and, possibly, gust induced velocity only. This leads to the prescribed wake model, Fig. 2.4b. Importantly, in this case the wake can still capture — and keep memory of — large wing bending, rigid-body motion and ailerons deflections. The comparison with Fig. 2.4a, however, shows that the roll up caused by the ailerons deflection is not accurate.

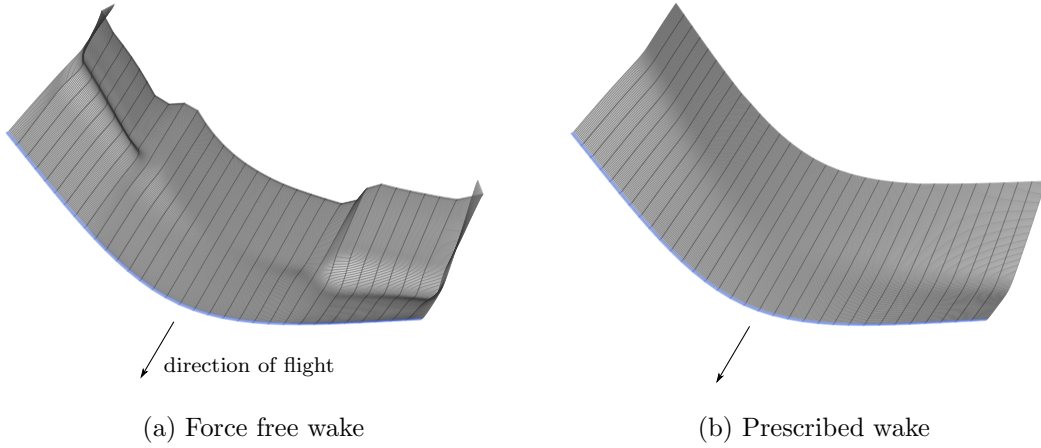


Figure 2.4: Comparison of different models of wake for a high-aspect-ratio wing during a rolling manoeuvre.

Wake roll up may be important when the characteristic frequency of the structural dynamics are large as compared to those associated to the flow field, u_∞/c [164]. For the studies presented in this work, in which the wing dynamics is relatively slow, as the vorticity structures grow in size they are also quickly carried downstream, and their impact on the induced velocities at the wing is reduced. A prescribed wake model has been found, therefore, to be a very good approximation and has been used throughout this work.

2.2.3 Aerodynamic loads

Once the bound circulation Γ_b is found, the inviscid loads acting on the lifting surface at each time-step are finally computed applying the unsteady Kutta-Joukowski theorem [165]. The force produced by a bound vortex ring can be divided into two component. The first is a quasi-steady contribution which accounts for leading edge suction effects. This depends on the circulation intensity Γ of the vortex ring according to

$$d\mathbf{f}_s = \rho_\infty \Gamma \mathbf{U} \times d\mathbf{s} \quad (2.62)$$

where $d\mathbf{s}$ is an infinitesimal segment of vorticity and ρ_∞ is the air density. The local velocity \mathbf{U} is tangent to the lifting surface only at the collocation points, eq. (2.56), hence this force may not be perfectly aligned to the panel surface normal if the wing vortex-lattice is not sufficiently refined.

The unsteady contribution derives from the $\frac{\partial \Phi}{\partial t}$ term in the unsteady Bernoulli's equation [166]

$$\frac{\partial \Phi}{\partial t} + \frac{1}{2} \rho_\infty |\mathbf{U}|^2 + \frac{p}{\rho_\infty} = \text{const} \quad (2.63)$$

and accounts for the added mass effect; note that in eq. (2.63) p is the flow pressure and

the gravity term has been neglected. The resulting force acts along the lifting surface normal, \hat{n} , and can be expressed as [165]

$$d\mathbf{f}_u = \rho_\infty \frac{\partial \Gamma}{\partial t} \hat{n} dS \quad (2.64)$$

where dS is a surface element.

An alternative way to obtain the aerodynamic loads is to compute the pressure jump between upper and lower surface of the wing lattice through the unsteady Bernoulli's equation [44]. This approach computes lifting loads accurately but it can not account for leading edge suction and, as a result, overestimates the induced drag. While corrections are available [44, 45], the unsteady Kutta-Joukowski theorem has been shown good accuracy in computing both lift and drag loads, as well as good convergence properties [153].

2.3 Multidisciplinary integration and fluid-structure interaction

Sec. 2.1 and 2.2 addressed one by one the modelling of the flexible-rigid body dynamics of geometrically nonlinear wings and of the inviscid flow surrounding them. This section will discuss how these solutions can be coupled for dealing with fluid-structure interaction problems. Together with the modelling aspects of the structural dynamics and the aerodynamics, the integration of the two methodologies forms a core part of SHARPy (Simulation of High Aspect Ratio Planes in Python), a framework for flight-dynamics analysis of very flexible aircraft.⁴

The fluid-structure interaction scheme has been based on an already existing Matlab implementation of this framework, which has been extensively verified in previous studies [16, 54, 75] and is described in high detail by Murua [52] and Hesse [156]. Here the two main aspects of the coupling process, namely the mapping between structural and aerodynamics disciplines and the time-stepping scheme, are discussed. In particular, as a large number of analysis is performed during the optimisation process, the latter has required modifications with respect to the original scheme developed by Murua [52], so as to increase the robustness of the integration process. This will be discussed in Sec. 2.3.2.

2.3.1 Mapping between structural and aerodynamics discretisations

The starting point for coupling the structural and aerodynamics solutions presented in Sec. 2.1 and 2.2 is to define a mapping scheme for retrieving the instantaneous 3D shape of the lifting surfaces lattices from the 1D beam description of the wing deformed

⁴SHARPy is open-source and free access to the code is available through the GitHub website at <https://github.com/SalvatoreMaraniello/SHARPy>.

configuration. This implies determining the vortex-lattice panels coordinates, ζ_b (defined in Sec. 2.2.2), from the nodal positions $\mathbf{R}(s_i, t)$, and orientation, $\Psi(s_i, t)$, of the local frame B with respect to the body frame A . For enforcing the impermeability condition at the vortex rings collocation points, eq. (2.56), however, the rate of change of ζ_b is also required. Therefore, the procedure also needs to include the rate of change of $\mathbf{R}(s_i, t)$ and $\Psi(s_i, t)$, as well as the velocities \mathbf{v} and $\boldsymbol{\omega}$ of the moving frame A and its orientation, which is described through a quaternion, χ .

The mapping process is defined upon the assumption that the spanwise discretisation of beam nodes and wing panels coincides. Together with the kinematic hypothesis that the wing cross-sections remain undeformed (Sec. 2.1.3), this simplifies considerably the mapping of both the lattice geometry and the aerodynamics loads. The use of the same spanwise discretisation for the structural and aerodynamic solution has the only downside of requiring a careful assessment of the wing discretisation. For flight-dynamics applications, in fact, the UVLM grid needs a high refinement in proximity of the wing tips, while a higher density of finite elements is commonly necessary at the wing root of the structural mesh, where loads and deflections are larger.

When the interface is initialised, the mapping is defined over the undeformed wing geometry. The coordinates of the j -th point of the wing lattice grid at the cross-section i are described in the corresponding local frame B as $\zeta_B(s_i, v_j)$, where s and v are curvilinear coordinates along the span-wise and chord-wise directions. Note that $\zeta_B(s_i, v_j)$ does not depend on time, as wing cross-sections rotate rigidly. As the wing deforms, their orientation is retrieved through the associated Cartesian rotation vector, $\Psi(s_i, t)$, while its position with respect to the body attached frame A is provided by $\mathbf{R}(s_i, t)$. The coordinated of the grid point can be, therefore, expressed in the inertial frame G as

$$\zeta_G(s_i, v_j, t) = \mathbf{r}_G(t) + C^{GA}(\chi(t)) [\mathbf{R}_A(s_i, t) + C^{AB}(\Psi(s_i, t)) \zeta_B(s_i, v_j)] \quad (2.65)$$

where \mathbf{r}_G is the FoR A position. Note that from eq. (2.65) the rate of change of the grid points due to the elastic dynamics can also be obtained. Their total speed in the inertial frame can finally be expressed as

$$\begin{aligned} \dot{\zeta}_G(s_i, v_j, t) = C^{GA}(\chi(t)) & \left[\mathbf{v}_A(t) + \tilde{\omega}_A(t) \mathbf{R}_A(s_i, t) + \right. \\ & \left. + \dot{\mathbf{R}}_A(s_i, t) + C^{AB}(\Psi(s_i, v_j, t)) \tilde{\Omega}_B \zeta_B(s_i, v_j) \right] \end{aligned} \quad (2.66)$$

Eq. (2.65) and (2.66) provide the surface lattice position and rate of change, which are required to enforce the impermeability condition in eq. (2.51). Once the distribution of circulation on both surface and wake lattices has been found, the forces acting on each segment of the lattice grid are obtained integrating eq. (2.62) and (2.64) over the vortex elements segments and areas, respectively. As the aerodynamics and structural discretisation match, loads are equally split between adjacent cross-sections first and,

finally, condensates at the beam nodes. The resulting forces feed the external force Q_{ext} term in eq. (2.42), thus closing the coupling.

Finally, it is worth noticing that the effect of control surfaces deflections is also included at this stage. Their movement is, in fact, modelled by displacing the corner points of the vortex rings used to discretise them.

2.3.2 Time integration

The structural and aerodynamics solutions presented in Sec. 2.1 and Sec. 2.2, together with the interface relations in Sec. 2.3, describe the evolution in time of a geometrically nonlinear aeroelastic system with coupled rigid-flexible body dynamics. As shown in Sec. 2.1.7 and 2.2.2, however, the time discretisation of the two solutions is based on different schemes. For rigid-flexible body dynamics problems, a second order implicit Newmark- β method has been employed for improving stability. For the UVLM solution, instead, an explicit first order integration ensures that the costly evaluation of the aerodynamics influence coefficient matrices in eq. (2.56) is performed only once per time-step. The main obstacle in implementing a coupled aeroelastic solution is, therefore, that of combining these integrations schemes together in a way that retains their good stability and numerical performances.

A first approach can consist in a fully coupled, monolithic, solution strategy. As the coupled system is nonlinear, this approach would require deriving the Jacobian terms coupling structural dynamics and aerodynamics. Such implementation would, however, lead to very stiff systems, as the characteristic eigenvalues associated to the two disciplines may differ of several orders of magnitude. This is a common issue in fluid-structure interaction problems which, as a result, are commonly solved through a partitioned solution, in which structural and aerodynamics solutions are integrated separately [154, 155].

According to how the information flows from one discipline to another and the level of coupling enforced, different partitioned architectures are obtained. The most accurate solution relies on a tightly coupled scheme, which can be obtained combining an outer fluid solution loop to a structure subiteration loop [167]. This scheme guarantees that both structural and aerodynamics residuals, eq. (2.42) and eq. (2.56), are verified, but is computationally expensive as large number of UVLM solutions is required.

However, when dealing with optimisation problems — hence, possibly, a large number of analysis — a scheme should guarantee not only accuracy, but also robustness and computational efficiency. To reduce the number of UVLM solutions per time-step, a loosely coupled scheme can be used. A widely spread approach consists in a staggered scheme [168], in which the structural solution at time-step $n + 1$ is evaluated using the aerodynamic load predicted at the previous time-step. In this case the residuals associated to the flow and structural solution is not verified, but only one UVLM solution is derived per time-step.

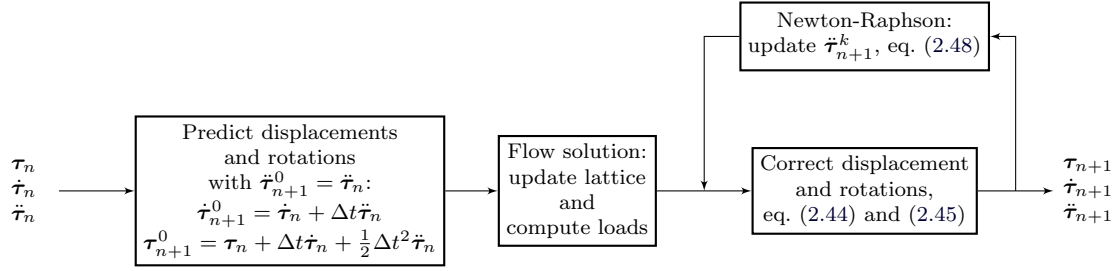


Figure 2.5: Loosely coupled scheme for aeroelastic solution.

A compromise between these two schemes is shown in Fig. 2.5. In this case, the aerodynamic loads are still computed once per time-step but the structural solution is now estimated at time-step $n + 1$ via an explicit Taylor expansion. As discussed in Sec. 2.1.7, this is obtained assuming the accelerations to be $\ddot{\tau}_{n+1} = \ddot{\tau}_n$ and predicting displacements and velocities, τ_{n+1} and $\dot{\tau}_{n+1}$, according to eq. (2.44) and eq. (2.45) — note that τ is defined as Sec. 2.1.7 such that $\tau = \{\eta, \int \nu, \int \chi\}^T$. While also in this case the structural and aerodynamics residuals are not verified, the unbalance is reduced.⁵ As a result, accuracy and robustness are improved with respect to a staggered scheme while maintaining the same computational cost. For this reason this approach has been preferred for all the studies presented in this work.

⁵For instance, in the numerical studies on rolling manoeuvres presented in Chap. 6, the magnitude of the initial residual associated to the structural inner loop in Fig. 2.5, and provided by eq. (2.47), would show reductions as large as 3 orders of magnitude when considering very flexible wings.

Chapter 3

Numerical solution of the optimal control problem

In this chapter the direct single-shooting framework for optimal control is described. This will be firstly used to control the dynamics of very flexible structures in vacuum and then applied to the manoeuvring of very flexible wings. The starting point is the definition of an optimal control problem, whose cost function and constraints depend on some performance requirements. A numerical solution can be obtained upon discretisation of the control input. Two parametrisations are employed in this work, namely discrete sines and B-splines. These have been selected for investigating possible advantages between using a local or a global set of basis function. Optimal actuations are obtained by solving an optimisation problem with respect to the coefficient parametrising the control input. The implementation is monolithic, hence an aeroelastic solution is required at each iteration of the optimisation process, and minimises the size of the resulting finite-dimensional optimisation problem. Importantly, this formulation can also be extended to co-design by simply including in the problem any design variable associated to the system to be controlled.

This process relies upon the numerical solution of a discrete optimisation problem. In this work, this is obtained using a SQP method, the SLSQP algorithm developed by Kraft [111]. In order to explore the suitability of this method for the analysis considered in this work, the second part of this chapter will outline the relevant theoretical background for illustrating the algorithm (Sec. 3.5). This is complemented by App. A and B, which include further details on the methodology, and Sec. 3.5.3, which briefly summarises the limitations of the method and alternative strategies for dealing with larger scale problems.

3.1 Problem statement

In this section, a brief introduction to the optimal control problems treated in this work

is provided. This follows the reviews of Lin et al.[105] and Allison and Herber [20], to which the reader is referred for further details. The optimal control is defined as an optimisation problem in which the design variables are a set of N_u time-dependent functions, the control input vector

$$\mathbf{u}(t) = \{u_m(t)\} \quad , \quad m = 1 \dots N_u \quad (3.1)$$

The problem takes, thus, the form

$$\begin{aligned} \min. \quad & I(t, \mathbf{y}, \mathbf{u}) \\ \text{w.r.t.} \quad & \mathbf{u}(t), \mathbf{y}(t) \\ \text{s.t.} \quad & \mathbf{c}(t, \mathbf{y}, \mathbf{u}) \geq 0 \\ & \dot{\mathbf{y}} = \mathbf{f}(t, \mathbf{y}, \mathbf{u}) \end{aligned} \quad (3.2)$$

where the array

$$\mathbf{y} = \{\boldsymbol{\eta}^T, \dot{\boldsymbol{\eta}}^T, \boldsymbol{\nu}^T, \boldsymbol{\chi}^T, \boldsymbol{\zeta}_b^T, \boldsymbol{\zeta}_w^T, \boldsymbol{\Gamma}_b^T, \boldsymbol{\Gamma}_w^T\}^T \quad (3.3)$$

defines the state of the spatially-discretised aeroelastic system discussed in Chap. 2. This is determined over the time horizon $[0, T]$ by the aeroelastic state equations

$$\dot{\mathbf{y}} = \mathbf{f}(t, \mathbf{y}, \mathbf{u}) \quad (3.4)$$

which are obtained combining:

- eq. (2.10) and (2.42), which define attitude, $\boldsymbol{\chi}$, velocities, $\boldsymbol{\nu}$, nodal displacements and rotations, $\boldsymbol{\eta}$ with their rates, $\dot{\boldsymbol{\eta}}$, of the flexible vehicle, modelled as a system of interconnected beams;
- eq. (2.56) and (2.59), which provide the circulation intensity of the wake and bound vortex-lattices, respectively $\boldsymbol{\Gamma}_w$ and $\boldsymbol{\Gamma}_b$, through enforcement of the nonpenetration boundary condition at the lifting surfaces and Kelvin's circulation theorem.
- eq. (2.62) and (2.64), which exploit the unsteady Kutta-Joukowski theorem to derive the aerodynamic force acting on each panel of the lifting surfaces.
- eq. (2.65) and (2.66), which allow retrieving positions and rates of change of the nodes of the lifting surfaces vortex-lattices.

Finally, in eq. (3.2) I is the cost functional to minimise and \mathbf{c} is a set of constraints. Note that these functionals are all problem dependent.

In general, cost and constraints will depend on both the state, \mathbf{y} , and the control input, \mathbf{u} . Referring to the generic functional in problem (3.2) as g , this can commonly be expressed in the Bolza form

$$g = h(\tilde{t}, \mathbf{y}(\tilde{t}), \mathbf{u}(\tilde{t})) + \int_0^T \mathcal{G}(t, \mathbf{u}, \mathbf{y}) dt \quad (3.5)$$

where h and \mathcal{G} are referred to as Mayer and Lagrangian term [105, 107] and $\tilde{t} \in [0, T]$. When g is the cost of the optimisation problem, for instance, it is typically assumed $\tilde{t} = T$ so as to use the Mayer term to specify terminal conditions — this form is, for instance, used in Chap. 4, where the optimal control aims to maximise the final tip velocity of a very flexible pendulum. Initial or final time constraints are enforced on the state of the system or the actuation input setting $\tilde{t} = 0$ or $\tilde{t} = T$ and assuming $\mathcal{G} = 0$. Continuous inequality or path constraints may instead be obtained either by allowing \tilde{t} to vary in the interval $[0, T]$ or through condensation techniques — e.g. using maximum and minimum functions or any of their continuously differentiable counterpart [105]. This choice affects the amount of constraints obtained once the problem is discretised and will be further discussed in Sec. 3.2. Similarly, bound constraints are enforced on the control input \mathbf{u} to limit its amplitude and rate of change as per:

$$\begin{aligned} \mathbf{u}_L(t) &\leq \mathbf{u}(t) \leq \mathbf{u}_H(t) \\ \dot{\mathbf{u}}_L(t) &\leq \dot{\mathbf{u}}(t) \leq \dot{\mathbf{u}}_H(t) \end{aligned} \quad \text{for } t \in [0, T] \quad (3.6)$$

In this work, bound constraints as per eq. (3.6) are employed in Chap. 4 and 5 to limit the actuating torque used to control the dynamics of a very flexible pendulum, while in Chap. 6 these will restrain the movement of the aerodynamic control surfaces used to manoeuvre very flexible wings. More details on the discretisation of the problem are given in the next section.

3.2 Numerical solution

This section introduces the direct single-shooting technique employed for the numerical solution of problem (3.2). In order to better motivate this choice, the discussion will start with a brief review of analytical and numerical difficulties associated to indirect methods and direct transcription (DT).

As introduced in Sec. 1.1.3, a solution to problem (3.2) can be attempted through an *optimise-discretise* approach [89, 93]. Assuming only equality constraints, and writing the cost functional in Bolza form as

$$I(t, \mathbf{u}, \mathbf{y}) = I(T, \mathbf{y}(T), \mathbf{u}(T)) + \int_0^T \mathcal{I}(t, \mathbf{u}, \mathbf{y}) dt \quad , \quad (3.7)$$

the Euler-Lagrange necessary conditions for optimality are derived by imposing that the first variation of the augmented performance index

$$\begin{aligned} \hat{I} &= I(t, \mathbf{u}, \mathbf{y}) + \int_0^T [\mathbf{p}_i (\mathbf{f}_i - \dot{\mathbf{y}}_i) + \boldsymbol{\lambda}_i \mathbf{c}_i] dt = \\ &= I(T, \mathbf{y}(T), \mathbf{u}(T)) + \int_0^T [\mathcal{I}(t, \mathbf{u}, \mathbf{y}) + \mathbf{p}_i (\mathbf{f}_i - \dot{\mathbf{y}}_i) + \boldsymbol{\lambda}_i \mathbf{c}_i] dt \end{aligned} \quad (3.8)$$

is null [88]. In eq. (3.8) the time dependent vectors $\mathbf{p}(t)$ and $\boldsymbol{\lambda}(t)$ are, respectively, adjoint variables and Lagrange multipliers. The $\delta\hat{I} = 0$ condition leads to a system of differential-algebraic equations. Aside for the aeroelastic state relations (3.4), this includes the *adjoint*

$$\dot{\mathbf{p}}_i = -\frac{\partial \mathcal{H}}{\partial \mathbf{y}_i} \quad (3.9)$$

and *control* equations

$$\frac{\partial \mathcal{H}}{\partial \mathbf{u}_i} = 0 \quad (3.10)$$

which have been expressed in terms of the Hamiltonian

$$\mathcal{H} = \mathbf{p}_i \mathbf{f}_i + \boldsymbol{\lambda}_i \mathbf{c}_i \quad . \quad (3.11)$$

These relations are finally completed by the transversality conditions

$$\mathbf{p}_i(0) = 0 \quad (3.12a)$$

$$\left(\mathbf{p}_i - \frac{\partial \mathcal{I}}{\partial \mathbf{y}_i} \right) \bigg|_{t=T} = 0 \quad (3.12b)$$

$$\left(\frac{\partial \mathcal{I}}{\partial t} + \mathcal{H} \right) \bigg|_{t=T} = 0 \quad (3.12c)$$

For a more detailed formulation, which includes the treatment of terminal constraints, the reader is reminded to Betts [88] or to the review from Limebeer and Rao [99].

Indirect methods attempt to solve the optimal control problem (3.2) by finding a root to the system composed by eq. (3.4), (3.9), (3.10) and (3.12). A first drawback is, therefore, the analytical development of these relations, which is a problem dependent, and often complex, task [131]. A more careful analysis will also reveal that eq. (3.9) to (3.12) depend on the active constraints; problem involving inequality constraints may therefore require partitioning the time horizon into *sub-arcs* characterised by different sets of active constraints [88]. Furthermore, and as it will be discussed further in Sec. 3.4, the Euler-Lagrange equations are only necessary conditions for optimality; as a result, the *control* equation (3.10) does not always allow to determine the the control \mathbf{u} . This situation leads to bang-bang or singular controls and requires special treatments [88] — the reader can, for instance, refer to the Goddard rocket problem [99]. Finally, even once all the solution sub-arcs have been identified, the multiple-points boundary values problem resulting from the enforcement of eq. (3.4), (3.9), (3.10) and (3.12) is likely to be ill-conditioned due to the non-physical nature of adjoint variables and Lagrange multipliers.

For these reasons, a *discretise-optimize* approach is required in most applications. In this case problem (3.2) is discretised in time and solved using nonlinear programming techniques [99]. As discussed in Sec. 1.1.3, in particular, DT results from an implicit solution strategy. Quadrature approximations are first employed to reduce the differ-

ential state equations (3.4) to a set of algebraic constraints; next, the optimiser solves simultaneously for state and control over a set of collocation points. Due to the large dimensionality of $\mathbf{y}(t)$, however, this approach could lead to very large optimisation problems, especially when considering the time horizons and range of frequencies characterising the dynamics of the studies included in this work. Each element of $\mathbf{y}(t)$, in fact, would require to be discretised in time and the size of this parametrisation should be refined enough to reconstruct the relevant frequencies of the wing aeroelastic response. In order to minimise the size of the resulting optimisation problem, therefore, the control vector parametrisation approach has been employed.

A considerable size-reduction of the finite-dimensional optimisation associated to problem (3.2) can be achieved by eliminating the aeroelastic state, $\mathbf{y}(t)$. For a given control input $\mathbf{u}(t)$, therefore, $\mathbf{y}(t)$ is determined by performing a full aeroelastic analysis and problem (3.2) is recast in the form of an MDF architecture [92]:

$$\begin{aligned} \min. \quad & I(t, \mathbf{y}(\mathbf{u}), \mathbf{u}) \\ \text{w.r.t.} \quad & \mathbf{u}(t) \\ \text{s.t.} \quad & \mathbf{c}(t, \mathbf{y}(\mathbf{u}), \mathbf{u}) \geq 0 \end{aligned} \tag{3.13}$$

where the dependency of the state on the control, $\mathbf{y} = \mathbf{y}(\mathbf{u})$, has been explicitly stated. Problem (3.13) can be discretised in time by expressing each control function, $u_m(t)$, as a linear combination of N_c basis functions, $\phi_n(t)$, defined over the time horizon $[0, T]$. This leads to

$$u_m(t) = \sum_{n=1}^{N_c} x_{c_{m,n}} \phi_n(t) \tag{3.14}$$

where \mathbf{x}_{cm} is an N_c length array containing the coefficients parametrising the m -th control input, $u_m(t)$. The discrete form of problem (3.13) becomes, thus,

$$\begin{aligned} \min. \quad & I(t, \mathbf{y}(\mathbf{x}_c), \mathbf{x}_c) \\ \text{w.r.t.} \quad & \mathbf{x}_c \\ \text{s.t.} \quad & \mathbf{c}(t, \mathbf{y}(\mathbf{x}_c), \mathbf{x}_c) \geq 0 \end{aligned} \tag{3.15}$$

where

$$\mathbf{x}_c = \left\{ \mathbf{x}_{c_1}^T, \dots, \mathbf{x}_{c_{N_u}}^T \right\}^T \tag{3.16}$$

groups the N_u arrays \mathbf{x}_{cm} defining the control input. Problem (3.15) can be solved via nonlinear optimisation techniques. Its size is minimised and only depends on the parametrisation chosen to describe the control input (Sec. 3.3). Importantly, the time grid over which the aeroelastic solution is obtained can be refined for capturing the aeroelastic frequencies necessary to resolve the system dynamics without affecting the size of the optimisation problem (3.15). The integration methods described in Sec. 2.1.7 and 2.3.2 can be used and, overall, no further modification to the solution process described

in Chap. 2 is necessary.

The extension of problem (3.15) to an MDO that simultaneously optimises control action and structural properties is straightforward. This only requires the inclusion of a set of structural design parameters, \mathbf{x}_s , and augmenting, if required, the vector \mathbf{c} with additional structural constraints:

$$\begin{aligned} \min. \quad & I(t, \mathbf{y}(\mathbf{x}_c, \mathbf{x}_s), \mathbf{x}_c, \mathbf{x}_s) \\ \text{w.r.t.} \quad & \mathbf{x}_c, \mathbf{x}_s \\ \text{s.t.} \quad & \mathbf{c}(t, \mathbf{y}(\mathbf{x}_c, \mathbf{x}_s), \mathbf{x}_c, \mathbf{x}_s) \geq 0 \end{aligned} \tag{3.17}$$

The general form of the inequality constraints used in this work has been shown in eq. (3.5). Some considerations are required for the discretisation of the Mayer term, h , when this is evaluated at each time of the horizon $[0, T]$, i.e. to discretise path constraints of the form:

$$h(t, \mathbf{y}(t), \mathbf{u}(t)) \geq 0 \quad , \quad t \in [0, T] \tag{3.18}$$

Note that this form also includes the actuation bound constraints introduced in eq. (3.18). A difficulty in treating these kind of constraints is that they need to be satisfied at each time instant in the time horizon $[0, T]$. In this implementation, a point-wise approach, in which the constraints are only enforced over a defined collocation grid, has been applied [107, 110, 137]. This solution does not guaranty that path constraints are not violated between grid points. However, the aeroelastic state $\mathbf{y}(t)$ typically varies smoothly in time, hence a bound on how much eq. (3.18) is violated can be imposed by adjusting the collocation grid according to the range of aeroelastic frequencies characterising the problem [107]. Similarly, for the bound constraints in eq. (3.18) the density of the collocation grid will be adapted based on the maximum frequency of the control input, which is determined by the parametrisation chosen (Sec. 3.3).

While this approach can generate a relatively large number of constraints, the computational cost of the optimisation is not impacted, as the sensitivity analysis is performed using finite differences. For adjoint based frameworks, on the other hand, condensation techniques would be necessary [105, 169], so as to contain the number of adjoint solutions required for evaluating the gradient. Point-wise enforcement, however, typically offers better convergence properties [116].

The treatment of continuous inequality constraints completes the discretisation process. Before discussing optimisation strategies for the solution of the resulting finite-dimensional problems (3.15) and (3.17), it is worth remarking that scaling can affect both the robustness and the convergence rate of the nonlinear programming algorithm used [88]. For this reason, and despite SQP methods being generally robust when dealing with badly scaled problems [138], in the numerical studies considered in this work the terms appearing in problems (3.15) and (3.17) are normalised so as to have the same order of magnitude. Therefore, the control inputs, \mathbf{x}_{c_i} , and the design parame-

ters, \mathbf{x}_{s_i} , are scaled with respect their upper bounds such that $|\mathbf{x}_{c_i}| \leq 1$ and $|\mathbf{x}_{s_i}| \leq 1$. The same approach is used to determine the scaling factors for the path constraints in eq. (3.18) but can not be applied to the objective function I . In this case, instead, an estimate of the magnitude of the cost function in the optimum region (which can be obtained through numerical studies on low-dimensional aeroelastic models or other kinds of simplified analyses) is used.

3.3 Control parametrisations

As shown in Sec. 3.2, a finite-dimensional version of problem (3.13) is obtained by discretising its control input, eq. (3.14). In this respect, many implementations found in literature use piecewise constant or linear parametrisations [110, 112, 113, 117], which are easy to build and offer good convergence properties [105]. However, to describe the movement of typical control actuators on a relatively large time domain, these choices would lead to set of basis functions of substantial size.

For example, numerical studies on dynamical control of very flexible structures in Chap. 4 and 5, will consider a time horizon of 2s and will require a small time-step of 2×10^{-4} s to integrate the system dynamics. Defining the control input on this time-grid would lead to a very large optimisation problem, whose solution is impractical unless an adjoint solver is employed. While automatic differentiation is possible [170], this is not easily applicable to the current SHARPy implementation, whose core routines are written both in Fortran and C++ and for which, therefore, an analytical derivation of the adjoint equations would be required. Furthermore, this level of refinement is not only unnecessary but could also be detrimental. In the example considered, for instance, defining the control input on the solution time grid would allow expressing very high frequencies (up to 10^3 Hz). These are far outside the range of interest of our studies (of the order of 10 Hz) and, with the aim of avoiding unrealistic steep changes, the control input would require smoothing, either enforcing additional constraints on its rate of change or applying a low frequency filter to its gradient during the optimisation process itself [171].

With the purpose of modelling smooth actuation signals while limiting the number of coefficients used to parametrise the control, N_c , only \mathcal{C}^1 continuous or higher parametrisations are considered for this work. As the dynamics of structures is strongly linked to the frequency of excitations of external disturbances and control forces, it is natural to use a parametrisation that can be easily linked to the frequency range of the control. An obvious candidate is the discrete Fourier series or, for control signals with $u(0) = u(T) = 0$, the discrete sine series (DSS) obtained using the following basis functions of the form:

$$\phi_n(t) = \sin 2\pi f_n t \quad \text{with:} \quad f_n = n f_0 \quad , \quad f_0 = \frac{1}{2T} \quad (3.19)$$

The DSS expansion of a general signal u defined over a domain $[0, T]$ can instead be obtained by applying a Fourier transform to the extended signal

$$\tilde{u} = \begin{cases} \tilde{u} = u(t) & , \quad t \in [0, T] \\ \tilde{u} = -u(-t + 2T) & , \quad t \in [T, 2T] \end{cases} \quad (3.20)$$

defined over the domain $[0, 2T]$. This parametrisation has the advantage of allowing to directly regulate the maximum actuation frequency of the control input. While sines are globally defined in time, however, they are collocated in the frequency domain, each harmonic being associated to a specific frequency f_n — see eq. (3.19). This feature does not pose an issue in terms of reconstruction properties,¹ but may reduce the robustness of the single-shooting approach. As the basis functions are global, in fact, large changes in control input may occur from an iteration to another of the optimisation process, possibly resulting in excessively high control forces and rate of changes and, overall, increasing the risk of instabilities arising during the numerical integration.

For this reason, local basis functions are also considered. Third order B-splines, in particular, have been chosen for their smoothness properties [109, 116, 137]. A set of B-splines basis functions of order p can be built recursively over a set of N_τ control points τ_n as [116]:

$$\phi_n^{(0)}(t) = \begin{cases} 1 & \text{if } \tau_n < t < \tau_{n+1} \\ 0 & \text{else} \end{cases} \quad (3.21)$$

and

$$\phi_n^{(p)}(t) = \frac{t - \tau_n}{\tau_{n+p} - \tau_n} \phi_n^{(p-1)}(t) + \frac{\tau_{n+p+1} - t}{\tau_{n+p+1} - \tau_{n+1}} \phi_{n+1}^{(p-1)}(t) \quad , \quad p > 0 \quad (3.22)$$

Note that, if N_τ control points are used, the number of spline basis required is $N_c = N_\tau + p - 1$. Third-order B-splines were found to provide good and smooth reconstructions for the applications in this work.

The frequency range of actuation can be regulated by noticing that, in order to capture a frequency, f_{max} , a spacing between control points $\Delta\tau \leq 1/(2f_{max})$ is necessary (Nyquist criterion). If control points are equally spaced, therefore, their total number, N_τ , is related to the maximum frequency captured by the parametrisation through: $N_\tau \approx 2Tf_{max} + 1$. This is observed in Fig. 3.1, where two B-spline basis, built assuming non-dimensional frequencies $2Tf_{max}$ equal to 16 and 32, are compared in both time (Fig. 3.1a) and frequency domain (Fig. 3.1b). In the time domain the length of the B-spline reduces as the spacing between control points, $\Delta\tau$ halves; higher rates \dot{u} and \ddot{u} are also reconstructed. Their DSS decomposition (Fig. 3.1b), on the other hand, shows a slower decay in the frequency domain, where the frequency range covered is

¹From Fourier's theorem any signal u defined over the domain $[0, T]$ can be reproduced by a large enough sine series.

approximately doubled. It results that, fixed a f_{max} value, DSS and B-splines basis have comparable size and similar reconstruction properties, although it should be noted that the frequency spectrum of each spline basis has a smooth decay to zero towards f_{max} , Fig. 3.1b. As it will be shown in Sec. 4.4, this means that harmonic components whose frequencies is near f_{max} are not reconstructed accurately. While local in time, however, spline basis have a distributed frequency content, thus providing opposite properties to the DSS basis during a sensitivity analysis.

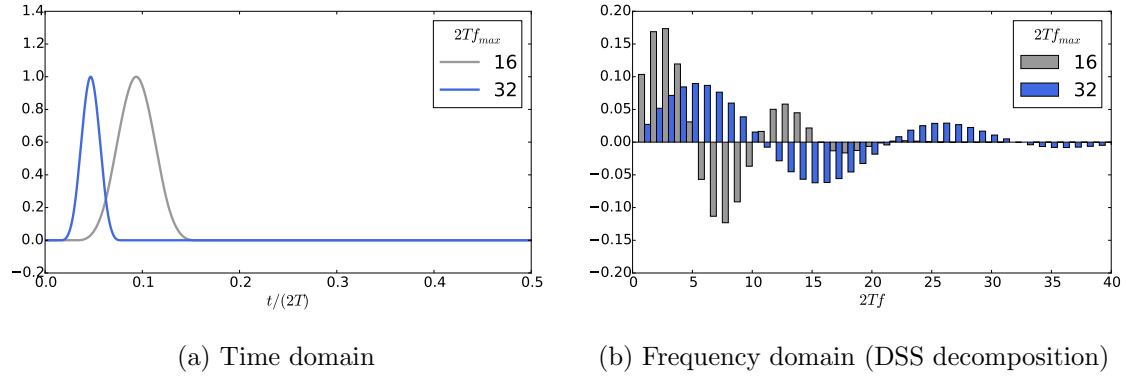


Figure 3.1: Comparison between third-order B-splines obtained when doubling the non-dimensional frequency $2Tf_{max}$.

3.4 Problem formulation vs. optimal control nature

Before discussing the optimisation algorithm used to solve the discrete optimisation problems (3.15) and (3.17), some considerations on the optimal rolling manoeuvres studied in Chap. 6 are included here. The aim is to show how the optimality conditions introduced in Sec. 3.2 can be used to identify relevant features of the sought optimal control. This knowledge can, in fact, allow to anticipate numerical difficulties in the solution of the associated finite-dimensional problem and shed light on how to overcome these.

For the purpose of this discussion, a simplified flight-dynamics model of the wing roll dynamics is considered:

$$\ddot{\Phi} = c\beta(t) \quad , \quad c = q_{\infty} S b \frac{C_{M_{\beta}}}{I_{xx}} \quad (3.23)$$

In eq. (3.23) Φ is the wing roll angle, while β the amplitude of the control surfaces. Aerodynamic damping is neglected and the constant c depends on the dynamic pressure (q_{∞}), the wing surface (S) and moment of inertia (I_{xx}), the control surfaces moment arm, b , and effectiveness, $C_{M_{\beta}}$.

An optimal control problem arises when aiming to determine the ailerons deflections time histories, $\beta(t)$, required to roll the wing of a prescribed angle, $\tilde{\Phi}$, in minimum time.

In its simplest form, this problem can be formulated as:

$$\begin{aligned}
 \min. \quad & I = \int_0^T 1 \, dt \\
 \text{w.r.t.} \quad & \mathbf{u}(t), \mathbf{y}(t) \\
 \text{s.t.} \quad & \dot{\mathbf{y}} = \mathbf{f}(t, \mathbf{y}, u) \\
 & |u| \leq \beta_{max} \\
 & \mathbf{y}(0) = 0 \\
 & \mathbf{y}(T)^T = (\tilde{\Phi}, 0)
 \end{aligned} \tag{3.24}$$

in which $u = \beta$, $\mathbf{y}^T = (\Phi, \dot{\Phi})$ and $\mathbf{f}^T = (y_2, cu)$. While initial and terminal conditions are enforced on the state, \mathbf{y} , the deflection amplitude is free at the boundaries. This is, however, bounded to be $|u(t)| < \beta_{max}$. When this inequality constraint is not active, the Hamiltonian (3.11) is $\mathcal{H} = 1 + p_1 y_2 + c p_2 u$ and the adjoint equations are

$$\begin{cases} \dot{p}_1 = 0 \\ \dot{p}_2 = -p_1 \end{cases} \Rightarrow \begin{cases} p_1(t) = P_1 \\ p_2(t) = -P_1 t + P_2 \end{cases} \tag{3.25}$$

with P_1 and P_2 being constant. The *control* equation (3.10) reduces instead to $p_2(t) = 0$. It results that an expression for the control can not be obtained through any of the optimality conditions in eq. (3.4), (3.9), (3.10) and (3.12). The problem can instead be solved either using slag variables [89, 172] or invoking Pontryagin minimum principle. This states that at each instant in time the optimal control, u^* , is a minimiser of the Hamiltonian, $\mathcal{H}(u)$, i.e. [99]:

$$u^* = \arg \min_u \mathcal{H} \tag{3.26}$$

The solution to problem (3.24) is, therefore, the bang-bang control:

$$u^* = \begin{cases} -\beta_{max} & , p_2 < 0 \\ \beta_{max} & , p_2 > 0 \end{cases} \tag{3.27}$$

It is worth noticing that u^* does not verify the *control* equation (3.10), proving that this condition is not necessary for optimality when inequality constraints are considered. As from eq. (3.25) $p_2(t)$ is linear, the solution will be composed by two sub-arcs, with switching time $\tau \mid p_2(\tau) = 0$. Assuming $\tilde{\Phi} > 0$, it can be inferred that $u^* = \beta_{max}$ on the first arc. A solution can be found by integrating the state equations over the two sub-arcs and enforcing initial and terminal conditions, as well as the continuity of the state vector at the junction $t = \tau$. It results that the time to roll the wing is $T = 2\sqrt{\frac{\tilde{\Phi}}{c\beta_{max}}}$, while the control switch happens at $\tau = \frac{T}{2}$. Optimal control and the associated wing response

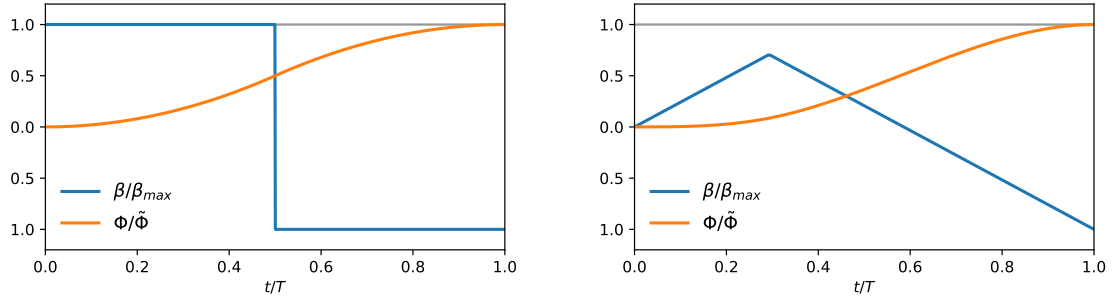
$$\Phi^*(t) = \begin{cases} \frac{1}{2}c\beta_{max}t^2 & , t < \tau \\ -\frac{1}{2}c\beta_{max}(t-T)^2 + \tilde{\Phi} & , t > \tau \end{cases} \tag{3.28}$$

are shown in Fig. 3.2a.

The optimal rolling manoeuvres defined in Chap. 6 impose a maximum rate of deflections on the actuators. Even in this case, however, optimal control requires a bang-bang strategy. This can be shown reformulating problem (3.24) as

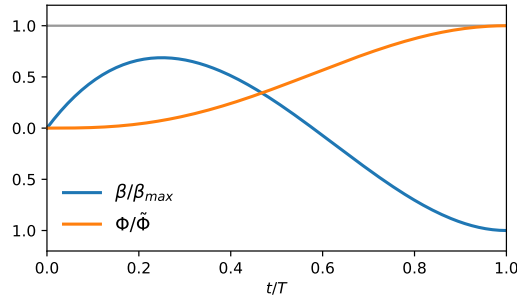
$$\begin{aligned}
 \min. \quad & I = \int_0^T 1 dt \\
 \text{w.r.t.} \quad & \mathbf{u}(t), \mathbf{y}(t) \\
 \text{s.t.} \quad & \dot{\mathbf{y}} = \mathbf{f}(t, \mathbf{y}, u) \\
 & |u| < \dot{\beta}_{max} \\
 & \mathbf{y}(0) = 0 \\
 & (y_1(T), y_2(T)) = (\tilde{\Phi}, 0)
 \end{aligned} \tag{3.29}$$

where the control variable is chosen to be $u = \dot{\beta}$ and the ailerons deflection amplitude, β , is treated as a state [88] — i.e. $\mathbf{y}^T = (\Phi, \dot{\Phi}, \beta)$ and $\mathbf{f}^T = (y_2, cy_3, u)$. While constrained to be initially null, no terminal condition is imposed on β .



(a) Bang-bang control with bounded amplitude — problem (3.24).

(b) Bang-bang control with bounded rates — problem (3.29)



(c) Smooth control with actuation penalty — problem (3.33)

Figure 3.2: Optimal ailerons deflections and wing response for problems (3.24), (3.29) and (3.33).

As in problem (3.24), the Hamiltonian, $\mathcal{H} = 1 + p_1 y_2 + c p_2 y_3 + p_3 u$, is linear in the control, hence u can not be defined through the *control* equation, $p_3 = 0$. Furthermore,

the adjoint relations

$$\begin{cases} \dot{p}_1 = 0 \\ \dot{p}_2 = -p_1 \\ \dot{p}_3 = -cp_2 \end{cases} \Rightarrow \begin{cases} p_1(t) = P_1 \\ p_2(t) = -P_1 t + P_2 \\ p_3(t) = \frac{P_1}{2} t^2 - P_2 t + P_3 \end{cases} \quad (3.30)$$

reveal that it can not be $p_3(t) = 0$ over a sub-arc of the solution. Therefore, the control is bang-bang

$$u^* = \begin{cases} -\dot{\beta}_{max} & , p_3 < 0 \\ \dot{\beta}_{max} & , p_3 > 0 \end{cases} \quad (3.31)$$

and, being $p_3(t)$ quadratic, it admits at most two switch times. In particular, as $y_3 = \beta$ is not constrained at $t = T$, the terminal condition $p_3(T) = 0$ holds, meaning that a maximum of two sub-arcs are admissible for $t < T$. Assuming that $u = \dot{\beta}_{max}$ in the first sub-arc and enforcing the continuity at the switch time, τ , the state equations can be integrated, leading to (Fig. 3.2b):

$$\beta = \begin{cases} \dot{\beta}_{max} t & , t < \tau \\ \dot{\beta}_{max} (2\tau - t) & , t > \tau \end{cases} \quad (3.32a)$$

$$\Phi = \begin{cases} \dot{\beta}_{max} \frac{c}{6} t^3 & , t < \tau \\ \dot{\beta}_{max} \frac{c}{6} [2\tau^3 - 6\tau^2 t + 6\tau t^2 - t^3] & , t > \tau \end{cases} \quad (3.32b)$$

$$\tau = \left(1 - \frac{\sqrt{2}}{2}\right) T \quad (3.32c)$$

$$T = \left(\frac{12}{2 - \sqrt{2}} \frac{\tilde{\Phi}}{c\dot{\beta}_{max}}\right)^{-\frac{1}{3}} \quad (3.32d)$$

In problem (3.29) no bounds on the maximum ailerons deflections have been imposed. If this was the case, the optimal control of Fig. 3.2b would result in additional sub-arcs corresponding to $\beta = \pm\beta_{max}$, which is the case of the numerical studies of Chap. 6. Similarly to what just shown, bounds could be imposed also on the ailerons acceleration, $\ddot{\beta}$, but this is avoided in the numerical studies. Instead, this is naturally introduced by the control parametrisation.

Problems (3.24) and (3.29) result in a bang-bang control as, in both cases, the Hamiltonian is linear in the control. This is avoided if their cost function is augmented with a quadratic penalty term depending on u . For example, problem (3.29) can be reformulated as

$$\begin{aligned} \min. \quad & I = \int_0^T (1 + \alpha u^2) dt \\ \text{w.r.t.} \quad & \mathbf{u}(t), \mathbf{y}(t) \\ \text{s.t.} \quad & \dot{\mathbf{y}} = \mathbf{f}(t, \mathbf{y}, u) \\ & \mathbf{y}(0) = 0 \\ & (y_1(T), y_2(T)) = (\tilde{\Phi}, 0) \end{aligned} \quad (3.33)$$

where, for simplicity, rate limits have been removed. The Hamiltonian becomes $\mathcal{H} = 1 + \alpha u^2 + p_1 y_2 + c p_2 y_3 + p_3 u$ and the *control* equation

$$2\alpha u + p_3 = 0 \Rightarrow u^* = -\frac{p_3}{2\alpha} \quad (3.34)$$

now allows to define the optimal control, u^* . The adjoint equations are as per eq. (3.30). Enforcing the terminal condition $p_3(T) = 0$, the system leads to

$$p_3(t) = (t - T) \left[\frac{P_1}{2}(t + T) - P_2 \right] \quad (3.35)$$

The solution has a single arc: integrating the state equations and enforcing initial and terminal conditions leads to:

$$\beta = \frac{20\tilde{\Phi}}{3c} \frac{t}{T^5} (6T^2 - 15Tt + 8t^2) \quad (3.36a)$$

$$\Phi = \frac{\tilde{\Phi}}{3} \frac{t^3}{T^5} (20T^2 - 25Tt + 8t^2) \quad (3.36b)$$

$$T = \left(1600\alpha \frac{\tilde{\Phi}^2}{c^2} \right)^{\frac{1}{6}} \quad (3.36c)$$

As shown in Fig. 3.2c, the ailerons deflection time history follows the same trend as those in Fig. 3.2a and 3.2b, but the control is now smooth.

Contrarily to the problems discussed so far, the numerical investigations of Chap. 6 only consider fixed time manoeuvres. This, in fact, allows to guarantee a constant control bandwidth at each iteration of the discrete optimisation problem (3.15) while also fixing the number of design variables (Sec. 3.3). The impact of this choice on the nature of the resulting optimal control can be analysed reformulating problem (3.24) as

$$\begin{aligned} \min. \quad & I = \int_0^T (y_1 - \tilde{\Phi})^2 dt \\ \text{w.r.t.} \quad & \mathbf{u}(t), \mathbf{y}(t) \\ \text{s.t.} \quad & \dot{\mathbf{y}} = \mathbf{f}(t, \mathbf{y}, u) \\ & |u| \leq \beta_{max} \\ & \mathbf{y}(0) = 0 \end{aligned} \quad (3.37)$$

where $u = \beta$, $\mathbf{y}^T = (\Phi, \dot{\Phi})$ and $\mathbf{f}^T = (y_2, cu)$. With respect to problem (3.24), rolling is now obtained through the minimisation of the quadratic error $(y_1 - \tilde{\Phi})^2$, rather than through the enforcement of terminal conditions. The Hamiltonian of this system, $\mathcal{H} = 2y_1 - 2y_1\tilde{\Phi} + \tilde{\Phi}^2 + p_1 y_2 + c p_2 u$, is also linear in the control, hence a bang-bang control arises when $p_2 \neq 0$. As opposed to problem (3.24), however, a singular arc is now

admitted when $p_2 = 0$: using the adjoint equations

$$\begin{cases} \dot{p}_1 = 2(\tilde{\Phi} - y_1) \\ \dot{p}_2 = -p_1 \end{cases} \quad (3.38)$$

this leads to the condition

$$y_1 = \tilde{\Phi} \quad (3.39)$$

The optimal control law for problem (3.37) is, therefore

$$u^* = \begin{cases} -\beta_{max} & , p_2 < 0 \\ 0 & , p_2 = 0 \\ \beta_{max} & , p_2 > 0 \end{cases} \quad (3.40)$$

which results in a bang-bang-singular sequence whenever time allowed for the manoeuvre, T , is large enough to achieve $\Phi = \tilde{\Phi}$.

Singular arcs can lead to numerical difficulties because the *control* equation is verified any control u . For example, the discrete optimisation problem (3.2) resulting from DT would not guaranteed to have a positive definite Hessian at the solution [87]. More generally, as optimisation algorithms typically rely on an approximation of the Hessian matrix (see Sec. 3.5 and B.2), singular arcs may result in slow convergence and/or an oscillatory behaviour of the control signal [88]. The singular arc in problem (3.37) can, however, be avoided by augmenting the cost function with a quadratic penalty term depending on the control input, as done in problem (3.33). This strategy has been, for instance, implemented in the numerical studies of Chap. 6 and allowed to avoid spurious oscillations of the control during the last phase of the manoeuvre.

3.5 The SLSQP algorithm

As discussed in Sec. 1.3, a quasi-Newton sequential quadratic programming algorithm, the SLSQP (Sequential Least Squares Quadratic Programming) is used in this work for solving the discrete optimisation problems (3.15) and (3.17). The algorithm has been developed by Kraft [111] for the TOMP (Trajectory Optimisation by Mathematical Programming) Fortran package [110], for which a Python interface is available through the SciPy package [148]. The SLSQP is based on a modified version of the Wilson, Han and Powell [151, 173, 174] SQP algorithm. The Hessian matrix of the Lagrangian associated to the optimisation problem is estimated through a BFGS update formula [138]. This approximation is built at each design point from the gradient of the cost and constraint functions, which are computed via FD. At each iteration, the quadratic sub-problem is, instead, solved using Lawson and Hanson's constrained least-squares method [110, 147, 175] — from which the SLSQP acronym originates.

In this section, the main features of this algorithm are discussed further. The aim is

to illustrate how this method suits the optimisation problems considered in this work and its limitations. These considerations may be especially relevant for future work aiming to apply this framework to larger-scale problems — refer, in this respect, to Sec. 3.5.3, where the algorithm efficiency is briefly discussed, and 7.3, where suggestions for future works are included. This section will start introducing general principle of constrained optimisation (Sec. 3.5.1) and will then move to discuss the Wilson-Han-Powell SQP strategy in Sec. 3.5.2. Further details on the method are included in App. A and B.

3.5.1 Optimality conditions

In this section, the optimal control and co-design problems (3.15) and (3.17) introduced in Sec. 3.1 are expressed in the form:

$$\begin{aligned}
 &\min. \quad I = I(\mathbf{x}) \\
 &\text{w.r.t.} \quad \mathbf{x} \\
 &\text{s.t.} \quad c_k(\mathbf{x}) = 0, \quad k \in \mathcal{E} \\
 &\quad \quad c_k(\mathbf{x}) \geq 0, \quad k \in \mathcal{I}
 \end{aligned} \tag{3.41}$$

where all the design variables are included in the vector \mathbf{x} , while equality ($k \in \mathcal{E}$) and inequality ($k \in \mathcal{I}$) constraints have been separated. In this work equality constraints only arise from initial/final conditions imposed on the actuation input (e.g. zero ailerons deflection and rate of changes are imposed at the beginning of the analysis), while inequality constraints result by evaluating the path constraints in (3.18) on a collocation grid.

The points \mathbf{x} satisfying the constraints of problem eq. (3.41) define the feasible set Ω . In an unconstrained problem, for a feasible point, \mathbf{x}^* , to be a minimum of I , the gradient of this function has to be null, $\nabla I(\mathbf{x}^*) = \mathbf{0}$, while its Hessian $\nabla^2 I(\mathbf{x}^*)$ positive semidefinite; the condition becomes sufficient if the latter is positive definite [138]. When constraints are included, optimal points must belong to the sub-space defined by the equality constraints, $\mathcal{C}_{\mathcal{E}}$. Furthermore, these may be located at the boundary of the feasible set, Ω , where the disequality constraints, $\mathcal{C}_{\mathcal{I}}$, have zero value. To identify these, the notion of active set

$$\mathcal{A}(\mathbf{x}) = \mathcal{E} \cup \{k \in \mathcal{I} \mid c_k = 0\} \tag{3.42}$$

is introduced. A necessary optimality condition is obtained referring to the Lagrangian

$$\mathcal{L}(\mathbf{x}, \boldsymbol{\lambda}) = I(\mathbf{x}) - \sum_{k \in \mathcal{E} \cup \mathcal{I}} \lambda_k c_k(\mathbf{x}) \tag{3.43}$$

where λ_k is the k -th component of the Lagrangian multipliers vector, $\boldsymbol{\lambda}$. The Karush-Kuhn-Tucker (KKT) relations [138, 176] provide a first-order necessary condition for the

optimality of the point \mathbf{x}^* :

$$\nabla_x \mathcal{L}(\mathbf{x}^*) = \nabla_x I(\mathbf{x}^*) - \sum_{k \in \mathcal{E} \cup \mathcal{I}} \lambda_k(\mathbf{x}^*) \nabla_x c_k(\mathbf{x}) = \mathbf{0} \quad (3.44a)$$

$$\mathbf{c}_{\mathcal{E}}(\mathbf{x}^*) = \mathbf{0} \quad (3.44b)$$

$$\mathbf{c}_{\mathcal{I}}(\mathbf{x}^*) \geq \mathbf{0} \quad (3.44c)$$

$$\boldsymbol{\lambda}(\mathbf{x}^*) \geq \mathbf{0} \quad (3.44d)$$

$$\lambda_k c_k(\mathbf{x}^*) = 0 \quad , \quad \text{for } k \in \mathcal{E} \cup \mathcal{I} \quad (3.44e)$$

Importantly, condition (3.44e) implies that $\lambda_k = 0$ for all the non-active constraints, $c_k(\mathbf{x}^*) > 0$. On the contrary, the magnitude of the Lagrangian multipliers associated to active constraints can be shown to be proportional to the sensitivity of the cost I to violations of the associated constraint. A proof of these relations, with also a geometrical insight, is provided by Nocedal and Wright [138]. Here it is worth remarking that an analogy exists between the KKT conditions (3.44) and Pontryagin's principle [90].

A second order optimality conditions is obtained by verifying that the Hessian of the Lagrangian with respect to the design variables, $\nabla_{xx}^2 \mathcal{L}(\mathbf{x}^*, \boldsymbol{\lambda}^*)$, is positive definite for all the feasible directions, \mathbf{w} , belonging to the the *critical* cone, $\mathcal{C}(\mathbf{x}^*, \boldsymbol{\lambda}^*)$,² i.e.:

$$\mathbf{w}^T \nabla_{xx}^2 \mathcal{L}(\mathbf{x}^*, \boldsymbol{\lambda}^*) \mathbf{w} > 0, \quad \forall \mathbf{w} \in \mathcal{C}(\mathbf{x}^*, \boldsymbol{\lambda}^*), \quad \mathbf{w} \neq \mathbf{0} \quad (3.45)$$

For further details the reader is remanded to any textbook on the topic [138, 176]. Instead, it is worth underlying here that gradient-based optimisation algorithm typically rely on approximations of the Hessian matrix, $\nabla_{xx}^2 \mathcal{L}$: therefore, the sufficient condition (3.45) is almost never checked [90] and numerical convergence tests, typically measuring the decrease of the the cost function, are employed instead [138].

3.5.2 Wilson-Han-Powell method

Sequential quadratic programming algorithms are a well established family of optimisation methods, especially suitable for the optimisation problems involving strongly non-linear constraints [137, 138]. At each iteration of the optimisation, the cost of problem (3.41) is approximated through a quadratic expansion and the solution of the resulting

²Feasible directions are such the that active constraints are not violated in a neighbourhood of \mathbf{x} and are identified upon linearisation of the problem constrains:

$$\mathcal{F}(\mathbf{x}) = \left\{ \mathbf{w} \mid \begin{array}{ll} \mathbf{w}^T \nabla c_k(\mathbf{x}) = 0, & \forall k \in \mathcal{E} \\ \mathbf{w}^T \nabla c_k(\mathbf{x}) \geq 0, & \forall k \in \mathcal{A}(\mathbf{x}) \cap \mathcal{I} \end{array} \right\}$$

For a set of points $(\mathbf{x}^*, \boldsymbol{\lambda}^*)$ satisfying the KKT conditions (3.44), the critical cone is the sub-set of \mathcal{F} including only directions perpendicular to the inequality active constraints:

$$\mathcal{C}(\mathbf{x}^*, \boldsymbol{\lambda}^*) = \left\{ \mathbf{w} \in \mathcal{F}(\mathbf{x}^*) \mid \mathbf{w}^T \nabla c_k(\mathbf{x}^*) = 0, \forall k \in \mathcal{A}(\mathbf{x}^*) \cap \mathcal{I} \text{ with } \lambda_k^* > 0 \right\}$$

quadratic programming (QP) sub-problem is used to determine the next design point. In this section the theoretical basis of the SQP formulation are established so as to introduce the Wilson-Han-Powell algorithm [139, 142, 143, 173], on which the SLSQP method is based [111]. Details on the Lawson and Hanson's constrained least-squares method [110, 147, 174, 175] used for the solution of each sub-problem, as well as a more detailed description on the Hessian approximation method and the step acceptance criterion used by the algorithm, are included for completeness in App. A and B, respectively.

Problem (3.41) defines a nonlinear optimisation problem in its most general form. The first order necessary optimality conditions in eq. (3.44), requires \mathbf{x} to verify

$$\mathbf{F} = \begin{Bmatrix} \nabla_x \mathcal{L}(\mathbf{x}) \\ \mathbf{c}_A(\mathbf{x}) \end{Bmatrix} = \begin{Bmatrix} \mathbf{g}(\mathbf{x}) - A^T(\mathbf{x})\boldsymbol{\lambda} \\ \mathbf{c}_A(\mathbf{x}) \end{Bmatrix} = \begin{Bmatrix} \mathbf{0} \\ \mathbf{0} \end{Bmatrix} \quad (3.46)$$

where $\mathbf{g}(\mathbf{x}) = \nabla_x I$ is the cost function gradient, $\mathbf{c}_A = \{c_k(\mathbf{x})\}$ for $k \in \mathcal{A}(\mathbf{x})$ is the active constraints column vector and the rows of the matrix A contain the gradient of the constraints with respect to the design variables, i.e. $A^T = \{\nabla_x c_k(\mathbf{x})\}$ for $k \in \mathcal{A}(\mathbf{x})$. The root of the nonlinear equation (3.46) can be found through the Newton-Raphson method. Being n an iteration counter, this leads to

$$\begin{pmatrix} H(\mathbf{x}_j) & -A^T(\mathbf{x}_n) \\ A(\mathbf{x}_n) & 0 \end{pmatrix} \begin{Bmatrix} \Delta \mathbf{x} \\ \Delta \boldsymbol{\lambda} \end{Bmatrix} = \begin{Bmatrix} A^T(\mathbf{x}_n)\boldsymbol{\lambda} - \mathbf{g}(\mathbf{x}_n) \\ -\mathbf{c}(\mathbf{x}_n) \end{Bmatrix} \quad (3.47)$$

where the Hessian matrix of the Lagrangian $H = \nabla_{xx}^2 \mathcal{L}(\mathbf{x}_n)$ has been introduced. If only equality constraints are present ($\mathcal{A} = \mathcal{E}$), eq. (3.47) can be solved recursively until the KKT necessary condition (3.46) is verified (Lagrange-Newton method, [146]).

More generally, replacing $\Delta \boldsymbol{\lambda} = \boldsymbol{\lambda}_{n+1} - \boldsymbol{\lambda}_n$ and solving for $\boldsymbol{\lambda}_{n+1}$ shows that eq. (3.46) is equivalent to the KKT condition of the following QP sub-problem [138]

$$\begin{aligned} \min. \quad & I(\mathbf{x}_n) + \mathbf{g}^T(\mathbf{x}_n)\Delta \mathbf{x} + \frac{1}{2}\Delta \mathbf{x}^T H(\mathbf{x}_n)\Delta \mathbf{x} \\ \text{w.r.t.} \quad & \Delta \mathbf{x} \\ \text{s.t.} \quad & \mathbf{c}_k(\mathbf{x}_n) + \nabla_x^T \mathbf{c}_k(\mathbf{x}) \Delta \mathbf{x} = 0, \quad k \in \mathcal{E} \\ & \mathbf{c}_k(\mathbf{x}_n) + \nabla_x^T \mathbf{c}_k(\mathbf{x}) \Delta \mathbf{x} \geq 0, \quad k \in \mathcal{I} \end{aligned} \quad (3.48)$$

in which the cost function is approximated around \mathbf{x}_n by a quadratic form and constraints are linearised. An important feature of this approach is that QP can always be solved, or shown to be infeasible, in a finite number of computations, typically through active-set strategies [138]. However, as the size of the problem increases, a large computational effort may be required to determine the active set at the solution point (App. A) due to the *combinatory* nature of this problem. The active-set strategy implemented in the SLSQP, in particular, is based on the least-squares method of Lawson and Henson [147], which performs well for small size problems. This is described in App. A.2 (algorithm 3). Importantly, the solution of the sub-problem (3.48) provides not only the search

direction, $\Delta \mathbf{x}$, but also an estimate of the active set at the following design point, $\mathcal{A}(\mathbf{x}_{n+1})$. Especially as \mathbf{x} approaches the optimum design point, this will generally provide a good initial guess for the solution of the next QP sub-problem, allowing to reduce the computational cost of identifying the active constraints [138].

The search direction $\Delta \mathbf{x}$ can be used to define the next design point explored by the optimiser, \mathbf{x}_{n+1} , around which a quadratic problem is defined; the process is repeated until convergence. This strategy is the foundation of the Wilson-Han-Powell method [173, 174], upon which the SLSQP algorithm is built, and is summarised in algorithm 1. Two important additions complete the scheme: a criterion for step acceptance and a method to approximate the Hessian of the Lagrangian.

While the step $\Delta \mathbf{x}$ solution of the local QP problem (3.48) is locally feasible, the constraints of problem (3.41) are nonlinear and will almost inevitably be violated at $\mathbf{x}_n + \Delta \mathbf{x}$. The step size requires, therefore, adjusting, so as to compromise a sufficient cost reduction with a reasonable violation of the constraints. This is achieved through an ℓ_1 merit function [111, 138], which is discussed in App. B.1. Finally, the evaluation of the Hessian term $H = \nabla_{xx}^2 \mathcal{L}$, which is required for building the KKT matrix of problem (3.48), needs to be addressed. For the numerical studies considered in this work, this operation is too costly to be performed numerically by FD, while an analytical expression would require a very involved derivation. Therefore, this term is approximated through the widely spread BFGS formula [138], which creates an approximation matrix that satisfies some of the properties of the exact Hessian matrix, namely the symmetry and the secant equation. Further details on this method are provided in App. B.2.

3.5.3 Algorithm efficiency

It is finally important to examine points of strength and weakness of the SLSQP algorithm (1). This discussion, in particular, complements the review in Sec. 1.1.5 with further technical details and linking to the implementation and numerical studies presented in this work. The aim is to underline how the algorithm compares to other optimisation methods and highlight whether, and possibly which, other strategies should be considered for larger scale aeroelastic optimisation problems.

The SLSQP is an active set SQP method, suitable when dealing with significant nonlinearities in the constraints and when the number of active constraints is comparable to the number of design variables — i.e. when the number of free variables is reduced [137, 138]. Especially when the active set does not change considerably from one iteration to another, this optimisation strategy can be very efficient, as a warm start-up is exploited (Sec. 3.5.2). This was typically the case of the studies considered in this work. A slow-down of the SLSQP algorithm was, however, observed in some of the numerical studies in which dynamics under resonance was controlled (Chap. 4 and 5). When high-frequency and large-amplitude oscillations arise in the control input, in fact, the active-set can change more frequently during the optimisation as the bound

constraints (3.6) are activated at different nodes of the collocation grid. However, the increase in computational cost was marginal, as this is dominated by the structural dynamics solution and the sensitivity analysis.

As introduced in Sec. 1.1.5, the SLSQP algorithm becomes less efficient when the dimensionality of the problem increases [43]. While a QR decomposition is exploited to speed up the solution of each QP sub-problem [147], in fact, Kraft's implementation does not exploits the sparsity of the Hessian matrix — neither for the BFGS update or the KKT system solution, eq. (3.44). Therefore, while the current implementation would still be adequate for higher fidelity aeroelastic analysis, it would not be suitable for very large optimisation problems even upon implementation of an adjoint based sensitivity analysis. A well established SQP based optimiser for very large problems is SNOPT [149], which approximates the Hessian of the Lagrangian with a limited memory quasi-Newton method. For the small/medium size problems as those considered in this work, instead, the effort required to solve the QP sub-problem is virtually null and the computational cost of the optimisation is driven by the number of aeroelastic analysis performed. In this respect, previous comparative studies showed that, especially under active constraints, the SLSQP algorithm may require less iterations to convergence then other SQP methods [43, 151] and it has, therefore, been preferred for the current implementation.

Algorithm 1 SLSQP (modified Wilson-Han-Powell SQP, [173, 174])

Requires:

definition of problem (3.41)
 starting point \mathbf{x}_0
 tolerance ϵ

Initialisation:

compute cost $\mathbf{x}_n = \mathbf{x}_0$
 compute cost $I(\mathbf{x}_0)$
 compute gradients $\mathbf{g}(\mathbf{x}_0)$ and $A(\mathbf{x}_0)$
 define $R_0 = I \approx \nabla_{xx}^{-1} \mathcal{L}(\mathbf{x}_0)$

while $|\Delta \mathbf{x}| > \epsilon$ **do**

Solve QP sub-problem:

call algorithm 3: output $\rightarrow \Delta \mathbf{x}$

\triangleright exploit $R \approx \nabla_{xx}^{-1} \mathcal{L}$

Line search:

$\alpha = 1$
while eq. (B.2) is not verified **do**
 $\mathbf{x}_{n+1} = \mathbf{x}_n + \alpha \Delta \mathbf{x}$
 evaluate $I(\mathbf{x}_{n+1})$, $\mathbf{c}_{\mathcal{E}}(\mathbf{x}_{n+1})$, $\mathbf{c}_{\mathcal{I}}(\mathbf{x}_{n+1})$
 evaluate ℓ_1 merit function, eq. (B.1)
 update α — Brent's method [177]

Update solution:

compute gradients $\mathbf{g}(\mathbf{x}_{n+1})$ and $A(\mathbf{x}_{n+1})$
 BFGS update, eq. (B.7): $R_n \rightarrow R_{n+1}$

return \mathbf{x}

Finally, and as already outlined in Sec. 1.1.5, for very large numbers of design variables and active constraints, interior points methods should also be considered [138, 150]. In these algorithms, all constraints are considered during the solution of each QP subproblem [141]. While this results in larger KKT system, eq. (3.47), its block structure is unchanged from one iteration to another. This is, therefore, exploited to reduce the computational cost of the QP solution.

Chapter 4

Optimal control of very flexible structures

In this chapter, optimal control is used to manipulate very flexible slender structures in vacuum. In the aeroelastic model illustrated in Chap. 2 nonlinearities are introduced through the geometrically-exact beam description of the aircraft primary components. Even in vacuum, therefore, their dynamics preserves a great part of the complexity associated to the control of very flexible aeroelastic systems, as large amplitude vibrations are possible. Controlling these is a necessary assessment of the optimal control approach described in Chap. 3, which will shed light on limitations and efficiency of this method when dealing with very flexible aerospace structures.

The remaining part of the chapter is structured as follows. At first, the GEBM implementation with constrained kinematics is verified (Sec. 4.1). Single-shooting is then applied to the control of a very flexible actuated pendulum. This study case was first proposed by Wang and Yu [171] and is described in Sec. 4.2. The pendulum is modelled as a very flexible beam and can undergo large rigid body rotations and geometrical deformations. Despite its simplicity, therefore, this system shares important features to very flexible wings, including inertial coupling between rigid and flexible body dynamics. As no external disturbances are accounted for, furthermore, the problem is fully deterministic and allows to easily assess the outcome of the control process. In Sec. 4.3 the parametrisations introduced in Sec. 3.3 are exercised for the optimal control of this system and results are compared against Wang and Yu [171]. The impact of actuation bandwidth and structural nonlinearities is further assessed in Sec. 4.4. Finally, a multi-resolution strategy is proposed for improving the convergence characteristics of the process (Sec. 4.5).

4.1 Structural model verification

The implementation of hinge kinematic constraints is initially tested for describing the motion of a rigid compound pendulum (i.e. having a distributed mass along its length) under large amplitude oscillations. As shown in Fig. 4.1, the hinge axis of rotation is parallel to the Y axis of the inertia frame, G , and the orientation of the pendulum is measured with respect to the vertical line through the angle Φ . The pendulum is modelled as a stiff beam of total mass $M = 1$ kg and length $b = 1$ m. Its cross-sectional properties are constant along its span and each section has a small rotatory inertia, $I_c = 10^{-4}$ kg m².

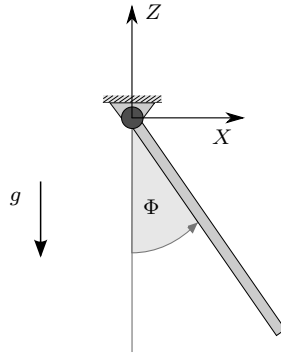


Figure 4.1: Geometry of rigid compound pendulum.

The rigid-body dynamic of this system is governed by

$$\ddot{\Phi} + \omega_0^2 \sin \Phi = 0 \quad , \quad \omega_0^2 = \frac{Mgb}{2I_Y} \quad (4.1)$$

where $g = 9.80 \text{ m s}^{-2}$ is the gravitational acceleration and the total inertia about the Y axis is:

$$I_Y = \int_0^b \left(\frac{M}{b} s^2 + I_c \right) ds = \frac{1}{3} Mb^2 + I_c b \quad (4.2)$$

At time zero, the pendulum has zero angular velocity ($\dot{\Phi} = 0$), hence the period of large amplitude oscillations, T , only depends on the initial angle, Φ_0 , between the pendulum and the vertical line (see Fig. 4.1). This can be expressed as

$$T = \frac{2\pi}{\omega_0} K \left(\sin \frac{\Phi_0}{2} \right) \quad (4.3)$$

where K is defined through the series [178]:

$$K(k) = \sum_{n=0}^{\infty} \frac{(2n)!}{(2^n n!)^2} k^{2n} \quad (4.4)$$

An analytical solution to eq. (4.1) is derived in Ref. [179]:

$$\Phi(t) = 2 \arcsin \left\{ \sin \frac{\Phi_0}{2} \operatorname{sn} \left[K \left(\sin^2 \frac{\Phi_0}{2} \right) - \omega_0 t, \sin^2 \frac{\Phi_0}{2} \right] \right\} \quad (4.5)$$

where $\operatorname{sn}(u, m)$ is the Jacobi elliptic function.

The case in which the pendulum has an initial angle with respect to the vertical line equal to $\Phi_0 = 90^\circ$ is studied. From eq. (4.3) the exact period of oscillations is $T = 1.936$ s. For the numerical solution, the structure is modelled with 8 quadratic beam elements of very large stiffness: note that, being elastic deflections negligible, only a few finite elements are sufficient for accurately modelling the gravitational load. Any source of friction is neglected but, despite the conservative nature of the system, an artificial viscosity $\nu = 10^{-4}$ has been required in order to damp out spurious high-frequencies and ensure, this way, the stability of the time-marching scheme (Sec. 2.1.7). A time-step of $10^{-3} T$ has been initially chosen. As shown in Fig. 4.2, the time histories of the X and Z components of the tip position are in excellent agreement with those derived through the analytical solution in eq. (4.1). The period of large amplitude oscillations is computed by averaging the lag between the stationary point of these time histories. The relative error with respect to the analytical solution is below the 0.05 %, hence within the accuracy of the measurement.

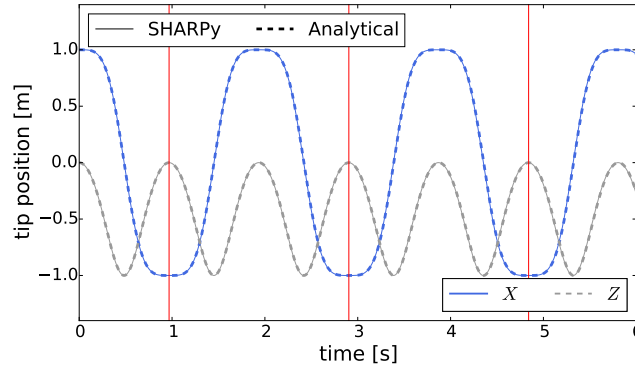


Figure 4.2: Time histories of the tip position of a free falling rigid pendulum in horizontal position at time $t = 0$ s.

In the numerical solution, the dynamics of the rigid pendulum is determined by the attitude of the local frame, A , which is described in terms of quaternions. This is obtained through the attitude propagation equation — eq. (2.10) — and depends on the angular velocity of the body frame, $\boldsymbol{\omega}$. To further assess the hinge kinematic constraints implementation, the same solution has been derived when modifying the initial attitude of the local frame A . This has been obtained by applying a pitch rotation Θ_0 about the X . As the hinge axis is unchanged in the inertial frame G , the dynamics of the pendulum is expected to be the same. However, the projection of the angular velocity

in the FoR A , ω_A , and the quaternions time histories, will vary as a consequence of the different orientation of the A frame.

This is reflected in Fig. 4.3, where the A frame attitude is shown for two different initial pitch angles, $\Theta_0 = 0$ deg (Fig. 4.3a) and $\Theta_0 = 45$ deg (Fig. 4.3b). In the latter case, in particular, pitch and yaw angles are not constant in time. Nonetheless, the accuracy of the solution is unchanged. In Fig. 4.4 the error of the numerical period of oscillations is shown against the time-step size — both are normalised with respect to the analytical period $T = 1.936$ s: as expected, curves related to different values of Θ_0 coincide. Note that the error decreases almost linearly with the time-step: while the Newmark- β integration scheme is superlinear (Sec. 2.1.7), the error here is dominated by the lower accuracy of the measurement of the oscillation period — averaging between a small amount of consecutive stationary points.

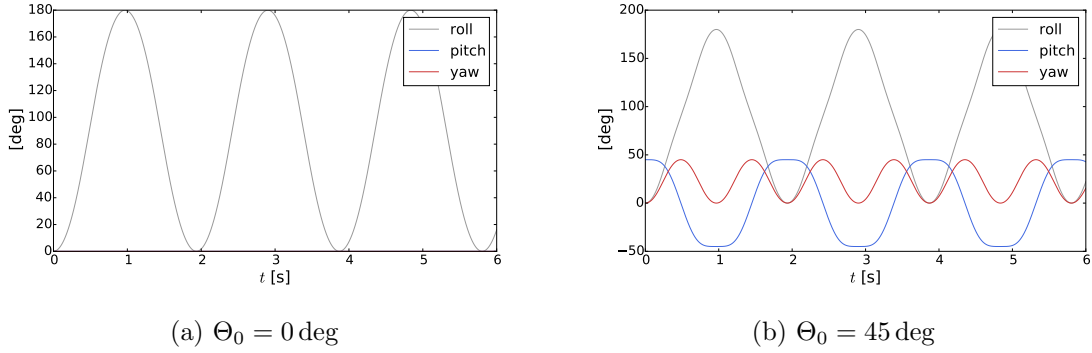


Figure 4.3: Time histories of the attitude of the local frame A , described in terms of pitch (Θ), roll (Φ) and yaw angles.

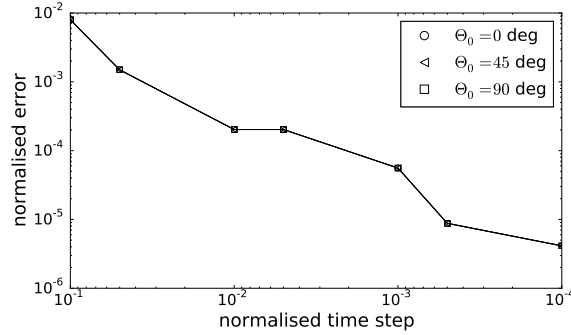


Figure 4.4: Error between the numerically predicted period of oscillation and the one provided by the analytical solution in eq. (4.3) for different time steps and initial pitch attitudes, Θ_0 , of the body frame A .

Finally, the hinge kinematic constraint are verified for a case in which flexibility effects are included. To this aim, the pendulum is assumed to have a bending stiffness $EI = 0.15 \text{ kg m}^2$. As in the previous cases, this is free falling from an horizontal position. The tip displacements compare have been compared against Wang and Yu [171], who also used a GEBM solver. As expected, the motion is planar and the agreement against

the reference is excellent.

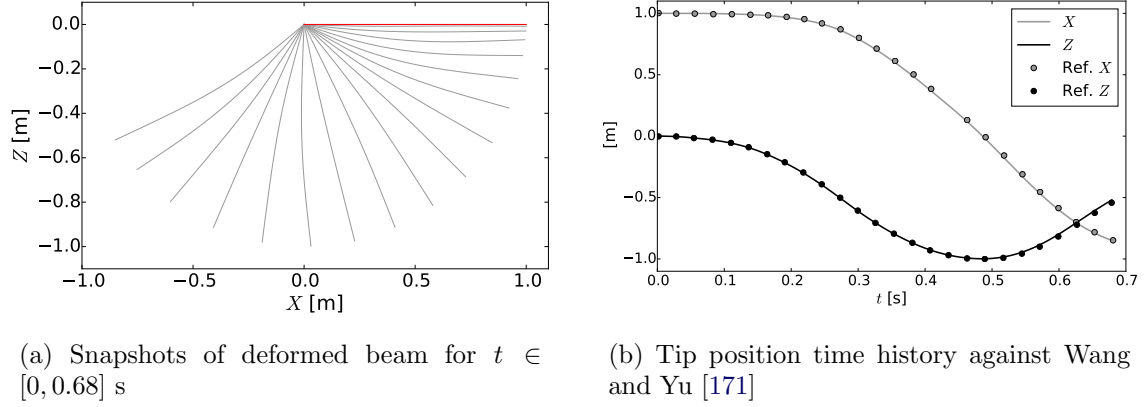


Figure 4.5: Free falling hinged flexible beam (the beam is horizontal at time $t = 0$ s).

4.2 Compound pendulum: problem description

The numerical studies in this chapter will refer to the flexible pendulum configuration proposed by Wang and Yu [171], which is sketched in Fig. 4.6. This is modelled as a hinged elastic beam and lies initially in a stable equilibrium position along the vertical direction (Z axis), gravity effects being accounted for. In order to control the system, an actuating torque, $M_Y(t)$, chosen to be zero at the initial and final time of the simulation, is applied at its root (Fig. 4.6), causing the pendulum to oscillate about the hinge point. The torque time history $M_Y(t)$, in particular, is optimised such as to maximise the leftward X velocity of the pendulum tip, v_X , measured in the global FoR at time $T = 2$ s. The problem is fully deterministic and any sources of friction or damping are not considered.

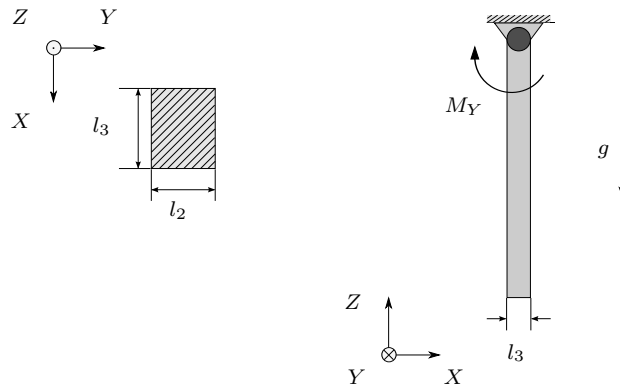


Figure 4.6: Flexible pendulum geometry

To account for the cost of actuation, Wang and Yu [171] augmented the cost function with the quadratic force regulator term

$$P[M_Y] = \frac{1}{2} \int_0^T \left[\pi_1 M_Y^2 + \pi_2 \left(\frac{dM_Y}{dt} \right)^2 \right] dt \quad (4.6)$$

which depends on both the magnitude and the rate of change of the actuation. The optimal control problem can thus be written, in its continuous form, as:

$$\begin{aligned} \min. \quad & I = \kappa_1 v_X(T) + \kappa_2 P \\ \text{w.r.t.} \quad & M_Y(t) \\ \text{s.t.} \quad & M_Y(0) = M_Y(T) = 0 \\ & -M_{max}(t) < M_Y(t) < M_{max}(t) \\ & -\Phi_{max} \leq \Phi(t) \leq \Phi_{max} \end{aligned} \quad (4.7)$$

where I is the augmented cost function and the constants κ_i and π_i are scaling parameters to ensure that all the terms in the cost function and the force regulator equations have same units and comparable magnitude; note, in particular, that κ_1 is required to have negative value. In the following, we will refer to problem (4.7) as the *augmented* problem. In the numerical implementation, M_Y is discretised by mean of DS (eq. 3.19) and B-spline (eq. 3.21, 3.22) basis functions; the optimisation is thus performed with respect to the coefficients of the parametrisation, x_c . Finally, Φ is the angle between the pendulum and the vertical direction as defined in Fig. 4.5: by setting $\Phi_{max} < 180$ deg this path constraint ensures that the control will not spin the pendulum but only exploit its oscillatory motion.

The augmented problem (4.7) defines a trade-off between performance (v_X term) and cost of actuation (P term). While this approach is in line with many practical control strategies (e.g. LQR feedback controllers), it introduces a trade-off between actuation effort and performance which can affect the convexity of the design space and lead to path dependent solutions in the optimisation process. Therefore, the optimal control problem has also been formulated in a constrained version:

$$\begin{aligned} \min. \quad & v_X(T) \\ \text{w.r.t.} \quad & M_Y(t) \\ \text{s.t.} \quad & P \leq P_{max} \\ & M_Y(0) = M_Y(T) = 0 \\ & -M_{max}(t) < M_Y(t) < M_{max}(t) \\ & -\Phi_{max} \leq \Phi(t) \leq \Phi_{max} \end{aligned} \quad (4.8)$$

The integral term P acts as a measure for the energy that the actuation can transfer into the dynamical system. Constraining this quantity allows, therefore, to bound the level of kinematic displacements displayed by the structure and, consequently, the

amount of nonlinear effects experienced of the system. As it will be shown in Sec. 4.4, this has a significant impact on the design space smoothness.

4.3 Optimal actuation of a compound pendulum

The optimal control problem for the flexible pendulum (Fig. 4.6) is initially solved using the augmented formulation defined in problem (4.7) and results are compared to those obtained by Wang and Yu [171]. The pendulum is modelled as a beam of constant rectangular cross-section with area $A = 10^{-2} \text{ m}^2$ and negligible rotational inertia; an isotropic material of Young's modulus $E = 1.2 \text{ Pa}$ and density $\rho = 100 \text{ kg m}^{-3}$ was used to reproduce the inertia and stiffness properties in Ref. [171]. The actuation was bounded not to exceed absolute value of $M_{max} = 3.5 \text{ N m}$, while cost and penalty term parameters appearing in problem (4.7) were set as per Ref. [171] to be

$$\begin{aligned}\kappa_1 &= -1 \text{ s m}^{-1} \quad , \quad \kappa_2 = 1 \\ \pi_1 &= 1 \text{ N}^{-2} \text{ m}^{-2} \text{ s}^{-1} \quad , \quad \pi_2 = 10^{-2} \text{ N}^{-2} \text{ m}^{-2} \text{ s}\end{aligned}$$

The gradient is computed numerically by forward FD with respect to the coefficients of the parametrisation modelling the input torque M_Y . As FD are subjected to both truncation and cancellation errors [170], an assessment of the optimal step-size to be use during the sensitivity analysis is included in App. C.

Since rigid body rotations and deformations are all planar, the only relevant elastic quantity is the bending stiffness in the plane of motion. Two beams, one being 10 times stiffer than the other, are obtained varying the sides of the cross-section l_2 and l_3 while keeping the sectional area. They are referred to as *stiff* and *flexible* pendulum in Tab. 4.1.

Case	l_2 [m]	l_3 [m]	EI [Nm ²]	f_r [Hz]	f_b [Hz]
<i>stiff</i> pendulum	0.1000	0.1000	10.0	0.50	7.76
<i>flexible</i> pendulum	0.3162	0.0316	1.0	0.50	2.45

Table 4.1: Pendula structural properties for the optimal control problem.

The characteristic frequencies in Tab. 4.1 have been computed around the underformed pendulum configuration. As the structure becomes more flexible, the natural frequency related to the first bending mode f_b drops and the coupling between flexible and rigid body dynamics increases. It is worth underlining that the natural frequencies in Tab. 4.1 are computed for small amplitude perturbations, hence assuming a linear vibrational dynamics: these figures, therefore, only provide an estimation of where the resonance points are located in the nonlinear structure.

For both cases proposed in Tab. 4.1 the optimal control problem is solved with B-spline and DSS parametrisations of different basis sizes, based on the maximum frequency, f_{max} , captured by the control. However, fixed a certain value of f_{max} , the size of DSS and B-spline basis are comparable (Sec. 3.3). In particular, for each parametrisation the basis size was chosen such as to exclude ($f_{max} < f_b$, low bandwidth control) and include ($f_{max} > f_b$, high bandwidth control) the flexible mode natural frequency of vibration. It should be finally noted that the range of frequencies of interest falls within the domain of simple optical recognition methods [180], making this set-up suitable for experimental verification.

4.3.1 *Stiff* pendulum

The *stiff* pendulum will be subject to the control actions in Tab. 4.2. In the table, N_c and f_{max} refer to the basis size of each parametrisation and the related maximum frequency of actuation. Optimal control results are presented in terms of cost (I), penalty factor (P) and final pendulum tip velocity, $v_X(T)$. N_I is the number of iterations required to complete the optimisations.

Parametrisation	N_c	f_{max} [Hz]	N_I	$v_X(T)$ [ms^{-1}]	P	I
spline	11	2	20	6.08	2.73	-3.35
DS	8	2	14	6.08	2.73	-3.35
spline	43	10	33	12.35	6.18	-6.17
DS	40	10	44	10.57	4.77	-5.80

Table 4.2: Optimal control results of the *stiff* pendulum using different parametrisations.

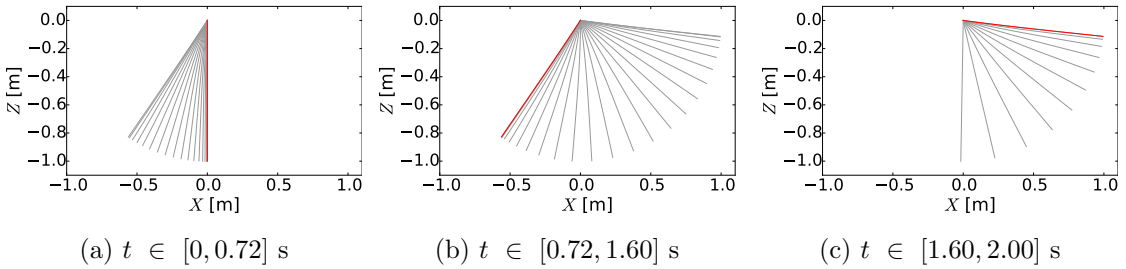


Figure 4.7: Snapshots (25 frames per second) of the *stiff* pendulum response for the optimal actuation with a control maximum frequency $f_{max} = 2$ Hz using a DSS parametrisation. (Initial shape in red)

When using $f_{max} = 2$ Hz, the optimal actuation does not excite the first bending mode of the pendulum, which, therefore, mostly swings rigidly. This can be observed in Fig. 4.7, where the snapshots of the actuated pendulum position, driven by the DSS modelled optimal torque, show no relevant elastic deformation. Comparing optimal actuation and tip displacements time histories against Ref. [171] demonstrates that both the spline and DSS parametrisation can capture well the rigid-body motion frequency

(Fig. 4.8), thus returning very similar performances (Tab. 4.2). As physically expected, the control moment, M_Y , excites the rigid-body motion only and uses the gravity potential energy to increase the final tip velocity, $v_X(T)$, while limiting the overall actuation cost, P .

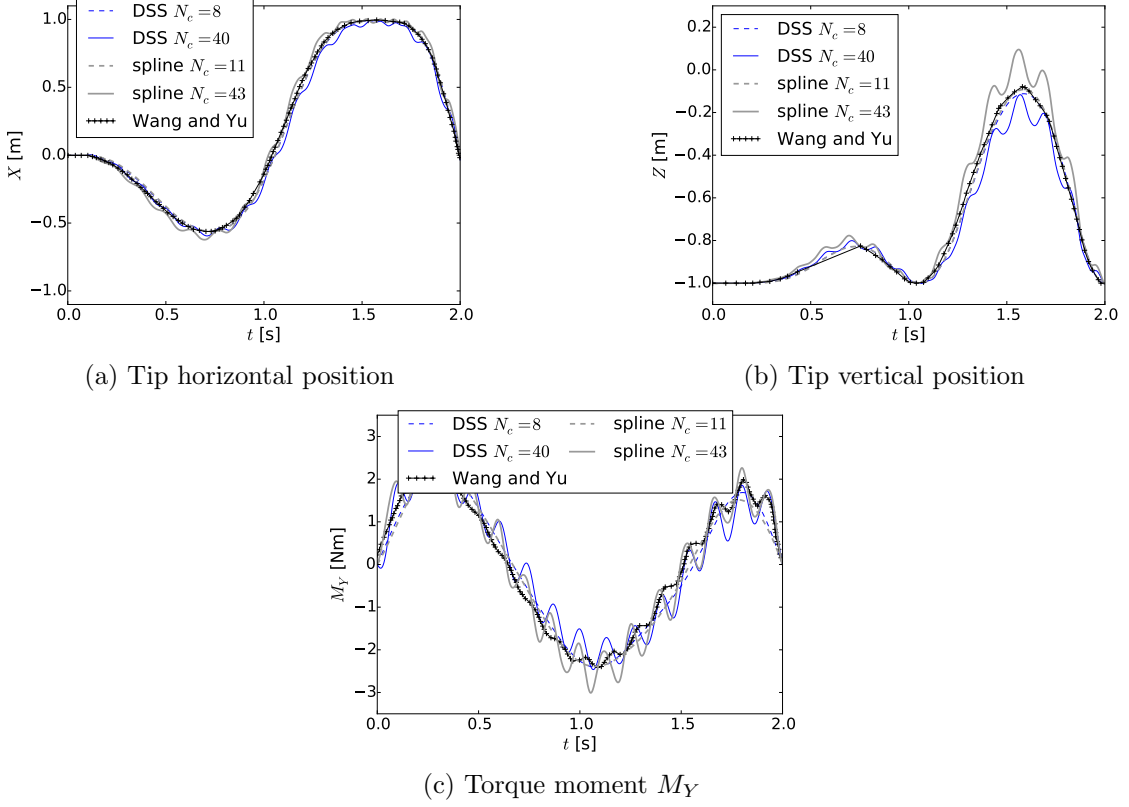


Figure 4.8: Time histories under optimal control of the *stiff* pendulum using different parametrisations of the torque signal.

Setting $f_{max} > f_b$ leads to a large increase of the final tip velocity, $v_X(T)$, as the first bending mode is excited. The active system is now capable of storing elastic energy, which is converted into kinetic energy as $t \rightarrow T$, providing a further contribution to v_X and enhancing the overall system performance. With both splines and DSS, the high frequency component is larger than in the solution obtained by Wang and Yu [171]. It has to be noticed, however, that results in Ref. [171] are obtained from optimisations that are stopped after only 10 iterations and a beam model that includes structural damping. This likely explains the small differences between both sets of results.

While the optimal actuation always shows to correctly exploit the system physics, the 10 Hz bandwidth solutions obtained with the two parametrisations point towards two different minima, corresponding to two different levels of control actuation, P . To verify the existence of local minima, the control design space has been sampled for a case in which the pendulum is actuated by a control parametrised with only two sine waves. To model a low bandwidth actuation, these were chosen to have frequencies

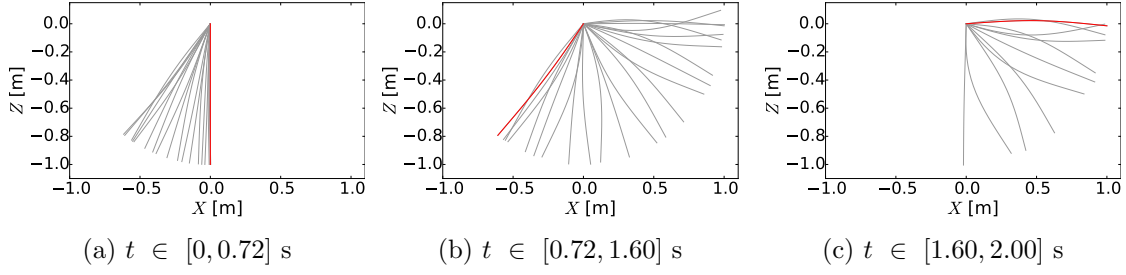


Figure 4.9: Snapshots (25 fps) of the *stiff* pendulum response for the optimal actuation obtained using a B-spline parametrisation with $N_c = 43$ control points ($f_{max} = 10$ Hz). Initial shape in red.

0.5 Hz and 0.75 Hz, with amplitudes $x_{0.5}$ and $x_{0.75}$ respectively. These are associated to a left/right and left/right/left rigid-body modes and, as physically expected, had been observed to have a large contribution in both the 2 Hz and 10 Hz DSS parametrised optimal actuations.

The contour lines of the cost I , obtained when varying the amplitude of the two sine waves, are showed in Fig. 4.10a, together with the isolines of the force regulator term, P (thick curves). The design space is smooth with a minimum at $(x_{0.5}, x_{0.75}) = (0.88, 1.83)$ Nm. Despite the reduced size of the parametrisation, cost and penalty at the minimum ($I = -2.94$ and $P = 2.46$) compare well with those obtained using a low bandwidth actuation ($f_{max} = 2$ Hz in Tab. 4.2).

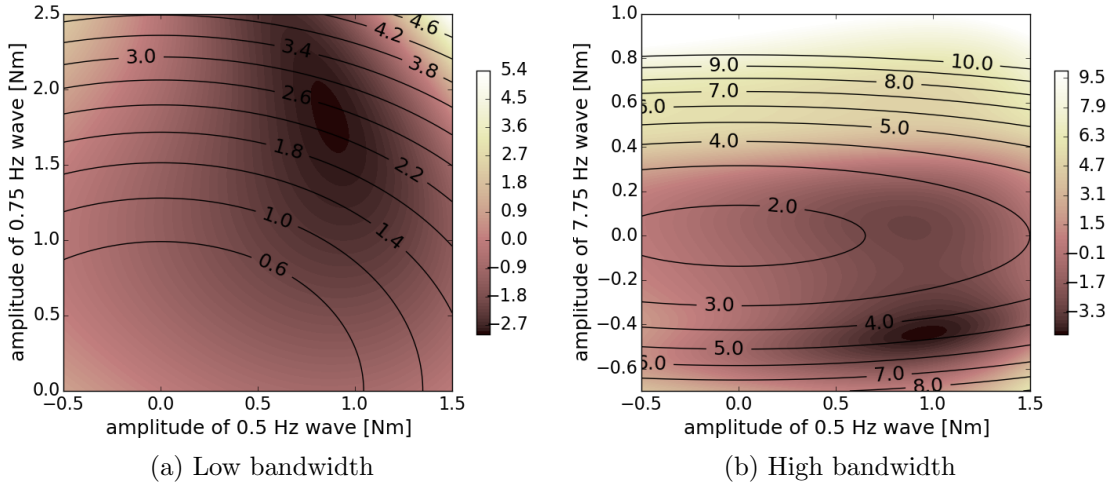


Figure 4.10: Cost function, I , associated to a *rigid* pendulum when varying the amplitude of the sine waves parametrising the actuating torque, M_Y .

To model a high bandwidth control, the amplitude $x_{0.75}$ of the 0.75 Hz sine wave was fixed to be 1.7 Nm and a high frequency sine wave (7.75 Hz, near the first natural frequency) of amplitude $x_{7.75}$ was added to the parametrisation. As before, both coefficients of the parametrisation were varied so as to reconstruct the cost function I over the control design space (Fig. 4.10b). While a minimum — corresponding to a

predominantly low-frequency actuation that only exploits the rigid-body dynamics — is still observed for $x_{7.75} \approx 0$, a new minimum, corresponding to a peak of structural resonance, appears. A further investigation on how both minima change with the amplitude and frequency of the excitation is included in Sec. 5.2.

Sampling the cost function I has therefore shown that when the control can exploit resonances, multiple minima can populate the design space. The reason why the high bandwidth actuations provided by splines and DSS lead to distinct point of minimum can then be linked to how different sets of basis functions reconstruct the actuation. While a control signal parametrised with a low number of spline basis can not be built for direct comparison with Fig. 4.10b, it is clear that as the mapping between parametrisation coefficients x_c and final cost I changes, so does the location of the minima.

4.3.2 *Flexible* pendulum

The study of the low-bandwidth actuated *stiff* pendulum has shown that, when the actuation can only excite the rigid-body mode of vibration, the design space is smooth and the actuations provided by splines and DSS parametrisations are in good agreement. As the pendulum flexibility is increased, however, the distance between rigid and flexible body characteristic frequencies, f_r and f_b , is drastically reduced (Tab. 4.1) and it becomes harder to excite one of the modes without exciting the other.

The implications of an increasing rigid-flexible body dynamics coupling are highlighted by the results obtaining using DSS and spline basis to parametrise two low-bandwidth actuations ($f_{max} < f_b$) having $f_{max} = 1.25$ Hz and a $f_{max} = 1.5$ Hz. The optimal torque time histories (Fig. 4.12a) and the associated cost, I , and penalty factor, P , compare well across parametrisations only when $f_{max} = 1.25$ Hz (Tab. 4.3). However, as clearly shown by the snapshots in Fig. 4.11, the DSS modelled actuation with $f_{max} = 1.5$ Hz can already excite the pendulum bending mode, allowing to reach a cost 22% lower than when using a splines parametrisation. This is verified in Fig. 4.12b, where the DS decompositions of the spline optimal actuations, which have been computed through eq. (3.20), are shown. While for the $f_{max} = 1.25$ Hz cases these can only excite the rigid-body dynamics, raising f_{max} allows the control to mildly excite the pendulum bending mode. The different resolution between the parametrisation becomes, at this point, critical: the DSS basis can express a strong frequency content around $f_{max} = 1.5$ Hz, whereas this can not be achieved using splines. The more aggressive control obtained using DSS (note that the force regulator term P almost doubles with respect to the corresponding spline case) is, therefore, justified by the different resolution.

As seen in Fig. 4.13, when using a higher bandwidth control ($f_{max} > f_b$), both discretisations capture well the very flexible beam dynamics. However, and as already discussed for the *rigid* pendulum in Sec. 4.3.1, the dynamics under resonance increases the path dependency of the results. This can be seen in Fig. 4.12c and 4.12d: while the final cost, I , compares well across parametrisations, the splines obtained solution

Parametrisation	N_c	f_{max} [Hz]	N_I	$v_X(T)$ [ms ⁻¹]	P	I
spline	8	1.25	29	4.63	1.59	-3.04
DS	5	1.25	16	4.48	1.59	-2.89
spline	9	1.5	22	5.40	2.19	-3.21
DS	6	1.5	40	8.42	4.50	-3.92
spline	19	4	57	15.92	5.73	-10.19
DS	16	4	53	13.11	3.48	-9.63

Table 4.3: Optimal control results of the *flexible* pendulum using different parametrisations.

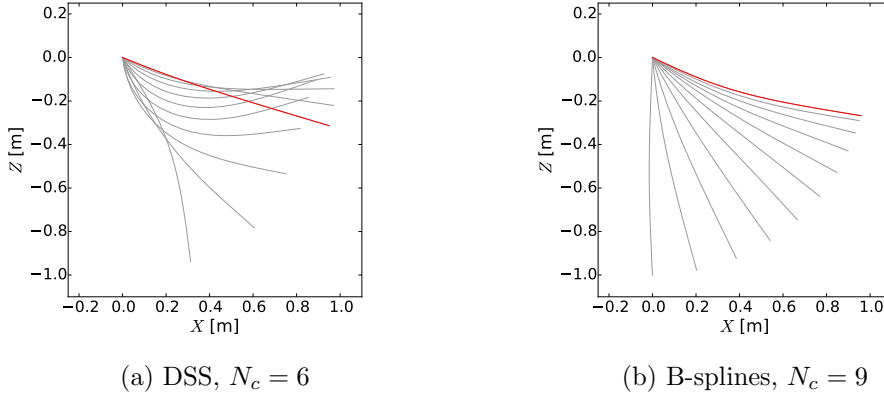


Figure 4.11: Snapshots (25 fps) of the *flexible* pendulum response for $t \in [1.60, 2.00]$ s with optimal control parametrisation having a maximum frequency $f_{max} = 1.5$ Hz. (Initial shape in red)

has now a considerably more aggressive actuation (Tab. 4.3). Results also include those from Wang and Yu [171], which account for damping in the model and, as before, show a smoother behaviour.

4.3.3 Path dependency vs. problem formulation

When dealing with resonance conditions the optimal actuation torque, M_Y , obtained from the augmented problem (4.7), was found to be parametrisation dependent. The control of the *flexible* pendulum has also underlined that the parametrisation resolution can also have an effect, especially when dealing with an increasing coupling between flexible and rigid body dynamics. To isolate the impact of the problem formulation from that of the parametrisation (which will be the focus of Sec. 4.4), the optimal control of the *stiff* and *flexible* pendulum is obtained now using the constrained formulation (4.8). Large deformations are still allowed due to a large maximum actuation ($P_{max} = 6$) and a high bandwidth ($f_{max} > f_b$). The results are shown in Tab. 4.4 and present a much higher consistency in the optimal control across both discretisations. Having removed the penalty term from the cost function definition, the optimal actuation always reaches, as expected, the limit $P_{max} = 6$. For the *stiff* pendulum case, the two parametrisations

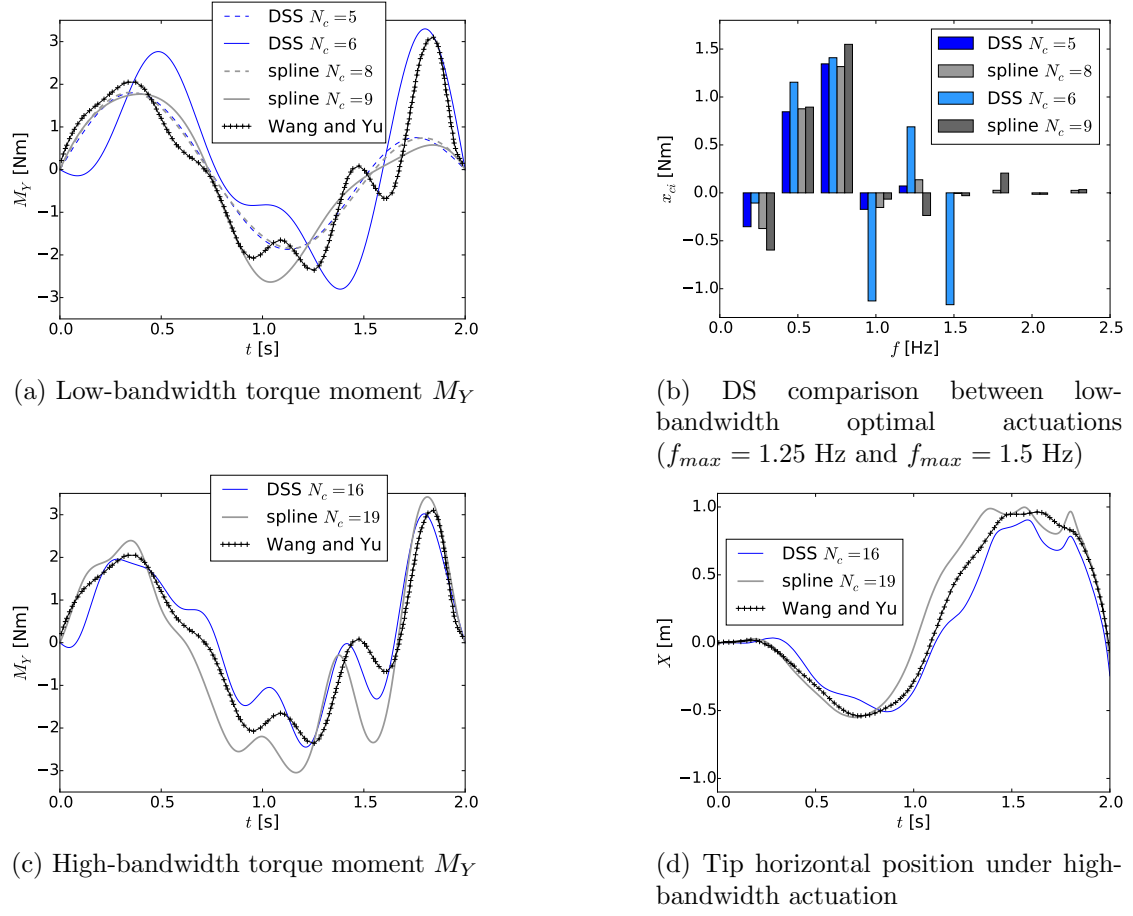


Figure 4.12: Time histories under optimal control of the *flexible* pendulum using different parametrisations of the torque signal.

are in extremely good agreement. As the system becomes more nonlinear (*flexible* pendulum), however, spline basis seem to be able to better capture the system resonance, leading to a 1.9% higher tip velocity $v_X(T)$.

Pendulum	Basis	f_{max} [Hz]	N_I	$v_X(T)$ [ms^{-1}]	P
<i>stiff</i>	spline	10	40	12.30	6.00
<i>stiff</i>	DS	10	170	12.27	6.06
<i>flexible</i>	spline	4	54	15.73	6.00
<i>flexible</i>	DS	4	158	15.43	5.96

Table 4.4: Optimal control results for the *stiff* and *flexible* pendulum using the constrained formulation (4.8) and setting $P_{max} = 6$.

Fig. 4.14 shows however that better performance of the spline is not linked to better reconstruction properties. Converting the spline parametrised optimal actuation in a DSS shows, in fact, that this has no relevant frequency content over $f_{max} = 4$ Hz (Fig. 4.14a). In fact, the spline optimal actuation is reconstructed using a DSS series

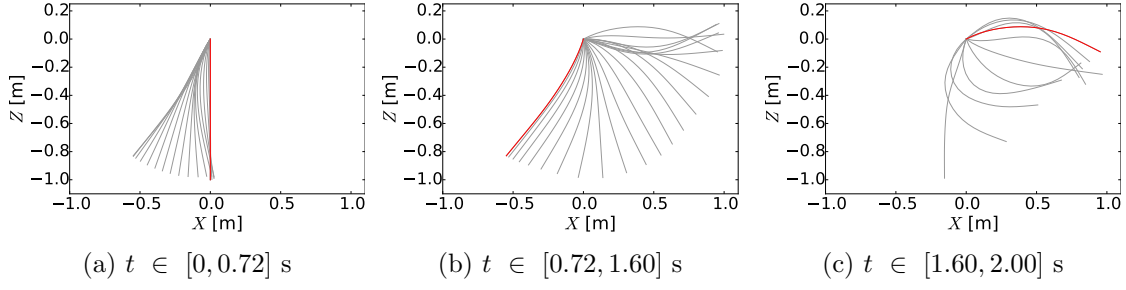


Figure 4.13: Snapshots (25 fps) of the *flexible* pendulum response for the optimal actuation obtained using a B-spline parametrisation with $N_c = 19$ control points ($f_{max} = 4$ Hz). Initial shape in red.

in Fig. 4.14b. Applying the reconstructed torque to the pendulum, a final tip velocity $v_X(T) = 15.62 \text{ ms}^{-1}$, which is in line with the performance provided by the spline optimal actuation, is achieved.

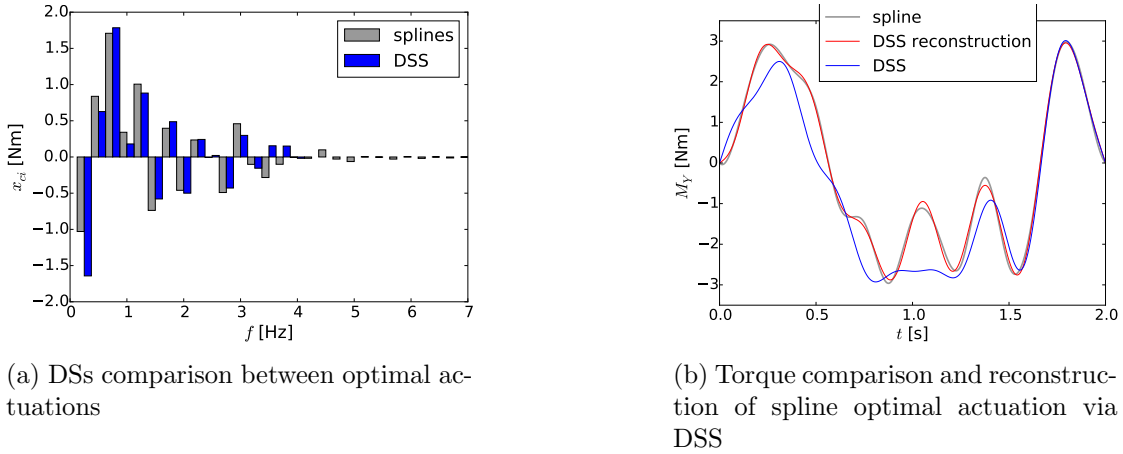


Figure 4.14: Comparison between spline and DSS optimal actuation for *flexible* pendulum case and no penalty factor.

It can thus be concluded that, despite the use of a *constrained* problem formulation, the two parametrisations can still converge to different minima as the nonlinearity of the system increases. While results are in very good agreement for the *stiff* pendulum, the DSS actuation leads to a control with a higher low frequencies for the *flexible* pendulum case (Fig. 4.14a). The use of a *constrained* problem formulation, however, reduces the gap between the two solutions, as the level of actuation, P_{max} — and consequently the final tip velocity, $v_X(T)$ — are now comparable. This formulation, which diverges from that of Wang and Yu [171], has been therefore chosen to further investigate the impact of both frequency resolution and level of actuation in the next section.

4.4 Parametrisation vs. system nonlinearity

In order to investigate further the duality between local and global parametrisations, the optimal control problem of the pendulum is solved using both B-splines and DSS for a range of beams of different stiffness. In both cases the number of basis functions is chosen such as to achieve a maximum frequency $f_{max} = 6$ Hz. The pendulum bending stiffness is varied by changing the dimension of the beam cross-section l_2 and l_3 (Fig. 4.6). With the aim of not altering the rigid-body mode natural frequency, f_r , the beam cross-sectional area is maintained constant ($A = 10^{-2}$ m), meaning that only one of the two structural parameters is actually independent.

Varying l_3 between $[0.05, 0.10]$ m resulted in a design space including situations for which the control maximum frequency, f_{max} , is either greater or smaller than the pendulum first bending natural frequency, f_b . More specifically, f_b varies linearly with l_3 , ranging between 3.88 Hz and 7.76 Hz and entering in the actuation range ($f_b = f_{max}$) when $EI = 5.98$ Nm² and $l_3 = 0.0773$ m. The lower bound for the beam stiffness is, furthermore, such that the resonance of the second bending mode of the beam is avoided. While this could also be exploited, it was not included in this exploratory study to simplify the analysis of the results.

So as to limit the impact of the problem definition, the constrained formulation (4.8) has been used (Sec. 4.3.3). In particular, the optimal control was solved for three levels of admissible actuation ($P_{max} = 2, 4, 6$) to assess the impact of increasing nonlinear effects on the solution; results are shown in Fig. 4.15. The design space can be divided into three regions according to whether the control can or can not excite the pendulum bending mode. When the bending natural frequency, f_b , is well below the maximum frequency of actuation f_{max} ($l_3 \lesssim 0.070$ m), the control signal can excite the rigid-flexible body dynamics, providing high performance. In this situation, in fact, the actuation has a high bandwidth in relation to the physical properties of the system ($f_{max} \gg f_b$). When $l_3 \gtrsim 0.085$ m, on the other hand, the same control with $f_{max} = 6$ Hz has now a low bandwidth. As a result, only the rigid body dynamics is exploited and performance decreases. At last, a transition region ($0.070 \text{ m} \lesssim l_3 \lesssim 0.085 \text{ m}$), in which resonance outsets, can be identified.

The classification introduced can be more clearly understood by looking at Fig. 4.16, where the magnitude $|x_{cm}|$, eq. (3.14), of the basis functions of the DSS parametrised optimal control is shown for a range of different pendula stiffness and actuation cost, P_{max} . As it can be seen, the control effort is concentrated in two regions, the first one located in the low frequency range so as to excite the rigid body dynamics. The second one is observed when f_b is in the control range: a peak around this frequency appears and, as the beam stiffness varies, this moves to follow the bending mode natural frequency. Increasing the level of actuation, P_{max} , larger geometrical deformations appear and resonance intensifies. The consequently higher level on nonlinearities in the problem is

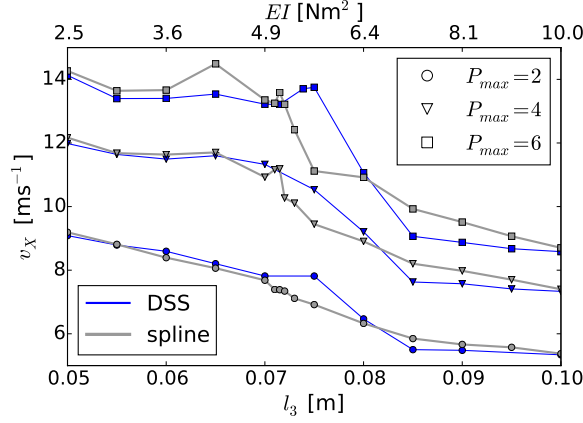


Figure 4.15: Design of experiment for different parametrisations and level of actuation P_{max} .

clearly reflected in the design space smoothness, which is visibly reduced when passing from $P_{max} = 2$ (Fig. 4.16a) to $P_{max} = 6$ (Fig. 4.16c).

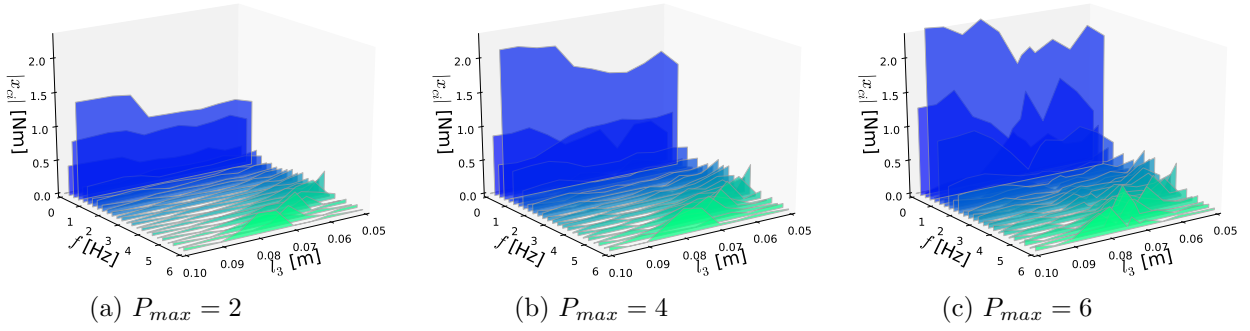
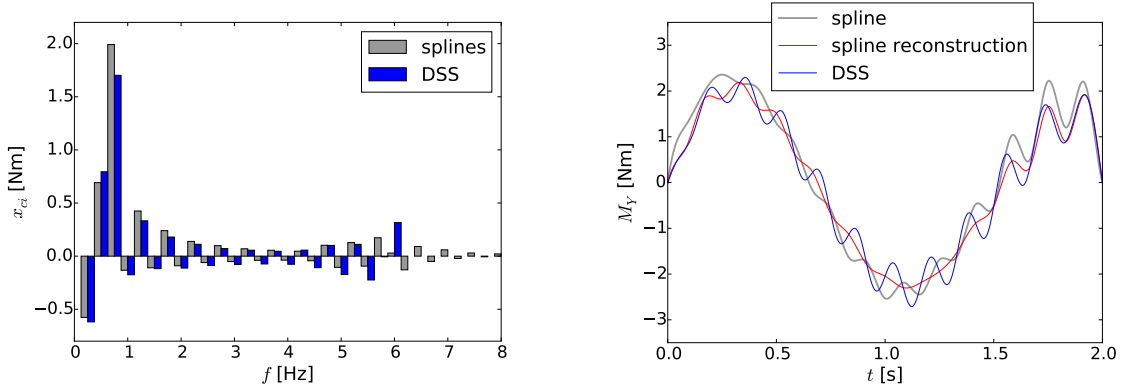


Figure 4.16: Optimal actuation frequency content ($|x_{ci}|$) using a DSS parametrisation ($f_{max} = 6$ Hz) and a constrained problem formulation (4.8). Different levels of actuation, P_{max} , are allowed.

Under low frequency actuation ($f_{max} \ll f_b$), spline basis can achieve slightly better performance because their spectrum extends above $f_{max} = 6$ Hz, allowing the torque to mildly excite the pendulum bending mode. The phenomenon is consistently stronger for larger values of actuations.

As expected, the transition region ($0.070 \text{ m} \lesssim l_3 \lesssim 0.085 \text{ m}$) sees a change in performance due to the switch from rigid-flexible to rigid body only dynamics. The difference increases with P_{max} , as stronger actuations induce a more intense level of resonance. The change in maximum tip velocity, v_X , is sharper when using a DSS, whose related optimal control generally provide higher performance than the spline one. Contrarily to what it was seen in Sec. 4.3.3, however, this is not linked to the DSS providing better convergence properties but to the fact that in the transition region the solution quality is dictated by the parametrisation frequency content.

This is demonstrated in Fig. 4.17, where the optimal actuations provided by the two parametrisations for the case $l_3 = 0.0750$ m and $P_{max} = 4$ are compared. The DSS representations of the two signals (Fig. 4.17a) shows that the DSS parametrised control has a higher frequency content around the bending natural frequency, $f_b = 5.63$ Hz: this allows to better excite the mode and achieve a larger final tip velocity, v_X . As observed in Fig. 4.17b, however, the optimal actuation obtained using a DSS cannot be reproduced using B-splines. In the specific case, therefore, DS generally outperform B-splines as they can better excite the high frequencies.



(a) DSS optimal coefficient against DS representation of spline solution

(b) Time histories and spline reconstruction of DSS optimal actuation

Figure 4.17: Optimal actuation in the transition region ($l_3 = 0.0750$ m and $P_{max} = 4$) using different parametrisations.

4.5 A multi-resolution strategy

In this section, a multi-resolution approach is proposed to improve the convergence properties of the optimal control process when strong nonlinearities appear in the structural solution. Fig. 4.15 shows that for high frequency actuations and mild level of nonlinearity ($P_{max} = 2, 4$), results compare well across different parametrisations. Both DS and B-splines can, in fact, reconstruct accurately not only the low frequencies but also the relevant high frequencies, necessary to induce the system resonance. When the level of actuation is increased ($P_{max} = 6$), peaks of resonance become more evident as a consequence of larger displacements and, in particular, a more violent resonance. As shown in Fig. 4.15, these tend to arise whenever the bending oscillation period is a divisor of the total simulation time T . While the location of the peaks is well captured by both basis, their amplitude becomes parametrisation dependent; this is clearly visible for the optimal control at $l_3 \approx 0.0650$ m. As it was already seen in Sec. 4.3.3, even in this case the mismatch is caused by a convergence slow down of the DSS parametrised control: the optimal spline actuation can be reconstructed using a DSS, reducing the gap in

performance to the 2.5%.

While the convergence slow down is more dramatic when using the DSS, the phenomenon is always observed around the peaks of resonance, also when using B-splines. In these areas, in fact, large changes in performance occur even for small variations in the actuation, as a consequence of the locally higher nonlinearity associated to the resonance. Local basis, however, tend to perform better as they scale more efficiently. During the sensitivity analysis, in fact, a variation applied to one of the basis functions only affects a portion of the domain, leading to an overall smaller perturbation of the original signal. For the same reason, when updating the actuation, changes in torque signal tend to be more contained than when using a DSS. As a consequence, smaller steps between one design point and another are taken by the optimiser. This facilitates the reconstruction of the design space around the peak regions, despite the high sensitivity of the cost function to variations of the design itself.

In order to improve the convergence of the optimisation process, a multi-resolution strategy, in which the optimal control problem is hierarchically solved for parametrisations of increasingly higher bandwidth, can be employed. The method is demonstrated here for the case of a pendulum of bending stiffness $EI = 6.4 \text{ Nm}^2$ and whose actuation is obtained through a large bandwidth DSS parametrisation ($f_{max} = 12 \text{ Hz}$). The steps of the process are summarised in Tab. 4.5, where the results obtained without applying a multi-resolution strategy are also reported (*direct* label). Initially, the actuation bandwidth is set to 6 Hz. Once an optimal actuation is found, this is increased of 2 Hz so as to refine the torque time history; the procedure is repeated until $f_{max} = 12 \text{ Hz}$.

Stage	N_c	f_{max} [Hz]	v_X [ms ⁻¹]	P
1	24	6	10.71	6.00
2	32	8	13.41	6.00
3	40	10	13.51	6.04
4	48	12	13.54	6.05
direct	48	12	12.22	6.02

Table 4.5: Optimal control results at different stages of a multi-resolution based process using a DSS parametrised actuation ($f_{max} = 12 \text{ Hz}$).

As expected, the pendulum final tip velocity, v_X , is drastically increased at the second stage of the process, as the actuation bandwidth becomes larger than the pendulum bending mode natural frequency ($f_b = 6.21 \text{ Hz}$). Further increments to the maximum actuation frequency, f_{max} , however, do not lead to any relevant change in v_X : contrarily, as the parametrisation becomes over-resolved ($f_{max} = 10, 12 \text{ Hz}$) the convergence of the optimisation process is compromised and the constraint $P \leq 6$ is not fully recovered. The link between over-resolution and convergence slowdown is even more clear when looking at the results obtained without multi-resolution analysis (*direct* label in the

table). In this case, not only the constraint $P \leq 6$ is not fully recovered, but also the final actuation time history shows to be not fully converged, as the v_X achieved is 8.9 % lower then the one provided by the multi-resolution approach.

Chapter 5

Co-design of flexible active structures

In this chapter, optimal control is extended to the combined structural/control optimisation of very flexible structures. The investigations in the previous chapter allowed to underline how problem definition and control input parametrisation affect the design space smoothness and, as a result, the outcome of optimal control. Starting from this knowledge, therefore, the following studies will aim to characterise the potential of co-design when applied to structural dynamics under geometrically-nonlinear effects. As in Chap. 4, this will imply an assessment of how the design space smoothness is affected when switching from optimal control to co-design.

The flexible pendulum proposed by Wang and Yu [171] (Sec. 4.2) will be used as test case also for the co-design approach. In fact, studies in Chap. 4 have outlined that, despite its simplicity, the dynamics of this system has several affinities with that of very flexible wings, including large amplitude vibrations and inertial coupling between rigid/flexible modes. The co-design problem considered is introduced in Sec. 5.1. As the pendulum bending stiffness has been shown to be the most relevant structural property to impact the system dynamics, it will be allowed to vary while the actuation itself is being defined. The effect of choosing a different starting condition for the actuation, as well as the potential disadvantages of using a sequential approach, is investigated in Sec. 5.2. Sec. 5.3 focuses on the efficiency of the process, showing how the convergence speed can be affected near resonance and how to tackle the issue. Finally, the impact of the frequency resolution chosen to model the actuation is discussed in Sec. 5.4.

5.1 Problem description

For all the co-design cases considered in this section, the beam rectangular cross-section (Fig. 4.6) is initially set to have a relatively high bending stiffness, $EI = 6.4 \text{ Nm}^2$, and size $l_2 \times l_3 = 0.080 \times 0.125 \text{ m}^2$. During the co-design, l_3 has been bounded to be

$l_3 \in [0.055 \text{ m}, 0.200 \text{ m}]$, while l_2 is constrained to maintain the beam cross-sectional area constant ($A = 10^{-2} \text{ m}^2$). As the bending mode natural frequency of the initial design is $f_b = 6.21 \text{ Hz}$, the basis size of the parametrisation has been adjusted so as to reach a maximum frequency f_{max} equal to 4 Hz, 6 Hz (as per the design of experiments in Fig. 4.15) and 12 Hz. The optimisation has been formulated as the constrained problem (4.8) with $P_{max} = 6$. This allows to test the co-design process for a highly nonlinear configuration while reducing the path dependency of the solution.

The constraint enforced on the sectional area maintains the mass distribution constant and, thus, the characteristic frequency associated to the rigid-body dynamics. To minimise the cost in problem (4.8), therefore, the co-design can only adjust the pendulum stiffness and tune its bending mode natural frequency with the frequency content of the actuation. While a larger number of structural design parameters could be considered, a single parameter facilitates our exploration as it allows for a much clearer analysis of the results. Furthermore, dealing with nonlinear dynamics and a large number of structural design variables would require the development of an adjoint based sensitivity analysis, which is beyond the scope of this work.

The main results obtained of the co-design problem have been summarised in Tab. 5.1 and 5.2. For each case, the size of the parametrisation, N_c , and the related maximum frequency of excitation, f_{max} , have been reported. The identifications *zero* and *opt* refer to the torque time-history at the beginning of the optimisation process, M_{Y0} : For the *opt* cases, the initial design uses the actuation found in pure optimal control problem; for the *zero* cases, it is simply chosen to be $M_{Y0}(t) = 0$ (*zero* cases). The optimal structural design is described both in terms of final geometry (l_3) and the bending mode natural frequency (f_b) of the non-actuated structure. System performance is quantified by the final tip velocity, $v_X(T)$, which is compared to the tip velocity given by the optimal control problem on the initial beam geometry (DOE in the tables).

ID	N_c	f_{max} [Hz]	l_3 [m]	f_b [Hz]	$v_X(T)$ [ms ⁻¹]	%
zero	16	4	0.0550	4.27	10.61	33.5%
zero	24	6	0.0739	5.73	13.70	28.0%
zero	48	12	0.0792	6.15	13.34	-0.5%
opt	16	4	0.0819	6.36	8.41	5.8%
opt	24	6	0.0800	6.21	10.71	0.0%
opt	48	12	0.0800	6.21	13.41	0.0%
DOE	16	4	0.0800	6.21	7.95	—
DOE	24	6	0.0800	6.21	10.71	—
DOE	48	12	0.0800	6.21	13.41	—

Table 5.1: Results of the combined optimisation problem using DSS control parametrisations of different basis size. Percentage values are with respect to the optimal control only case (DOE).

ID	N_c	f_{max} [Hz]	l_3 [m]	f_b [Hz]	$v_X(T)$ [ms ⁻¹]	%
zero	19	4	0.0550	4.27	12.55	45.6%
zero	27	6	0.0717	5.56	13.54	24.0%
zero	51	12	0.0828	6.43	12.64	-9.2%
opt	19	4	0.1465	11.4	8.65	0.3%
opt	27	6	0.0800	6.21	10.92	0.0%
opt	51	12	0.0800	6.21	13.71	0.0%
DOE	19	4	0.0800	6.21	8.62	—
DOE	27	6	0.0800	6.21	10.92	—
DOE	51	12	0.0800	6.21	13.71	—

Table 5.2: Results of the combined optimisation problem using spline control parametrisations of different basis size. Percentage values are with respect to the optimal control only case (DOE).

5.2 Initial condition: sequential vs. co-design

First, we will focus on the co-design results obtained when initialising the torque actuation with a previously computed pure optimal control solution (*opt* cases). This defines a situation similar to a sequential optimization, and in fact, it is clear from Tab. 5.1 and 5.2 that co-design brings almost no changes in either the structural design and in the actuation with respect to the initial design. This can also be observed by comparing the *DOE* and *opt* curves in Fig. 5.1, where the optimal actuations obtained with 4 Hz and 6 Hz bandwidth parametrisations are shown.

For the larger bandwidth controls ($f_{max} = 6$ Hz, 12 Hz) this can be explained noticing that at the start of the optimisation the actuation M_{Y0} , which is the solution of an optimal control problem, already excites the bending mode of the pendulum (note, for instance, the high frequency component in the *DOE* curve in Fig. 5.1a). As the process is initiated from a resonance condition, control force and the structural design are de facto *locked* into a local minimum. Further changes in the structure size would only lead to poorer performance, the system moving away from the resonance condition. Conversely, changes in the actuation signal would also imply moving away from resonance. As no descending direction can be found, the optimisation is interrupted after few iterations.

When the starting torque includes only lower frequencies ($f_{max} = 4$ Hz), the phenomenology that limits the performance improvements is similar. The initial excitation (see the *DOE* curve in Fig. 5.1b) exploits the rigid-body dynamics of the pendulum and, being far from resonance conditions, system performance can initially only be improved by stiffening the design, which ensures that all the energy transferred to the pendulum is stored by the rigid mode. Consequently, the co-design leads to a stiffer beam with only a small refinement on the actuation so as to better exploit the rigid-body dynamics of the system (see the *opt* curve in Fig. 5.1b).

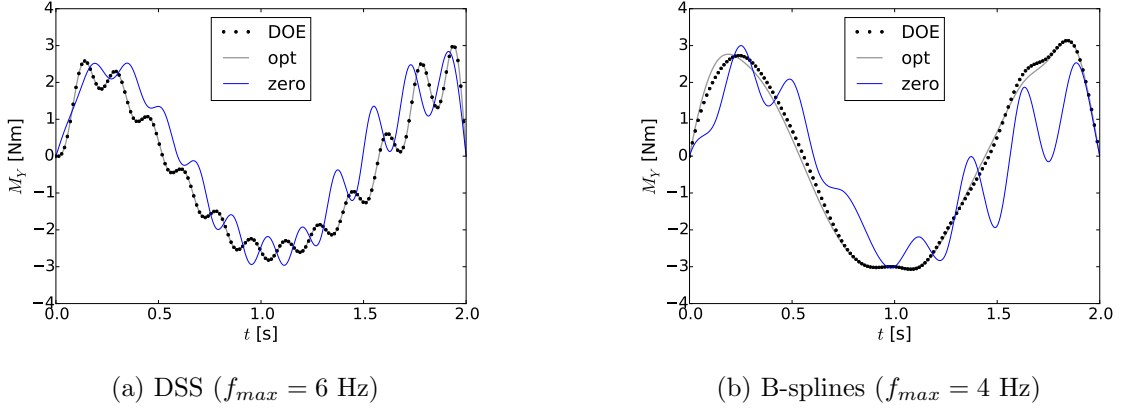


Figure 5.1: Optimal actuation provided by the co-design using different starting conditions and parametrisations.

The changes in the control design space leading to *locking* can be better understood with the reduced basis already introduced in Sec. 4.3.1. To reproduce a high-bandwidth actuation, the amplitude of the sine basis of frequencies 0.5 Hz ($x_{0.5}$) and 7.75 Hz ($x_{7.75}$) was varied, while the 0.75 Hz wave amplitude was fixed to 1.7 Nm. The final tip velocity of the pendulum, $v_X(T)$, associated to different points ($x_{0.5}, x_{7.75}$) is shown in Fig. 5.2a. The isolines of the force regulator term P are also highlighted (black curves). Three high velocity regions, strongly dependent on the amplitude of the 7.75 Hz wave, are observed. For $P \leq 6$, the maximum velocity, $v_X(T) = 9.36 \text{ ms}^{-1}$, is found at point A = (0.95, -0.49) Nm. This is associated to a condition of resonance, as the bending mode natural frequency is $f_b = 7.76 \text{ Hz}$. As the initial structural design ($l_3 = 0.1 \text{ m}$) is varied, the system moves away from resonance. The high velocity regions initially move (Fig. 5.2b and 5.2c) and gradually smooth out (Fig. 5.2d and 5.2e). This shows that in the co-design space ($l_3, x_{0.5}, x_{7.75}$) a maximum is located around $l_3 = 0.1 \text{ m}$, i.e. where the bending mode natural frequency tunes with the actuation frequency of 7.75 Hz.

The mechanism determining the position of the high tip velocities regions in Fig. 5.2a is linked to the phase between the high frequency component of the actuation and the response of the pendulum in terms of its tip horizontal position. The global maximum (point A) is associated to the rigid-flexible body dynamics, while a second minimum, associated to predominantly rigid-body dynamics, is located at point B = (1.00, 0.063) Nm. The actuation torque, M_Y , and the X tip position time histories of these cases are shown in Fig. 5.3 for $t \in [1.8, 2] \text{ s}$. As expected, for the actuation corresponding to point A, the high frequency component of M_Y synchronises with the displacements in such a way that, as $t \rightarrow T$, the tip velocity due to the structural vibration adds to the rigid-body rotation. Note that this is achieved for a negative amplitude of the 7.75 Hz wave, $x_{7.75}$. As expected, when $x_{7.75}$ increases and changes sign, the final tip velocity reduces because resonance provides a negative velocity increment. When, however, $x_{7.75} \gtrsim 0.5 \text{ Nm}$, $v_X(T)$ can be observed to grow again (Fig. 5.2a), meaning that the phase between actu-

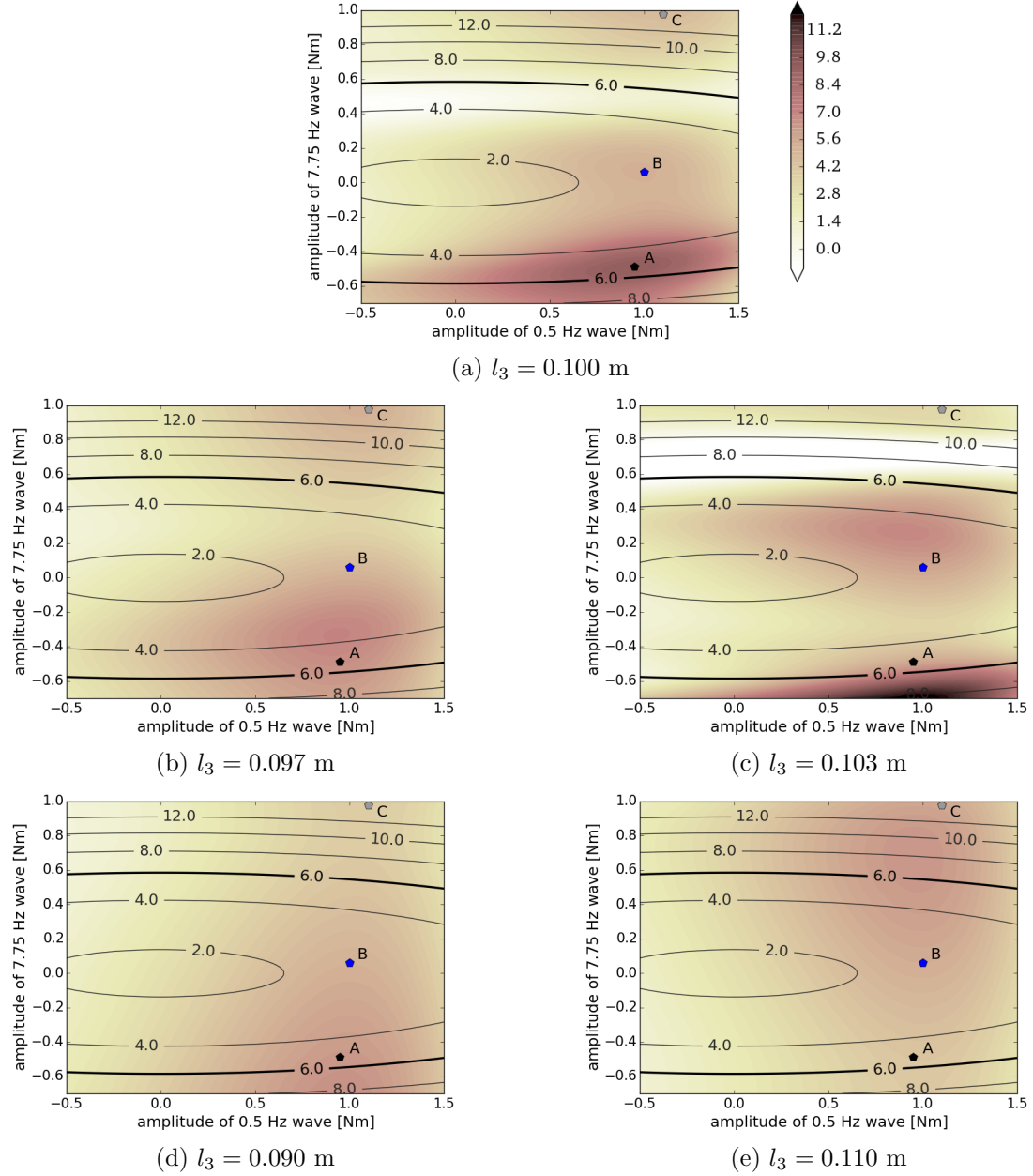


Figure 5.2: Visualisation of velocity profile for a high bandwidth actuation, modelled with a reduced number of sine waves, for structural designs in the neighbourhood of $l_3 = 0.1$ m. Points A, B and C correspond to the coordinates of the local maxima found for $l_3 = 0.1$ m

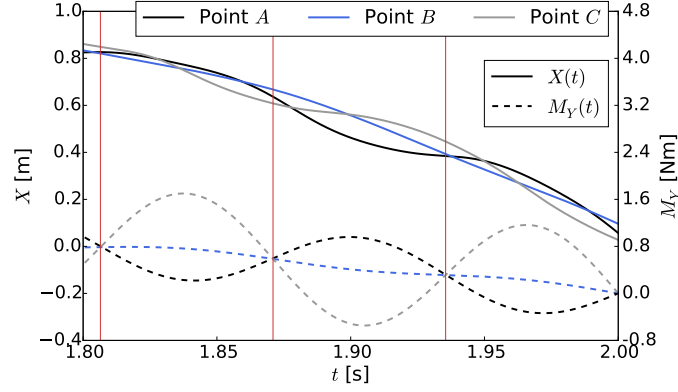


Figure 5.3: Tip horizontal position and torque moment M_Y time histories for $t \geq 1.8$ s. Results are for the *stiff* pendulum under the reduced DSS parametrised actuations corresponding to points A, B and C in Fig. 5.2a.

ation and pendulum tip response also depends on the actuation amplitude, $x_{7.75}$. This is also shown in Fig. 5.3, where the time histories of the actuation corresponding point C = (1.10, 0.98) Nm in Fig. 5.2a are presented. This nonlinear effect is linked to the large rigid-body rotations of the pendulum and the changing in geometric stiffness.

5.3 Robustness of the design

Contrarily to what it was observed in the previous section, when a null starting torque is used (*zero* cases in Tab. 5.1 and 5.2) structural design and final system performance undergo a significant evolution. The outcome of the process largely depends in this case on the control bandwidth. Generally, the co-design is driven towards a resonance region, which, as it was already seen in Sec. 4.4, implies a slowdown of convergence, particularly for DSS parametrised controls. As a result, the optimiser typically does not fully recover the integral constraint $P \leq P_{max}$. To overcome this, the following two-stage strategy was found to be an effective solution: once variations in the structural design are negligible between iterations, the pendulum geometry is fixed (end of first stage) and the actuation is refined by solving a pure optimal control problem (second stage). The improvements obtained by using the two-stage approach to refine the actuation are summarised in Tab. 5.3; as expected, the benefit is higher when the solution is closer to a peak of resonance — i.e. when $f_{max} > f_b$.

The causes of the convergence slow down can be further investigated referring to the spline parametrised solution obtained with a 6 Hz bandwidth control. In this case, the optimiser correctly drives the structural design towards the peak region located around $l_3 = l_{ref} = 0.0715$ m (curve $P_{max} = 6$ in Fig. 4.15). The neighbourhood of the peak of resonance is shown in more details in Fig. 5.4. Here the coefficients of the optimal actuation \mathbf{x}_c (Fig. 5.4b), and the resulting control signal (Fig. 5.4d), are compared for

Basis	f_{max} [Hz]	l_3 [m]		f_b [Hz]		$v_X(T)$ [ms ⁻¹] not refined refined		Gain %
splines	4	0.0550	4.27	12.55	12.55	12.55	12.55	0.0%
splines	6	0.0717	5.56	11.55	13.54	11.55	13.54	17.2%
splines	12	0.0828	6.43	12.35	12.64	12.35	12.64	2.3%
DSS	4	0.0550	4.27	10.50	10.61	10.50	10.61	1.0%
DSS	6	0.0739	5.73	12.56	13.70	12.56	13.70	9.1%
DSS	12	0.0792	6.15	11.72	13.34	11.72	13.34	13.8%

Table 5.3: Performance gains obtained using a two-stage co-design strategy.

structural designs in the vicinity of the peak of resonance. Despite the variations in the structure size being small,¹ $\Delta l_3 = \pm 0.007 l_{ref}$, the changes in the optimal actuation are, in proportion, considerably larger. This can be easily observed by comparing Fig. 5.4b against Fig. 5.4a, where the optimal control coefficients around $l_3 = l_{ref} = 0.0715$ m, found enforcing a lower cost of actuation ($P_{max} = 2$), are shown. Note that, in the latter case, nonlinear effects are significantly smaller.

The change in optimal actuation can be quantified by measuring the integral norm

$$\epsilon = \frac{\int_0^T (M_Y - M_{Y_{ref}})^2 dt}{\int_0^T M_{Y_{ref}}^2 dt} \quad (5.1)$$

where $M_{Y_{ref}}$ and M_Y are the optimal actuations at the reference, $l_{ref} = 0.0715$ m, and the perturbed, $l_3 = l_{ref} \pm \Delta l_3$, design points (Fig. 5.4d). While perturbations in structural design are around 0.7%, the norm in eq. (5.1) reaches values 16 times higher, being in both cases $\epsilon \approx 11\%$. Large values of ϵ imply that, fixing the actuation and applying even a small change in the structural design, the system will tend to move far away from the optimal control condition. Not only, therefore, performance will decrease consistently, but, as discussed in Sec. 4.4, the parametrisation of the actuation will usually require a large number of iterations to adjust to the new structural design.

5.4 Impact of frequency resolution

From Tab. 5.1 and 5.2, it can be observed that setting $M_{Y0}(t) = 0$ at the beginning of the co-design generally gives better performance. Moreover, improvements are consistently larger when reducing the bandwidth of the control. When the highest bandwidth control is used ($f_{max} = 12$ Hz), the actuation is capable of inducing resonance also on the initial design. Consequently, no major changes in the structural design occur, as this is driven towards the nearest peaks of resonance. The disadvantage of exploring a non-smooth region using a gradient based approach is shown by the fact that, while the DS

¹It is interesting to notice that, being the relation between l_3 and the bending mode natural frequency, f_b , linear, percentage variation in l_3 and f_b are equal.

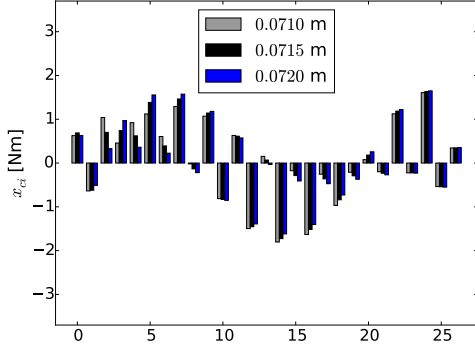
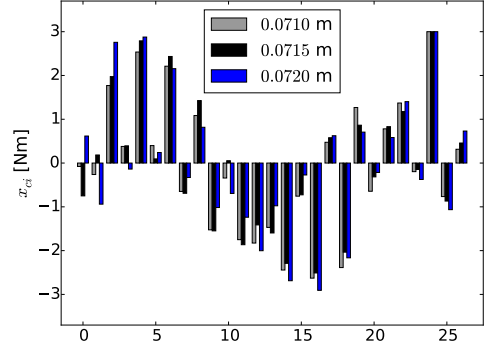
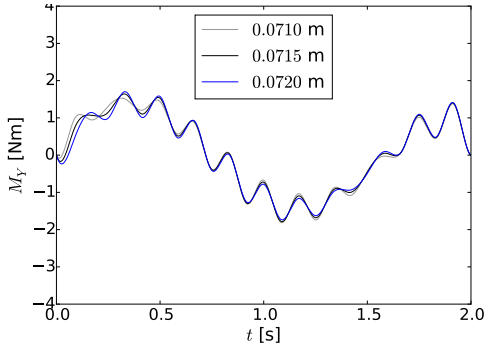
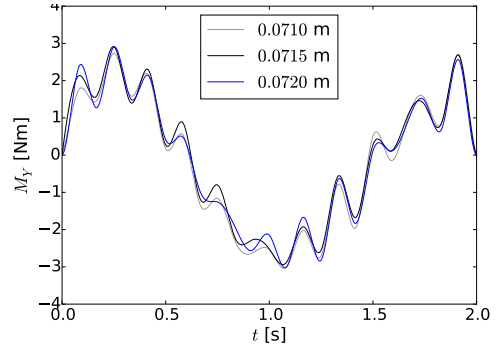
(a) Optimal actuation coefficients for $P_{max} = 2$ (b) Optimal actuation coefficients for $P_{max} = 6$ (c) Optimal actuation for $P_{max} = 2$ (d) Optimal actuation for $P_{max} = 6$

Figure 5.4: Optimal control torque (parametrised with B-splines) for structural designs in the proximity of $l_{ref} = 0.0715$ m for small ($P_{max} = 2$) and large ($P_{max} = 6$) amplitude oscillations.

parametrisation improves performance, with B-splines it degenerates and resonance is reduced at the solution.

Decreasing the actuation bandwidth, instead, leads to important performance increases with respect to the optimal control problem, regardless of the parametrisation used. The pendulum stiffness is, in fact, always reduced so as to drive its bending mode natural frequency towards the range on actuation of the control (note the f_b values in Tab. 5.1 and Tab. 5.2). When $f_{max} = 6$ Hz, the structural design is moved towards the peak of resonance located in the region $l_3 \in (0.070 \text{ m}, 0.075 \text{ m})$ and clearly visible from the design of experiments in Fig. 4.15. When $f_{max} = 4$ Hz, the increase in flexibility is even larger and the lower bound of the structural design space, $l_3 = 0.0550$ m, is hit.

Especially in this case, the combined optimisation is shown to be capable of driving the structural design to a configuration where the initial control (with its limitations in terms of maximum frequency resolution), can fully exploit the physical properties of the system. The performance gains with respect to the optimal-control-only case (DOE label in Tab. 5.1 and 5.2) are as large as 45%, due to the switch from rigid to flexible-rigid body dynamics. This effect is clearly reflected by the development of a high frequency component in the optimal actuation signal (*zero* label in Fig. 5.1b). Also for

the $f_{max} = 6$ Hz case, where a mild level of resonance can already be induced on the initial design, the stiffness reduction achieved via co-design allows to better exploit it (compare the *DOE* and *zero* curves in Fig. 5.1a).

The dependency of the co-design-derived optimal solution on the actuation bandwidth has important implications when a multi-resolution strategy (Sec. 4.5) is employed for the co-design problem. When the combined optimisation is hierarchically solved using actuations of increasing bandwidth, in fact, the final structural design is driven by the bandwidth used to initialise the process. This is shown in more detail in Tab. 5.4, where the integrated multi-resolution design approach is demonstrated for a case in which the actuation is parametrised with a DSS. The optimisation is initiated using both a control bandwidth of 4 Hz and 6 Hz (stage 0): once the first combined optimisation is terminated, this is restarted after incrementing the maximum actuation frequency, f_{max} , of 2 Hz. Note that at stage 0 structural design and actuation are the same as in the 4 Hz and 6 Hz bandwidth *zero* cases in Tab. 5.1.

When the multi-resolution process is started with a 6 Hz bandwidth actuation, *locking* between structural design and control force prevents any changes of the structural properties. Therefore, when a 12 Hz bandwidth is reached, the integrated design provided by the 12 Hz *zero* case in Tab. 5.1 is not retrieved. The final tip velocity value, $v_X(T)$, is, however, comparable as in both cases resonance is exploited. When the process is started from a 4 Hz bandwidth solution, on the other hand, structural design and actuation are not initially *locked* in a peak of resonance, being the bending natural frequency of the pendulum ($f_b = 4.27$) outside the actuation range. As a result, design and actuation are refined during the first stage and the final tip velocity of the pendulum, $v_X(T)$, increases by 7.1%. Once, however, structural design and actuation are *locked*, no further change is observed as the actuation bandwidth is increased.

The solutions in the multi-resolution process obtained from an initial 4 Hz bandwidth actuation in Tab. 5.4, can be compared against the corresponding co-design solutions in Tab. 5.1. In all cases, the final tip velocities and the level of actuation are very similar. However, the structural design obtained via multi-resolution is consistently more flexible. The low bandwidth actuation chosen at the first stage, in fact, leads to a considerable reduction of the pendulum bending stiffness. Especially in this case, the strong influence of this parameter on the final structural design is clear.

Overall, the results obtained using a zero starting condition for the actuation prove the potential of adopting a gradient based co-design approach even for resonant, strongly nonlinear systems. On the one hand, and similarly to what was observed with a sequential optimisation strategy (Sec. 5.2), the occurrence of structural-actuation *locking* around peaks of resonance can limit the progress of the optimisation, especially when a large bandwidth is used. This means that some initial sampling of the structural domain needs to be performed. On the other hand, however, co-design allows to explore much larger portions of the design space, even when this implies a drastic change in the sys-

Case	Stage	N_c	f_{max} [Hz]	l_3 [m]	f_b [Hz]	$v_X(T)$ [ms ⁻¹]
Initial bandwidth of 4 Hz	0	16	4	0.0550	4.27	10.61
	1	24	6	0.0584	4.53	13.44
	4	48	12	0.0584	4.53	13.44
Initial bandwidth of 6 Hz	0	24	6	0.0739	5.73	13.70
	3	48	12	0.0739	5.73	13.70

Table 5.4: Results of the combined optimisation using a multi-resolution strategy and a DSS parametrisation. Two different actuation bandwidth of 4 Hz and 6 Hz has been chosen to start the process.

tem dynamics (such as those switching from a rigid to a flexible-rigid body dynamics). The rate of sampling of the structural design space, or conversely the overall number of co-design solutions to be found, can, thus, be conveniently reduced, facilitating the exploration of larger portions of the design space as compared to zero order or traditional sequential optimisation approaches.

Chapter 6

Optimal manoeuvres with very flexible wings

In this chapter, optimal control is used to identify rolling manoeuvres with geometrically-nonlinear wings. Studies in Chap. 4 have already highlighted that an appropriate definition of the optimal control objectives and selection of the parametrisation frequency bandwidth lead to sufficiently smooth design spaces, even when the structural dynamics is characterised by large amplitude vibrations and strong geometrical-nonlinearities. The investigations presented in this chapter will extend these findings to aeroelastic systems, hence assessing the benefit of using a geometrically-nonlinear description and optimal control for identifying efficient manoeuvres for very flexible vehicles. An important element to be considered will be the ability of the method to deal with, and possibly exploit, the dynamics associated to the large wing deflections.

Numerical studies will focus on rolling manoeuvres and wings of very low stiffness. These will be partially-supported through a hinge constraint, which allows isolating the dynamics associated to the wing flexibility. In Sec. 6.1 their equilibrium and rolling manoeuvrability features are studied as a function of the airframe stiffness. A flight dynamics description of the hinged wings roll dynamics is also developed using elastified stability derivatives (Sec. 6.2). This will be shown to capture the relevant dynamics under slow actuation or for stiff wings. Finally, the wings aeroelastic optimal control is addressed in Sec. 6.3. To assess the optimal control methodology and underline the advantages of a nonlinear aeroelastic description, actuation time histories are also built based on the elastified flight-dynamics description (Sec. 6.3.1). Exploiting the geometrically-nonlinear aeroelastic description, optimal control will expand the space of achievable manoeuvres, hence allowing for a quick response while limiting structural vibrations (Sec. 6.3.2) or producing large lateral forces with minimal lift losses (Sec. 6.3.3).

6.1 Rolling dynamics of very flexible wings

Key aspects of rolling manoeuvrability using very flexible wings are investigated in this section. To this aim, computer models of hinged HALE wings have first been built in Sec. 6.1.1. This setting allows to keep pitch and yaw attitudes constant, such that the wings can be stabilised without horizontal and vertical tailplanes. Using the nonlinear time-domain aeroelastic description of Chap. 2, their stability is first studied in Sec. 6.1.2, while the roll response to prescribed aileron deflections is shown as a function of the wing stiffness in Sec. 6.1.3. This section, in particular, outlines how large bending and torsional deflections affect the rolling performance.

6.1.1 Equilibrium of the hinged wing

The hinged-wing model is based on the high-aspect-ratio wing configuration first introduced by Patil et al [67]. As proposed later by Murua et al. [45], and with the aim of investigating the impact of the wing flexibility on its manoeuvrability, its stiffness is scaled by a factor, σ . The properties of the resulting model are summarised in Tab. 6.1. The wing is only allowed to rotate about the root chord axis.

Property	Value	
Wing span	32	m
Chord	1	m
Elastic axis	0.5	m (from leading edge)
Inertial axis	0.5	m (from leading edge)
Mass per unit length	0.75	kg m ⁻¹
Moment of inertia	10 ⁻¹	kg m
Extensional stiffness	10 ⁷	N m ²
Torsional stiffness	$\sigma \cdot 10^4$	N m ²
Spanwise bending stiffness	$2 \sigma \cdot 10^4$	N m ²
Chordwise bending stiffness	$5 \cdot 10^6$	N m ²

Table 6.1: Hinged wing properties.

For the numerical studies, σ is varied in the range $1 \div 50$ and flight conditions correspond to an altitude of 20 km and a speed of 30 m s⁻¹. As shown in Fig. 6.1a, for each value of σ the pitch attitude, measured as the angle between the wing root chord and the free stream velocity, has been adjusted so as to support a total weight of 75 kg (731.6 N). A front view of the wings in steady level fly shows that large bending deflections, comparable to the wing span, occur as the wing flexibility is increased (Fig. 6.1b): for $\sigma = 1$, for instance, the tip vertical deflection is almost 50 % of the wing semispan, $b/2$. As better shown in Fig. 6.1c, these tilt the aerodynamic force sideways towards the wing symmetry plane, meaning that higher angles of attack — and thus higher aerodynamic loads — are required to provide the target lift $L = 731.6$ N. This effect is, however,

counteracted by large torsional deformations, which increase the wing sections incidence at the tips. As a result, and in order for the lift to be constant, a non monotonic trend of the root chord angle of attack is observed as σ is varied (Fig. 6.1a).

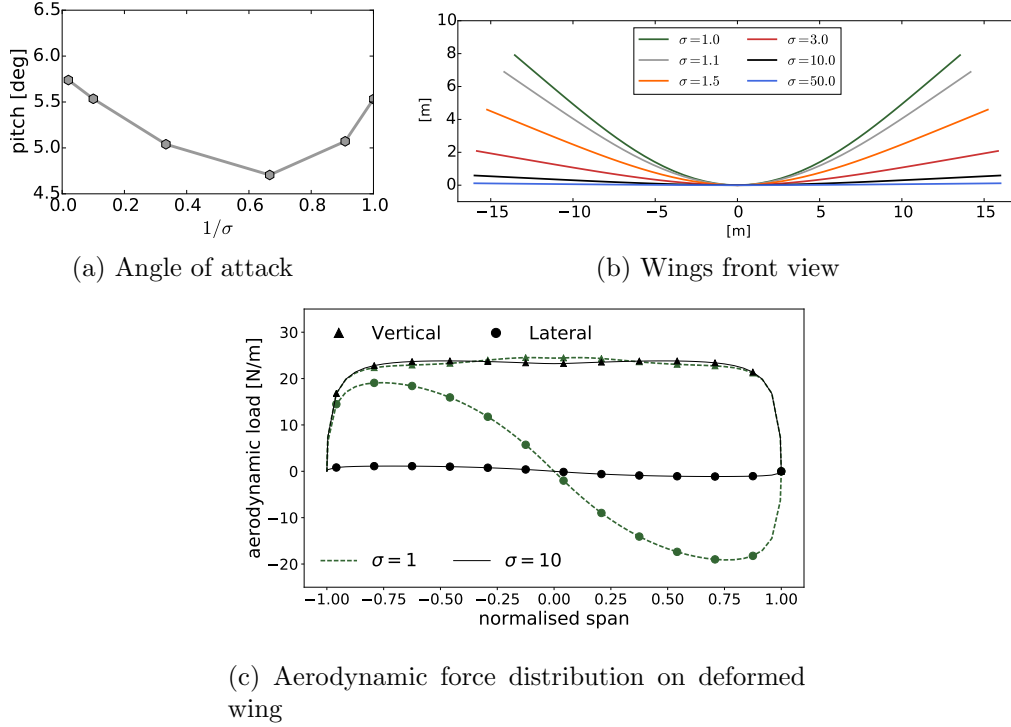


Figure 6.1: Steady-level flight trimmed conditions for different values of the stiffness parameter σ .

6.1.2 Model verification and stability study

In order to verify the aeroelastic description of Chap. 2, flutter of the flexible wings in hinged configuration has been investigated. This is done through time-domain analysis: the aeroelastic modes are excited through a small deflection of the ailerons and the wing response at different speeds, U_∞ , is observed. This is varied in the range $[20, 32] \text{ m s}^{-1}$ with step increases of 0.1 m s^{-1} . After a convergence study, the wing structure has been discretised using 24 quadratic beam elements and the UVLM wake length has been fixed to be 20 chords. The wing panelling, M , is chosen so as to ensure an accurate resolution of the range of reduced frequencies, $k = \frac{1}{2} \frac{\omega c}{U_\infty}$, for which flutter was expected as per:

$$M \geq N_M \frac{k}{\pi}$$

where $N_M = 20$ is the number of vortex rings included in each wavelength $L = 2\pi \frac{U_\infty}{c}$. With these setting, $M = 4$ was found sufficiently refined to capture unstable modes with

reduced frequencies $k \leq 0.63$.¹ Finally, the time-step is obtained from eq. (2.60), so as to ensure that the vortex lattice rows are equally spaced.

Initially the flutter speed of the $\sigma = 1$ wing at a pitch attitude of 4 deg is computed in both a clamped and hinged configuration. Flutter was found to occur over a velocity of 21.4 m s^{-1} with a frequency of 3.27 Hz, showing a good agreement with Patil et al. [67], who used a finite-state air-loads model [57]. The hinge constraint did not affect the flutter speed. In this case, an anti-symmetric aileron deflection was applied, so as to excite the wing anti-symmetric modes. However, for deflections large enough to induce relevant changes on the deformed wing shape, flutter could be seen to initiate at a lower speed on the semi-wing where tip deflections would be higher. The correlation between wing deflections and structural vibrations is also observed in the studies on roll dynamics presented in the next section. This effect has been already reported in literature [67, 181] and is caused by a reduction of the torsional mode frequency, which facilitates aeroelastic coupling.

The instability identified above for the $\sigma = 1$ wing occurs also for $\sigma = 1.1$ and $\sigma = 3$. This is, however, associated to a *humped* mode, i.e. the wings are again aeroelastically stable at higher flying speeds. This is seen in Tab. 6.2 which reports, for different σ values, the range of speeds in which limit cycle oscillations could be observed in the wing response — note that the wings attitude is set as per Fig. 6.1a. Importantly, all wings are stable at a flying speed of 30 m s^{-1} . However, as it will be shown in Sec. 6.1.3 and

Wing stiffness	Speed range
$\sigma = 1$	$U_\infty \in [20.2, 21.8] \text{ m s}^{-1}$
$\sigma = 1.1$	$U_\infty \in [21.4, 23] \text{ m s}^{-1}$
$\sigma = 1.5$	$U_\infty \in [24.5, 25.7] \text{ m s}^{-1}$
$\sigma = 3, 10, 50$	$U_\infty > 32 \text{ m s}^{-1}$

Table 6.2: Flutter speeds for wings of different stiffness, σ , at flying attitude as per Fig. 6.1a.

6.3, the low frequency structural modes are only lightly damped for the most flexible wings (e.g., $\sigma \leq 1.1$). These are the vertical bending mode (Fig. 6.2a), which has frequency of 0.33 Hz ($\sigma = 1$) and 0.35 Hz ($\sigma = 1.1$) and the in-plane bending/torsional mode (Fig. 6.2b), with frequencies of 0.92 Hz and 1.10 Hz when going from a $\sigma = 1$ to a $\sigma = 1.1$ wing, respectively. The dynamics associated to these modes will be further discussed in Sec. 6.1.3.

6.1.3 Roll dynamics under fixed control

The rolling performance of hinged flexible wings will be now investigated. The pitch attitude has been chosen as in Fig. 6.1a, such that all wings produce the same total

¹This corresponds to frequencies below 4 Hz at the lowest considered speed of 20 m s^{-1} and below 7 Hz at the maximum speed of 35 m s^{-1} .

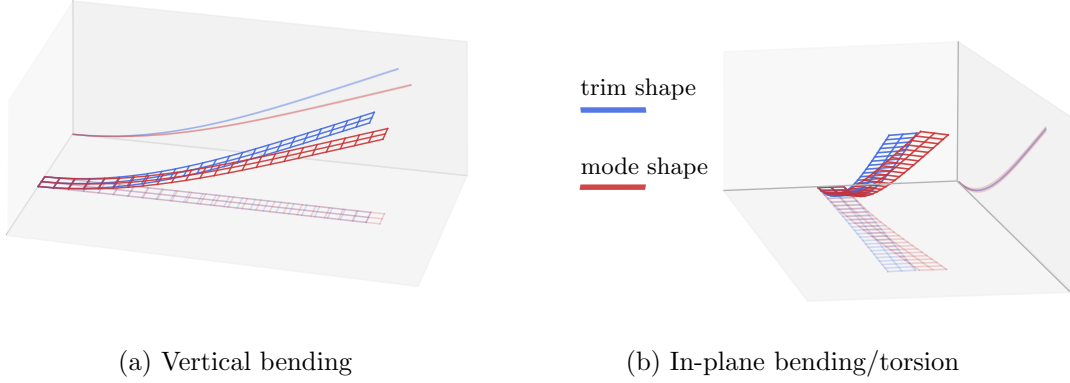


Figure 6.2: Visualisation of first two natural modes — vertical bending and in-plane bending/torsion — of a $\sigma = 1.1$ wing clamped at its root.

lift, $L = 731.6$ N. Large ailerons are placed at the wing tips, extending for 25 % of the wing span and having a chordwise dimension of 25 % c . Rolling is induced applying an anti-symmetric aileron deflection $\beta_L = -\beta_R$ (Fig. 6.3a) so as to move the left (port) wing upwards — see the snapshots of the wing response in Fig. 6.3b. The control surfaces deflections are assumed to be positive when increasing the local lift.

As in the previous section, the wing is modelled through 24 quadratic beam elements, while the UVLM wake is 20 chords long and the wing lattice is built using $M = 4$ chordwise panels. This discretisation was found to be adequate for capturing the relevant dynamics. In these studies, in fact, aeroelastic effects are not associated to high values (below 0.12) of the reduced frequency $k = \frac{1}{2} \frac{\omega c}{U_\infty}$ — where $\omega \approx 7.2$ rad s⁻¹ is the frequency associated to the slowly damped bending/torsional modes observed for $\sigma \leq 1.1$. Also the wake roll-up was found to have little impact on the aerodynamic loads and has been therefore neglected for limiting the computational cost associated to the optimisations in Sec. 6.3 — the time required for each aeroelastic analysis is, in fact, reduced of roughly the 80 % by freezing the wake. The chordwise panelling implies a single row of vortex rings modelling the ailerons: this was found adequate to model the dynamics of the flexible wings [75], but the increase in aerodynamic force produced by the ailerons under potential-flow assumptions is slightly underestimated.² For example, for a $\sigma = 50$ wing, the roll rate produced as a result of the ailerons input in Fig. 6.3a is 2.2 % below the converged values (obtained for $M = 12$).

Fig. 6.4 shows the roll attitude, measured at the hinge axis, and the side force, F_Y — normalised with respect to the steady level flight lift, L — achieved during the manoeuvre for wings of stiffness parameters ranging between $\sigma = 1$ and $\sigma = 50$. In first place, the lateral stability of a very stiff ($\sigma = 50$) hinged wing with no dihedral

²It is worth remarking that potential flow theory does not model control surfaces accurately [52]. Therefore, even a finer chord-wise panelling would not produce a substantial improvement of the model fidelity.

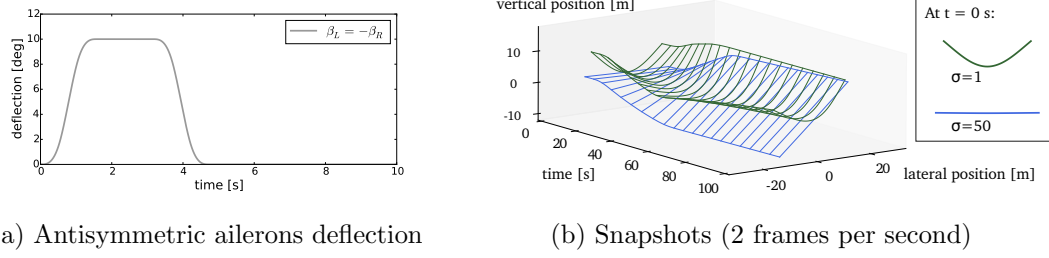


Figure 6.3: Ailerons deflection used for the study of the nominal rolling manoeuvre performance of flexible wings and snapshots of wing response for $\sigma = 1$ and $\sigma = 50$.

and sweep is briefly discussed. As observed in both Fig. 6.4a and Fig. 6.4b, this is in a neutral equilibrium position with respect to rolling: as the ailerons are retreated, the wing stabilises around a roll angle of 38.6 deg, producing a side force $F_Y = 49\%L$.

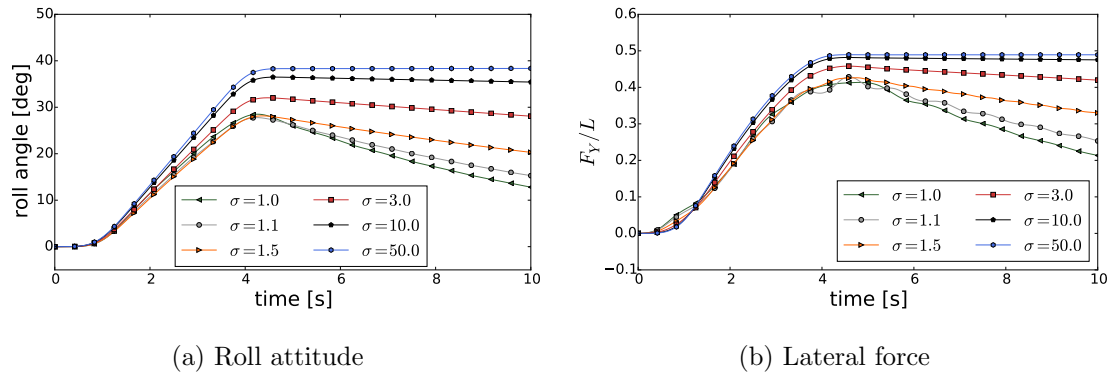


Figure 6.4: Roll attitude and lateral force time history for an ailerons antisymmetric deflection with different values of the stiffness parameter σ .

As the wing becomes more flexible, however, three main effects can be observed. In first place, the authority of the control surfaces is reduced: the lower σ , in fact, the smaller are the roll angle and the side force achieved during the manoeuvre (Fig. 6.4). Due to the large side loads associated to the wing bending, however, while the drop in roll attitude is as large as 25 % when going from $\sigma = 50$ to $\sigma = 1$, the loss of maximum lateral force is just below 13 %. In a second phase, a stabilising moment, which tends to restore the original roll attitude, arises once the ailerons are retreated. Again, this effect intensifies when deflections are larger: while the stiffer wing ($\sigma = 50$) maintains a constant side force at the end of the manoeuvre, the decay rate is as high as 23.7 N s^{-1} for the most flexible one ($\sigma = 1$). For $\sigma = 1.1$ and $\sigma = 1.0$, furthermore, the wing in-plane bending/torsional mode is excited, leading to slowly damped oscillations of the time history of the lateral force. In the remaining part of this section, all these effects are discussed in more detail. In all cases, wake roll-up has been neglected and a prescribed wake model has been assumed instead. Nonetheless, the error in lateral force prediction

associated to this assumption is very small and never exceeds the 0.2 %.

The reduction in control authority is mainly due to large torsional deformations, which is essentially a linear aeroelastic effect. Their negative impact is understood by looking at wing loads during the manoeuvre. Fig. 6.5a compares the aerodynamic loads 3 s into the rolling manoeuvre — when the ailerons are fully deployed and the rolling rate is steady — along the span of a moderately stiff ($\sigma = 10$) and a very flexible ($\sigma = 1$) wing. To allow for a fair comparison, the force components are projected on the body frame A. The sudden change in lift per unit span produced by the ailerons deflection is considerably smaller for $\sigma = 1$, thus reducing the net rolling moment with respect to the rigid wing. The effect is caused by adverse torsional deflections. These are observed in Fig. 6.6a, where the y component of the Cartesian rotation vector at the tips of a $\sigma = 1.1$ wing is used to quantify the amount of torsion. Also the center wing load distribution acts against rolling (Fig. 6.5a): this effect is, however, associated to the wing roll rate.

Large bending deflections have a small impact in reducing the control authority. This is connected to the fore-shortening effect [71]: as bending increases, the wing tips get closer to the axis of rotation, thus reducing the ailerons moment arm. Asymmetric wing deflections, however, amplify this effect. During rolling, in fact, the right wing (moving downwards) stretches up, as the bending load decreases. On the other hand, the port wing (which also experiences a small reduction in loads due to the decrease in effective angle of attack associated to the rigid-body rotation) maintains a larger bending and, therefore, a stronger fore-shortening effect. The resulting asymmetry is shown in Fig. 6.6b for a $\sigma = 1.1$ wing. Finally, it is worth noticing that in this configuration the reduction in control authority occurring in the more flexible wings is partially stemmed by the gravity force. For low values of σ , in fact, the wing center of mass is raised above the axis of rotation, hence gravity provides a positive contribution to roll — see also eq. (6.2).

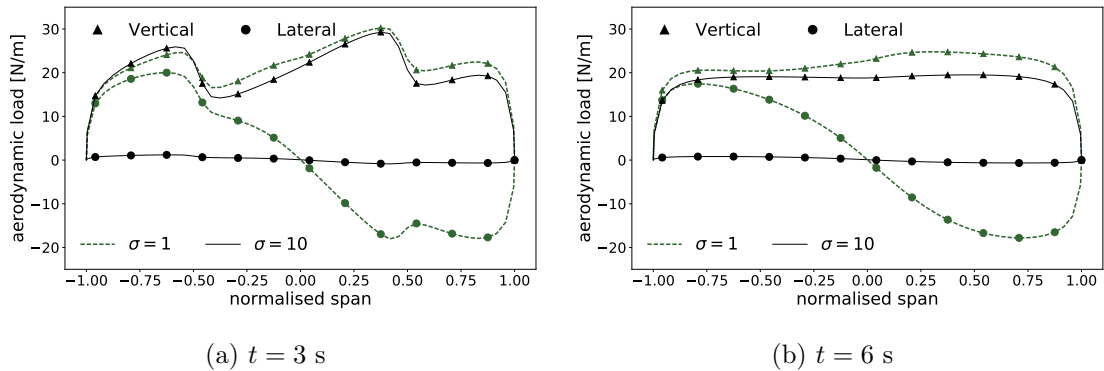
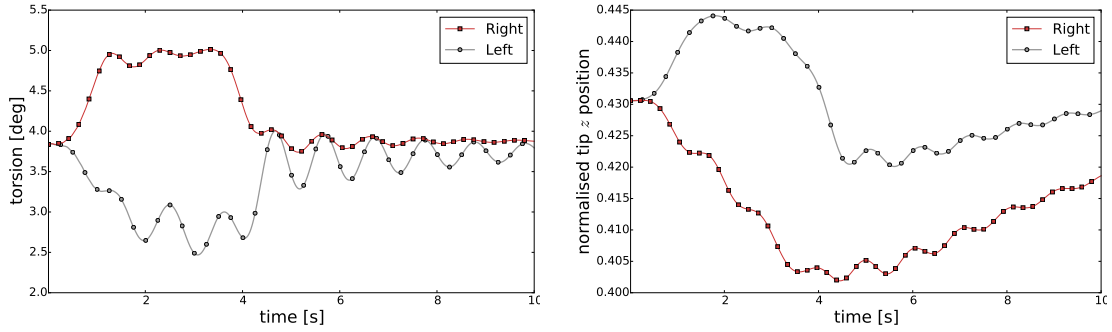


Figure 6.5: Comparison of loads distribution at different times of the nominal rolling manoeuvre for wings having a stiffness of $\sigma = 1$ and $\sigma = 10$.

The stabilising rolling moment observed in Fig. 6.4 once the aileron deflection is returned to zero is also connected to the bending deformations, which, effectively, give



(a) Tip torsion angle (positive when the leading edge moves upwards) (b) Tip vertical position (positive in upwards direction)

Figure 6.6: Tip bending deflection (normalised by the semi-wing span) and torsion during the nominal rolling manoeuvre for a wing of stiffness parameter $\sigma = 1.1$.

the wing a dihedral angle. As the axis of rotation is not aligned with the air stream, the sections of the starboard wing, moving downwards, will have a higher angle of attack than those of the left wing. This is observed in Fig. 6.5b, where the span-wise aerodynamic load distribution at time $t = 6$ s, i.e. when the ailerons are not longer deflected, is shown. While the stiffer wing shows a symmetric loads distribution, the flexible one has higher lift on the right side. It is worth underlining that this effect would also be observed on a rigid wing with dihedral angle, but would disappear if the wings rotate about an axis parallel to the free air stream velocity. Asymmetric deflections also increases the magnitude of the stabilising moment. As seen in Fig. 6.6b for $\sigma = 1.1$, as the wing rolls back ($t > 4$ s), its right side remains more stretched. This, together with the damping effect produced by the rolling rate, guarantees a higher local angle of attack than on the left wing.

During the second phase of the manoeuvre, torsional deflections do not produce significant differences in local angle of attack between left and ring wing (see Fig. 6.6a, $t > 4$ s). The time histories of the tip torsion show, however, that for $\sigma = 1.1$ in-plane bending/torsional mode are excited with a frequency of oscillations of around 1.05 Hz. Vibrations are significantly stronger on the left wing (moving upward). Here, in fact, bending deflections are larger: the frequency of the torsional mode is, therefore, reduced [67, 181], and the torsion/bending coupling is facilitated. Contrarily, on the right wing, vibrations are smaller amplitude and damp faster (Fig. 6.6a and 6.6b). As observed in Fig. 6.4b, the left wing vibrations have an impact on the manoeuvre, as they cause the lateral force to oscillate for $t > 3$ s. For $\sigma = 1.1$, the wing has bent quite significantly, hence the changes in aerodynamic force produced by the local changes of angle of attack from wing torsions directly translate into variations of the overall lateral force, F_Y .

Overall, the reduction in control authority observed in very flexible wings can be mainly attributed to the wing torsion, which is a linear aeroelastic effect. Geometrical nonlinearities from the wing bending may also have an important impact on the rolling

dynamics. In particular, the effective dihedral associated to large bending of the very flexible wings produces asymmetric changes of the local angle of attack between left and right wing. Hence, if the axis of rotation is not aligned with the flow speed, a stabilising moment is observed even in absence of side-slip. Also, as the wing bends there are larger bending/torsional couplings, which results in more complex (“instantaneous”) mode shapes.

6.2 Roll Dynamics using elastified stability derivatives

To assess the importance of geometrically-nonlinear effects in the aeroelastic description, a simplified model of the flexible-wing dynamics has also been assembled using elastified stability derivatives [3, 60]. This will be referred to as elastified flight-dynamics model (EFDM). As the studies presented in Sec. 6.1.3 are based on a hinged wing model, the EFDM will only address the wing roll dynamics. The approach can be, however, similarly extended to include other rigid-body degrees of freedom. The theoretical development of the EFDM model is presented in Sec. 6.2.1, while in Sec. 6.2.2 the wing responses predicted through this description is assessed against the full aeroelastic solution of Chap. 2.

6.2.1 Elastified flight-dynamics model

As shown in Fig. 6.7, the attitude between the body attached FoR A is expressed with respect to the inertial frame G through the angles (Θ, Φ) associated, respectively, to a pitch and roll rotation. The free stream velocity vector, \mathbf{U}_∞ , is parallel to the X axis of the G frame and the wing position is identified through the unit vectors $\hat{\mathbf{c}}$ and $\hat{\mathbf{n}}$, which are, respectively, tangent and perpendicular to its root chord. The wing is hinged so as to roll about the x axis of body attached FoR A, while its pitch attitude is fixed. Note that in this set-up the free stream velocity has no side-slip. This would be accounted for by including yaw rotations, Ψ , to the velocity vector, thus retrieving a description based upon a triad (Θ, Φ, Ψ) for the rotation between wind and body attached axes [157]. However, this is not considered here.

For a given free-stream dynamic pressure $q_\infty = 1/2\rho_\infty U_\infty^2$ (where ρ_∞ is the air density), under the hinge kinematic constraint ($\dot{\Theta} = 0$) and neglecting structural dynamic effects ($\dot{\boldsymbol{\eta}} = 0$), the wing roll dynamics is dictated by

$$I_{xx}(\boldsymbol{\eta}(\mathbf{p}))\ddot{\Phi} = M_{gx}(\Theta, \Phi, \boldsymbol{\eta}(\mathbf{p})) + M_{ax}(\Theta, \Phi, \dot{\Phi}, \beta_L, \beta_R, \boldsymbol{\eta}(\mathbf{p})) \quad (6.1)$$

where M_{gx} and M_{ax} are the x components of the moments produced, respectively, by gravity and aerodynamic forces and I_{xx} is the wing inertia about the x axis. In general, all terms in eq. (6.1) will depend on the wing shape, defined here by the displacements and rotations, $\boldsymbol{\eta}$, along the wing reference axis. The parameters determining these have

been collected into the vector $\mathbf{p} = (\Theta, \Phi, \dot{\Phi}, \beta_L, \beta_R)$.

Geometrically-nonlinear effects linked to gravity forces also need to be quantified. While flight-dynamics models do not commonly account for them, these are here included for improving the accuracy of the EFDM description when large wing deflections occur. These, in fact, shift upwards the wing center of mass, hence a moment

$$M_{gx}(\Theta, \Phi, \boldsymbol{\eta}) = g \cos \Theta [S_z(\boldsymbol{\eta}) \sin \Phi - S_y(\boldsymbol{\eta}) \cos \Phi] \quad (6.2)$$

where

$$S_i = \int_{-b/2}^{b/2} m R_{Ai}(s, \boldsymbol{\eta}(\mathbf{p})) ds \quad (6.3)$$

is generated about the hinge axis, x . In eq. (6.3), the integration is extended over the wing span, b , and m is the structural density. $R_{Ai}(s, \boldsymbol{\eta})$ refers to the components of the wing position at the curvilinear coordinate s (in the body-attached frame A , Fig. 2.1). This is computed starting from the positions and rotations of the FEs discretising the wing, $\boldsymbol{\eta}$. Therefore, S_y and S_z are proportional to the position of the wing centre of mass along the y and z axis of the body frame A , respectively. In particular, $S_y \neq 0$ only if wing deflections are not symmetric, while S_z increases as large bending deflections occur.

The aerodynamic rolling moment M_{ax} in eq. (6.1) depends upon the control surfaces deflections, $(\beta_L$ and $\beta_R)$, the wing roll rate $\dot{\Phi}$ and shape, $\boldsymbol{\eta}$. Depending on the wing design and flight condition, a large wing dihedral may be produced. In this case, since rolling does not happen about an axis aligned along the free stream velocity, the local changes of angle of attack at the wing cross-sections will not be symmetric along the span, thus adding a new contribution to the roll dynamics. Consequently, a further dependency of M_{ax} on the roll attitude, Φ , has to be included.

The aerodynamic moment in eq. (6.1), M_{ax} , is computed for a given set of flight parameters \mathbf{p}^* — to which corresponds a certain wing shape $\boldsymbol{\eta}(\mathbf{p}^*)$. The moments are

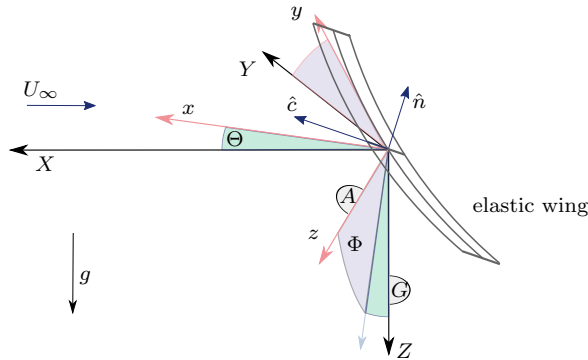


Figure 6.7: Definition of frames of references used for the flight-dynamics model

then linearised around \mathbf{p}^* as

$$M_{ax} = M_{ax}(\mathbf{p}^*, \boldsymbol{\eta}(\mathbf{p}^*)) + q_\infty c b^2 C_{M_{p_i}}(\mathbf{p}^*, \tilde{\boldsymbol{\eta}}) \Delta p_i \quad (6.4)$$

where the stability and control derivatives with respect to the flight parameter p_i , with $i = 1, \dots, 5$ are obtained here using finite-differences in the full aeroelastic model of Chap. 2, but other estimates may also be used. Each derivative $C_{M_{p_i}}$ depends on the wing shape, $\tilde{\boldsymbol{\eta}}$, associated to the perturbed term in eq. (6.4). For stiff airframes, zero deflections may be assumed, while static aeroelastic effects can be captured by setting $\tilde{\boldsymbol{\eta}}$ to be the deformed wing shape at the flight point \mathbf{p}^* , i.e. $\tilde{\boldsymbol{\eta}} = \boldsymbol{\eta}(\mathbf{p}^*)$. To account for aeroelastic effects linked to the variations of the i -th flight parameter, Δp_i , stability and control derivatives are evaluated at $\tilde{\boldsymbol{\eta}} = \boldsymbol{\eta}(p_i^* + \Delta p_i)$. Following this approach, elastified derivatives are obtained through finite differences on the full aeroelastic model. In the next section, the EFDM model will allow for a further insight into the physics of lateral manoeuvres and to quantify geometrically nonlinear effects.

6.2.2 Elastified stability derivatives

Using the above description, a simplified EFDM of the hinged flexible wings of Sec. 6.1 is built by linearising the aerodynamic moment around the steady level flight equilibrium position $\mathbf{p}^* = (\Theta^*, 0, 0, 0, 0)$, where Θ^* is prescribed as shown in Fig. 6.1a. To populate eq. (6.4), the wing stability derivatives are evaluated around \mathbf{p}^* by finite differences on the nonlinear aeroelastic model of Chap. 2 while allowing for large deflections.

Fig. 6.8 shows the stability derivatives measured when including (*elastified*) or not (*rigid*) the effect of elastic deformations — hence, with reference to eq. (6.4), when evaluating the perturbed moment assuming $\tilde{\boldsymbol{\eta}} = \boldsymbol{\eta}(\mathbf{p}^*)$ and $\tilde{\boldsymbol{\eta}} = \boldsymbol{\eta}(\mathbf{p}^* + \Delta \mathbf{p})$, respectively. Note that these correspond to the same lift but different angles of attack (Fig. 6.1a). As expected, the most important terms are the control derivative C_{M_β} and the damping term $C_{M_{\dot{\Phi}}}$ associated to the roll rate of change $\dot{\Phi}$. The derivative associated to the roll attitude C_{M_Φ} was, instead, found to be relatively small, yet non-negligible, for very flexible configurations. This term introduces the restoring moment for wings of low σ value. The damping coefficient associated to the roll rate, $C_{M_{\dot{\Phi}}}$, has an almost 50 % reduction when going from a $\sigma = 50$ to a $\sigma = 1$ wing, but no major difference is observed when aeroelastic corrections are included, meaning that this contribution is mainly connected to the large bending deflections of the wing in steady level flight.

While C_{M_Φ} and $C_{M_{\dot{\Phi}}}$ do not show significant variations when allowing for aeroelastic corrections, however, the control authority, C_{M_β} , is drastically reduced as the wing flexibility increases. As discussed in Sec. 6.1.3 this important effect is mainly driven by the adverse twist produced by the ailerons (Fig. 6.6a). The small drop of the rigid C_{M_β} (around 5 % when passing from a $\sigma = 50$ to a $\sigma = 1$ wing), results, instead, from the fore-shortening effect. Although in the EFDM the rolling moment generated by gravity

is computed exactly via eq. (6.2), the term

$$C_{M_g} = \frac{1}{q_\infty c b^2} \frac{\partial M_{gx}}{\partial \Phi} \quad (6.5)$$

has also been included in Fig. 6.8 to show that, despite the wing roll axis not passing through its center of mass, gravity has little importance in these cases. Also, the elastified C_{M_g} trend overlaps with the rigid one, proving that changes of I_{xx} , S_y and S_z in eq. (6.1) and (6.2) are here almost negligible.

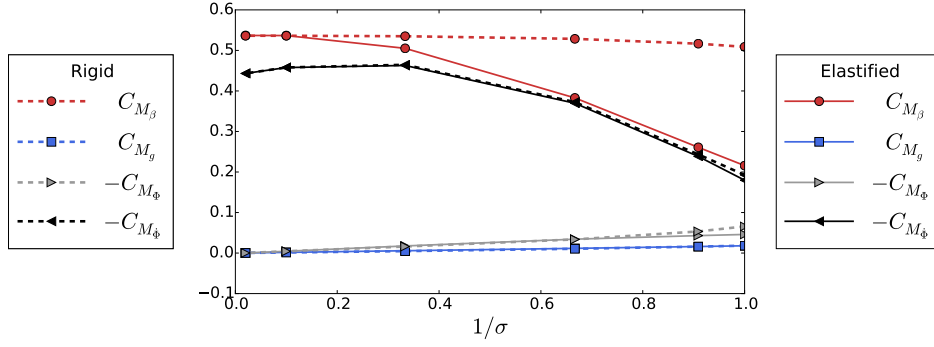


Figure 6.8: Rigid and elastified stability derivatives for wings of different flexibility, σ , around a level flight equilibrium point.

Substituting the elastified stability derivatives of Fig. 6.8 into eq. (6.1) and (6.4) leads to the following equation for the hinged wing roll dynamics:

$$I_{xx} \ddot{\Phi} - q_\infty c b^2 \left(C_{M_{\dot{\Phi}}} \dot{\Phi} + C_{M_\Phi} \Phi \right) = M_{gx}(\Phi) + q_\infty c b^2 C_{M_\beta} \beta(t) \quad (6.6)$$

where M_{gx} is computed according to eq. (6.2). In order to compare the predictions of the EFD model against the results obtained through a full aeroelastic analysis (Sec. 6.1.3), however, the lateral force, F_Y , is also required. This is obtained as a post-processing step once eq. (6.6) is solved with respect to Φ . To this aim, the vertical force in the body frame A is assumed to be proportional to the wing root angle of attack, α . At each roll attitude, α is given by

$$\alpha(\Phi) = \arctan \left(\frac{\hat{\mathbf{u}}_\infty \cdot \hat{\mathbf{n}}(\Phi)}{\hat{\mathbf{u}}_\infty \cdot \hat{\mathbf{c}}} \right) \quad (6.7)$$

where $\hat{\mathbf{c}}$ and $\hat{\mathbf{n}}$ are the unit vectors parallel and normal to the wing root chord (Fig. 6.7) and $\hat{\mathbf{u}}_\infty$ is aligned with the free-stream velocity. All quantities are projected in G coordinates, hence only $\hat{\mathbf{n}}$ depends on the roll angle as the wing rolls about $\hat{\mathbf{c}}$. Scaling and rotating the steady level flight lift, L , allows to express the lateral force in the inertial frame G as

$$F_Y = \sin \Phi \frac{\alpha(\Phi)}{\alpha(0)} L \quad (6.8)$$

where $\alpha(0) = \Theta^*$ is the wing root angle of attack at the beginning of the manoeuvre

(Fig. 6.1a).

In Fig. 6.9 the lateral force, F_Y , predicted by eq. (6.8) as a function of the roll attitude, is compared against the one resulting from the rolling manoeuvres presented in Fig. 6.4 and computed via a full aeroelastic analysis. The differences between a very flexible ($\sigma = 1$) and a very stiff ($\sigma = 50$) wing are very small, although eq. (6.8) does not capture the small hysteresis observed for $\sigma = 1$, which are mostly due to changes in wing inertia due to the large displacements. In this case, in fact, due to the large bending, the extra aerodynamic load produced by a deflection of the ailerons contributes to the lateral force even when the wing is close to its steady level flight configuration ($\Phi \rightarrow 0$, Fig. 6.1b). This effect is also observed in the lateral force time histories in Fig. 6.4b around $t = 1$ s, and vanishes for large σ as the wing dihedral diminishes.

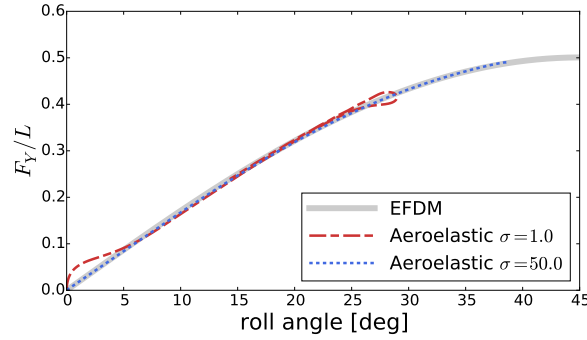


Figure 6.9: Total lateral force, expressed as a function of roll attitude through the analytical relation (6.8) and through a full aeroelastic analysis, for a very flexible ($\sigma = 1$) and a stiff ($\sigma = 50$) wing.

The wing response to the antisymmetric ailerons deflection in Fig. 6.3a can now be approximated using the elastified flight-dynamics equations (6.6) and (6.8). The comparison against the nonlinear aeroelastic solution of Sec. 6.1.3 is shown in Fig. 6.10 for $\sigma = 1.1$ and $\sigma = 50$. As expected, when geometrically-nonlinear effects are negligible ($\sigma = 50$), both models are in excellent agreement. As these become important, however, some differences can be observed, mostly during the second phase of the manoeuvre ($t > 4$ s). Fig. 6.11 shows the contribution to the total moment for $\sigma = 1.1$ from each term in eq. (6.6). During the initial phase of the manoeuvre (ailerons fully deflected, $t < 4$ s), the most significant ones are the ailerons input and the roll rate damping. The good match against the nonlinear aeroelastic response shows that the impact of the adverse torsional deformations — produced by the deflection of the control surfaces (Fig. 6.6a) — is well captured through the elastification of the C_{M_β} derivative. Importantly, this also proves that this effect remains predominantly linear despite the large changes in wing shape occurring during the manoeuvre (Fig. 6.6b). Also the roll rate damping is well estimated. As the aeroelastic correction only accounts for instantaneous geometry changes, it is clear that the nominal manoeuvre for this configuration is slow enough for aeroelastic effects

to remain quasi-stationary.

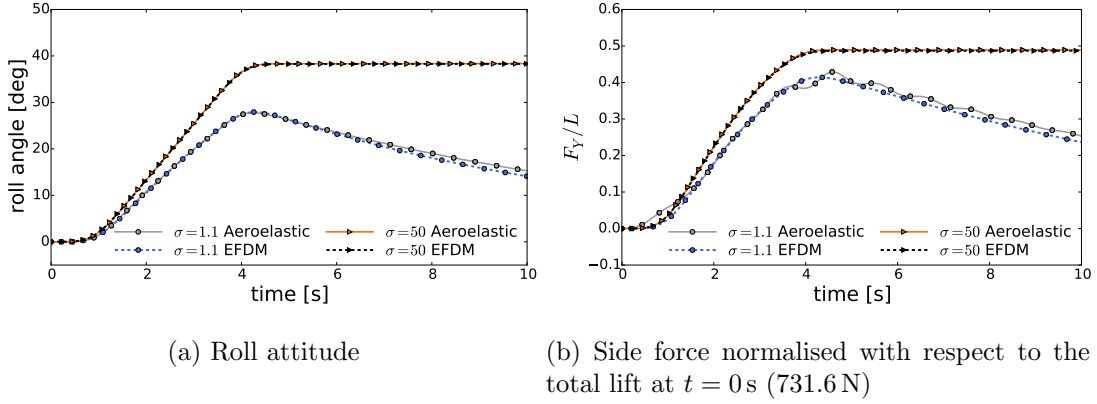


Figure 6.10: Wing response to an antisymmetric aileron deflection from elastified flight-dynamics model and full aeroelastic analysis.

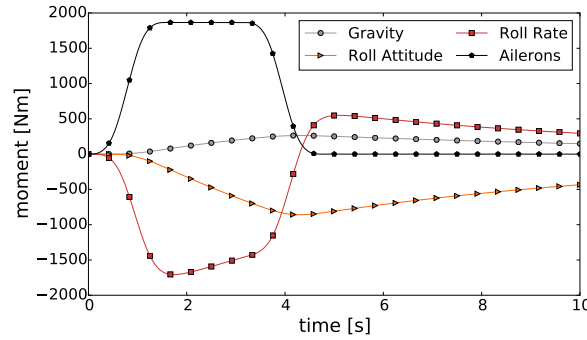


Figure 6.11: Decomposition into the terms appearing in eq. (6.6) of the total rolling moment for $\sigma = 1$ under the aileron deflection defined in Fig. 6.3a.

For $t > 4$ s the restoring moment associated to the roll attitude becomes predominant, while the impact of gravity is rather limited (Fig. 6.11). In the EFDM description, however, this is over-predicted, leading to a growing error in the roll response (Fig. 6.10a). The elastification of the C_{M_Φ} derivative, therefore, does not fully capture the geometrical nonlinearities associated to this phase of the manoeuvre, namely the asymmetries in wing bending deflections and the resulting changes of local angle of attack (Sec. 6.1.3). Regarding this, it is worth recalling that the aeroelastic correction has little effect on C_{M_Φ} (Fig. 6.8), as it only accounts for the static effects. The small inconsistency between the EFDM and the full aeroelastic prediction, therefore, indicates that the coupling between rigid and flexible dynamics — only captured by the latter model — becomes more important in this phase.

Overall, the EFDM is seen to give a good approximation for the rolling dynamics even for very flexible wings. The main drawback of this simplified description is clearly that no structural dynamics is captured; for instance, the oscillations of lateral force

linked to the wing torsional/bending dynamics are lost (Fig. 6.10b). When seeking optimal manoeuvres on very flexible wings, this will imply severe constraints on actuation bandwidth that may limit performance, as will be seen in the next section.

6.3 Optimal control of flexible wings

Results in Sec. 6.1.3 have shown that, even for rather simple aileron commands, the response of very flexible wings can be quite involved. The task of scheduling aileron deflections becomes, therefore, more elaborate, especially when the aim is to identify manoeuvres for best performance under a given metric. In this section they will be obtained from the solution of an optimal control problem. In Sec. 6.3.1, time histories of aileron commands obtained through this approach will be compared against those identified using the simplified elastified flight-dynamics description. This comparison will assess the single-shooting based framework and the relative importance of geometrically-nonlinear effects and structural dynamics when designing manoeuvres with very flexible wings.

When using the single-shooting approach, the best-performing rolling manoeuvres will be obtained as a solution to the optimal control problem (3.15). For the studies presented in this section, in particular, the control input is provided by the left and right wing aileron deflections, hence $\mathbf{u}(t) = \{\beta_L(t), \beta_R(t)\}$. Defining a rolling manoeuvre for a flying wing typically requires a trade-off between competing performance objectives, hence leading to an inherently multi-objective problem. In order to recast this into a problem of the form (3.15), the cost function, I , is scalarised and expressed as a weighted sum of multiple objectives, I_j ,

$$I = \sum_j w_j I_j \quad (6.9)$$

In all the study proposed, the objective to roll the wing until a target lateral force F_T — equal to the 40% of the steady level flight lift, L — is produced. Two variations of this manoeuvre are considered. Firstly, the focus is in rolling the wing as fast as possible while minimising wing vibrations and control effort. This formulation, which requires dividing the manoeuvre into segments, is used in for assessing the single-shooting framework in Sec. 6.3.1 and discussed in more detail in Sec. 6.3.2. A second study will instead investigate strategies to compromise large gains in lateral force with a moderate lift loss (Sec. 6.3.3). In both cases, the deriving optimisation problem is inherently multi-objective, as a trade-off between conflicting requirements is necessary (namely short transient vs. low vibrations and large lateral force vs. low lift loss). This aspect is expressed in the optimisation problem by defining the cost function I as a weighted sum of multiple objectives, eq. (6.9). The impact of the wing flexibility on the optimal actuation is also investigated by defining the manoeuvre for wings of different stiffness parameters σ .

All wings are again assumed to fly at a speed of 30 m s^{-1} and their pitch attitude is adjusted so as to produce the same lift, L , in steady level flight (Fig. 6.1a). In all the optimisation studies the ailerons are initially set to zero angle and, unless otherwise stated, this has been parametrised using 2 control points per second, thus achieving a maximum nominal excitation frequency $f_{max} = 1 \text{ Hz}$. For the most flexible wings ($\sigma \leq 1.1$) this resolution is enough to capture the first bending (around 0.3 Hz) and in-plane bending plus torsional mode (around 1 Hz). Realistic travel limits and a maximum rate of deflection are ensured by enforcing:

$$\begin{aligned} |\beta_*(t)| &\leq \beta_{max} \\ |\dot{\beta}_*(t)| &\leq \dot{\beta}_{max} \end{aligned} \quad \text{for } t \in [0, T] \quad (6.10)$$

Maximum travel limit and rate of deflection are set to be $\beta_{max} = 10 \text{ deg}$ and $\dot{\beta}_{max} = 15 \text{ deg s}^{-1}$, respectively. Similarly to what has been done in Sec. 4.2, a path constraint

$$|\Phi(t)| \leq 90 \text{ deg} \quad (6.11)$$

has also been enforced on the wing roll attitude: this avoids unrealistic roll angles and indirectly speeds-up the optimisation convergence by reducing the design space size.

6.3.1 Assessment of the optimal control approach

In this first study, aileron commands are constrained to be antisymmetric ($\beta_L = -\beta_R$) and the optimal control description is achieved decomposing the rolling manoeuvre into two segments. During the initial, transient, stage ($t < T_s$), the control is asked to move the system from one equilibrium point (steady level flight) to another (wing at constant roll attitude): the aim is to achieve this as quickly as possible, hence no penalty is imposed on the amount of actuation required. In the second segment ($t \geq T_s$), the main objective is to stabilise the wing maintaining the lateral force constant. During this phase a penalty is associated to the control surfaces rate of deflection, $\dot{\beta}$. Importantly, this aims to guarantee not only a cheap actuation strategy, but also that the control leads the system towards a steady state (wing rolled with $\dot{\beta} = 0$). Using a quadratic norm to measure the gap between the instantaneous lateral aerodynamic force, F_Y , and the target force, F_T , the cost function, I , is therefore defined as:

$$I = \int_0^{T_s} w_T E(t)^2 dt + \int_{T_s}^T \left(w_S E(t)^2 + w_p \dot{\beta}(t)^2 \right) dt, \quad E(t) = F_Y(t) - F_T \quad (6.12)$$

The weights in eq. (6.12) depend on the type of control being sought, namely how fast the response should be, how important it is to reduce vibrations during the second stage and which level of actuation can be accepted. These aspects will be discussed in Sec. 6.3.2. For this initial study, these are set to be $w_T = 10^{-4} \text{ N}^{-2} \text{ s}^{-1}$, $w_S = 10^3 w_T$, and

$w_P = 5 \times 10^{-2} \text{ deg}^{-2}\text{s}$, which were chosen after a preliminary investigation to ensure that the integral terms in eq. (6.12) have comparable magnitude. In particular, a relatively large weight is associated to the lateral force gap, E , to reduce the oscillations of this force during the second segment of the manoeuvre. The manoeuvre is simulated for a total time $T = 15 \text{ s}$, while the time-step is set according to eq. (2.60). The time allowed for the transient stage, T_s , could be potentially defined as a result of the optimisation itself. However, this was not necessary here. From eq. (6.12), in fact, it is expected that during the initial part of the manoeuvre the control will aim to roll the wing at the maximum rate, hence T_s could be estimated from the wings responses to a prescribed control input in Sec. 6.1.3. In particular, this was fixed to be $T_s = 5 \text{ s}$ and $T_s = 4 \text{ s}$ for $\sigma = 1.1$ and a $\sigma = 50$, hence being inversely proportional to the wings control surfaces authority.

A reference input can be easily derived by inspection using the simplified flight-dynamics description introduced in Sec. 6.2.1 and 6.2.2. At the beginning of the manoeuvre, ailerons are deflected at their maximum rate and to their maximum amplitude (no penalty is enforced on the actuation), so as to roll the wing as fast as possible. The roll attitude required to produce the target lateral force, F_T , can be obtained through eq. (6.8): once this is known, the time for which the ailerons are fully deflected can be tuned. Finally, solving eq. (6.1) for steady-state conditions provides the aileron inputs required to stabilise the wing roll — note that these are kept constant to minimise the penalty term in eq. (6.12). The time histories provided by this approach for $\sigma = 1.1$ and $\sigma = 50$ are shown in Fig. 6.12a. Note that the $\sigma = 1.1$ control input has been derived also for maximum nominal actuation frequencies, f_{max} , below 1 Hz. This parameter, in fact, determines the maximum rates $\dot{\beta}$ and $\ddot{\beta}$ on the controls (Sec. 3.3) and, thus, allows to regulate how strongly the wing structural dynamics is excited.

The nonlinear aeroelastic responses to the input in Fig. 6.12a is presented in Fig. 6.12b and 6.12c in terms of wing roll attitude and lateral force produced. These results show that, overall, the key features of the wings dynamics are always captured. The ailerons have more authority on the rigid wing, hence less actuation time is required. For $\sigma = 1.1$ the full deflection is required for a longer time and a nonzero angle is necessary at the steady state to cancel the stabilising rolling moment produced by the wing dihedral (Sec. 6.1.3). The control input generated for $\sigma = 50$ is appropriate to reach and maintain the target lateral force F_T , as the EFDM description approximates well the dynamics of stiff wings. Despite the aeroelastic corrections, on the other hand, on a very flexible wing ($\sigma = 1.1$) the ailerons do not stabilise the wing around the correct roll attitude (Fig. 6.12b) and the lateral force is 12 % larger than required at the steady state (Fig. 6.12c). This reflects the findings of Sec. 6.2.2, which showed how the EFDM model loses fidelity in the second part of the manoeuvres, when the geometrical nonlinearities linked to the asymmetries between left and right wing deflections become relevant.

Importantly, when the nominal excitation frequency is above 0.5 Hz, the lateral force

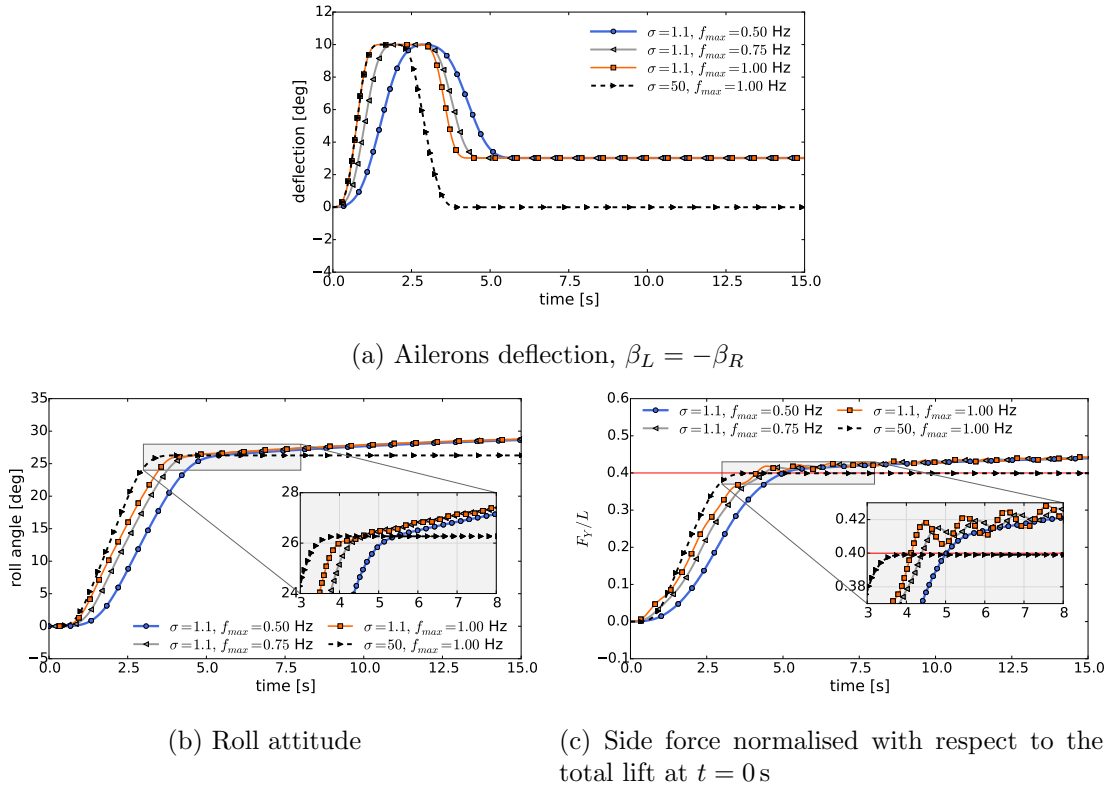


Figure 6.12: Reference anti-symmetric actuations and aeroelastic response for wings different stiffness. The control inputs have been derived for different maximum excitation frequency, f_{max} , based on the EFDM description.

F_Y also has a slowly damped oscillatory behaviour, which reflects the presence of wing vibrations. As observed in Fig. 6.13, where the time histories of the wing tips horizontal position and torsional angle are shown, these are caused by the in-plane bending/torsional mode becoming excited. As the EFDM includes no information on the wing vibrations and the actual frequencies vary as the wing bends, rate limits should be introduced in the definition of manoeuvres with this simplified descriptions. This requires bounding both $\dot{\beta}$ and $\ddot{\beta}$ to reduce the frequency content of the control input, as shown in Fig. 6.12a.

Finally, the reference actuations provided by the EFDM description are compared to those obtained through eq. (6.12) in Fig. 6.14. The corresponding nonlinear aeroelastic responses are included in Fig. 6.15. For the very stiff wing ($\sigma = 50$), the aileron input obtained via single shooting correlates very well with the reference case and, therefore, the aeroelastic responses are also in excellent agreement. The only difference arises at $t \approx 3.5$ s (see Fig. 6.14), when the single-shooting solution changes sign. While this control diminishes the time required for the wing to settle around its steady-state roll attitude, the reduction of the cost function in eq. (6.12) is minimal (below 0.1%) and, in fact, no relevant impact on the lateral dynamics is observed (see Fig. 6.15). As expected,

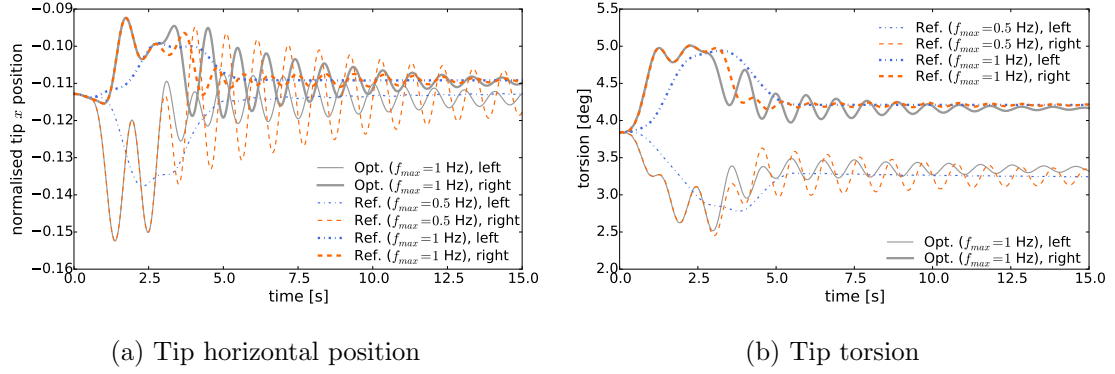


Figure 6.13: Details of the $\sigma = 1.1$ wing full aeroelastic response to the ailerons input in Fig. 6.14.

“elastification” of the stability derivatives is an adequate, and computationally cheap, approximation for the dynamics of stiff wings.

As no feedback regulator is employed in this model, in order to avoid structural vibrations the maximum actuation frequency of the $\sigma = 1.1$ reference input needed to be reduced from 1 Hz to 0.5 Hz (refer to both Fig. 6.12 and Fig. 6.13), thus cutting the maximum $\dot{\beta}$ and $\ddot{\beta}$ rates of 50 % and 75 %, respectively. This, however, was not required for the control input derived via a full aeroelastic solution, which, therefore, reaches the target lateral force, F_T , considerably faster — the time required to produce 95 % F_T is, for instance, reduced of 16.4 %. Lateral force and roll attitude are also stabilised with great accuracy (Fig. 6.15): in this case, in fact, the wing structural dynamics is well captured and during the optimisation the aileron input frequency content can be adjusted accordingly (Fig. 6.14). As a result, the bending and torsional oscillations arising on the left (moving upward) wing are reduced without having to impose rate limits (Fig. 6.13). Interestingly, as the ailerons movement is constrained to be anti-symmetric, a small level of vibration is generated on the right wing. This, however, can be further damped allowing the control surfaces to move independently, as done in Sec. 6.3.3.

Overall, optimisation on the full aeroelastic description managed to overcome the limitations of the elastified flight-dynamics model. In first place, this is higher fidelity and accounts for geometrical changes occurring during the manoeuvre: while negligible for stiff wings — where, in fact, the EFDM approximation is excellent — these have been shown to be relevant for very flexible ones. Most importantly, building the open-loop control upon a full aeroelastic description allows to consider more aggressive, and better performing, actuation input. The EFDM model, in fact, can not account for the wing elastic dynamics and how this interacts with the rigid dynamics. As a result, for $\sigma = 1.1$ the ailerons input based on this description can lead to wing vibrations, strong enough to be observed in the F_Y time history. When using a purely flight-dynamics description, therefore, the actuation frequency must be bounded in the frequency domain, so as not

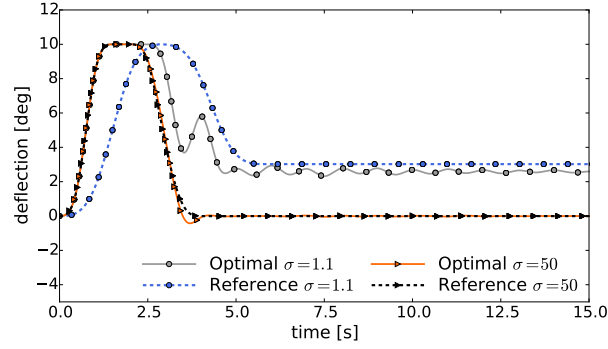


Figure 6.14: Optimal anti-symmetric actuations $\beta_L = -\beta_R$ for wings of different stiffness obtained via single-shooting (using a full aeroelastic model) against the reference cases (based on the EFDM description).

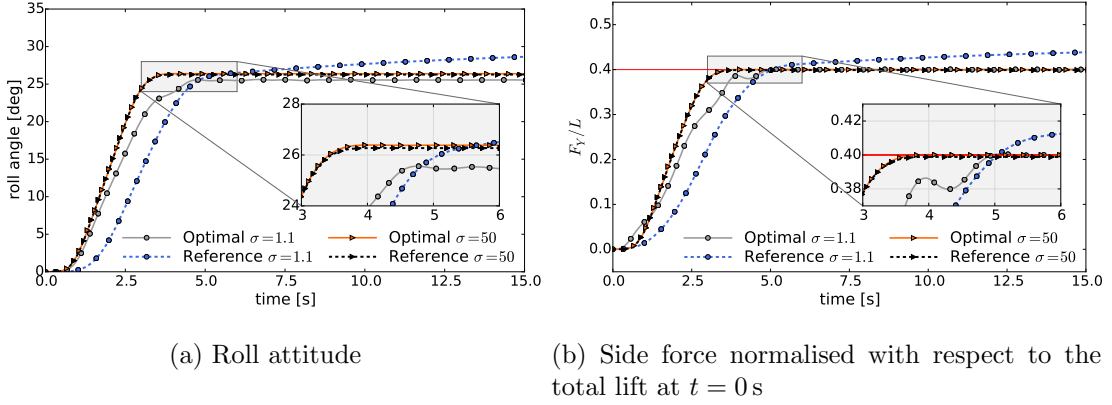


Figure 6.15: Wings response, computed through a full aeroelastic analysis, to the ailerons input in Fig. 6.14.

to excite lowly damped structural modes. This limitation becomes even more strict as the original wing shape is altered during manoeuvring and the natural frequencies of its structural modes change. While structural vibrations could also be addressed through feedback control, from a MDO perspective it is clear that even this solution is not likely to be optimal, as manoeuvre identification and vibrations control should be addressed contemporary [123]. Instead, optimal control based on a nonlinear aeroelastic description can explore scenarios in which structural vibrations may occur during manoeuvring, which is a realistic hypothesis for novel, lighter and lighter, airframes [182].

6.3.2 Trade-off between fast and smooth wing response

In the previous section, a *segmented* formulation has been chosen for defining the cost associated to the rolling manoeuvre, eq. (6.12). During the second segment, the actuation is penalised ($w_P \neq 0$) and a larger weight, $w_S = 10^3 w_T$, is associated to the lateral force error $E = F_Y - F_T$ (segmentation). This cost function ultimately reflects a trade-off

between having a fast response during the first stage of the manoeuvre and an accurate lateral force tracking in the second phase. This concept is further investigated now for a very flexible wing ($\sigma = 1.1$). To this aim, the optimal time histories of aileron commands have been computed when, respectively, removing the actuation penalty — i.e. setting $w_P = 0$ while keeping $w_S = 10^3 w_T$ in eq. (6.12) — and dropping the segmentation hypothesis — i.e. assuming $w_S = w_T$ as $w_P \neq 0$. The resulting aileron input, and the associated wing responses, are compared to those obtained employing a segmented formulation with penalty in Fig. 6.16.

When equal weights are applied to the transient and final stages of the manoeuvre (no segmentation, $w_S = w_T$), the most aggressive control is generated. The ailerons, in fact, are deflected to their maximum for a longer period (Fig. 6.16a), leading to a faster increase of the lateral force, F_Y (Fig. 6.16b). On the other hand, however, F_Y overshoots and oscillates around the target lateral force value, F_T , as the wing vibrates during the second segment of the manoeuvre. The zoom-in in Fig. 6.16b, in particular, highlights the small-scale effects associated to the structural dynamics from the large-scale flight mechanics response: while small amplitude, oscillations are not-negligible. This behaviour occurs as the optimiser minimises the only relevant contribution to the cost associated to the manoeuvre, namely the error accumulated during the transient stage ($t < T_S = 5$ s). This reduction can be observed in Fig. 6.17a, where the kernel of the cost integral in eq. (6.12)

$$k(t) = \begin{cases} w_T (F_Y(t) - F_T)^2 & t \leq T_S \\ w_T (F_Y(t) - F_T)^2 + w_P \dot{\beta}(t)^2 & t > T_S \end{cases} \quad (6.13)$$

is compared against the one associated to aileron input and wing response obtained through a segmented formulation. From the same figure it can be observed that, as a low weight is associated to the error $E = F_Y - F_T$, the small amplitude oscillations of F_Y for $t > 5$ s do not produce relevant increases to the integral kernel. At the optimiser level,

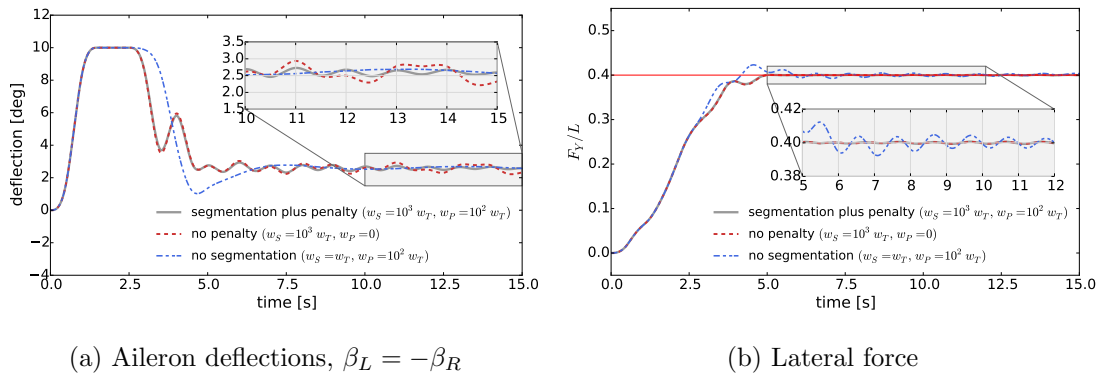
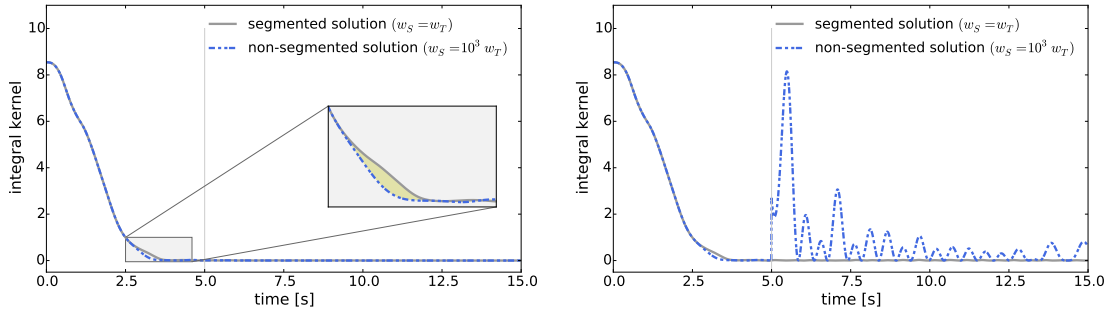


Figure 6.16: Impact of segmentation in defining the optimal actuation on a very flexible wing ($\sigma = 1.1$).



(a) Kernel assuming $w_S = w_T$ for optimal manoeuvres derived with ($w_S = 10^3 w_T$) and without ($w_S = w_T$) segmentation. (b) Kernel assuming $w_S = 10^3 w_T$ for optimal manoeuvres derived with ($w_S = 10^3 w_T$) and without ($w_S = w_T$) segmentation.

Figure 6.17: Integral kernel of eq. (6.12) for optimal manoeuvres computed with and without segmentation of the cost function. The kernel is evaluated for different values of the weight w_S , associated to the lateral force error during the second stage of the manoeuvre.

therefore, no advantage is seen in damping the wing vibrations. As shown in Fig. 6.17b, on the other hand, a non-negligible error would be produced if a segmented formulation was used, hence explaining why a segmented formulation allows to maintain the lateral force, F_T .

So far it has been shown that, if the weight associated to the lateral force error accumulated during the second phase of the manoeuvre (w_S) is large enough, wing vibrations are controlled whether the actuation is penalised or not (Fig. 6.16b). However, the control surfaces time histories in Fig. 6.16a show that only when a penalty is also enforced on the actuation the system also tends to a steady state. In this case, in fact, not only F_Y but also the aileron commands reach a constant value, settling around $\beta_L = -\beta_R = 2.6$ deg. Otherwise, undamped, small amplitude, oscillations appear. This, in particular, reveals that multiple solutions exist and that the penalty term enforced on the rate of actuation allows to select, amongst them, the one compatible with a steady state.

6.3.3 Unconventional manoeuvres - combining lateral and vertical dynamics

The versatility of the optimal control approach allows us to investigate also unconventional actuation strategies and gain a better understanding of the limit performance of very flexible wings. In order to illustrate this, the rolling manoeuvre is reformulated for exploring the trade-off between achieving a target lateral force and limiting the lift loss associated to rolling. This could also be obtained by increasing the flying speed or the vehicle pitch attitude, but here ailerons, and asymmetric wing deflections, will be

exploited to produce additional lift. This leads to the following cost function

$$I = \int_0^T \left[w_Y (F_Y(t) - F_T)^2 + w_Z (F_Z(t) - L)^2 \right] dt \quad (6.14)$$

where the objective is to minimise the gap in lateral and vertical force. Their relative importance is weighted through $w_Y = 10^{-4} \text{ N}^{-2} \text{ s}^{-1}$ and $w_Z = 0.5 w_Y$; no other term (e.g. actuation penalty and/or segmentation) has been added in order to keep the problem simple. The manoeuvre is initially defined and analysed for a wing of intermediate stiffness ($\sigma = 1.5$): in a first case, anti-symmetric aileron deflections are enforced, while in second one these are allowed to move independently. The optimal ailerons input obtained, and the corresponding time histories of lateral and vertical aerodynamic forces, are shown in Fig. 6.18.

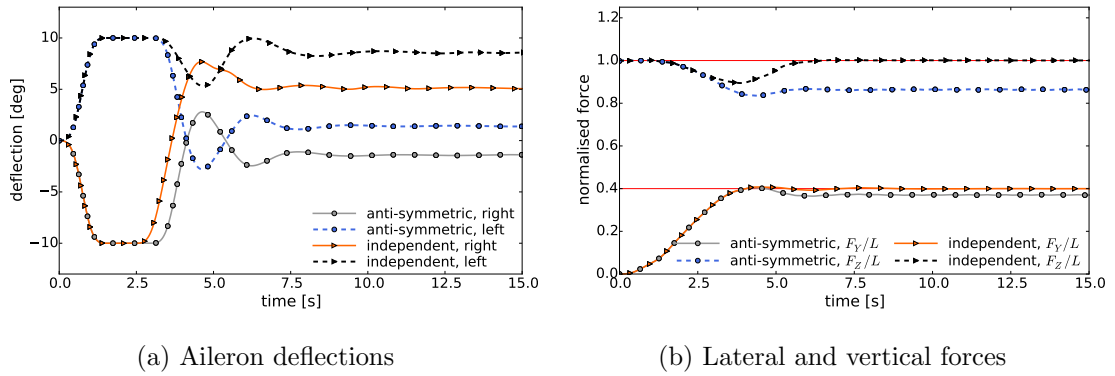


Figure 6.18: Optimal aileron inputs, and wing response, associated to the lift-constrained rolling manoeuvre of a $\sigma = 1.5$ wing for anti-symmetric and independent actuation.

During the initial part of the manoeuvre ($t < 2.5$ s), the cost in eq. (6.14) is dominated by the lateral force error, $F_Y - F_T$: even when ailerons are allowed to move independently, therefore, these are deflected in opposite directions and to their maximum amplitude, so as to produce the largest achievable rolling moment (Fig. 6.18a). As a steady state is approached, however, two considerably different configurations are reached. When control surfaces deflections are enforced to be anti-symmetric, their amplitude at the end of the manoeuvre is uniquely determined: in fact, for a given roll attitude, there exist only one amplitude $\beta_L = -\beta_R$ capable of stabilising the wing — i.e. to counteract the rolling moment associated to the wing dihedral (Sec. 6.1.3). As a result, the trade-off in eq. (6.14) is achieved by reducing the roll angle — and the lateral force, F_Y — so as to increase the lift force (Fig. 6.18b): at the steady state these are $F_Y = 93\%L$ and $F_Z = 88\%L$. It is worth noticing that these values directly depend on the relative weights between w_Y and w_Z .

If the control surfaces can be moved independently, instead, once the wing has been rolled (and, hence, the error term associated to the lateral force minimised), both ailerons are deflected downwards, so as to increase the local aerodynamic force. As a result, a

larger wing dihedral is produced. This is shown in Fig. 6.19b by comparing the wing deformed reference line at the end of the manoeuvre — and the corresponding aerodynamic load distribution — to the one obtained with anti-symmetric aileron deflections. In this configuration, the lateral loads associated to the wing curvature can be exploited efficiently. The left wing, which is almost aligned with the horizontal direction, provides a major contribution to the total vertical force, while the right wing — whose tip has an angle of 56 deg with respect to the horizontal line — mainly generates lateral force. As a result, from $t \approx 6$ s the full target lateral force F_T is achieved without any lift loss.

It is worth remarking that the, due to their large surface area, ailerons not only increase the wing curvature, but they also provide an important contribution to the total aerodynamic force (Fig. 6.19b) and maintain the wing attitude. At the end of the manoeuvre, in fact, left and right control surfaces have a different deflection (Fig. 6.18a), so as to counteract the stabilising moment associated to the wing dihedral. While the key feature of this manoeuvre is that the wing shape is morphed, the deflections time histories are also optimised: from Fig. 6.18a, for instance, it can be observed that the right aileron is deflected to the maximum amplitude for a shorter time than the left one, as a large change of incidence is required to reach its final position (at an angle of approximately 5 deg).

The impact of the wing stiffness on the lift-constrained manoeuvre is finally investigated. To this aim, the performance, measured in terms of steady state lateral and vertical force, of wings of different stiffness is compared in Tab. 6.3 for cases where the control surfaces can be moved independently or anti-symmetrically. When enforc-

Wing stiffness	Anti-symmetric		Independent	
	F_Y/F_T	F_Z/L	F_Y/F_T	F_Z/L
$\sigma = 1.1$	0.93	0.88	0.93	0.90
$\sigma = 1.5$	0.93	0.86	1.00	1.00
$\sigma = 50$	0.90	0.85	1.00	1.00

Table 6.3: Steady state performance of wings of different stiffness σ when allowing, or not, the control surfaces to move independently. Note that $F_T = 0.4L$.

ing anti-symmetric commands, performance directly improves with the wing flexibility. Here, a flexible wing ($\sigma = 1.1$) shows increases above 3 % of both lateral and vertical force with respect to the stiff wing ($\sigma = 50$). Flexible wings can, in fact, exploit the aerodynamic side loads associated to the large curvature (as shown in Fig. 6.1c) to limit the lift losses associated to roll while still producing high lateral forces.

For $\sigma = 1.5$, it has already been shown that the target lateral and vertical forces can be fully maintained with independent aileron commands. In this case, in fact, the control can adjust not only the steady state roll attitude, but also the wing shape and the aileron deflections. A similar result is obtained also when the wing is stiffer ($\sigma = 50$): as shown by the loads distribution in Fig. 6.19c, however, in this case the wing has

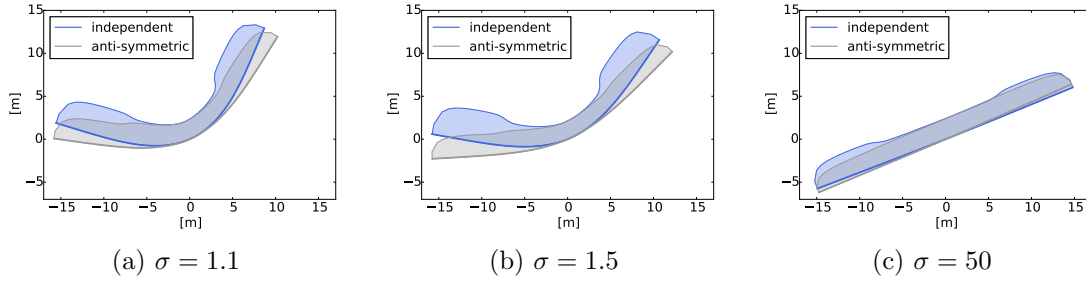


Figure 6.19: Front view of the aerodynamic loads acting on a wings of different stiffness parameter, σ , at the end of a rolling manoeuvre performed using both anti-symmetric and independent aileron commands.

no dihedral, hence only the (large) ailerons are used to compensate for the lift losses. Results in Tab. 6.3 for $\sigma = 1.1$ underline, however, the existence of a critical value of stiffness below which, regardless of the actuation strategy adopted (independent vs. anti-symmetric deflections) the wing rolling performance is bounded and both lateral and vertical forces are largely below the respective target values.

This phenomenon is associated to the fact that the control surfaces can not be deflected enough to compensate the deficit in vertical and lateral force without producing an excessively large dihedral. To assess this, the roll attitude and steady-state forces produced for $\sigma = 1.1$ (tip displacement in steady flight over 40%) have been sampled in Fig. 6.20a for different amplitudes of the deflections on left and right ailerons, β_L and β_R . In order to provide a term of comparison, the same has been done in Fig. 6.20b for $\sigma = 1.5$ (level-flight tip displacement just below 30%). In both figures, points *A* corresponds to aileron deflections obtained at the steady state by solving the optimal control problem in eq. (6.14). It is worth noticing that the space has been conveniently sampled in terms of $\beta_L + \beta_R$ and $\beta_L - \beta_R$: the first term, in fact, is proportional the amount of lift produced by the ailerons, while the second is linked to the lateral dynamics. This can be more clearly observed in Fig. 6.21, where the $\sigma = 1.1$ wing deformed configuration, and the associated aerodynamic loads, corresponding to the points *A*, *B*, *C* and *D* of Fig. 6.20a have been compared to each other.

In both Fig. 6.20a and 6.20b the contour lines of the lateral force, F_Y , are roughly parallel to the $\beta_L - \beta_R$ isolines, as roll attitude and lateral force are correlated. For the $\sigma = 1.1$ wing, however, also the lines of constant vertical force, F_Z , are aligned along the same direction. Starting from point *A*, therefore, a change in roll attitude (i.e. of $\beta_L - \beta_R$) always leads to a decrease in either lateral (point *B*) or vertical (point *C*) force (see also Fig. 6.21a and 6.21b). On the other hand, increasing the overall load acting on the wing by deflecting the ailerons further down is also counter-productive (point *D*) and an even larger effective dihedral is produced, such that the small lift gain on the right wing is cancelled by the reduction of vertical force on the left wing (Fig. 6.21c). Due to its similitude to ailerons reversal, this aeroelastic effect is here referred to as

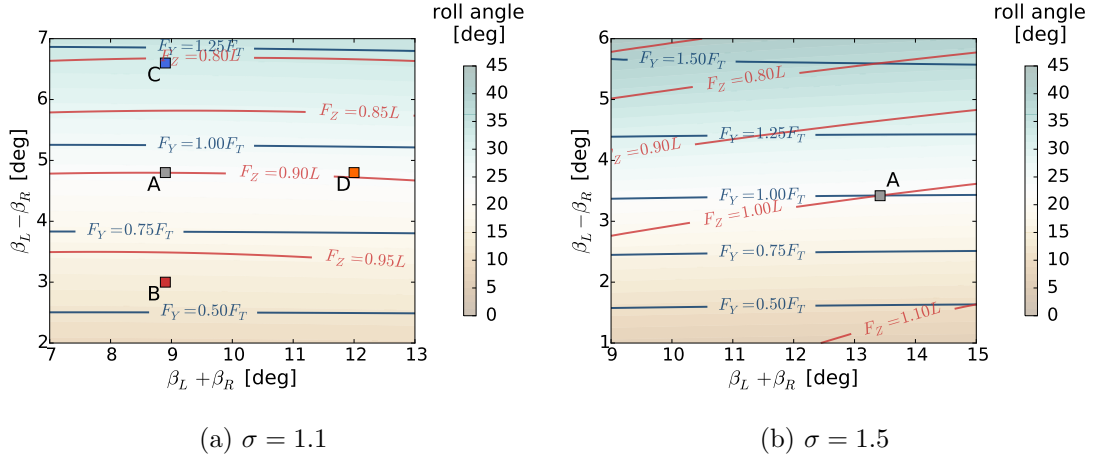


Figure 6.20: Visualisation of the roll attitude and isolines of the lateral and vertical forces produced at the steady state by a $\sigma = 1.1$ and a $\sigma = 1.5$ wing for different aileron deflections (β_L, β_R) . Points A, B, C and D correspond to representative configurations.

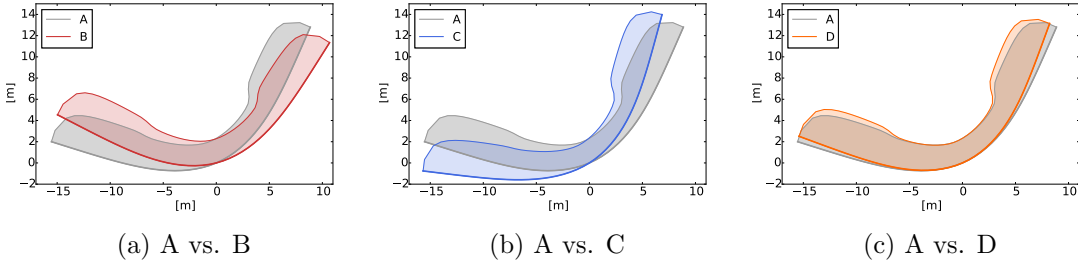


Figure 6.21: Comparison of the aerodynamic loads and wing deformed configuration of representative points of the space (β_L, β_R) shown in Fig. 6.20a.

bending reversal: in the first case, in fact, a deflection of the control surfaces produces unfavourable bending, while in the second one adverse twist. Bending-induced static instabilities have also been reported, with respect to the forward-flight speed, on very flexible flying wings [69].

As it has been seen, for very low wing flexibility deflecting the control surfaces produces an excessively large effective dihedral. Furthermore, lift increases are limited by the adverse twist occurring along the wing span. A slightly higher wing stiffness ($\sigma = 1.5$), instead, allows to exploit the ailerons for compensating the lift gap: in Fig. 6.20b, in fact, the vertical force, F_Z , always increases with $\beta_L + \beta_R$ and, as expected, the steady-state aileron commands predicted via single shooting (see also the time histories in Fig. 6.18a) correspond to the intersection between the $F_Y = F_T$ and $F_Z = L$ lines (point A in Fig. 6.20b). Therefore, there is a minimum level of bending stiffness which is necessary to avoid bending reversal and achieve a given steady-state rolling manoeuvre on a very flexible vehicle.

Chapter 7

Conclusions

This chapter will outline the main contributions of this dissertation. A critical summary of this work is first reported in Sec. 7.1, while its key contributions are discussed in Sec. 7.2. With respect to other works in nonlinear aeroelasticity, this research has been highly exploratory, as it required a detour through optimisation and optimal control theory. Its multidisciplinary nature can be viewed not only as its main point of strength, but also as a potential source of weakness. While, in fact, this work may stimulate several research questions, a large room for improving framework and methodology is left for future researchers. Some recommendations on this point are, therefore, listed in Sec. 7.3.

7.1 Summary

A methodology to identify optimal manoeuvres with very flexible wings has been proposed. To model their flight-dynamics a nonlinear aeroelastic description has been required. This has been obtained coupling a geometrically-exact beam model of the wing with an unsteady vortex lattice description of its low-speed aerodynamics. To robustify the time-integration process while containing its computational cost, a loosely coupled scheme, in which the aerodynamic loads are based on an explicit prediction of the structural displacements, rotations and velocities, is used for the aeroelastic solution. Embedding this into an optimal control framework allows to obtain the control inputs time-histories required to perform a desired manoeuvre from an optimisation problem. This has been solved upon parametrisation of the control input and using a gradient-based algorithm.

In the first part of the work, this implementation has been assessed for the control of a very flexible actuated pendulum in vacuum and used to explore the co-design of open-loop control and structural properties of this system. Due to the little amount of literature available on the topic, exploratory studies aimed to identify key aspects of the methodology. These addressed the impact on the process outcome of geometrically-nonlinearities, the problem definition (i.e. the level of control authority) and the time-

frequency resolution of the control action parametrisation. This latter, in particular, was found to be the most relevant factor driving the design for both optimal control and co-design.

This assessment has been carried out comparing optimal control actions of different bandwidth, parametrised with both local (B-splines) and global (DSS) set of basis functions. A transition region, in which the different reconstruction properties of splines and DSS leads to a gap in the final achievable performance, was identified. Elsewhere a good consistency across parametrisations has been found, particularly for low-medium levels of actuation (and, thus, moderate nonlinear effects) while increasing the authority of the control leads to multiple local peaks of resonance. A multi-resolution strategy has also been proposed to speed-up the optimisation convergence in these non-smooth regions. The effect of an increasing rigid-flexible body dynamics coupling and large amplitude deflections have also been investigated. Overall, optimal control has been demonstrated to capture and exploit the structural resonances, regardless of the level of nonlinearity shown by the system — note, for instance, that as the pendulum undergoes large deflections, its bending mode natural frequency decays.

In the co-design studies, the pendulum flexibility was allowed to vary while defining the actuation law itself. We have shown that *locking* between structure and control around the same resonance/excitation frequency prevents the exploration of large portions of the design space during sequential design or when high bandwidth actuations are employed. Lower bandwidth control actions, instead, allow exploring larger portions of the design space, driving the structural design in regions where the control can exploit the coupled rigid-flexible dynamics. While the portability of the approach to more complex structural systems — e.g. whose dynamics is driven by more modes of vibration — still requires a further assessment, these results have demonstrated the potential of gradient based co-design in vibrations control and structural dynamics, even for highly nonlinear problems.

Finally, the methodology has been used to identify optimal rolling manoeuvres for a set of representative HALE aircraft wings in hinged configuration. The key features of their rolling dynamics have been first investigated as a function of their structural stiffness. When their flexibility is very high, adverse twist deformations — which are a linear aeroelastic effect — appear as the ailerons deflect, thus reducing the control authority. In addition to that, the wing dihedral associated to bending, as well as the asymmetric displacements between starboard and port wing, produce geometrical nonlinearities that diminish the damping associated to the roll rate while increasing the wing stability. In all the studies the wings are aeroelastically stable but relevant structural vibrations occur during manoeuvring. In particular, these were always found to be asymmetric, with higher intensity on the wing with larger bending.

Using the single-shooting method, the trade-off between a number of performance indices associated to the wing roll dynamics can be investigated. This has been made

possible by identifying the manoeuvre in a multi-objective optimisation problem. Dividing these into segments allows to compromise a fast wing response with a low level of subsequent structural vibrations (although not necessarily during the initial transient dynamics, where they can contribute to increase performance). Independent ailerons deflections and geometrical nonlinearities, instead, could be exploited to define unconventional manoeuvre objectives, hence leading to lateral force gains while limiting the lift losses. Importantly, these investigations also pointed out specific handling quality limitations of very flexible wings, such as bending reversal, which could otherwise be identified only through an extensive sampling of different actuation scheduling strategies.

Overall, through relatively simple examples, it has been shown that optimal control, based upon a nonlinear description of the flexible vehicle dynamics, can deal with the complexity of these systems and also exploit very specific features of their dynamics. Studies on the control of slender structures assessed the robustness of the approach, which could successfully exploit geometrically-nonlinear effects (inertial coupling and resonance under large amplitude vibrations) to improve performance. Under limited structural dynamics, co-design can also enhance the active system and explore efficiently the design space.

The numerical investigations on rolling manoeuvres, on the other hand, underlined the advantages of a nonlinear aeroelastic description. As opposed to conventional flight-dynamics models, scheduling is not required to account for geometrical changes, which can instead be exploited to enhance performance. Optimal control, furthermore, also addresses structural vibrations. Aggressive control strategies can, thus, be accounted for from the earliest stages of the design process, even when feedback laws are not available. This may benefit the design of novel solar powered aircraft by allowing for smaller control surfaces or lighter airframes while still guaranteeing manoeuvrability. In conclusion, the approach provides a valuable alternative not only for exploring novel actuation strategies, but also to assess and quantify the limit performance of light and very flexible wings.

7.2 Key contributions

1. A Python-based environment for optimal aeroelastic control

As introduced in Chap. 1, the SHARPy framework is based on a previous Matlab implementation, SHARP, which the author contributed to transfer to a Python environment and augmented with new features. The main contributions involved:

- the geometrically-exact structural solution, with improvements of the time integration scheme and the addition of methods for enforcing kinematic constraints;
- the flight-dynamics solution, where the GEBM and UVLM solvers have been coupled allowing for arbitrary kinematics. The aeroelastic coupling scheme imple-

mentation has been, furthermore, generalised to allow for an easy switch between different schemes (e.g. from loose to strong coupling);

- the generalisation of the interface defining the aeroelastic problem (e.g. to the wing flying conditions and the allowed kinematics, the position and behaviour of its control surfaces and the time-integration/coupling options);
- the inclusion of several methods for post-processing, which were required, for instance, to evaluate cost and constraints during the optimisation;

In order to perform the optimal control and co-design studies presented in this work, furthermore, the following additions to the code (mainly included in the PyOpt package) were also required:

- specific libraries for optimal control, which mainly included methods for control vector parametrisation and constraints enforcement.
- the inclusion of efficient — within the limits of a finite-differences-based approach — parallelised tools for optimisation which could exploit HPC.

The version of SHARPy including these updates is available open-source on GitHub at the URL: <https://github.com/SalvatoreMaraniello/SHARPy>.

2. A methodology for optimising the dynamic performance of flexible structures under large deflections

Focusing on the vibrational dynamics of slender structures in vacuum, optimal control allowed to capture, and exploit, the vibrational dynamics under large, geometrically nonlinear deflection. The studies presented outlined that:

- The most relevant parameter impacting the quality of the actuation input is its time/frequency resolution, measured with respect to the reference natural frequencies of the structure. Importantly, while under large deflections these vary, optimal control allowed to capture this effect.
- While these problems are inherently characterised by multiple minima, an adequate characterisation of objective and constraints allows to remove/reduce the path dependency of the results, i.e. to obtain a smoother design space suitable to gradient-based optimisation. For instance, it has been observed in Chap. 4 that consistency across parametrisation can be increased by regulating the actuation effort.
- Under these circumstances, gradient-based approaches provide an effective way to drive the optimisation as large design spaces, i.e. with the vibration dynamics ranging from small linear displacements to large oscillations with coupled rigid-flexible body dynamics, can be explored.

3. Guidelines for the co-design of systems under structural dynamics

Studies on optimal dynamic performance for structures in vacuum were extended for analysing the advantages of a combined structural/control optimisation, so as to highlight under which circumstances this approach may benefit the design of system characterised by nonlinear vibrations. It was observed that:

- Co-design attempts starting from a previously computed optimal control solution do not result in relevant changes to structure size and control law. Once tuned on the same resonance/excitation frequency, structure and control *lock* in the initial design. The approach, in summary, becomes equivalent to sequential design, thus inheriting its limitations.
- High bandwidth actuations can drive the structural design towards local minima (associated to the nearest peaks of resonance in the problems considered), thus defeating the purpose of co-design.
- Under low bandwidth control input requirements, instead, the co-design will drive the structural natural frequencies in the region of authority of the control, despite large geometrical nonlinearities. This, in particular, suggests that when the system performance do not depend on resonance conditions, co-design may explore wider portion of the design space.

Overall, in systems undergoing structural vibrations, co-design should be used to explore the design space locally. When structural dynamics is limited, instead, larger changes in structural design/actuation may be allowed. To the knowledge of the author, this has not been attempted before.

4. A computationally-tractable optimal control approach to identify manoeuvres with very flexible wings

The understanding gained applying optimal vibrations control and co-design to very flexible slender beams has been finally exploited in the definition of rolling manoeuvres for very flexible hinged wings. The quest for a *smooth* design space or, alternatively, for an *adequate* problem definition translated into specifying multiple objectives for the optimal control. Overall, defining this around a nonlinear description of the wing aeroelastic behaviour allows to exploit the richness of this formulation and remove, this way, some of the conservatism associated to standard approaches used for identifying vehicle manoeuvres. Numerical studies evidenced that:

- More aggressive control strategies can be explored even at an early development stage, when feedback laws for controlling the structural dynamics may not be available. If possible, and regardless how much large deflections change the natural frequencies of the wing, the optimal input will, in fact, address vibrations. Importantly, this implies that:

- better flight-performance may be obtained;
 - if aggressive actuation input are used, solar-powered HALE aircraft may employ smaller control surfaces without losing manoeuvrability.
- As the manoeuvres is defined only through the specification of a final state to reach, and while path constraints are imposed, the trajectory is not prescribed, hence unconventional actuation strategies are possible. This is important when dealing with systems whose dynamics, both due to large geometrical changes and rigid-flexible dynamics coupling, departs from that of conventional, stiffer airframes.

From these points it also emerges that optimal control can be an useful tool for exploring the limit performance of new generation wings exhibiting large deflections. Furthermore, optimal actuations can define an upper-bound for the expected performance of feedback control laws, especially when time-domain aeroelastic effects are outside the linear regime.

5. A detailed analysis of geometrically nonlinear aeroelastic effects associated to rolling of very flexible wings

Studies on rolling manoeuvring with very flexible wings underlined some key dynamical features of these systems. The stiffness reduction has been observed to be linked to both linear (adverse twist) and nonlinear (large asymmetric bending deflections) aeroelastic effects, which overall decrease the wing authority and augment its stability. For the manoeuvres considered the aerodynamics was quasi-steady, hence the roll dynamics could be described accordingly also through a flight-dynamics description accounting for static aeroelastic corrections. Aside from neglecting the structural dynamics, however, this formulation also depends on the wing deformed configuration at trim, hence extensive scheduling of the stability derivatives would be required to cover the full flight-envelope.

The trim-dependency of the flight-dynamics approximation also makes it inadequate when large geometrical changes occur within a single manoeuvre: this has been shown in Chap. 6, where the full nonlinear aeroelastic description has been required for defining lift-constrained rolling manoeuvres. In this case, the dynamics under optimal actuation highlighted the presence of static instabilities (bending reversal) associated to very flexible wings. This nonlinear effect is analogous to ailerons reversal, hence deflecting the control surfaces produces unfavourable bending, rather than torsional, deflections. This, in particular, shows that the proposed approach can be an efficient tool to explore controllability and manoeuvrability of novel wings with unconventional dynamics.

7.3 Recommendations for future work

This conclusive section will discuss some of the points which, in the author's opinion, could further improve the methodology and the current framework. This list is not meant to be complete but will hopefully provide valuable points for inspiring future research on the topic.

Upscaling the optimal control framework

The current formulation has dealt with constrained vehicle kinematics and a limited number of actuators. For larger problems, the development of a more computationally efficient sensitivity analysis would be required. An adjoint model, in particular, may reduce the computational cost of problems with a large number of design variables (i.e. high-frequency control vector parametrisations or large co-design problems). However, this implementation would require also developing a framework for algorithmic differentiation and a lagged adjoint solver, as the coupling terms of the aeroelastic system are not currently available [183]. For such method to be computationally-efficient, however, the number of constraints needs to be reduced. This is especially true for bound and path constraints, which in this framework have been implemented through grid enforcement. Differentiable condensation techniques are available in literature [105, 169], but their robustness may require a careful assessment — which could, however, be carried out using the current framework.

Before considering very fine time-discretisations, furthermore, the employment of gradient smoothing techniques [171], similarly to what is done in shape optimisation [184], should be considered for avoiding spurious high-frequency oscillations. Finally, for very large optimisation problems, the framework should be interfaced with a large-scale optimisation algorithm, such as SNOPT [149] or IPOPT [150].

Co-design of complex flexible structures

Studies on co-design of very flexible structures in vacuum demonstrated the potential gains of co-design and its limitations. As seen in Chap. 5, resonance dynamics can lead to unfavourable interactions between control input and structural design, thus limiting the effectiveness of co-design under high bandwidth actuations. In this case, an integrated design should be applied only locally. Contrarily, the process was shown to be effective when resonance is limited. These investigations, however, focused on systems with constrained kinematic and limited size control/structural design variables. An assessment on the effectiveness of co-design for structural systems exhibiting a larger number of degrees of freedom and several natural modes, in which the control/structural dynamics interaction may be particularly involved, is, therefore, required. Further developments may lead to large scale aeroelastic co-design studies.

Co-design of aeroelastic systems

As outlined in Chap. 1, few attempts of structure/actuator/control aeroservoelastic optimization of flying vehicles are found in literature [134, 135]. In both the works from Haghighat et al. [134] and Jackson and Livne [135], in particular, reduced-order models and linearised formulations have been used. These do not apply to the modelling of very flexible systems, such as HALE aircraft and HAWT blades, where co-design could lead to considerable design improvements. Using a full aeroelastic description, however, the co-design of these systems could also be considered.

Results for slender structures under vibrational dynamics showed that the improvements of the active system performance can be quite limited if structural design and control input lock around specific frequencies of vibrations. This unfavourable condition may be reverted — or, at least, limited — when dealing with aeroelastic systems: in these cases, in fact, reducing vibrations typically improves the systems performance and locking may, therefore, not occur. While for this reason co-design may be found to be more effective, other phenomena associated to the presence of local minima in the extended control/structural space could occur.

Design with feedback control systems

Studies included in this work did not consider dynamics under disturbances, hence the implementation of feedback control laws for regulating the wing structural dynamics was not required. When arising, in fact, structural vibrations would be addressed by the optimal control (e.g. through segmentation of the cost function, Sec. 6.3.2).

To provide more realist design conditions, optimal manoeuvre could be defined using aeroelastic models with embedded feedback control. Such studies could highlight how the open-loop control input interacts with the stabilisation action of the feedback control. For example, in Sec. 6.3.1 it was observed that during the transient dynamics optimal control adjusts so as to excite as little as possible the wing vibrational modes. Similarly, it can be inferred that optimal control could facilitate/compensate the feedback control action, so as to better stabilise the system. These studies could also assume dynamics under disturbance. Finally, regarding the open-loop and feedback control as independent systems to be optimised, defining optimal actuations and feedback regulator gains/sensors placement simultaneously may lead to considerable enhancements of the active aeroelastic wing dynamic performance.

Bibliography

- [1] D.H. Baldelli, P.C. Chen, and J. Panza. Unified Aeroelastic and Flight Dynamic Formulation via Rational Function Approximations. *Journal of Aircraft*, 43(3):763–772, 2006. doi: 10.2514/1.16620.
- [2] P.L. Jakab. Wood to Metal: The Structural Origins of the Modern Airplane. *Journal of Aircraft*, 36(6): 914–918, 1999. doi: 10.2514/2.2551.
- [3] C. E. S. Cesnik, R. Palacios, and E. Y. Reichenbach. Reexamined Structural Design Procedures for Very Flexible Aircraft. *Journal of Aircraft*, 51(5):1580–1591, 2014. doi: 10.2514/1.C032464.
- [4] J. D. Anderson. *Introduction to Flight*. McGraw-Hill, Singapore, internatio edition, 2005.
- [5] R. Johnstone and N. Arntz. CONDOR - High Altitude Long Endurance (HALE) Autonomously Piloted Vehicle (APV). In *Aircraft Design, Systems and Operations Conference*, Reston, Virigina, sep 1990. doi: 10.2514/6.1990-3279.
- [6] C. Rasmussen, R. Canfield, and M. Blair. Joined-Wing Sensor-Craft Configuration Design. *Journal of Aircraft*, 43(5):1470–1478, 2004. doi: 10.2514/6.2004-1760.
- [7] C.E.S. Cesnik, P.J. Senatore, W. Su, E.M. Atkins, and C.M. Shearer. X-HALE: A Very Flexible Unmanned Aerial Vehicle for Nonlinear Aeroelastic Tests. *AIAA Journal*, 50(12):2820–2833, dec 2012. doi: 10.2514/1.J051392.
- [8] J. D. Anderson. *Fundamentals of Aerodynamics*. McGraw-Hill, 1991.
- [9] M.K. Bradley and C.K. Droney. Subsonic Ultra Green Aircraft Research: Phase I. Technical Report April, Boeing Research & Technology, Huntington Beach, California, 2011.
- [10] R. Cavallaro and L. Demasi. Challenges, Ideas, and Innovations of Joined-Wing Configurations: A Concept from the Past, an Opportunity for the Future. *Progress in Aerospace Sciences*, 87:1–93, 2016. doi: 10.1016/j.paerosci.2016.07.002.
- [11] E. W. Pendleton, D. Bessette, P. B. Field, G. D. Miller, and K. E. Griffin. Active Aeroelastic Wing Flight Research Program: Technical Program and Model Analytical Development. *Journal of Aircraft*, 37(4): 554–561, 2000. doi: 10.2514/2.2654.
- [12] W.P. Rodden and J.R. Love. Equations of Motion of a Quasisteady Flight Vehicle Utilizing Restrained Static Aeroelastic Characteristics. *Journal of Aircraft*, 22(9):802–809, 1985. doi: 10.2514/3.45205.
- [13] L. Meirovitch and I. Tuzcu. The Lure of the Mean Axes. *Journal of Applied Mechanics*, 74(3):497–504, 2007. doi: 10.1115/1.2338060.
- [14] T.E. Noll, J.M. Brown, M.E. Perez-Davis, S.D. Ishmael, G.C. Tiffany, and M. Gaier. Investigation of the Helios Prototype Aircraft Mishap. Technical Report January, 2004.
- [15] D. H. Hodges. A Mixed Variational Formulation Based on Exact Intrinsic Equations for Dynamics of Moving Beams. *International Journal of Solids and Structures*, 26(11):1253–1273, 1990. doi: 10.1016/0020-7683(90)90060-9.
- [16] H. Hesse and R. Palacios. Reduced-Order Aeroelastic Models for Dynamics of Maneuvering Flexible Aircraft. *AIAA Journal*, 52:1–16, 2014. doi: 10.2514/1.J052684.
- [17] C.-S. Chang, D. H. Hodges, and M. J. Patil. Flight Dynamics of Highly Flexible Aircraft. *Journal of Aircraft*, 45(2):538–545, 2008. doi: 10.2514/1.17640.
- [18] C. M. Shearer and C. E. S. Cesnik. Nonlinear Flight Dynamics of Very Flexible Aircraft. *Journal of Aircraft*, 44(5):1528–1545, sep 2007. doi: 10.2514/1.27606.
- [19] R. Palacios, J. Murua, and R. G. Cook. Structural and Aerodynamic Models in Nonlinear Flight Dynamics of Very Flexible Aircraft. *AIAA Journal*, 48(11):2648–2659, 2010. doi: 10.2514/1.J050513.
- [20] J. T. Allison and D. R. Herber. Multidisciplinary Design Optimization of Dynamic Engineering Systems. *AIAA Journal*, 52(4):691–710, 2014. doi: 10.2514/1.J052182.

- [21] Y. Bazilevs, M.-C. Hsu, I. Akkerman, S. Wright, K. Takizawa, B. Henicke, T. Spielman, and T. E. Tezduyar. 3D simulation of wind turbine rotors at full scale. Part I: Geometry modeling and aerodynamics. *International Journal for Numerical Methods in Fluids*, 65(1-3):207–235, 2011.
- [22] Y. Bazilevs, M.-C. Hsu, and J. Kiendl. 3D simulation of wind turbine rotors at full scale. Part II: fluidstructure interaction modeling with composite blades. *International Journal for Numerical Methods in Fluids*, 65(1-3):236–253, 2011.
- [23] S. Buoso and R. Palacios. Electro-aeromechanical modelling of actuated membrane wings. *Journal of Fluids and Structures*, 58:188–202, 2015. doi: 10.1016/j.jfluidstructs.2015.08.010.
- [24] R. Palacios and C.E.S. Cesnik. Cross-Sectional Analysis of Nonhomogeneous Anisotropic Active Slender Structures. *AIAA Journal*, 43(12):2624–2638, 2005.
- [25] J. Ditz, R. Palacios, and S. T. Pinho. Homogenisation of slender periodic composite structures. *International Journal of Solids and Structures*, 50(9):1473–1481, 2013. doi: 10.1016/j.ijsolstr.2013.01.017.
- [26] Y. Wang, R. Palacios, and A. Wynn. A method for normal-mode-based model reduction in nonlinear dynamics of slender structures. *Computers and Structures*, 159:26–40, 2015. doi: 10.1016/j.compstruc.2015.07.001.
- [27] P.F. Pai. *Highly Flexible Structures: Modeling, Computation, and Experimentations*. AIAA Education Series, AIAA, Reston, VA, 2007.
- [28] M.O.L. Hansen, J.N. Sørensen, S. Voutsinas, N. Sørensen, and H.A. Madsen. State of the art in wind turbine aerodynamics and aeroelasticity. *Progress in Aerospace Sciences*, 42(4):285–330, jun 2006. doi: 10.1016/j.paerosci.2006.10.002.
- [29] B.F. Ng, H. Hesse, R. Palacios, J.M.R. Graham, and E.C. Kerrigan. Aeroservoelastic state-space vortex lattice modeling and load alleviation of wind turbine blades. *Wind Energy*, 2014. doi: 10.1002/we.
- [30] B.F. Ng, R. Palacios, E.C. Kerrigan, J.M.R. Graham, and H. Hesse. Aerodynamic load control in horizontal axis windturbines with combined aeroelastic tailoring and trailing-edge flaps. *Wind Energy*, 2015. doi: 10.1002/we.1830.
- [31] J. Xiang, Y. Yan, and D. Li. Recent advance in nonlinear aeroelastic analysis and control of the aircraft. *Chinese Journal of Aeronautics*, 27(1):12–22, 2014. doi: 10.1016/j.cja.2013.12.009.
- [32] J.C. Simo and L. Vu-Quoc. On the Dynamics of Flexible Beams Under Large Overall Motions The Plane Case: Part II. *Journal of Applied Mechanics*, 53(4):855–863, 1986.
- [33] J.C. Simo and L. Vu-Quoc. On the Dynamics in Space of Rods Undergoing Large Motions A Geometrically Exact Approach. *Computer Methods in Applied Mechanics and Engineering*, 66(2):125–161, feb 1988. doi: 10.1016/0045-7825(88)90073-4.
- [34] J.C. Simo and L. Vu-Quoc. A three-dimensional finite-strain rod model. Part II: Computational aspects. *Computer Methods in Applied Mechanics and Engineering*, 58:79–116, 1986.
- [35] M. Geradin and A. Cardona. *Flexible Multibody Dynamics: A Finite Element Approach*. John Wiley & Sons Ltd, Chichester, UK, 2001.
- [36] M.A. Crisfield and G. Jelenic. Objectivity of strain measures in the geometrically exact three-dimensional beam theory and its finite-element implementation. *Proceedings of the Royal Society of London*, 455: 1125–1147, 1999. doi: 10.1098/rspa.1999.035.
- [37] O.A. Bauchau, A. Epple, S. Heo, and D. Guggenheim. Interpolation of Finite Rotations in Flexible Multibody Dynamics Simulations. In *Proceedings of the Institution of Mechanical Engineers, Part K: Journal of Multi-body Dynamics*, 222(K4), pages 353–366, 2008.
- [38] R.J. Simpson and R. Palacios. Numerical aspects of nonlinear flexible aircraft flight dynamics modeling. *54th AIAA/ASME/ASCE/AHS/ASC Structures, Structural Dynamics, and Materials Conference*, pages 1–25, apr 2013. doi: 10.2514/6.2013-1634.
- [39] C.E.S. Cesnik and E.L. Brown. Modelling of High Aspect Ratio Active Flexible Wings for Roll Control. In *43rd AIAA/ASME/ASCE/AHS/ASC Structures, Structural Dynamics, and Materials*, pages 1–15, 2002. doi: 10.2514/6.2002-1719.
- [40] W. Su and C.E.S. Cesnik. Strain-based geometrically nonlinear beam formulation for modeling very flexible aircraft. *International Journal of Solids and Structures*, 48(16-17):2349–2360, 2011. doi: 10.1016/j.ijsolstr.2011.04.012.
- [41] D.H. Hodges. Geometrically Exact, Intrinsic Theory for Dynamics of Curved and Twisted Anisotropic Beams. *AIAA Journal*, 42(6):1131–1137, 2004.
- [42] J.R.R.A. Martins, J.J. Alonso, and J. Reuther. A Coupled-Adjoint Sensitivity Analysis Method for High-Fidelity Aero-Structural Design. *Optimization and Engineering*, 6(1):33–62, 2005.

-
- [43] Z. Lyu, Z. Xu, and J.R.R.A. Martins. Benchmarking Optimization Algorithms for Wing Aerodynamic Design Optimization. In *The Eighth International Conference on Computational Fluid Dynamics*, page 18, Chengdu, Sichuan, China, 2014.
 - [44] J. Katz and A. Plotkin. *Low-Speed Aerodynamics*. Cambridge University Press, New York, 2001. doi: 10.1017/CBO9780511810329.
 - [45] J. Murua, R. Palacios, and J. M. R. Graham. Applications of the unsteady vortex-lattice method in aircraft aeroelasticity and flight dynamics. *Progress in Aerospace Sciences*, 55:46–72, 2012. doi: 10.1016/j.paerosci.2012.06.001.
 - [46] V. Mukhopadhyay. Historical Perspective on Analysis and Control of Aeroelastic Responses. *Journal of Guidance, Control, and Dynamics*, 26(5):673–684, 2003. doi: 10.2514/2.5108.
 - [47] E. Livne. Future of Airplane Aeroelasticity. *Journal of Aircraft*, 40(6):1066–1092, 2003. doi: 10.2514/2.7218.
 - [48] T.M. Kier. Comparison of Unsteady Aerodynamic Modelling Methodologies with Respect to Flight Loads Analysis. In *AIAA Atmospheric Flight Mechanics Conference and Exhibit*, pages 1–14, San Francisco, CA, 2005. doi: 10.2514/6.2005-6027.
 - [49] T.M. Kier. Integrated Flexible Dynamic Maneuver Loads Models based on Aerodynamic Influence Coefficients of a 3D Panel Method. In *56th AIAA/ASCE/AHS/ASC Structures, Structural Dynamics, and Materials Conference*, pages 1–21, 2015. doi: 10.2514/6.2015-0185.
 - [50] J.R. Wright and J. E. Cooper. *Introduction to Aircraft Aeroelasticity and Loads*. John Wiley & Sons Ltd, 2007.
 - [51] T. Mauermann. *Flexible Aircraft Modelling for Flight Loads Analysis of Wake Vortex Encounters*. PhD thesis, Technische Universitat Carolo-Wilhelmina zu Braunschweig, 2010.
 - [52] Joseba Murua. *Flexible Aircraft Dynamics with a Geometrically-Nonlinear Description of the Unsteady Aerodynamics*. PhD thesis, Imperial College London, 2012.
 - [53] Z. Wang, P. C. Chen, D. D. Liu, and D. T. Mook. Nonlinear-Aerodynamics/Nonlinear-Structure Interaction Methodology for a High-Altitude Long-Endurance Wing. *Journal of Aircraft*, 47(2):556–566, 2010. doi: 10.2514/1.45694.
 - [54] J. Murua, H. Hesse, R. Palacios, and J. M. R. Graham. Stability and Open-Loop Dynamics of Very Flexible Aircraft Including Free-Wake Effects. In *52nd AIAA/ASME/ASCE/AHS/ASC Structures, Structural Dynamics and Materials Conference*, Denver, Colorado, 2011. doi: 10.2514/6.2011-1915.
 - [55] E. Livne and T.A. Weisshaar. Aeroelasticity of Nonconventional Airplane Configurations — Past and Future. *Journal of Aircraft*, 40(6):1047–1065, 2003.
 - [56] M. J. Patil, D.H. Hodges, and C.E.S. Cesnik. Nonlinear Aeroelastic Analysis of Complete Aircraft in Subsonic Flow. *Journal of Aircraft*, 37(5):753–760, 2000. doi: 10.2514/2.2685.
 - [57] D. A. Peters, S. Karunamoorthy, and W-M. Cao. Finite State Induced Flow Models Part I: Two-Dimensional Thin Airfoil. *Journal of Aircraft*, 32(2):313–322, 1995.
 - [58] L. Meirovitch and I. Tuzcu. Unified Theory for the Dynamics and Control of Maneuvering Flexible Aircraft. *AIAA Journal*, 42(4):714–727, apr 2004. doi: 10.2514/1.1489.
 - [59] P.P. Friedmann. Renaissance of Aeroelasticity and Its Future. *Journal of Aircraft*, 36(1):105–121, 1999. doi: 10.2514/2.2418.
 - [60] R. Lind and M. Brenner. *Robust Aeroservoelastic Stability Analysis*. Advances in Industrial Control. Springer, London, 2012. doi: 10.1007/978-1-4471-0849-8.
 - [61] R.D. Milne. Dynamics of the Deformable Aeroplane. Technical Report 3345, British Aeronautical Research Council, London: Her Majesty’s Stationery Office, 1964.
 - [62] R. D. Milne. Some Remarks on The Dynamics of Deformable Bodies. *AIAA Journal*, 6(3):556–558, 1968.
 - [63] B. Raghavan and M.J. Patil. Flight Control for Flexible, High-Aspect-Ratio Flying Wings. *Journal of Guidance, Control, and Dynamics*, 33(1):64–74, 2010. doi: 10.2514/1.45471.
 - [64] A.R. Dusto, G.W. Brune, G.M. Dornfield, J.E. Mercer, S.C. Pilet, P.E. Rubbert, R. C. Schwanz, P. Smutny, E. N. Tinoco, and J. A. Weber. A Method for Predicting the Stability Characteristics of an Elastic Airplane. Volume 1: FLEXSTAB Theoretical Description. Technical report, NASA, 1974.
 - [65] L. Meirovitch and I. Tuzcu. Integrated Approach to the Dynamics and Control of Maneuvering Flexible Aircraft. Technical report, NASA, 2003.
 - [66] M Drela. Integrated Simulation Model for Preliminary Aerodynamic, Structural, and Control-Law Design of Aircraft. In *40th AIAA Structures, Structural Dynamics and Materials Conference*, St. Louis, Missouri, 1999. AIAA Paper 1999-1394. doi: 10.2514/6.1999-1394.
 - [67] M. J. Patil, D. H. Hodges, and C. E. S. Cesnik. Nonlinear Aeroelasticity and Flight Dynamics of High-Altitude Long-Endurance Aircraft. *Journal of Aircraft*, 38(1):88–94, 2001. doi: 10.2514/2.2738.

- [68] M.H. Love, P.S. Zink, P.A. Wieselmann, and H. Youngren. Body Freedom Flutter of High Aspect Ratio Flying Wings. In *46th AIAA/ASME/ASCE/AHS/ASC Structures, Structural Dynamics, and Materials Conference*, pages 1–23, Austin, Texas, 2005. doi: 10.2514/6.2005-1947.
- [69] M. J. Patil and D. H. Hodges. Flight Dynamics of Highly Flexible Flying Wings. *Journal of Aircraft*, 43(6):1790–1799, nov 2006. doi: 10.2514/1.17640.
- [70] M.J. Patil and D.H. Hodges. Limit-Cycle Oscillations in High-Aspect-Ratio Wings. *Journal of Fluids and Structures*, 15(1):107–132, 2001. doi: 10.1006/jfls.2000.0329.
- [71] M. J. Patil and D. H. Hodges. On the importance of aerodynamic and structural geometrical nonlinearities in aeroelastic behavior of high-aspect-ratio wings. *Journal of Fluids and Structures*, 19:905–915, 2004. doi: 10.1016/j.jfluidstructs.2004.04.012.
- [72] B. Raghavan and M.J. Patil. Flight Dynamics of High Aspect-Ratio Flying Wings: Effect of Large Trim Deformation. *Journal of Aircraft*, 46(5):1808–1812, 2009. doi: 10.2514/1.36847.
- [73] W. Su and C. E. S. Cesnik. Nonlinear Aeroelasticity of a Very Flexible Blended-Wing-Body Aircraft. *Journal of Aircraft*, 47(5):1539–1553, 2010. doi: 10.2514/1.47317.
- [74] J. Murua, R. Palacios, and J.M.R. R. Graham. Assessment of Wake-Tail Interference Effects on the Dynamics of Flexible Aircraft. *AIAA Journal*, 50(7):1575–1585, 2012. doi: 10.2514/1.J051543.
- [75] H. Hesse, R. Palacios, and J. Murua. Consistent Structural Linearization in Flexible Aircraft Dynamics with Large Rigid-Body Motion. *AIAA Journal*, 52(3):528–538, 2014. doi: 10.2514/1.J052316.
- [76] B.P. Hallissy and C.E.S. Cesnik. High-fidelity Aeroelastic Analysis of Very Flexible Aircraft. *52nd AIAA/ASME/ASCE/AHS/ASC Structures, Structural Dynamics and Materials Conference*, pages 1–22, 2011. doi: 10.2514/MSDM11.
- [77] A. Klöckner, M. Leitner, D. Schlabe, and G. Looye. Integrated Modelling of an Unmanned High-Altitude Solar-Powered Aircraft for Control Law Design Analysis. In *Advances in Aerospace Guidance Navigation and Control - Selected Papers of the Second CEAS Specialist Conference on Guidance, Navigation and Control*, pages 535–548. Springer, Berlin Heidelberg, 2013.
- [78] M. J. Patil and D. H. Hodges. Output Feedback Control of the Nonlinear Aeroelastic Response of a Slender Wing. *Journal of Guidance, Control, and Dynamics*, 25(2):302–308, 2002. doi: 10.2514/2.4882.
- [79] I. Tuzcu, P. Marzocca, E. Cestino, G. Romeo, and G. Frulla. Stability and Control of a High-Altitude, Long-Endurance UAV. *Journal of Guidance, Control, and Dynamics*, 30(3):713–721, 2007. doi: 10.2514/1.25814.
- [80] M.J. Dillsaver, C.E.S. Cesnik, and I.V. Kolmanovsky. Gust Load Alleviation Control for Very Flexible Aircraft. In *AIAA Atmospheric Flight Mechanics Conference*, pages 1–18, 2011. doi: doi:10.2514/6.2011-6368.
- [81] R. G. Cook, R. Palacios, and P. Goulart. Robust Gust Alleviation and Stabilization of Very Flexible Aircraft. *AIAA Journal*, 51(2):330–340, feb 2013. doi: 10.2514/1.J051697.
- [82] S. Haghighat, Hugh H.T. Liu, and J.R.R.A. Martins. Model-Predictive Gust Load Alleviation Controller for a Highly Flexible Aircraft. *Journal of Guidance, Control, and Dynamics*, 35(6):1751–1766, 2012. doi: 10.2514/1.57013.
- [83] R.J.S. Simpson, R. Palacios, H. Hesse, and P. Goulart. Predictive Control for Alleviation of Gust Loads on Very Flexible Aircraft. In *55th AIAA/ASME/ASCE/AHS/SC Structures, Structural Dynamics, and Materials Conference*, pages 1–25, National Harbor, Maryland, 2014. doi: 10.2514/6.2014-0843.
- [84] Y. Wang, A. Wynn, and R. Palacios. Nonlinear Modal Aeroservoelastic Analysis Framework for Flexible Aircraft. *AIAA Journal*, 54(10):1–16, 2016. doi: 10.2514/1.J054537.
- [85] C. M. Shearer and C. E. S. Cesnik. Trajectory Control for Very Flexible Aircraft. *Journal of Guidance, Control, and Dynamics*, 31(2):340–357, 2008. doi: 10.2514/1.29335.
- [86] M. Dillsaver, C. E. S. Cesnik, and I. Kolmanovsky. Trajectory Control of Very Flexible Aircraft with Gust Disturbance. *AIAA Atmospheric Flight Mechanics (AFM) Conference*, 2013. doi: 10.2514/6.2013-4745.
- [87] J.T. Betts. Survey of Numerical Methods for Trajectory Optimization. *Journal of Guidance, Control, and Dynamics*, 21(2):193–207, 1998. doi: 10.2514/2.4231.
- [88] J.T. Betts. *Practical Methods for Optimal Control and Estimation Using Nonlinear Programming*. The Boeing Company, Seattle, Washington, 2010. doi: <http://dx.doi.org/10.1137/1.9780898718577>.
- [89] R.W.H. Sargent. Optimal control. *Journal of Computational and Applied Mathematics*, 124:361–371, 2000.
- [90] B. A. Conway. A Survey of Methods Available for the Numerical Optimization of Continuous Dynamic Systems. *Journal of Optimization Theory and Applications*, 152(2):271–306, 2012. doi: 10.1007/s10957-011-9918-z.
- [91] A.E. Bryson. Optimal Control - 1950 to 1985. *IEEE Control Systems*, 16(3):26–33, 1996. doi: 10.1109/37.506395.

-
- [92] J. R. R. A. Martins and A. B. Lambe. Multidisciplinary Design Optimization: A Survey of Architectures. *AIAA Journal*, 51(9):2049–2075, 2013. doi: 10.2514/1.J051895.
 - [93] L.T. Biegler. Introduction to Dynamic Process Optimization. In *Nonlinear Programming: Concepts, Algorithms, and Applications to Chemical Processes*, chapter 8, pages 213–249. SIAM, 2010.
 - [94] J.H. Breakwell. The Optimization of Trajectories. *Society for Industrial and Applied Mathematics*, 7(2): 215–247, 1959.
 - [95] A.T. Klesh and P.T. Kabamba. Solar-Powered Aircraft: Energy-Optimal Path Planning and Perpetual Endurance. *Journal of Guidance, Control, and Dynamics*, 32(4):1320–1329, 2009. doi: 10.2514/1.40139.
 - [96] D.-M. Ma, J.-K. Shiau, Y.-J. Su, and Y.-H. Chen. Optimal Level Turn of Solar-Powered Unmanned Aerial Vehicle Flying in Atmosphere. *Journal of Guidance, Control, and Dynamics*, 33(5):1347–1356, 2010. doi: 10.2514/1.48761.
 - [97] C.R. Hargraves and S.W. Paris. Direct Trajectory Optimization Using Nonlinear Programming and Collocation. *Journal of Guidance Control and Dynamics*, 10(4):338–342, 1987. doi: 10.2514/3.20223.
 - [98] F. Fahroo and I.M. Ross. Direct Trajectory Optimization by a Chebyshev Pseudospectral Method. *Journal of Guidance, Control, and Dynamics*, 25(1):160–166, jan 2002. doi: 10.2514/2.4862.
 - [99] D.J.N. Limebeer and A.V. Rao. Faster, Higher, and Greener: Vehicular Optimal Control. *IEEE Control Systems*, 35(2):36–56, 2015. doi: 10.1109/MCS.2014.2384951.
 - [100] P. Williams. Hermite-Legendre-Gauss-Lobatto Direct Transcription in Trajectory Optimization. *Journal of Guidance, Control, and Dynamics*, 32(4):1392–1395, jul 2009. doi: 10.2514/1.42731.
 - [101] J. T. Betts and E. J. Cramer. Application of Direct Transcription to Commercial Aircraft Trajectory Optimization. *Journal of Guidance, Control, and Dynamics*, 18(1):151–159, 1995. doi: 10.2514/3.56670.
 - [102] R.G. Drury and J.F. Whidborne. Quaternion-Based Inverse Dynamics Model for Expressing Aerobatic Aircraft Trajectories. *Journal of Guidance, Control, and Dynamics*, 32(4):1388–1391, jul 2009. doi: 10.2514/1.42883.
 - [103] S. C. Spangelo and E. G. Gilbert. Power Optimization of Solar-Powered Aircraft with Specified Closed Ground Tracks. *Journal of Aircraft*, 50(1):232–238, 2013. doi: 10.2514/1.C031757.
 - [104] S. Hosseini and M. Mesbahi. Energy-Aware Aerial Surveillance for a Long-Endurance Solar-Powered Unmanned Aerial Vehicles. *Journal of Guidance, Control, and Dynamics*, 39(9):1–14, 2016. doi: 10.2514/1.G001737.
 - [105] Q. Lin, R. Loxton, and K. L. Teo. The Control Parameterization Method for Nonlinear Optimal Control: A Survey. *Journal of Industrial and Management Optimization*, 10(1):275–309, 2014. doi: 10.3934/jimo.2014.10.275.
 - [106] H.J. Kelley. Gradient Theory of Optimal Flight Paths. *ARS Journal*, 30(10):947–954, 1960. doi: 10.2514/8.5282.
 - [107] I. Spangelo. *Trajectory Optimization for Vehicles Using Control Vector Parameterization and Nonlinear Programming*. PhD thesis, Norwegian Institute of Technology, 1994.
 - [108] H. Leonpacher, S.S. Douglas, N.H. Woolley, and D. Kraft. Trajectory Optimization Involving Sloshing Media. *Optimal Control Applications and Methods*, 23(1):45–57, 2002. doi: 10.1002/oca.701.
 - [109] B. C. Fabien. Piecewise Polynomial Control Parameterization in the Direct Solution of Optimal Control Problems. *Journal of Dynamic Systems, Measurement, and Control*, 135(3), 2013. doi: 10.1115/1.4023401.
 - [110] D. Kraft. Algorithm 733; TOMP—Fortran modules for optimal control calculations. *ACM Transactions on Mathematical Software*, 20(3):262–281, 1994. doi: 10.1145/192115.192124.
 - [111] D. Kraft. A Software Package for Sequential Quadratic Programming. Technical report, DLR German Aerospace Center Institute for Flight Mechanics, Köln, Germany, 1988.
 - [112] R.W.H. Sargent and G.R. Sullivan. The Development of an Efficient Optimal Control Package. In J. Stoer, editor, *Proceedings of the Eighth IFIP Conference on Optimization Techniques, Part 2*, number November, pages 158–168. Springer, Heidelberg, 1978. doi: 10.1007/BFb0006520.
 - [113] C.C. Pantelides, R.W.H. Sargent, and V.S. Vassiliadis. Optimal Control of Multi-Stage Systems Described by High-Index Differential-Algebraic Equations. In *Computational Optimal Control*. Birkhauser, Basel, 1994.
 - [114] V.S. Vassiliadis, R.W.H. Sargent, and C.C. Pantelides. Solution of a Class of Multistage Dynamic Optimization Problems. 2. Problems with Path Constraints. *Industrial & Engineering Chemistry Research*, 33(9):2123–2133, sep 1994. doi: 10.1021/ie00033a015.
 - [115] W.F. Feehery and P.I. Barton. Dynamic optimization with state variable path constraints. *Computers & Chemical Engineering*, 22(9):1241–1256, 1998. doi: 10.1016/S0098-1354(98)00012-X.

- [116] M. Schlegel, K. Stockmann, T. Binder, and W. Marquardt. Dynamic optimization using adaptive control vector parameterization. *Computers & Chemical Engineering*, 29(8):1731–1751, 2005. doi: 10.1016/j.compchemeng.2005.02.036.
- [117] T. Binder, A. Cruse, C.A. Cruz Villar, and W. Marquardt. Dynamic optimization using a wavelet based adaptive control vector parameterization strategy. *Computers & Chemical Engineering*, 24(2-7):1201–1207, jul 2000. doi: 10.1016/S0098-1354(00)00357-4.
- [118] V.S. Vassiliadis, R.W.H. Sargent, and C.C. Pantelides. Solution of a Class of Multistage Dynamic Optimization Problems. 1. Problems without Path Constraints. *Industrial & Engineering Chemistry Research*, 33(9):2111–2122, sep 1994. doi: 10.1021/ie00033a014.
- [119] E. Polak. On the Use of Consistent Approximations in the Solution of Semi-Infinite Optimization and Optimal Control Problems. *Mathematical Programming*, 62(1-3):385–414, feb 1993. doi: 10.1007/BF01585175.
- [120] D. Leineweber, H.G. Bock, J.P. Schlöder, J.V. Gallitzendorfer, A. Schafer, and P. Jansohn. A Boundary Value Problem Approach to the Optimization of Chemical Processes Described by DAE Models. Technical report, University of Heidelberg, 1997.
- [121] D. Trivedi, D. Dienno, and C.D. Rahn. Optimal, Model-Based Design of Soft Robotic Manipulators. *Journal of Mechanical Design*, 130(9):091402, 2008. doi: 10.1115/1.2943300.
- [122] J. Xu and I. Kroo. Aircraft Design with Active Load Alleviation and Natural Laminar Flow. *Journal of Aircraft*, 51(5):1–14, sep 2014. doi: 10.2514/1.C032402.
- [123] H.K. Fathy, J.A. Reyer, P.Y. Papalambros, and A.G. Ulsoy. On the Coupling between the Plant and Controller Optimization Problems. In *Proceedings of the American Control Conference*, pages 1864–1869, Arlington, 2001.
- [124] J. Onoda and R.T. Haftka. An Approach to Structure/Control Simultaneous Optimization for Large Flexible Spacecraft. *AIAA Journal*, 25(8):1133–1138, 1987.
- [125] S.S. Rao. Combined Structural and Control Optimization of Flexible Structures. *Engineering Optimization*, 13(1):1–16, 1988. doi: 10.1080/03052158808940943.
- [126] H. Asada, J.H. Park, and S. Rai. A Control-Configured Flexible Arm: Integrated Structure Control Design. In IEEE, editor, *Proceedings of the 1991 IEEE International Conference on Robotics and Automation*, pages 2356–2362, Sacramento, California, 1991.
- [127] Z. Xianmin, L. Jianwei, and S. Yunwen. Simultaneous optimal structure and control design of flexible linkage mechanism for noise attenuation. *Journal of Sound and Vibration*, 299(4-5):1124–1133, 2007. doi: 10.1016/j.jsv.2006.08.002.
- [128] N. Alujević, G. Zhao, B. Depraetere, P. Sas, B. Pluymers, and W. Desmet. H2 optimal vibration control using inertial actuators and a comparison with tuned mass dampers. *Journal of Sound and Vibration*, 333(18):4073–4083, 2014. doi: 10.1016/j.jsv.2014.04.038.
- [129] H. Nishigaki and K. Kawashima. Motion Control and Shape Optimization of a Suitlike Flexible Arm. *Structural Optimization*, 15:163–171, 1998.
- [130] J. B. Cardoso, P. P. Moita, and A. J. Valido. Design and Control of Nonlinear Mechanical Systems for Minimum Time. *Shock and Vibration*, 15(3-4):315–323, 2008. doi: 10.1155/2008/741205.
- [131] J.T. Allison, T. Guo, and Z. Han. Co-Design of an Active Suspension Using Simultaneous Dynamic Optimization. *Journal of Mechanical Design*, 136(8):14, jun 2014. doi: 10.1115/1.4027335.
- [132] S. Suzuki. Simultaneous structure/control design synthesis for aero-servo-elastic system. *Finite Elements in Analysis and Design*, 14(2-3):197–208, 1993. doi: 10.1016/0168-874X(93)90020-Q.
- [133] S. Suzuki and S. Yonezawa. Simultaneous Structure/Control Design Optimization of a Wing Structure with a Gust Load Alleviation System. *Journal of aircraft*, 30(2):268–274, 1993.
- [134] S. Haghighat, J. Martins, and H.H.T. Liu. Aeroservoelastic Design Optimization of a Flexible Wing. *Journal of Aircraft*, 49(2):432–443, mar 2012. doi: 10.2514/1.C031344.
- [135] T. Jackson and E. Livne. Integrated Aeroservoelastic Design Optimization of Actively Controlled Strain-Actuated Flight Vehicles. *AIAA Journal*, 52(6):1105–1123, jun 2014. doi: 10.2514/1.J050941.
- [136] D.W. Zingg, M. Nemec, and T.H. Pulliam. A comparative evaluation of genetic and gradient-based algorithms applied to aerodynamic optimization. *Revue européenne de mécanique numérique*, 17(1-2):103–126, mar 2008. doi: 10.3166/remn.17.103-126.
- [137] A. Barclay, P.E. Gill, and J Ben Rosen. SQP Methods and Their Application to Numerical Optimal Control. In *Variational Calculus, Optimal Control and Applications*, volume 124, chapter SQP, pages 207–222. Springer, 1998. doi: 10.1007/978-3-0348-8802-8-21.
- [138] J. Nocedal and S.J. Wright. *Numerical Optimization*. Springer Science+Business Media, 2006.
- [139] P.T. Boggs, W. J. Tolle, and J.W. Tolle. Sequential Quadratic Programming. *Acta Numerica*, 4, 1996. doi: 10.1017/S0962492900002518.

-
- [140] P.E. Gill and M.E. Leonard. Quasi-Newton Methods for Unconstrained Optimization. *SIAM Journal on Optimization*, 12(1):209–237, 2001.
 - [141] A. Forsgren, P.E. Gill, and M.H. Wright. Interior methods for nonlinear optimization. *SIAM Review*, 44(4):525–597, 2002. doi: 10.1137/S0036144502414942.
 - [142] S.P. Han. A Globally Convergent Method for Nonlinear Programming. *Journal of Optimization Theory and Applications*, 22(3):297–309, 1977. doi: 10.1007/BF00932858.
 - [143] M.J.D. Powell. *A fast algorithm for nonlinearly constrained optimization calculations*, pages 144–157. Springer Berlin Heidelberg, Berlin, Heidelberg, 1978. doi: 10.1007/BFb0067703.
 - [144] D. Goldfarb and A. Idnani. A Numerically Stable Dual Method for Solving Strictly Convex Quadratic Programs. *Mathematical Programming*, 27(1):1–33, 1983. doi: 10.1007/BF02591962.
 - [145] A. Forsgren, P.E. Gill, and E. Wong. Primal and Dual Active-Set Methods for Convex Quadratic Programming. *Mathematical Programming*, 159(1-2):469–508, sep 2016. doi: 10.1007/s10107-015-0966-2.
 - [146] W. Sun and Y.-X. Yuan. *Optimization Theory and Methods: Nonlinear Programming*. Springer, optimization edition, 2006. doi: 10.1007/b106451.
 - [147] C.L. Lawson and R.J. Hanson. *Solving Least Squares Problems*. Society for Industrial and Applied Mathematics, Philadelphia, jan 1974. doi: <http://dx.doi.org/10.1137/1.9781611971217>.
 - [148] E. Jones, T. Oliphant, P. Peterson, and Others. SciPy: Open Source Scientific Tools for Python, 2001.
 - [149] P.E. Gill, W. Murray, and M.A. Saunders. SNOPT: An SQP Algorithm for Large-Scale Constrained Optimization. *SIAM Journal on Optimization*, 12(4):979–1006, 2002. doi: 10.1137/S1052623499350013.
 - [150] A. Wachter and L.T. Biegler. On the Implementation of an Interior-Point Filter Line-Search Algorithm for Large-Scale Nonlinear Programming. *Mathematical Programming*, 106(1):25–57, 2006. doi: 10.1007/s10107-004-0559-y.
 - [151] R.E. Perez, P.W. Jansen, and J.R.R.A. Martins. pyOpt: a Python-based object-oriented framework for nonlinear constrained optimization. *Structural and Multidisciplinary Optimization*, 45(1):101–118, may 2012. doi: 10.1007/s00158-011-0666-3.
 - [152] H. Hesse and R. Palacios. Consistent structural linearisation in flexible-body dynamics with large rigid-body motion. *Computers & Structures*, 110-111:1–14, 2012. doi: 10.1016/j.compstruc.2012.05.011.
 - [153] R. J. S. Simpson, R. Palacios, and J. Murua. Induced-Drag Calculations in the Unsteady Vortex Lattice Method. *AIAA Journal*, 51(7):1775–1779, 2013. doi: 10.2514/1.J052136.
 - [154] S. Piperno, C. Farhat, and B. Larrouturou. Partitioned Procedures for the Transient Solution of Coupled Aeroelastic Problems Part I: Model Problem, Theory and Two-Dimensional Application. *Computer Methods in Applied Mechanics and Engineering*, 124(1-2):79–112, jun 1995. doi: 10.1016/0045-7825(95)92707-9.
 - [155] S. Piperno and C. Farhat. Partitioned Procedures for the Transient Solution of Coupled Aeroelastic Problems Part II: Energy Transfer Analysis and Three-Dimensional Applications. *Computer Methods in Applied Mechanics and Engineering*, 190(24):3147–3170, 2001. doi: 10.1016/S0045-7825(00)00386-8.
 - [156] H. Hesse. *Consistent Aeroelastic Linearisation and Reduced-Order Modelling in the Dynamics of Manoeuvring Flexible Aircraft*. PhD thesis, Imperial College London, 2013.
 - [157] B.L. Stevens and F.L. Lewis. *Aircraft Control and Simulation*. John Wiley & Sons, New York, NY, USA, 1992.
 - [158] R. Palacios. Nonlinear Normal Modes in an Intrinsic Theory of Anisotropic Beams. *Journal of Sound and Vibration*, 330(8):1772–1792, 2011. doi: 10.1016/j.jsv.2010.10.023.
 - [159] L. Meirovitch. *Fundamentals of Vibrations*. McGraw-Hill, New York, NY, 2001.
 - [160] T.C. Fung. Numerical Dissipation in Time-Step Integration Algorithms for Structural Dynamic Analysis. *Progress in Structural Engineering and Materials*, 5(3):167–180, 2003. doi: 10.1002/pse.149.
 - [161] C.M. Shearer and C.E.S. Cesnik. Modified Generalized Alpha Method for Integrating Governing Equations of Very Flexible Aircraft. In *47th AIAA/ASME/ASCE/AHS/ASC Structures, Structural Dynamics, and Materials Conference*, Newport, Rhode Island, 2006. doi: 10.2514/6.2006-1747.
 - [162] R.M. James. On the remarkable accuracy of the vortex lattice method. *Computer Methods in Applied Mechanics and Engineering*, 1(1):59–79, jun 1972. doi: 10.1016/0045-7825(72)90021-7.
 - [163] S.G. Voutsinas. Vortex methods in aeronautics: how to make things work. *International Journal of Computational Fluid Dynamics*, 20(1):3–18, 2006. doi: 10.1080/10618560600566059.
 - [164] B.K. Stanford and P.S. Beran. Analytical Sensitivity Analysis of an Unsteady Vortex-Lattice Method for Flapping-Wing Optimization. *Journal of Aircraft*, 47(2):647–662, 2010. doi: 10.2514/1.46259.
 - [165] S.D. Pesmajoglou and J.M.R. Graham. Prediction of Aerodynamic Forces on Horizontal Axis Wind Turbines in Free Yaw and Turbulence. *Journal of Wind Engineering and Industrial Aerodynamics*, 86:1–14, 2000.
 - [166] G.K. Batchelor. *An Introduction to Fluid Dynamics*. Cambridge University Press, Cambridge, 2000. doi: 10.1017/CBO9780511800955.

- [167] Bret Stanford and Philip Beran. Formulation of Analytical Design Derivatives for Nonlinear Unsteady Aeroelasticity. *AIAA Journal*, 49(3):598–610, 2011.
- [168] C. Farhat and M. Lesoinne. Two Efficient Staggered Algorithms for the Serial and Parallel Solution of Three-Dimensional Nonlinear Transient Aeroelastic Problems. *Computer Methods in Applied Mechanics and Engineering*, 182(3):499–515, 2000. doi: 10.1016/S0045-7825(99)00206-6.
- [169] G.J. Kennedy. Strategies for Adaptive Optimization with Aggregation Constraints Using Interior-Point Methods. *Computers & Structures*, 153:217–229, 2015. doi: 10.1016/j.compstruc.2015.02.024.
- [170] J.R.R.A. Martins and J.T. Hwang. Review and Unification of Methods for Computing Derivatives of Multidisciplinary Computational Models. *AIAA Journal*, 51(11):2582–2599, nov 2013. doi: 10.2514/1.J052184.
- [171] Q. Wang and W. Yu. Sensitivity Analysis of Geometrically Exact Beam Theory (GEBT) Using the Adjoint Method with Hydra. In *52nd AIAA/ASME/ASCE/AHS/ASC Structures, Structural Dynamics and Materials Conference*, pages 1–15, Denver, Colorado, apr 2011.
- [172] D.N. Burghes and M.A. Graham. *Introduction to Control Theory, Including Optimal Control*. Ellis Horwood Ltd., 1980. doi: 10.1002/oca.4660020210.
- [173] K. Schittkowski. The nonlinear programming method of Wilson, Han, and Powell with an augmented Lagrangian type line search function - Part 1: Convergence Analysis. *Numerische Mathematik*, 38:83–114, 1981. doi: 10.1007/BF01395811.
- [174] K. Schittkowski. The Nonlinear Programming Method of Wilson, Han and Powell with an Augmented Lagrangian Type line Search Function - Part 2: an Efficient Implementation with Linear Least Squares Subproblems. *Numerische Mathematik*, 38:115–127, 1981.
- [175] J. Stoer. On the Numerical Solution of Constrained Least-Squares Problems. *SIAM Journal on Numerical Analysis*, 8(2):382–411, 1971.
- [176] L.T. Biegler. *Nonlinear Programming, Concept, Algorithms, and Applications to Chemical Processes*. SIAM, Philadelphia, 2010.
- [177] R.P. Brent. *Algorithms for Minimization without Derivatives*. Prentice-Hall, 1973.
- [178] R.A. Nelson and M.G. Olsson. The Pendulum - Rich Physics from a Simple System. *American Journal of Physics*, 54(2):112–121, 1986. doi: 10.1119/1.14703.
- [179] A. Belendez, C. Pascual, D.I. Mendez, T. Belendez, and C. Neipp. Exact Solution for the Nonlinear Pendulum. *Revista Brasileira de Ensino de Física*, 29(4):645–648, 2007. doi: 10.1590/S1806-11172007000400024.
- [180] M. Sabatini, P. Gasbarri, G.B. Palmerini, and R. Monti. Operational Modal Analysis via Image Based Technique of Very Flexible Space Structures. *Acta Astronautica*, 89:139–148, aug 2013. doi: 10.1016/j.actaastro.2013.04.005.
- [181] D.M. Tang and E.H. Dowell. Effects of Geometric Structural Nonlinearity on Flutter and Limit Cycle Oscillations of High-Aspect-Ratio Wings. *Journal of Fluids and Structures*, 19:291–306, 2004. doi: 10.1016/j.jfluidstructs.2003.10.007.
- [182] E.L. Burnett, B.T. Holm-Hansen, C.J. Atkinson, and P.M. Flick. Design and flight test of active flutter suppression on the X-56A multi-utility technology test-bed aircraft. *The Aeronautical Journal*, 120(1228): 893–909, 2016.
- [183] J. Reuther, J.J. Alonso, J.R.R.A. Martins, and S. Smith. A coupled aero-structural optimization method for complete aircraft configurations. *AIAA Paper 99-0187*, jan 1999. doi: 10.2514/6.1999-187.
- [184] A. Jameson and J. Reuther. Control Theory Based Airfoil Design Using the Euler Equations. In *5th AIAA/US AF/NASA/ISSMO Symposium on Multidisciplinary Analysis and Optimization, Panama City Beach, FL*. AIAA Paper 94-4272, 1994.
- [185] R. Fletcher and M.J.D. Powell. On the Modification of LDLT Factorizations. *Mathematics of Computation*, 28(128):1067–1087, 1974. doi: 10.2307/2005366.
- [186] J.R.R.A. Martins, P. Sturdza, and J.J. Alonso. The Complex-Step Derivative Approximation. *ACM Transactions on Mathematical Software*, 29(3):245–262, 2003. doi: 10.1145/838250.838251.
- [187] P.E. Farrell, D.A. Ham, S.W. Funke, and M.E. Rognes. Automated Derivation of the Adjoint of High-Level Transient Finite Element Programs. *SIAM Journal on Scientific Computing*, 35(4):C369–C393, 2013. doi: 10.1137/120873558.

Appendix A

Numerical methods for quadratic programming

Sequential quadratic programming algorithms approximate the cost function of the non-linear optimisation problem introduced in (3.41) through a series of quadratic expansion, as shown in eq. (3.48). To complement the discussion in Sec. 3.5.2, therefore, this appendix will focus on the solution of quadratic problems of the form:

$$\begin{aligned}
 \min. \quad & \frac{1}{2} \mathbf{x}^T H \mathbf{x} + \mathbf{x}^T \mathbf{g} \\
 \text{w.r.t.} \quad & \mathbf{x} \\
 \text{s.t.} \quad & \mathbf{a}_k^T \mathbf{x} = \mathbf{b}_k, \quad k \in \mathcal{E} \\
 & \mathbf{a}_k^T \mathbf{x} \geq \mathbf{b}_k, \quad k \in \mathcal{I}
 \end{aligned} \tag{A.1}$$

These problems can always be solved, or shown to be infeasible, in a finite number of computations [138]. Methods for the solution of problem (A.1) can, in particular, be classified according to the properties of the Hessian matrix H [145]. In the following, this will be assumed to be positive semi-definite, meaning that the resulting QP problem is convex. In this case, a local solution — if any exists — will also be a global minimiser; based on eq. (3.45), however, its uniqueness can only be guaranteed for strictly convex problems, hence if H is positive definite.

A.1 Primal active set strategy

At first, the case in which \mathcal{I} is an empty set will be discussed. Under this assumption, the KKT conditions (3.44) translate into the following system

$$\begin{pmatrix} H & -A^T \\ A & 0 \end{pmatrix} \begin{Bmatrix} \mathbf{x} \\ \boldsymbol{\lambda} \end{Bmatrix} = \begin{Bmatrix} -\mathbf{g} \\ \mathbf{b} \end{Bmatrix} \tag{A.2}$$

where the A matrix is defined such that its k -th row is equal to \mathbf{a}_k , i.e. $A^T = [\mathbf{a}_k], k \in \mathcal{E}$. While a solution to the equality-constrained problem can be found directly through eq. (A.2), as a preparation for the most general inequality constraints problem, it is convenient to express this in incremental form. Setting $\mathbf{x}_{j+1} = \mathbf{x}_j + \Delta\mathbf{x}$ and $\boldsymbol{\lambda}_{j+1} = \boldsymbol{\lambda}_j + \Delta\boldsymbol{\lambda}$, where j is an iteration counter, eq. (A.2) becomes:

$$\begin{pmatrix} H & -A^T \\ A & 0 \end{pmatrix} \begin{Bmatrix} \Delta\mathbf{x} \\ \Delta\boldsymbol{\lambda} \end{Bmatrix} = \begin{Bmatrix} H\mathbf{x}_j + \mathbf{g} \\ A\mathbf{x}_j - \mathbf{b} \end{Bmatrix} \quad (\text{A.3})$$

The left hand side matrix is also referred to as KKT matrix. If this is invertible, the solution of eq. (A.3) will also be associated to a global minimiser, \mathbf{x}^* , of problem (A.1) as eq. (3.45) is also satisfied [138].

When inequality constraints are present, the KKT condition in eq. (A.3) can still be exploited. In this case, however, the A matrix will need to include all the active constraints at the optimum, i.e. $A^T = [\mathbf{a}_k]$ for $k \in \mathcal{A}(\mathbf{x}^*)$. The solution process revolves, therefore, around determining the active set \mathcal{A} . An iterative strategy can be used to address this point: a working set, \mathcal{W}_j , will be used to approximate the active set \mathcal{A} , at the j -th iteration. This allows to formulate the incremental problem

$$\begin{aligned} \min. \quad & \frac{1}{2}\Delta\mathbf{x}^T H \Delta\mathbf{x} + \Delta\mathbf{x}^T (H\mathbf{x}_j + \mathbf{g}) \\ \text{w.r.t.} \quad & \Delta\mathbf{x} \\ \text{s.t.} \quad & \mathbf{a}_k^T \Delta\mathbf{x} = 0, \quad k \in \mathcal{W}_j \end{aligned} \quad (\text{A.4})$$

which can be solved for $\Delta\mathbf{x}$ through eq. (A.3). Importantly, the increment $\Delta\mathbf{x}$ will be feasible with respect to all the constraints belonging to the current working set \mathcal{W}_j . As those not belonging to \mathcal{W}_j may be violated, however, $\Delta\mathbf{x}$ is scaled through the parameter [146]

$$\alpha_j = \min \left\{ 1, \min_{k \notin \mathcal{W}_j, \mathbf{a}_k^T \Delta\mathbf{x}_k < 0} \frac{b_k - \mathbf{a}_k^T \mathbf{x}_j}{\mathbf{a}_k^T \Delta\mathbf{x}_k} \right\} \quad (\text{A.5})$$

If $\alpha_j < 1$, at the following design point $j+1$, $\mathbf{x}_{j+1} = \mathbf{x}_j + \alpha_j \Delta\mathbf{x}$, a new constraint will be activated. This is therefore included in the working set and a new solution to problem (A.4) is found.

This loop is repeated until \mathbf{x} converges, i.e. until a null increment $\Delta\mathbf{x}$ is obtained from problem (A.4). Based on the KKT conditions in eq. (3.44), however, for \mathbf{x} to be a minimiser the Lagrangian multipliers obtained from eq. (A.3) have to be negative. If this does not hold, the constraint associated to the most negative Lagrangian multiplier is dropped from the working set, and a new solution to problem (A.4) is found [138].

The approach described, also referred to as primal active set method [138, 145], is summarised by algorithm (2). It involves two loops: an external one, in which a check of the Lagrangian multipliers verifies the feasibility of the solution, and an internal one, in which the cost is minimised along feasible directions. Other strategies for the solution

of the QP problems [138, 144–146] lead, instead, to the analysis of its dual form, which is discussed in the next section.

Algorithm 2 Active set method

Requires:

arrays defining problem (A.1)

Initialisation:

assume a working set \mathcal{W}

solve KKT system (A.2) for \mathbf{x} and $\boldsymbol{\lambda}$

```

while  $\exists k \in \mathcal{W} \mid \lambda_k < 0$  : ▷ check condition (3.44d)
    remove  $k$  from working set:  $\mathcal{W} - \{k\} \rightarrow \mathcal{W}$ 
    while  $\Delta \mathbf{x} \neq \mathbf{0}$  and  $\Delta \boldsymbol{\lambda} \neq \mathbf{0}$ : ▷ check convergence sub-problem
        solve KKT system, eq. (A.3)
        compute scaling parameter  $\alpha$ , eq. (A.5)
        if  $\alpha < 1$ :
            select activated constraint:  $k \notin \mathcal{W} \mid \frac{b_k - \mathbf{a}_k^T \mathbf{x}}{\mathbf{a}_k^T \Delta \mathbf{x}_k} = \alpha$ 
            add  $k$  to working set:  $\mathcal{W} + \{k\} \rightarrow \mathcal{W}$ 
        update:  $\mathbf{x} + \Delta \mathbf{x} \rightarrow \mathbf{x}$ 
    return  $\mathbf{x}$ 

```

A.2 Least-squares method of Lawson and Henson

Starting from the KKT condition in eq. (3.44), it can be derived that problem (3.41), which will be referred to as primal, is equivalent to the dual problem [146]

$$\begin{aligned}
 & \max. && \mathcal{L}(\mathbf{x}, \boldsymbol{\lambda}) \\
 & \text{w.r.t.} && \mathbf{x}, \boldsymbol{\lambda} \\
 & \text{s.t.} && \nabla_{\mathbf{x}} \mathcal{L}(\mathbf{x}, \boldsymbol{\lambda}) = \mathbf{0} \\
 & && \boldsymbol{\lambda} \geq \mathbf{0}
 \end{aligned} \tag{A.6}$$

and that at its solution point $\mathcal{L}(\mathbf{x}^*, \boldsymbol{\lambda}^*) = I(\mathbf{x}^*)$. The concept of duality can be used to explain Lawson and Henson's method for the QP which is developed in the SLSQP algorithm.

The dual form of the QP problem (A.1), in particular, is derived from eq. (A.6) using the equality constraint

$$\nabla_{\mathbf{x}} \mathcal{L}(\mathbf{x}, \boldsymbol{\lambda}) = \mathbf{0} \quad \Rightarrow \quad \mathbf{x} = H^{-1} (A^T \boldsymbol{\lambda} - \mathbf{g}) \tag{A.7}$$

to eliminate the dependency on the design vector \mathbf{x} . This leads to

$$\begin{aligned}
 & \min. && \frac{1}{2} \boldsymbol{\lambda}^T (A H^{-1} A^T) \boldsymbol{\lambda} - \boldsymbol{\lambda}^T (\mathbf{b} + A H^{-1} \mathbf{g}) \\
 & \text{w.r.t.} && \boldsymbol{\lambda} \\
 & \text{s.t.} && \lambda_k \geq 0, \quad k \in \mathcal{I}
 \end{aligned} \tag{A.8}$$

in which the matrix inversion is possible only if H is positive definite, thus limiting the applicability of these methods to strictly convex QP problems [146].

In the constraint least-squares method of Lawson and Henson [147], problem (A.1) is defined in a least-squares form, i.e. using the cost function $|E\mathbf{x} - \mathbf{f}|^2$. This is possible whenever the Hessian can be factorised through a symmetric indefinite factorisation [174]

$$H = LDL^T \quad (\text{A.9})$$

where L and D being lower triangular and a diagonal matrix — note that if the H is positive definite, a Cholesky factorisation is retrieved ($D = I$). The equivalence with the cost function defined in problem (A.1) is obtained setting $E = D^{1/2}L^T$ and $\mathbf{f} = D^{-1/2}L^{-1}\mathbf{g}$ [174]. In the method proposed by Lawson and Henson [147], the primal problem (A.1) is recast into the dual form (A.8), which is solved through the active set approach described in algorithm (2) [174]. As it will be now explained, however, this process is made more effective by exploiting the special form of the dual problem (A.8).

For a given working set, $\mathcal{W} \subseteq \mathcal{I}$, in fact, the KKT system associated to the dual form (A.8) is

$$\begin{pmatrix} \tilde{H} & \tilde{I}^T \\ \tilde{I} & 0 \end{pmatrix} \begin{Bmatrix} \boldsymbol{\lambda} \\ \mathbf{w} \end{Bmatrix} = \begin{Bmatrix} -\tilde{\mathbf{g}} \\ \mathbf{0} \end{Bmatrix} \quad (\text{A.10})$$

where $\tilde{H} = AH^{-1}A^T$, $\tilde{\mathbf{g}} = \mathbf{b} + AH^{-1}\mathbf{g}$. The vector \mathbf{w} has values equal to the the active inequality constraints of the primal problem, i.e. $\tilde{I}^T\mathbf{w} = A\mathbf{x} + \mathbf{b}$. Importantly, the rectangular matrix associated to the active constraints gradient, $\tilde{I}(\mathcal{W})$, is such that

$$\tilde{I}(\mathcal{W})\boldsymbol{\lambda} = \boldsymbol{\lambda}_{\mathcal{W}} = \mathbf{0} \quad (\text{A.11})$$

where $\boldsymbol{\lambda}_{\mathcal{W}}$ contains only the Lagrangian multipliers of the constraints included in the working set, \mathcal{W} . This is a null vector. The incremental form of the KKT equation is also reported for completeness:

$$\begin{pmatrix} \tilde{H} & \tilde{I}^T \\ \tilde{I} & 0 \end{pmatrix} \begin{Bmatrix} \Delta\boldsymbol{\lambda} \\ \Delta\mathbf{w} \end{Bmatrix} = \begin{Bmatrix} H\boldsymbol{\lambda}_j + \tilde{\mathbf{g}} \\ \boldsymbol{\lambda}_j \end{Bmatrix} \quad (\text{A.12})$$

With reference to the general active set algorithm (2), the following simplifications are, therefore, possible. During the internal loop, the solution of the KKT system in eq. (A.12) can be limited to the degrees of freedom associated to non-active constraints as, from eq. (A.11), the Lagrangian multipliers of the active constraints are known to be zero. Furthermore, this solution does not require solving for \mathbf{w} , as $\{\tilde{I}^T\Delta\mathbf{w}\}_k = 0$, $\forall k \notin \mathcal{W}$, thus reducing the size of the matrix to be inverted. The efficiency of the process is improved further using a QR decomposition of the system and, as constraints are activated or removed, updating directly the factorising matrices [147]. Finally, during the external loop, the check of the \mathbf{w} elements signs can be done by evaluating the

residual: $\tilde{I}^T \mathbf{w} = \tilde{H} \tilde{\boldsymbol{\lambda}} + \tilde{\mathbf{g}}$, which can be non-zero only for $k \in \mathcal{W}$.

The process described leads to algorithm (3). Note that the main structure is identical to algorithm (2), but the KKT system solutions and the convergence/feasibility checks are changed. Once the Lagrangian vector is found, the design \mathbf{x} is retrieved through eq. (A.7). While this requires inverting the Hessian matrix, in a SQP implementation this operation is not required, as the inverse of the Hessian is typically obtained directly through the BFGS approximation (App. B.2).

Algorithm 3 QP solution of Lawson and Henson [147]

Requires:

arrays defining problem (A.1)

Initialisation:

compute \tilde{H} and $\tilde{\mathbf{g}}$ ▷ from primal (A.1) to dual (A.8) problem

assume all constraint active, $\mathcal{W} = \mathcal{I}$

$\boldsymbol{\lambda} = \mathbf{0}$

while $\exists k \in \mathcal{W} \mid \{\tilde{H} \tilde{\boldsymbol{\lambda}} + \tilde{\mathbf{g}}\}_k < 0$: ▷ check condition (3.44d)

remove k from working set: $\mathcal{W} - \{k\} \rightarrow \mathcal{W}$

update QR factorisation (sub-system $k \notin \mathcal{W}$)

while $\Delta \boldsymbol{\lambda} \neq \mathbf{0}$: ▷ check convergence sub-problem

solve KKT system for $k \notin \mathcal{W}$, eq. (A.12)

compute scaling parameter α , eq. (A.5)

if $\alpha < 1$:

select activated constraint: $k \notin \mathcal{W} \mid -\boldsymbol{\lambda} / \Delta \boldsymbol{\lambda}_k = \alpha$

add k to working set: $\mathcal{W} + \{k\} \rightarrow \mathcal{W}$

update QR factorisation (sub-system $k \notin \mathcal{W}$)

update: $\boldsymbol{\lambda} + \Delta \boldsymbol{\lambda} \rightarrow \boldsymbol{\lambda}$

Retrieve \mathbf{x} using eq. (A.7) ▷ speed up if H^{-1} is available

return \mathbf{x}

Appendix B

Details of the SLSQP algorithm

In this appendix, details of the SLSQP implementation (algorithm 1, [111]) introduced in Sec. 3.5 are discussed. These are the criterion of the line search ℓ_1 test function used to determine the step-length between the design points of two consecutive iterations of the optimisation process (Sec. B.1), and the BFGS method for approximating the system Hessian (Sec. B.2). The narration follows closely the textbooks from Nocedal and Wright [138] and Sun and Yuan [146], to which the reader is remanded for further details on the topic.

B.1 ℓ_1 test function

The descending direction determined through the QP approximation of problem (3.41), will generally violate the nonlinear constraints of the original problem [108, 138]. In line search methods, in particular, the search direction determined by the QP solution is not modified but the step size can be reduced: in any case, however, exploring infeasible points of the design space may be unavoidable. This, on the other hand, is not necessarily an issue as a faster path to the optimal design point may be achieved [138].

In order to determine whether a step reduction is required, merit functions can be used. These are generally built combining a term measuring the cost reduction with a penalty term, whose value increases as constraints are violated. The SLSQP algorithm, in particular, adopts an ℓ_1 penalty function of the form [138, 146]:

$$m(\alpha, \boldsymbol{\mu}) = I(\mathbf{x}) + \left(\sum_{k \in \mathcal{E}} \mu_k |c_k(\mathbf{x})| + \sum_{k \in \mathcal{I}} \mu_k \max \{0, -c_k(\mathbf{x})\} \right) \quad (\text{B.1})$$

where $\boldsymbol{\mu}$ is an array of penalty factors. In the original algorithm of proposed by Han [142], the coefficients of $\boldsymbol{\mu}$ are all assumed to be equal. Under this assumption, in fact, it can be proven that the series of design points produced by the SQP algorithm would accumulate around a KKT point of problem (3.41) [142, 146]. Better scaling and a faster convergence are, however, obtained allowing the coefficients μ_k to vary. In particular,

Powell related their magnitude to the corresponding Lagrangian multipliers, which are available from the QP sub-problem solution. More details on the method can be found in the original paper by Powell [143] or in Sun and Yuan textbook [146]. Here it is worth remarking that, while this test function leads to a computationally faster algorithm, its robustness is reduced because cycling can occur [146].

The merit function $m(\mathbf{x}_n + \alpha \Delta \mathbf{x}, \boldsymbol{\mu})$ is minimised with respect to the normalised step $\alpha \in (0, 1]$ using a modified version of Brent's method [177], which is obtained combining a Golden section search with successive quadratic minimisations [111]. In order to keep the number of analysis down, a mild criterion is used for convergence and α is accepted as long as the decrease in merit function m is large enough. This is verified through the Armijo-like condition [138]

$$m(\mathbf{x}_n + \alpha \Delta \mathbf{x}, \boldsymbol{\mu}) \leq m(\mathbf{x}, \boldsymbol{\mu}) + \eta \frac{\partial m}{\partial \alpha}(\mathbf{x}, \boldsymbol{\mu}) \alpha, \quad \eta \in (0, 1) \quad (\text{B.2})$$

where $\frac{\partial m}{\partial \alpha}$ is the directional derivative of m along the direction $\Delta \mathbf{x}$, which can be cheaply computed starting from the gradients of cost and constraints, \mathbf{g} and \mathbf{A} , at point \mathbf{x}_n .

B.2 Approximation of Hessian matrix

Finally, the Broyden, Fletcher, Goldfarb and Shanno (BFGS) approximation, used for estimating the Hessian $\nabla_{xx}^2 \mathcal{L}(\mathbf{x}_n)$ appearing in the quadratic sub-problem (3.48), is discussed. This approach is used in a wide range of optimisation algorithms, based on both line search and trust region methods, as it can achieve super-linear convergence using a model of $\mathcal{L}(\mathbf{x})$ which solely uses informations about its gradient.

The starting point for deriving this approximation is the assumption that Lagrangian \mathcal{L} is quadratic with respect to the design vector \mathbf{x} , i.e.

$$\mathcal{L}(\mathbf{x}_n + \Delta \mathbf{x}, \boldsymbol{\lambda}) = \mathcal{L}(\mathbf{x}_n, \boldsymbol{\lambda}_n) + \nabla^T \mathcal{L}(\mathbf{x}_n, \boldsymbol{\lambda}_n) \Delta \mathbf{x} + \frac{1}{2} \Delta \mathbf{x}^T B_n \Delta \mathbf{x} \quad (\text{B.3})$$

where the approximation of the Hessian, $B_n \approx \nabla_{xx}^2 \mathcal{L}(\mathbf{x}_n, \boldsymbol{\lambda}_n)$, has been introduced. Enforcing that this approximation estimates exactly the gradient at the points \mathbf{x}_n and $\mathbf{x}_{n+1} = \mathbf{x}_n + \Delta \mathbf{x}$ implies that B_n has to verify the secant equation [138]

$$B_n \Delta \mathbf{x} = \mathbf{Y} \quad (\text{B.4})$$

where $\mathbf{Y} = \nabla \mathcal{L}(\mathbf{x}_{n+1}, \boldsymbol{\lambda}_n) - \nabla \mathcal{L}(\mathbf{x}_n, \boldsymbol{\lambda}_n)$. It can be shown that such a matrix exists only if the curvature condition,

$$\Delta \mathbf{x}^T \mathbf{Y} > 0 \quad (\text{B.5})$$

is true [146]. If this does not hold, \mathbf{Y} can be modified according to Powell correction [143, 146], which is based on geometrical considerations.

Other conditions can be imposed to define B_n . Therefore, this is assumed to be symmetric and, based on the optimality condition in eq. (3.45), positive definite. Note, however, that this condition does not necessary apply to the Hessian of the Lagrangian unless the problem is unconstrained [138]; while this makes the BFGS update less effective for constrained problems, the technique still performs adequately in practice. These relations, however, are still not sufficient for uniquely defining B_n . Therefore, this must be obtained from an optimisation problem that selects, amongst all the possible choices for B_n , the one which minimises the difference with respect to the Hessian at the previous time-step (Davidon-Fletcher-Powell scheme [138]). Another option consists, instead, in solving this problem for the inverse of B , $R = B^{-1}$. This idea originated from unconstrained optimisation theory, where the B matrix coincides with the KKT matrix to be inverted — see eq. (3.47), and leads to the following problem

$$\begin{aligned}
 \min. \quad & \|R_n - R_{n-1}\| \\
 \text{w.r.t.} \quad & R_n \\
 \text{s.t.} \quad & R_n = R_n^T \\
 & R_n \mathbf{Y} = \Delta \mathbf{x}
 \end{aligned} \tag{B.6}$$

where $\|\cdot\|$ indicated the Frobenius norm [138]. The solution to problem (B.6) provides the BFGS update formula:

$$R_{n+1} = R_n + (I - \rho \Delta \mathbf{x} \mathbf{Y}^T) R_n (I - \rho \mathbf{Y} \Delta \mathbf{x}^T) + \rho \Delta \mathbf{x} \Delta \mathbf{x}^T \tag{B.7}$$

where $\rho = (\mathbf{Y}^T \Delta \mathbf{x})^{-1}$ and \mathbf{Y} is corrected according to Powell formula if the curvature condition, eq. (B.5), is not verified [143, 174]. Note that this problem does not explicitly required R to be positive-definite; however, it can be shown that this property is verified as long as the first term of the series, R_0 , does it [138]. No preferred criterion exists, however, for approximating R_0 ; a common, computationally cheap, strategy — also adopted in this numerical implementation, consists in initialising it as an identity matrix [111, 138, 174]. An advantage of the BFGS method is that it allows to only store and update the LDL factorisation of R [185].

An analogous update formula can be obtained for the Hessian approximation $B = R^{-1}$. In the SLSQP algorithm, however, this is not necessary as only R is required for setting up the dual problem (A.8) and converting, through eq. (A.7), the dual solution into updates of the design vector, $\Delta \mathbf{x}$.

Appendix C

Gradient convergence test

The gradient of the cost and constraints functions of the optimal control problems proposed in Chap. 4, 5 and 6 are all computed by forward finite-differences:

$$\tilde{\nabla} I_i = \frac{I(\mathbf{x} + \Delta x \mathbf{e}_i)}{\Delta x} \quad , \quad i = 1 \dots N_x \quad (\text{C.1})$$

where $\tilde{\nabla} I$ is numerical gradient of the generic function I , Δx the FD step-size and \mathbf{e}_i the i -th unit vector in the N_x -dimensional space where the design parameters vector, \mathbf{x} , is defined. The choice of the step-size is not trivial as eq. (C.1) is subjected to both truncation (Δx too large) and subtractive cancellation (Δx too small) errors [170]. If a closed-form expression of I is available, the optimal choice of Δx will typically only depend on the machine precision, which drives the cancellation error [186]. Determining the state of the aeroelastic system described in Chap. 2 however, requires solving a Newton-Raphson iteration at each time-step of the numerical integration process (Sec. 2.1.7). Therefore, the accuracy of eq. (C.1) also depends on the relative tolerance used to establish the convergence of this process.

As a reference value is not available, the accuracy of the FD-computed gradient $\tilde{\nabla} I$ is estimated through the second-order Taylor reminder [187]:

$$\mathcal{T} = \left| I(\mathbf{x} + h\delta\mathbf{x}) - I(\mathbf{x}) - h \delta\mathbf{x} \cdot \tilde{\nabla} I(\mathbf{x}) \right| = \mathcal{O}(h^2) \quad (\text{C.2})$$

which is obtained from the first order Taylor expansion of I around point \mathbf{x} in the direction $\delta\mathbf{x}$; h measures the size of the perturbation. If the FD-gradient is accurate, in particular, the Taylor reminder \mathcal{T} should be of order $\mathcal{O}(h^2)$, eq. (C.2). The FD step-size Δx used for evaluating the gradient can, therefore, be optimised so as to minimise \mathcal{T} .

This approach has been used to adjust the step-size Δx used to compute the gradients associated to the optimisation studies in Chap. 4 and 5. To this aim, the residual \mathcal{T} associated to the cost function of problem (4.8) has been considered. Its convergence with respect to the perturbation size h has been studied for pendula of different flexibilities and for both DSS and B-spline parametrisation. Typical trends are shown in Fig. C.1

for the case of a stiff pendulum $l_3 = 0.1$ m actuated using both a DSS (Fig. C.1a) and a B-splines (Fig. C.1b) parametrised torque — in both cases, the maximum excitation frequency is set to 2 Hz. The FD gradient $\tilde{\nabla}I$ has been computed according to eq. (C.1) assuming different normalised step-sizes, Δx , and for each a different $\mathcal{T} = \mathcal{T}(h)$ trend is obtained.

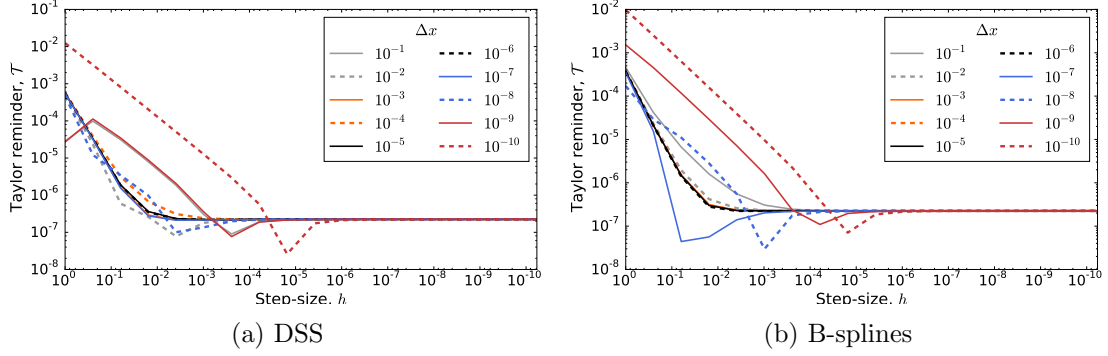


Figure C.1: Second-order Taylor reminder, \mathcal{T} , as a function of the perturbation size, h . The FD gradient is computed for different steps, Δx .

As observed in the region $h > 10^{-3}$ of both Fig. C.1a and Fig. C.1b, the steepest convergence rates are obtained when $\Delta x \approx 10^{-4} \div 10^{-6}$. This is, in fact, the case in which the order of magnitude of Δx approaches the tolerance used for determining the convergence of the Newton-Raphson iteration, and the truncation error is of the same magnitude of the cancellation error. As h tends to zero, all curves flatten as the evaluation of \mathcal{T} according to eq. (C.2) becomes inaccurate. The Taylor reminder, in particular, becomes of the order of the tolerance used during the Newton-Raphson iteration.

It is finally worth noticing that, as nonlinearities are introduced by the structural solution (the UVLM is otherwise linear, 2), the convergence of the Taylor residual for the problems considered in Chap. 6 follows very similar trends to the one shown in Fig. C.1. Even in this case, optimal FD step-size were found to be of the order of the tolerance used in the time-marching scheme.